Photoelastic study of dense granular free-surface flow rheology and size segregation

Amalia Lucia Thomas

Christ's College
University of Cambridge

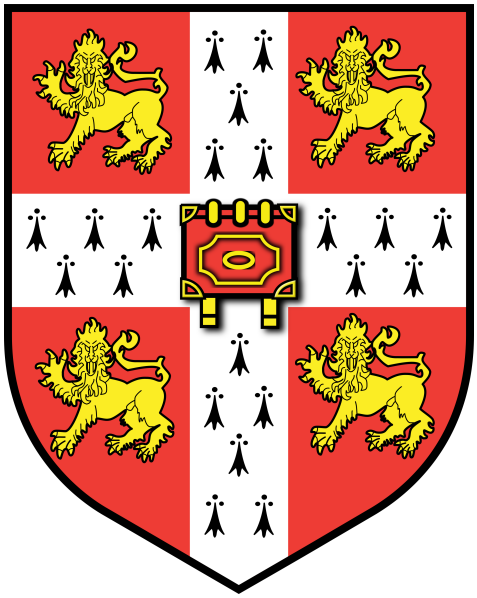

This dissertation is submitted for the degree
of Doctor of Philosophy

September 2019

I declare that this dissertation is the result of my own work and includes nothing which is the outcome of work done in collaboration except as declared in the Preface and specified in the text.

It is not substantially the same as any that I have submitted, or, is being concurrently submitted for a degree or diploma or other qualification at the University of Cambridge or any other University or similar institution except as declared in the Preface and specified in the text. I further state that no substantial part of my dissertation has already been submitted, or, is being concurrently submitted for any such degree, diploma or other qualification at the University of Cambridge or any other University or similar institution except as declared in the Preface and specified in the text.

It does not exceed the prescribed word limit for the relevant Degree Committee.

Photoelastic study of dense granular free-surface flow rheology and size segregation

Amalia Lucia Thomas

Abstract

One of the biggest challenges facing experimental studies of granular rheology is the opacity of the constitutive particles, which prevents direct observations of their behaviour and interactions. This thesis describes a series of original experiments where instantaneous forces between individual particles within the bulk of 2D flows are quantified. The specific type of granular flow we study is gravity-driven, dry, and in the slow to intermediate regime. Here we describe a novel adaptation of the photoelastic technique and explain how we applied it in an original setup to offer unprecedented insight into the force distribution within granular flows, as this has never been achieved experimentally in dynamic systems before.

Firstly, using particle tracking and photoelastic force measurements we report coarse-grained profiles for packing fraction, velocity, shear rate, inertial number, and stress tensor components, as well as statistical observations drawn from the measurable forces. Despite the highly fluctuating and seemingly random nature of the force network, we draw analogies between discrete and continuous flow models and characterise force chain preferential orientations.

Secondly, we interpret current rheological models in the context of our experimental system, and hence propose that non-local effects may in fact be dependent on the local force network fluctuation rate. The results of this work further the community's understanding of granular force networks and complement the physical concepts applied in current non-local rheological models. Finally, we model how differences in the force network between mono- and bi-disperse avalanching granular media lead to the mechanisms that drive granular size segregation. This work then also provides quantitative, tangible support to granular segregation models based on the physical mechanisms that drive it.

As the first experimental observations of their kind, our experiments can be used to validate existing and even future theoretical and numerical research. Furthermore, the physical mechanisms proposed in this work can be used to construct future models of granular behaviour that lie beyond the scope of this particular thesis.

To my family.

Contents

CHAPTER 1

Introduction

Synopsis

We introduce the lines of research within granular flows that this thesis addresses. In particular, we are interested in the dynamics of dense, cohesionless, single-phase flows, and in how these differ from classical fluids. In addition, we want to physically explain what properties of granular flows cause phenomena that are specific to granular media only, focusing on size segregation. In this introductory chapter we present a review of the current literature on these topics, and point out the areas that remain unexplained. The areas motivate our study relate to (1) the effect of side-wall friction, (2) non-local rheology models, and (3) granular size segregation, and for each subtopic we present the concise questions that we aim to answer in this dissertation. Finally, we lay out the structure of this thesis and specify how each section contributes to addressing our motivating fundamental questions.

1.1 Scope of interest

Granular materials can display behaviours reminiscent of solids, liquids or even gasses depending on the mean particle energy. Analogies with such systems has helped characterize different granular regimes, but particularly intermediate-energy systems, resembling fluids, often present properties that are unique to granular structures [60]. Examples of granular-specific phenomena, that are not present in classical fluids are the *Reynold's dilatancy* of granular flows [108], *Janssen's pressure saturation* of granular piles [63], and shear induced [7] segregation of particles by size, density, shape or surface properties [115]. In this fluid-like regime the marked differences with classical fluids are attributed to the existence of static friction; the fact that temperature

does not play a role, as thermal energy (as separate from granular temperature) is usually too weak to affect the motion of the particles; and the fact that inter-particle interactions are primarily inelastic [61]. Until the roles of these differences are fully understood it will be difficult to develop a unified theory for the rheology of granular flows. The combined complexities of inter-particle interactions result in the uneven distribution of forces: in granular systems stresses are not evenly distributed among all particles, but travel through well-defined paths called force chains [85]. As a result some particles in the bulk of a granular system are not subjected to any force other than their own weight (*rattlers*), while others carry more than the average. This work therefore focuses on the characterization of force chains in dynamic granular flows, considering chains to be the result of the combined effect of the properties that make granular systems unique and that are difficult to evaluate individually.

According to dimensional analysis, dry granular flows can be characterised by the dimensionless inertial number [41]

$$I \equiv \frac{\dot{\gamma} d}{\sqrt{P/\rho_0}}, \tag{1.1}$$

where $\dot{\gamma}$ represents the shear rate, d the particle diameter, P the pressure and ρ_0 the density of the particle material. The inertial number can be interpreted as the ratio between a microscopic timescale, $d/\sqrt{P/\rho_0}$, related to the time taken by particles to fall into a gap of size d under pressure P, and the macroscopic timescale, given by $1/\dot{\gamma}$, linked to the plastic deformation of the material. As defined, I is a local variable (that depends on the state of the system at each point only) and its value roughly specifies the regime of a granular system according to the following categories [26, 20]:

- Quasi-static regime, when $I \lesssim 10^{-3}$,
- Dense flow or intermediate regime, when $10^{-3} \lesssim I \lesssim 1$,
- Collisional flow, when $1 \lesssim I$.

The exact thresholds that define each regime may vary depending on the choice of definitions for the constitutive variables, $\dot{\gamma}$, d, P and ρ_0 [41, 38]. In addition, the transition between regimes is not abrupt but gradual, and it is yet unclear how far into the quasi-static and collisional regime the models for intermediate flows are valid, and vice-versa. Thus, besides the differences between granular behaviour and the corresponding continuum analogy, we are also interested in better characterising the transition between static and flowing regions.

The experiments from which the results of this dissertation are drawn make a novel use of an experimental technique based on the material property of *photoelasticity*,

which is described in detail in Chapter 2. The technique has never before been applied to measure dynamic forces on discs that are not force-balanced due to technological restrictions that we have overcome. Applying the photoelastic technique we directly observe and quantify inter-particle forces in the bulk of two-dimensional free-surface, gravity-driven 2D flows. The flows we produce contain regions that range from quasi-static to dense-inertial regime, so we can also investigate the applicability of current rheology models to the transition. We thus study the force network and investigate which aspects of it cause behaviours that cannot be seen in continuum models for classical solid and fluid media.

To summarise, the overarching objective of this thesis is to investigate the distribution of forces in free-surface granular flows. Because 'granular flows' involve a very wide range of geometries and regimes, we focus our study on two-dimensional free-surface avalanches of discs down an inclined narrow chute which contain regions in quasi-static and dense inertial regimes. Unlike in classical fluids, forces in granular media are distributed unevenly along paths called force chains. However, despite this marked difference in the fundamental structure of force distribution, granular media are often modelled as a continuous phase. Our first aim is to characterise the distribution of forces while assessing how side-wall friction affects our results. Secondly, we wish to evaluate existing rheology theories in an experimental context to test the fundamental physical processes they assume relate the flow kinematics to the dynamics. Finally, given the success of the continuum approach towards describing some granular behaviour, we want to explain the properties of granular force distribution that are behind phenomena that do not occur in classical fluids. We particularly focus on one granular-specific phenomenon with many industrial and natural applications, *size segregation*, by which particles of different sizes naturally tend to move towards different locations in a granular flow.

1.2 Free-surface flows

1.2.1 Granular avalanches

Gravity-driven, free-surface granular flows are very common both in nature and in industry. We define these flows as mixtures of a loose solid phase and an interstitial fluid which naturally move down a slope due to the sole action of gravity [106]. We focus specifically on the cases where the interstitial fluid does not have a significant role in the transport of momentum (*single-phase flows*). In addition, we assume that the discrete particles that make up the solid phase do not exert tensile forces between each other (they are *cohesionless*). By not considering the effect of cohesion and interstitial

fluids, we constrain the variables of our study while remaining physically relevant to many real-life applications.

It is known that the slope on which a granular material rests needs to be greater than a certain angle before the downslope component of gravity exceeds the mean static friction between particles, and flow can be initiated [76]. The maximum angle of inclination (with respect to the direction normal to gravity) at which a granular material can stay at rest is called the *static angle of repose*, θ_s, and its tangent defines the effective static coefficient of friction,

$$\tan(\theta_s) = \mu_s. \tag{1.2}$$

On the other hand, when the slope of a gravity-driven granular flow is reduced below the *dynamic* angle of repose, the flow will freeze. The static angle of repose is generally larger than the dynamic angle, and avalanches may be triggered when a static pile is inclined at an angle between the two. Moreover, between two critical slopes there exists a minimum height $h_{stop}(\theta)$ [103] below which the particles are motionless, and if a flow thins to this value it will freeze too. This is evidenced by a deposited layer that remains after avalanches have passed. The mechanisms that drive the initiation, length and stopping of an avalanche are complex and remain an open line of investigation [66, 4], but for a given influx of particles a continuous steady-state flowing regime can be investigated.

1.2.2 Effect of side-walls in narrow channels

The packing fraction and velocity profiles of granular flows in narrow channels are greatly affected by side-wall friction [120]. Jop *et al.* (2005) [66] reported that, for the same flow rate per unit width, flows are thinner and faster in narrow channels, when compared to the velocity profiles in a wide channel. Steady flows in a narrow channel have a linear velocity profile (rather than a Bagnold or exponential profile) near the free surface followed by an exponential tail into a quasi-static, or creeping, layer below. Many authors [121, 66, 28, 5, 37] agree on the shape of the velocity profile of the top flowing layer, but the distance into the bottom layer to which the particles creep has not been fully characterised yet. Understanding how a flowing layer in the dense inertial regime interacts with a quasi-static layer below can have important implications to our understanding of entrainment [19, 86, 58], which is an open topic with important physical implications [28].

Taberlet *et al.* (2003) [121] proposed that the heap in the quasi-static regime is stabilised by the flowing layer above it due to side-wall friction increasing with the depth-integrated pressure. The argued that for a steady flux a *side-wall stabilised heap*

or *super-stable heap* (SSH) will increase the angle of the flowing layer such that at this angle ϕ (different from the chute inclination angle, θ) the driving force (the downstream component of gravity) exceeds not only the friction between particle layers, but also the friction with the walls, which increases with depth from the free surface. They thus modelled, from force balance,

$$\tan\phi = \mu_s + \mu_w \frac{H}{W}, \tag{1.3}$$

where μ_w is an effective coefficient of friction between the particles and the walls, H is the depth of the flowing layer and W the width of channel.

According to this model, the inclination of the free surface is a consequence of the wall friction and is not an intrinsic property of the rheology of the granular material [66, 111]. The rheology of flows in narrow channels will be affected by the increase in the shearing forces with depth from the free surface: complemented by lateral friction, the ratio between shear and normal stress, μ, decreases when going deeper in the pile. Then, at the depth from the free surface where μ reaches the yield threshold, the material should stop and the SSH begins [68]. However, in practice the transition between flow and SSH is not abrupt, and creeping can be seen at depths where $\mu < \mu_s$. Beyond this explanation, there is yet no model for the rheology of flows in narrow channels that include the effect of side-wall friction explicitly [120].

The work discussed in later chapters of this thesis is closely concerned with the effect of side-walls. All the theories cited [66, 121, 68, 120, 111] apply to granular flows in narrow channels where the width $W > nd$, for a natural number n and the average particle diameter d. In the experiments described in this work $W \simeq d$, making the system quasi-two-dimensional.

1.3 Rheology models

1.3.1 Local, $\mu(I)$ rheology

A key parameter to the rheological description of granular flows is the stress ratio μ. Given the constitutive relationship between the flow internal stress tensor, $\bar{\bar{\sigma}}$, and the rate of strain tensor, $\bar{\bar{\mathcal{T}}}$,

$$\bar{\bar{\sigma}} = P\bar{\bar{\mathcal{I}}} + \frac{\mu P}{||\bar{\bar{\mathcal{T}}}||}\bar{\bar{\mathcal{T}}}, \tag{1.4}$$

where the double-bar notation denotes second-order tensors, $\bar{\bar{\mathcal{I}}}$ is the identity tensor, P is the pressure calculated as the trace of the symmetric stress tensor, and the variable

μ represents the ratio between shear and normal stress [80],

$$\mu = \frac{\tau}{P}, \tag{1.5}$$

where τ represents the shear stress. An important step in our understanding of granular rheology was given when the variable μ was described in terms of the constitutive particle friction coefficient and a volume fraction (implicit in the definition of density, ρ_0) depending solely on the inertial number I [41] (defined in Equation 1.1). This hypothesis implies that rheology depends only on the local value of the variables, namely that the local shear stress depends only on the local shear rate. Rheological models that follow this logic are therefore called *local rheology models*.

In addition, a widely accepted property of gravity-driven granular flows is their ability to flow only when the angle of inclination exceeds a critical angle of repose [88]. By drawing an analogy between the stress ratio and the particle friction coefficient, local rheology models represent granular systems much like Bingham fluids, with an incipient yield stress ratio, μ_s. Several attempts were therefore made to model the rheology of granular flows as Bingham fluids, with a critical shear stress below which no flow is possible and a complex dependence of the internal stresses on shear rate when flowing. The yield value of stress ratio, μ_s, is interpreted as a constant static coefficient of friction, and for flowing media local models propose μ is a function only of the dimensionless inertial number I (Equation 1.1), $\mu = \mu(I)$.

For small ranges of I ($10^{-4} \leq I \leq 0.2$), Da Cruz *et al.* (2005) [26] proposed from simulations that

$$\mu(I) = \mu_s + aI, \tag{1.6}$$

for a constant a. Later Hatano (2007) [51] built on their results to propose a power law instead

$$\mu(I) = \mu_s + aI^n. \tag{1.7}$$

Jop *et al.* (2006) [67] studied a wider range of inertial numbers, $I \approx 0.01 - 0.5$, of flows in the slow to intermediate regime, and furthermore proposed a model that incorporates observations from simulations [26, 56] and experimental [104, 117] studies, where μ tends to a limiting value, μ_2, for high values of I. The model they proposed for the relationship between μ and I, that captures all these characteristics, is

$$\mu(I) = \mu_s + \frac{\mu_2 - \mu_s}{I_0/I - 1}, \tag{1.8}$$

where I_0 is a constant to be found empirically for each system.

1.3.2 Non-local rheology

Local rheology theory is based on the assumptions that the shear stress τ depends only on the local shear rate $\dot{\gamma}$ and pressure P [38], and that there is no flow when $\mu < \mu_s$. Although this may be true in some scenarios, for instance in the triggering of an avalanche, the basic assumptions of a local rheology fail to explain dynamic phase transitions [43, 16], shear banding [97] or apparent 'creeping zones' [109, 15]. A wide range of phenomena, such as size-dependent flow thresholds [103], nozzle jamming at a finite opening [13, 116], and secondary rheology [95, 107] have been associated with *non-local* effects. Motivated by this lack of explanation, *non-local* rheology theories aim to model relationships between the stress tensor and various state variables, different from $\dot{\gamma}$. Several such models have been proposed [90, 93, 64, 96, 110, 75], but for the moment there still lacks a universal theory that captures the fundamental physics behind the vast variety of non-local phenomena [52, 72], and that is moreover well-posed [81, 9].

The foremost problem facing granular rheology studies is the discord over a clear-cut set of state variables from which to derive forces. A key concept introduced to describe granular flow rheology is *fluidity*. In classical fluid dynamics, the fluidity f refers to the inverse of the viscosity [11],

$$f = \frac{\dot{\gamma}}{\tau}. \tag{1.9}$$

This definition conceptually implies that a low fluidity refers to a solid-like behaviour while a high fluidity refers to a system that is more similar to a liquid.

Pouliquen & Forterre (2009) [105] proposed an original description of non-locality based on the idea of a process activated by force-chain fluctuations. In their analogy with viscous liquid state transitions, *temperature* is defined by the rate of rearrangements in the force network, rather than individual particle fluctuations as is done in thermal systems. They assumed the rate of plastic deformation, $\dot{\gamma}$, proportionally affects the rate of generation of new random force network within a granular flow.

Cooperative model

Based on this principle, Kamrin & Koval (2012) [71] proposed an analogy between granular systems and the Kinetic Elasto-Plastic model [70]. In this model plastic events trigger other plastic events near them, introducing the notion of local stress diffusion. They therefore define the lengthscale ξ as the *cooperative length*, which characterises the distance to which motion at one point affects the state of other points. According to local rheology, given a yield shear stress τ_y, the local fluidity $f_{loc}(\tau < \tau_y) = 0$, but

ξ defines the range of *non-locality*, along which the real fluidity f is an extension of the local fluidity f_{loc}. For a flow varying only in $\hat{z}$, this is done mathematically by introducing a non-local Laplacian term:

$$f - f_{loc} = \xi^2 \frac{\partial^2 f}{\partial z^2}. \tag{1.10}$$

For granular flows, Kamrin & Koval (2012) [71] argued that as it is friction that determines the closeness to yielding, in contrast to standard fluids, the dynamic friction between particles that defines the shear stress τ between layers is expected to be affected by the pressure. Hence, Kamrin & Koval (2012) [14, 71] additionally suggested that for granular materials the constitutive relationship for the granular fluidity g should be rescaled by the pressure under the definition

$$g = \frac{\dot{\gamma}}{\mu}. \tag{1.11}$$

Using the expression for local rheology derived from Equation 1.8

$$I(\mu) = \mathcal{H}(\mu - \mu_s)\frac{(\mu - \mu_s)}{b}, \tag{1.12}$$

where $b = (\mu_2 - \mu_s)/I_0$ and $\mathcal{H}$ represents the Heaviside function, and combining it with Equation 1.1 to model $\dot{\gamma}$, the *local* granular fluidity is defined

$$g_{loc} = \mathcal{H}(\mu - \mu_s)\frac{\mu - \mu_s}{bd\mu}\sqrt{\frac{P}{\rho}}. \tag{1.13}$$

By then fitting parameter ξ to the non-local law extended from Equation 1.10

$$g - g_{loc} = \xi^2 \frac{\partial^2 g}{\partial z^2}, \tag{1.14}$$

where g is defined by Equation 1.11 and g_{loc} by Equation 1.13, the cooperative length-scale ξ for each specific system can be calculated.

Gradient expansion model

Bouzid *et al.* (2015) [15] took a different approach to model the non-locality principle proposed by Pouliquen & Forterre (2009) [105]. They pointed out that the cooperative motion of particles not only facilitates flowing when a given point is surrounded by a more fluid zone, but it also resists flowing when it is surrounded by a more solid neighbourhood. Both flow-encouraging and flow-discouraging behaviours are captured by their alternative granular fluidity model based on the introduction of *relative fluidity*,

κ, such that

$$\kappa = l^2 \frac{\nabla^2 f}{f}, \tag{1.15}$$

where l represents their definition of *cooperative length-scale* of the order of a few particle diameters.

Bouzid *et al.* (2015) [15] added that the fundamental definition of fluidity proposed should be a *state variable*; g should be given by a coarse-grained field determined from the state of the system. In other words, the fluidity must be a coarse-grained field that can be determined from the state of the system, and does not depend on the stress tensor which is not a state variable itself. They showed that otherwise in a non-homogeneous system fluidity will not be continuous across a stress discontinuity.

Indeed, Bouzid *et al.* (2015) [15] challenge whether the granular fluidity g should be defined as the inverse of viscosity at all, as viscosity only really has meaning in classical fluid dynamics. They unify the definition for fluidity as

$$g = \frac{\dot{\gamma}}{\mathcal{Y}} \tag{1.16}$$

and propose expanding the constitutive relation around $\mathcal{Y} = \mu(I)$, valid in the homogeneous case, as

$$\mathcal{Y} = \mu(I)\chi(\kappa), \quad \text{with} \quad \chi(\kappa) \simeq 1 - \kappa + \mathcal{O}(\kappa^2). \tag{1.17}$$

To solve the resulting differential equation to predict a velocity profile, Bouzid *et al.* (2015) [15] suggest several alternative definitions for fluidity, which they stress need not be the inverse of viscosity. Among their suggestions they include the difference between number of contacts per grain and number of sliding contacts per grain (distance to isostaticity); the distance $\phi_c - \phi$ where ϕ represents the local volume fraction and ϕ_c the volume fraction at the limit $I \to 0$; and finally they settle on using the inertial number I, which requires the assumption of a quasi-incompressible system (which may not be true in granular solid-like state [9]).

1.3.3 Motivating questions: Microscopic description of granular fluidity

It has been established that granular fluidity can be modelled from a mathematical perspective and tailored empirically to specific systems. However, a great challenge in the field remains that there still exists no consensus on what the physical mechanisms responsible for non-local effects are. Indeed, the concept of granular fluidity remains physically unexplained. The fluidity g influences the flow by relating the local stress

and strain rate through Equation 1.11 or 1.16, but there is still no agreement on how to describe g in terms of kinematically observed state variables only.

Several different microscopic variables have been used to describe non-local effects. For examples, Pouliquen & Forterre (2009) [105] described stress diffusion through stress fluctuations, Jop *et al.* (2012) [69] connected granular fluidity (as the inverse of viscosity) to the standard deviation of the strain-rate tensor, and Zhang & Kamrin (2017) [133] proposed that granular fluidity can be well described in terms of only velocity fluctuations, δv, and packing fraction, ϕ, as

$$g = \frac{\delta v}{d} F(\phi), \tag{1.18}$$

where d is the particle diameter and F is a function that defines the dependency of g with ϕ.

All the models proposed have been verified against numerical simulations for specific systems but not experimentally. In this work we make direct observations of the forces that cause localised rearrangements in areas where no motion would be expected according to local rheology models. Hence, we aim to use our novel insight into the force network to explain the physical mechanisms that drive non-local effects.

1.4 Size segregation

1.4.1 Impact of the phenomenon

Segregation is one of the phenomena that is characteristic of granular media. This phenomenon cannot occur in classical fluids and therefore is an example of the insufficiency of granular flow models built through analogies with continuum fluid dynamics. In contrast to classical fluids where mixing is enhanced by shearing motions, in granular systems shear [7] can drive the segregation of particles by size, density, shape or surface properties. The scope of this work covers dense, dry granular avalanching scenarios where cohesionless particles [83] that only differ in size separate because each group has preference for a certain location. In broad terms, the initial avalanche dilation causes the appearance of gaps in the bulk, into which smaller particles percolate preferentially and then lever the larger ones upwards. As a result the fully developed avalanche is segregated with an inversely-graded particle size distribution, defined [89] as big particles flowing above the small ones. Then, since the flow is faster farther from the base, the large particles tend to accumulate at the avalanche front, where they are overrun, and recirculated by segregation [47].

Segregation can occur at impressively fast rates and have significant impact on

avalanche dynamics, due to a feedback between particle size distribution and flow rheology. In nature, segregation is instrumental to the entrainment, deposition and transport of materials in rock [87, 39, 23] and snow avalanches [49, 78, 118, 10], debris flows [57, 128] and dense pyroclastic flows [18, 59]. The understanding of such flows can lead to more accurate hazard predictions and improved safety measures [24]. In addition, segregation-driven sedimentation is a critical factor in the shaping of the coastal geomorphology [98] and the formation and migration of sand dunes [6, 55].

In industry segregation can be exploited when sorting different components of a mixture (for example in the separation of different types of garbage). In contrast, when the aim of mixing is to obtain a uniform granular material, segregation can be problematic, as occurs in the processing of pharmaceutical [119, 79], agricultural [82], chemical [12, 31, 91] and metal powders [17]. Therefore, a precise model for this phenomenon, taking into account the microscopic particle characteristics and macroscopic flow properties, could lead to higher efficiencies in numerous production processes [124].

1.4.2 Models based on physical mechanisms

Although the phenomenon had been previously observed, investigations of segregation in inclined chute flows date back thirty years when Savage & Lun (1988) [113] applied information-entropy concepts to model what they proposed to be the two main driving mechanisms: *kinetic sieving* and *squeeze expulsion*.

Kinetic sieving is the name given to the natural gravity-induced process that explains why small particles are more likely than the larger ones to fall into gaps formed between other particles as they move. Basically, small particles can fit more easily into narrow gaps, and tend to fill them before the gaps expand enough for the large particles to fit. This sieving effect explains why a small particle species may have a larger net downward flux within the bulk flow than a large species, but does not explain the net upwards flux of the large particles. Squeeze expulsion is the process by which a force imbalance in a particle compressed by two neighbours results in it being pushed out of the line (the force chain) they formed. As defined, this mechanism is not preferential to any direction nor particle size, but accounts for a possible mechanism that would drive large particles upwards.

Dolgunin & Ukolov (1995) [32] suggested that diffusion-like processes caused by the random spatial distribution of the particle velocities were also relevant to the segregation process even for dense granular flows. Such diffusive mechanisms would explain earlier observations of segregation being inhibited by large particle speeds [113]. In fact, it was later proved that in more energetic regimes, where the flow is dilute and dominated by binary collisions, kinetic theory successfully predicts that the granular temperature gradient leads to particle segregation [65, 54, 3, 74]. However, an equally

successful theory to quantify segregation effects in dense granular flows is still to be developed [36].

Many authors have since identified up to thirteen different mechanisms that drive segregation in a variety of flows [115, 27, and references therein]. However, the relative importance of each depends on particle geometry and flow energy. For dense, cohesionless, gravity-driven granular flows it is generally agreed that the relevant segregation mechanisms are kinetic sieving, squeeze expulsion, angle of repose segregation (whereby materials whose repose angle is smaller flow over those with larger angle), trajectory segregation (by which smaller or more angular particles are more affected by frictional effects) and fluidization (where different drag forces tend to fluidize or entrain certain particles [73]).

1.4.3 Motivating questions: Origin of driving forces

The first theoretical models published on size segregation in dense, inclined chute flows focused on explaining patterns such as the formation and evolution of concentration shocks [129]. The model developed by Savage & Lun (1988) [113], and its derivations, used statistical mechanics based on the geometrical likelihood of kinetic sieving and mass balance, and although it agreed reasonably well with laboratory experiments, it failed to represent underlying physical concepts. For example, their model was independent of gravity (or any external spatial gradient) when it is clearly the driving force. Similarly, the theory developed from Dolgunin & Ukolov's (1995) [32] balance between segregating and diffusive fluxes failed to account for the driving forces and particle properties [74].

Alternatively, Savage & Hutter (1991) [112] introduced an avalanche dynamics theory based on depth-averaged conservation laws, which has been adopted and extended to model stratification patterns by a large branch of authors [48, 125, 45, 38, 47, 131, 44, 77]. However, there are as of yet no theories that couple size segregation to the non-depth-averaged evolving flow field [46]. A general theory able to explain the effect of inter-particle interactions on segregation and its relationship to the flow mobility and basal deposition remains to be found [114].

1.5 Experimental granular dynamics

An important factor in the slow progress of granular rheology and segregation models is the fact that they are difficult to validate experimentally. In the cases of both nonlocal rheology and segregation, the macroscopic results are visible and measurable, but unlike with fluid flows it is not yet possible to measure the microscopic behaviour of

individual particles within a granular flow in real time. A hurdle facing the granular dynamics community today is the lack of understanding of the link between microscopic quantities and macroscopic behaviour.

Due to the difficulties in testing theoretical models experimentally, the discrete element method (DEM) [25, 102, 126, 92, 50] is widely used by the granular community, as reliable predictions can be obtained if all particle properties and inter-particle interactions are carefully incorporated. A few examples, relevant to this work, of DEM applied to simulate granular systems are in the study of mixing and segregation of granular mixtures [99], hopper discharge [62, 101], and snow and rock avalanches [123, 2]. These methods offer a means to non-intrusively obtain information within a granular flow, but they offer no guarantee that they are calibrated to simulate realistic systems, and therefore still need to be verified experimentally.

Experimentally, some authors have recorded the evolving particle velocity and size distribution through the avalanche side-wall by performing particle tracking or image velocimetry [122, 21, 84, 34], or using a calibration curve to infer concentrations [131], but in these cases the flow is necessarily affected by side-wall effects [66]. Another approach is to divide a flow originated from a movable hopper into layers using splitter plates [113, 32, 129] to extract concentration profiles for the different particle sizes along the avalanche. However, this method is intrusive [113] and produces results with low vertical resolution. Nevertheless, several authors [46, 127] have alluded to the hope that emerging non-invasive experimental techniques [8], including index-matching, photoelasticity and X-ray tomography, may soon be able to shed light on microscopic processes.

Non-invasive tomographic techniques [1, 40, 29, 94, 30] have been used to obtain high resolution information about the vibration and deformation of individual particles, from which contact forces can be quantified. These techniques have provided very accurate results in three-dimensional systems with very high spatial resolution, but in dynamic systems these techniques are limited by the temporal resolution of the information obtained. Moreover they can only be applied on very specific granular materials and the analysis of the experimental data is extremely computationally expensive. Photoelasticity remains the most approachable technique for measuring inter-particle forces, with the caveat that it has only be applied to quasi-static two-dimensional systems. Dynamic 2D photoelatic measurements used to this day [132] provide information about the shape and evolution of the force network in large assemblies of particles, but do not quantify microscopic interactions. Measurements of forces on photoelastic spheres have been successful [100, 130], but only for simple and highly controlled systems.

In the experimental setup developed for this work we have access to an unprece-

dented experimental insight into the force network in dynamic granular free-surface flows. On one hand, this allows direct observation of the relationship between microscopic force behaviour and macroscopic non-local effects. We aim to capture the origin of the forces that cause localised, sporadic motion of particles where local rheology predicts none. Mainly, we are concerned with the relevance of the shear rate in the modelling of rheology in the regimes achieved in the experiments discussed in this thesis, that is, in quasi-static and inertial flow regimes. Especially in quasi-static regions, the dissociation between rheology and shear rate is currently particularly baffling to the granular community, and our ability to measure both is most promising.

Secondly, this new insight into inter-particle force magnitudes means that if a segregating particle can be tracked in the flow, we can directly observe the mechanism by which inter-particle forces push certain particle species to specific locations in the flow. The benefit of capturing the mechanisms that drive segregation is that the dependency of the segregation rate on the local flow kinematic variables could then be physically explained rather than empirically fitted to a model. Examples of variables, relevant to the experiments performed in this thesis, that have been observed to affect the segregation rate are shear rate [17, 42, 35], packing fraction [33, 17, 113, 48, 47], particle size dispersity [113, 48, 45, 42], velocity fluctuation gradients [53, 22], and pressure [42]. In consequence, this work serves the second purpose of verifying the dependencies assumed in the segregation models referenced.

1.6 Motivation and layout

Throughout this chapter we have presented a summary of the literature on which the analysis made in this thesis is based. We have divided our interest into three complementary areas: (1) characterising the force network in granular flows, taking into account the role of side-wall friction; (2) describing non-locality in terms of microscopic local variables; and (3) differentiating the force network in granular media from the force distribution in classical fluids in a way that leads to granular-specific behaviour, particularly size segregation.

In Chapter 2 we describe the experimental technique we will use to address the motivating questions. This technique is based on the material property of *photoelasticity*, by which clear materials change refractive index anisotropically when a force is applied to them. We present the equations applied to measure the photoelastic response of these materials and characterise the specific photoelastic material we use to carry out experiments. Then, in Chapter 3 we describe the experimental setup. We explain how we produce 2D avalanches of discs and how the design allows us to measure forces between individual pairs of particles in the flow. We also describe a few preliminary

experiments that justify several design decisions.

Chapter 4 reports the results of carrying out experiments over a smooth and rough base. Because the avalanches produced are constrained to a channel where only one layer of discs can flow, side-walls play an important role in the kinematics of the flow. We thus compare our results to 3D granular flows in narrow channels and analyse the behaviour of the stress tensor components, which we can calculate directly by coarse-graining photoelastic force measurements.

Chapter 5 focuses on experiments over a rough base where we get the thickest super-stable heap. Then, we look at the transition between a dense-inertial flow and a creeping zone underneath it. By measuring the rate at which the force network fluctuates with depth, we interpret the implications of the force fluctuation rate on stress diffusion and on non-local models. We also illustrate the success of the technique to measure force fluctuations and propose how it could be used to fully characterise the cooperative length used in non-local models.

Chapter 6 analyses the differences in the force distribution in mono-dispersed and bi-dispersed flows. We do this by comparing the results of previous chapters with bi-dispersed flows that have (a) uniform particle distribution and (b) a single large particle in a bed of small ones. On carrying out many repetitions of the experiments, we are able to measure the average and standard deviation of the particle paths, which inherently contains the probability of a large particle to be pushed towards the free surface. In addition, we are able to describe in detail the mechanisms by which large particles are moved between layers, shedding light on the true physical processes that drive granular size segregation.

The last chapter summarises the novel results produced for this dissertation and make an assessment of how well our aims were met. We finally propose adaptations of the experiments we have carried out that could further our line of investigation. We show the extent of the success of applying the technique in our experimental setup, and show that it promises many interesting results beyond those obtained for the purpose of this work.

Bibliography

[1] J. E. Andrade and C. F. Avila. Granular element method (GEM): linking inter-particle forces with macroscopic loading. *Granular Matter*, 14:51–61, 2012.

[2] C. Ancey. Plasticity and geophysical flows: A review. *Journal of Non-Newtonian Fluid Mechanics*, 142:4–35, 2007.

[3] B. Ö. Arnarson and J. T. Willits. Thermal diffusion in binary mixtures of smooth,

nearly elastic spheres with and without gravity. *Physics of Fluids*, 10(6):1324–1328, 1998.

[4] M. I. Arran and N. M. Vriend. Intermittency between avalanche regimes on grain piles. *Physical Review E*, 97(6):060901, 2018.

[5] R. Artoni and P. Richard. Effective wall friction in wall-bounded 3d dense granular flows. *Physical Review Letters*, 115(15):158001, 2015.

[6] R. Bagnold. *The Physics of Wind Blown Sand and Desert Dunes*. Methuen Publishing, 1941.

[7] R. A. Bagnold. Experiments on a gravity-free dispersion of large solid spheres in a newtonian fluid under shear. *Proceedings of the Royal Society of London. Series A. Mathematical and Physical Sciences*, 225(1160):49–63, 1954.

[8] R. Bandyopadhyay. Novel experimentally observed phenomena in soft matter. *Pramana*, 81(1):3–34, 2013.

[9] T. Barker, D. G. Schaeffer, M. Shearer, and J. M. N. T. Gray. Well-posed continuum equations for granular flow with compressibility and μ (I)-rheology. *Proceedings of the Royal Society A*, 473(2201):20160846, 2017.

[10] P. Bartelt and B. W. McArdell. Granulometric investigations of snow avalanches. *Journal of Glaciology*, 55(193):829–833, 2009.

[11] G. K. Batchelor. An introduction to fluid dynamics. *Cambridge University Press*, 2000.

[12] K. Bergfeldt, L. Piculell, and P. Linse. Segregation and association in mixed polymer solutions from Flory- Huggins model calculations. *The Journal of Physical Chemistry*, 100(9):3680–3687, 1996.

[13] W. A. Beverloo, H. A. Leniger, and J. Van de Velde. The flow of granular solids through orifices. *Chemical Engineering Science*, 15(3-4):260–269, 1961.

[14] L. Bocquet, A. Colin, and A. Ajdari. Kinetic theory of plastic flow in soft glassy materials. *Physical Review Letters*, 103(3):036001, 2009.

[15] M. Bouzid, A. Izzet, M. Trulsson, E. Clément, P. Claudin, and B. Andreotti. Non-local rheology in dense granular flows. *The European Physical Journal E*, 38(11):125, 2015.

[16] M. Bouzid, M. Trulsson, P. Claudin, E. Clément, and B. Andreotti. Nonlocal rheology of granular flows across yield conditions. *Physical Review Letters*, 111:238301, 2013.

[17] J. Bridgwater, W. S. Foo, and D. J. Stephens. Particle mixing and segregation in failure zones—theory and experiment. *Powder technology*, 41(2):147–158, 1985.

[18] E. S. Calder, R. S. J. Sparks, and M. C. Gardeweg. Erosion, transport and segregation of pumice and lithic clasts in pyroclastic flows inferred from ignimbrite at Lascar Volcano, Chile. *Journal of Volcanology and Geothermal Research*, 104(1-4):201–235, 2000.

[19] H. Chen, G. B. Crosta, and C. F. Lee. Erosional effects on runout of fast landslides, debris flows and avalanches: a numerical investigation. *Geotechnique*, 56(5):305–322, 2006.

[20] F. Chevoir, J.-N. Roux, F. da Cruz, P. G. Rognon, and G. Koval Jr. Friction law in dense granular flows. *Powder Technology*, 190(1-2):264–268, 2009.

[21] E. Clément, J. Duran, and J. Rajchenbach. Experimental study of heaping in a two-dimensional "sand pile". *Physical Review Letters*, 69(8):1189, 1992.

[22] S. L. Conway, X. Liu, and B. J. Glasser. Instability-induced clustering and segregation in high-shear Couette flows of model granular materials. *Chemical Engineering Science*, 61(19):6404–6423, 2006.

[23] G. B. Crosta, P. Frattini, and N. Fusi. Fragmentation in the Val Pola rock avalanche, Italian alps. *Journal of Geophysical Research: Earth Surface*, 112(F1), 2007.

[24] X. Cui, J. M. N. T. Gray, and T. Johannesson. Deflecting dams and the formation of oblique shocks in snow avalanches at Flateyri, Iceland. *Journal of Geophysical Research: Earth Surface*, 112(F4), 2007.

[25] P. A. Cundall, and O. D. L. Strack. A discrete numerical model for granular assemblies. *Geotechnique*, 29(1): 47–65, 1979.

[26] F. Da Cruz, S. Emam, M. Prochnow, J.-N. Roux, and F. Chevoir. Rheophysics of dense granular materials: Discrete simulation of plane shear flows. *Physical Review E*, 72(2):021309, 2005.

[27] S. R. de Silva, A. Dyrøy, and G. G. Enstad. Segregation mechanisms and their quantification using segregation testers. In *IUTAM Symposium on segregation in granular flows*, pages 11–29. Springer, 2000.

[28] R. Delannay, M. Louge, P. Richard, N. Taberlet, and A. Valance. Towards a theoretical picture of dense granular flows down inclines. *Nature Materials*, 6(2):99, 2007.

[29] J. A. Dijksman, F. Rietz, K. Lorincz, M. Van Hecke and W. Losert. Refractive Index Matched Scanning of Dense Granular Materials. *Review of Scientific Instruments*, 83:011301, 2012.

[30] J. A. Dijksman, H. Zheng and R. P. Behringer. Imaging Soft Sphere Packings in a Novel Triaxial Shear Setup. *Powders and Grains* 1542 AIP Conference Proceedings:457, 2013.

[31] S. Dixit, J. Crain, W. C. K. Poon, J. L. Finney, and A. K. Soper. Molecular segregation observed in a concentrated alcohol–water solution. *Nature*, 416(6883):829, 2002.

[32] V. N. Dolgunin and A. A. Ukolov. Segregation modeling of particle rapid gravity flow. *Powder Technology*, 83(2):95–103, 1995.

[33] J. A. Drahun and J. Bridgwater. The mechanisms of free surface segregation. *Powder Technology*, 36(1):39–53, 1983.

[34] A. N. Edwards and N. M. Vriend. Size segregation in a granular bore. *Physical Review Fluids*, 1(6):064201, 2016.

[35] Y. Fan and K. M. Hill. Phase transitions in shear-induced segregation of granular materials. *Physical Review Letters*, 106(21):218301, 2011.

[36] Y. Fan, C. P. Schlick, P. B. Umbanhowar, J. M. Ottino, and R. M. Lueptow. Modelling size segregation of granular materials: the roles of segregation, advection and diffusion. *Journal of Fluid Mechanics*, 741:252–279, 2014.

[37] E. D. Fernández-Nieto, J. Garres-Díaz, A. Mangeney, and G. Narbona-Reina. 2D granular flows with the μ (I) rheology and side walls friction: A well-balanced multilayer discretization. *Journal of Computational Physics*, 356:192–219, 2018.

[38] Y. Forterre and O. Pouliquen. Flows of dense granular media. *Annual Review of Fluid Mechanics*, 40:1–24, 2008.

[39] S. J. Friedmann, N. Taberlet, and W. Losert. Rock-avalanche dynamics: insights from granular physics experiments. *International Journal of Earth Sciences*, 95(5):911–919, 2006.

[40] R. Hurley, E. Marteau, G. Ravichandran and J. E. Andrade. Extracting inter-particle forces in opaque granular materials: Beyond photoelasticity. *Journal of the Mechanics and Physics of Solids*, 63:154–166, 2014.

[41] GDR Midi. On dense granular flows. *The European Physical Journal E*, 14(4):341–365, 2004.

[42] L. A. Golick and K. E. Daniels. Mixing and segregation rates in sheared granular materials. *Physical Review E*, 80(4):042301, 2009.

[43] J. Goyon, A. Colin, G. Ovarlez, A. Ajdari, and L. Bocquet. Spatial cooperativity in soft glassy flows. *Nature*, 454(7200):84, 2008.

[44] J. M. N. T. Gray and C. Ancey. Multi-component particle-size segregation in shallow granular avalanches. *Journal of Fluid Mechanics*, 678:535–588, 2011.

[45] J. M. N. T. Gray and V. A. Chugunov. Particle-size segregation and diffusive remixing in shallow granular avalanches. *Journal of Fluid Mechanics*, 569:365–398, 2006.

[46] J. M. N. T. Gray, P. Gajjar, and P. Kokelaar. Particle-size segregation in dense granular avalanches. *Comptes Rendus Physique*, 16(1):73–85, 2015.

[47] J. M. N. T. Gray and B. P. Kokelaar. Large particle segregation, transport and accumulation in granular free-surface flows. *Journal of Fluid Mechanics*, 652:105–137, 2010.

[48] J. M. N. T. Gray and A. R. Thornton. A theory for particle size segregation in shallow granular free-surface flows. *Proceedings of the Royal Society A: Mathematical, Physical and Engineering Sciences*, 461(2057):1447–1473, 2005.

[49] S. S. Grigorian, M. E. Eglit, and I. L. Iakimov. New statement and solution of the problem of the motion of snow avalanche. *Snow, Avalanches & Glaciers. Tr. Vysokogornogo Geofizich Inst*, 12:104–113, 1967.

[50] Y. Guo and J. S. Curtis. Discrete element method simulations for complex granular flows. *Annual Reviews of Fluid Mechanics*, 47:21–46, 2015.

[51] T. Hatano. Power-law friction in closely packed granular materials. *Physical Review E*, 75(6):060301, 2007.

[52] D. L. Henann and K. Kamrin. Continuum modeling of secondary rheology in dense granular materials. *Physical Review Letters*, 113(17):178001, 2014.

[53] S. S. Hsiau and M. L. Hunt. Kinetic theory analysis of flow-induced particle diffusion and thermal conduction in granular material flows. *Journal of Heat Transfer*, 115(3):541–548, 1993.

[54] S. S. Hsiau and M. L. Hunt. Granular thermal diffusion in flows of binary-sized mixtures. *Acta mechanica*, 114(1-4):121–137, 1996.

[55] R. E. Hunter. Basic types of stratification in small eolian dunes. *Sedimentology*, 24(3):361–387, 1977.

[56] I. Iordanoff and M. M. Khonsari. Granular lubrication: toward an understanding of the transition between kinetic and quasi-fluid regime. *Journal of Tribology*, 126(1):137–145, 2004.

[57] R. M. Iverson. The physics of debris flows. *Reviews of Geophysics*, 35(3):245–296, 1997.

[58] R. M. Iverson. Elementary theory of bed-sediment entrainment by debris flows and avalanches. *Journal of Geophysical Research: Earth Surface*, 117(F3), 2012.

[59] R. M. Iverson and J. W. Vallance. New views of granular mass flows. *Geology*, 29(2):115–118, 2001.

[60] H. M. Jaeger and S. R. Nagel. Physics of the granular state. *Science*, 255(5051):1523–1531, 1992.

[61] H. M. Jaeger, S. R. Nagel, and R. P. Behringer. The physics of granular materials. *Physics today*, 49:32–39, 1996.

[62] A. Janda, I. Zuriguel, and D. Maza. Flow rate of particles through apertures obtained from self-similar density and velocity profiles. *Physical Review Letters*, 108:248001, 2012.

[63] Z. Janssen. Experiments on corn pressure in silo cells. *Verein Deutsch. Ing*, 39:1045, 1895.

[64] J. T. Jenkins. Dense shearing flows of inelastic disks. *Physics of Fluids*, 18(10):103307, 2006.

[65] J. T. Jenkins and F. Mancini. Kinetic theory for binary mixtures of smooth, nearly elastic spheres. *Physics of Fluids A: Fluid Dynamics*, 1(12):2050–2057, 1989.

[66] P. Jop, Y. Forterre, and O. Pouliquen. Crucial role of sidewalls in granular surface flows: consequences for the rheology. *Journal of Fluid Mechanics*, 541:167–192, 2005.

[67] P. Jop, Y. Forterre, and O. Pouliquen. A constitutive law for dense granular flows. *Nature*, 441(7094):727, 2006.

[68] P. Jop, Y. Forterre, and O. Pouliquen. Initiation of granular surface flows in a narrow channel. *Physics of Fluids*, 19(8):088102, 2007.

[69] P. Jop, V. Mansard, P. Chaudhuri, L. Bocquet, and A. Colin. Microscale rheology of a soft glassy material close to yielding. *Physical Review Letters*, 108(14):148301, 2012.

[70] K. Kamrin. Nonlinear elasto-plastic model for dense granular flow. *International Journal of Plasticity*, 26(2):167–188, 2010.

[71] K. Kamrin and G. Koval. Nonlocal constitutive relation for steady granular flow. *Physical Review Letters*, 108(17):178301, 2012.

[72] K. Kamrin and D. L. Henann. Nonlocal modeling of granular flows down inclines. *Soft Matter*, 11(1):179–185, 2015.

[73] W. R. Ketterhagen, J. S. Curtis, C. R. Wassgren, and B. C. Hancock. Modeling granular segregation in flow from quasi-three-dimensional, wedge-shaped hoppers. *Powder Technology*, 179(3):126–143, 2008.

[74] D. V. Khakhar, J. J. McCarthy, and J. M. Ottino. Mixing and segregation of granular materials in chute flows. *Chaos: An Interdisciplinary Journal of Nonlinear Science*, 9(3):594–610, 1999.

[75] P. Kharel and P. Rognon. Shear-induced diffusion in non-local granular flows. *Europhysics Letters*, 124(2):24002, 2018.

[76] M. G. Kleinhans, H. Markies, S. J. De Vet, F. N. Postema, et al. Static and dynamic angles of repose in loose granular materials under reduced gravity. *Journal of Geophysical Research: Planets*, 116(E11), 2011.

[77] J. Kowalski and J. N. McElwaine. Shallow two-component gravity-driven flows with vertical variation. *Journal of Fluid Mechanics*, 714:434–462, 2013.

[78] A. G. Kulikovskii and M. E. Eglit. Two-dimensional problem of the motion of a snow avalanche along a slope with smoothly changing properties. *Journal of Applied Mathematics and Mechanics*, 37(5):792–803, 1973.

[79] F. Lai, J. A. Hersey, and J. N. Staniforth. Segregation and mixing of fine particles in an ordered mixture. *Powder Technology*, 28(1):17–23, 1981.

[80] R. Lespiat, S. Cohen-Addad, and R. Höhler. Jamming and flow of random-close-packed spherical bubbles: an analogy with granular materials. *Physical Review Letters*, 106(14):148302, 2011.

[81] S. Li and D. L. Henann. Material stability and instability in non-local continuum models for dense granular materials. *Journal of Fluid Mechanics*, 871:799–830, 2019.

[82] J. A. Lindley. Mixing processes for agricultural and food materials: 1. fundamentals of mixing. *Journal of Agricultural Engineering Research*, 48:153–170, 1991.

[83] C. Lozano, I. Zuriguel, A. Garcimartín, and T. Mullin. Granular segregation driven by particle interactions. *Physical review letters*, 114(17):178002, 2015.

[84] R. M. Lueptow, A. Akonur, and T. Shinbrot. Piv for granular flows. *Experiments in Fluids*, 28(2):183–186, 2000.

[85] T. S. Majmudar and R. P. Behringer. Contact force measurements and stress-induced anisotropy in granular materials. *Nature*, 435(7045):1079, 2005.

[86] A. Mangeney, O. Roche, O. Hungr, N. Mangold, G. Faccanoni, and A. Lucas. Erosion and mobility in granular collapse over sloping beds. *Journal of Geophysical Research: Earth Surface*, 115(F3), 2010.

[87] A. S. McEwen. Mobility of large rock avalanches: Evidence from Valles Marineris, Mars. *Geology*, 17(12):1111–1114, 1989.

[88] A. Mehta and G. C. Barker. The dynamics of sand. *Reports on Progress in Physics*, 57(4):383, 1994.

[89] G. V. Middleton. Subaqueous sediment transport and deposition by sediment gravity flows. *Marine Sediment Transport and Environment Management*, 1976.

[90] P. Mills, D. Loggia, and M. Tixier. Model for a stationary dense granular flow along an inclined wall. *Europhysics Letters*, 45(6):733, 1999.

[91] S. Minko, I. Luzinov, V. Luchnikov, M. Müller, S. Patil, and M. Stamm. Bidisperse mixed brushes: Synthesis and study of segregation in selective solvent. *Macromolecules*, 36(19):7268–7279, 2003.

[92] B. K. Mishra. A review of computer simulation of tumbling mills by the discrete element method: Part I-contact mechanics. *International Journal of Mineral Processing*, 71:73-–93, 2003.

[93] L. S. Mohan, K. K. Rao, and P. R. Nott. A frictional cosserat model for the slow shearing of granular materials. *Journal of Fluid Mechanics*, 457:377–409, 2002.

[94] S. Mukhopadhyay and G. Peixinho. Packings of deformable spheres. *Physical Review E*, 84:011302, 2011.

[95] K. Nichol, A. Zanin, R. Bastien, E. Wandersman, and M. van Hecke. Flow-induced agitations create a granular fluid. *Physical Review Letters*, 104(7):078302, 2010.

[96] P. R. Nott. A non-local plasticity theory for slow granular flows. In *EPJ Web of Conferences*, volume 140, page 11015. EDP Sciences, 2017.

[97] P. D. Olmsted. Perspectives on shear banding in complex fluids. *Rheologica Acta*, 47(3):283–300, 2008.

[98] J. S. Olson. Lake michigan dune development 1. wind-velocity profiles. *The Journal of Geology*, 66(3):254–263, 1958.

[99] J. M. Ottino and D. V. Khakhar. Mixing and segregation of granular materials. *Annual Reviews of Fluid Mechanics*, 32:55–91, 2000.

[100] P. Yu, S. Frank-Richter, A. Borngen and M. Sperl. Monitoring three-dimensional packings in microgravity. *Granular Matter*, 16(2):165–173, 2014.

[101] J. P. Peralta, M. A. Aguirre, J. C. Geminard and L. A. Pugnaloni. Apparent mass during silo discharge: Nonlinear effects related to filling protocols. *Powder Technology*, 311:265–272, 2017.

[102] T. Poschel, and T. Schwager, Computational Granular Dynamics: Models and Algorithms. *Springer*, 2005.

[103] O. Pouliquen. Scaling laws in granular flows down rough inclined planes. *Physics of Fluids*, 11(3):542–548, 1999.

[104] O. Pouliquen and Y. Forterre. Friction law for dense granular flows: application to the motion of a mass down a rough inclined plane. *Journal of Fluid Mechanics*, 453:133–151, 2002.

[105] O. Pouliquen and Y. Forterre. A non-local rheology for dense granular flows. *Philosophical Transactions of the Royal Society of London A: Mathematical, Physical and Engineering Sciences*, 367(1909):5091–5107, 2009.

[106] S. P. Pudasaini and K. Hutter. *Avalanche dynamics: dynamics of rapid flows of dense granular avalanches*. Springer Science & Business Media, 2007.

[107] K. A. Reddy, Y. Forterre, and O. Pouliquen. Evidence of mechanically activated processes in slow granular flows. *Physical Review Letters*, 106(10):108301, 2011.

[108] O. Reynolds. Lvii. on the dilatancy of media composed of rigid particles in contact. with experimental illustrations. *The London, Edinburgh, and Dublin Philosophical Magazine and Journal of Science*, 20(127):469–481, 1885.

[109] P. Richard, A. Valance, J. F. Métayer, P. Sanchez, J. Crassous, M. Louge, and R. Delannay. Rheology of confined granular flows: Scale invariance, glass transition, and friction weakening. *Physical Review Letters*, 101(24):248002, 2008.

[110] P. G. Rognon, T. Miller, B. Metzger, and I. Einav. Long-range wall perturbations in dense granular flows. *Journal of Fluid Mechanics*, 764:171–192, 2015.

[111] L. Sarno, L. Carleo, M. N. Papa, and P. Villani. Experimental investigation on the effects of the fixed boundaries in channelized dry granular flows. *Rock Mechanics and Rock Engineering*, 51(1):203–225, 2018.

[112] S. B. Savage and K. Hutter. The dynamics of avalanches of granular materials from initiation to runout. part i: Analysis. *Acta Mechanica*, 86(1-4):201–223, 1991.

[113] S. B. Savage and C. K. K. Lun. Particle size segregation in inclined chute flow of dry cohesionless granular solids. *Journal of Fluid Mechanics*, 189:311–335, 1988.

[114] C. P. Schlick, Y. Fan, P. B. Umbanhowar, J. M. Ottino, and R. M. Lueptow. Granular segregation in circular tumblers: theoretical model and scaling laws. *Journal of Fluid Mechanics*, 765:632–652, 2015.

[115] M. Schröter, S. Ulrich, J. Kreft, J. B. Swift, and H. L. Swinney. Mechanisms in the size segregation of a binary granular mixture. *Physical Review E*, 74(1):011307, 2006.

[116] H. G. Sheldon and D. J. Durian. Granular discharge and clogging for tilted hoppers. *Granular Matter*, 12(6):579–585, 2010.

[117] L. E. Silbert, D. Ertaş, G. S. Grest, T. C. Halsey, D. Levine, and S. J. Plimpton. Granular flow down an inclined plane: Bagnold scaling and rheology. *Physical Review E*, 64(5):051302, 2001.

[118] R. S. J. Sparks and S. R. Young. The Eruption of Soufrière Hills Volcano, Montserrat, from 1995 to 1999. *Geological Society of London*, 21:45, 2002.

[119] J. N. Staniforth, J. E. Rees, and J. B. Kayes. Relation between mixing time and segregation of ordered mixes. *Journal of Pharmacy and Pharmacology*, 33(1):175–176, 1981.

[120] N. Taberlet, P. Richard, and R. Delannay. The effect of sidewall friction on dense granular flows. *Computers & Mathematics with Applications*, 55(2):230–234, 2008.

[121] N. Taberlet, P. Richard, A. Valance, W. Losert, J. M. Pasini, J. T. Jenkins, and R. Delannay. Superstable granular heap in a thin channel. *Physical Review Letters*, 91(26):264301, 2003.

[122] H. Takahashi, A. Suzuki, and T. Tanaka. Behaviour of a particle bed in the field of vibration i. analysis of particle motion in a vibrating vessel. *Powder Technology*, 2(2):65–71, 1968.

[123] T. Takahashi. Debris flow. *Annual Review of Fluid Mechanics*, 13:57–77, 1981.

[124] P. Tang and V. M. Puri. Methods for minimizing segregation: a review. *Particulate Science and Technology*, 22(4):321–337, 2004.

[125] A. R. Thornton, J. M. N. T. Gray, and A. J. Hogg. A three-phase mixture theory for particle size segregation in shallow granular free-surface flows. *Journal of Fluid Mechanics*, 550:1–25, 2006.

[126] C. Thornton. Granular Dynamics, Contact Mechanics and Particle System Simulations. *Springer*, 2015.

[127] B. Turnbull, E. T. Bowman, and J. N. McElwaine. Debris flows: experiments and modelling. *Comptes Rendus Physique*, 16(1):86–96, 2015.

[128] J. W. Vallance. Lahars. *Encyclopedia of volcanoes*, 2000.

[129] J. W. Vallance and S. B. Savage. Particle segregation in granular flows down chutes. In *IUTAM Symposium on Segregation in Granular flows*, pages 31–51. Springer, 2000.

[130] L. Wang1, Y. Ju, H. Xie, G. Ma, L. Mao and K. He. The mechanical and photoelastic properties of 3D printable stress visualized materials. *Scientific reports*, 7(1):10918, 2017.

[131] S. Wiederseiner, N. Andreini, G. Épely-Chauvin, G. Moser, M. Monnereau, J. M. N. T. Gray, and C. Ancey. Experimental investigation into segregating granular flows down chutes. *Physics of Fluids*, 23(1):013301, 2011.

[132] A. A. Zadeh, J. Barés, T. A. Brzinski, K. E. Daniels, J. Dijksman, N. Docquier, H. Everitt, J. E. Kollmer, O. Lantsoght, D. Wang, M. Workamp, Y. Zhao and H. Zheng. Enlightening force chains: a review of photoelasticimetry in granular matter. *arXiv preprint*, arXiv:1902.11213, 2019.

[133] Q. Zhang and K. Kamrin. Microscopic description of the granular fluidity field in nonlocal flow modeling. *Physical Review Letters*, 118(5):058001, 2017.

CHAPTER 2

Photoelastic technique

Synopsis

In this chapter we discuss the background theory and implementation of the photoelastic technique. To start with, we explain the effect of the photoelastic material property on the polarisation of transmitted light in terms of the material internal stresses. We model a continuous stress distribution for a two-dimensional disc under compression by multiple forces at any point and angle to its surface. Then, we show the photoelastic patterns that can be expected to be obtained from such discs, and develop the dependency of the light intensity to the external forces magnitudes. At this point the limitations and difficulties of applying the photoelastic technique to measure forces are presented, as they impact the design of our experimental setup described in the next chapter.

In the second part of this chapter, we characterise the photoelastic material used, *Clear Flex 50*, and compare it to other materials used worldwide for photoelastic studies. We then justify our preference for *Clear Flex 50* over the available alternatives.

Finally, we compare the theoretical fringe patterns modelled in the first part of this chapter to the experimentally observed photoelastic patterns. The similarity between the two is the foundation of the optimisation algorithm to estimate force magnitudes and directions from observation, which we also explain in detail in this chapter.

2.1 Theoretical background

The term *double refringence*, or *birefringence*, is applied to optically anisotropic materials when their refractive index depends on the direction of polarisation and propagation

of the transmitted light. On entering a birefringent medium, the incident light vector can be modelled as a sinusoidal function resolved into two perpendicularly polarised components that propagate with different velocities. As a result, as a ray propagates in this medium, a phase shift develops between the component polarised in the direction of lower refractive index, i.e. the fast axis, and the other that oscillates along the slow axis. On emerging from the birefringent material, the relative linear phase difference, δ, between the two components is

$$\delta = \delta_f - \delta_s = h(n_f - n_s), \tag{2.1}$$

where the subscripts f and s represent the fast and slow axes respectively, n_f and n_s are the refractive indices in the two directions, and h is the distance travelled through the material. In turn the relative angular phase difference is

$$\Delta = \frac{2\pi}{\lambda}\delta = \frac{2\pi}{\lambda}h(n_f - n_s), \tag{2.2}$$

where λ is the wavelength of the transmitted light.

Some transparent materials are optically isotropic when unstressed but become birefringent if a load is applied to them. This related phenomenon is known as *temporary birefringence* or *photoelasticity*, and is experienced by materials whose refractive index in a given polarisation direction varies according to the internal stress created as a consequence of an external load on the material. Needless to say, this can be an extremely useful property for studying the distributions of stresses in numerous arrangements.

The relationship between the principal stresses at a point within a photoelastic material, σ_1, σ_2 and σ_3, and the change in the refractive indices in three principal, perpendicular directions, n_1, n_2 and n_3, was quantified by Maxwell in 1852, in what is today known as the *Stress-Optic Law*:

$$\begin{aligned} n_2 - n_1 &= c(\sigma_1 - \sigma_2), \\ n_3 - n_1 &= c(\sigma_2 - \sigma_3), \\ n_1 - n_3 &= c(\sigma_3 - \sigma_1). \end{aligned} \tag{2.3}$$

The proportionality constant c is called the *relative stress-optic coefficient* and is measured in the unit *Brewster*, where $1\ Br = 10^{-12}\ \mathrm{m^2N^{-1}}$. For practical purposes c is often considered a constant that carries the properties of the specific material used, but many authors have studied its dependency on wavelength and temperature (a phenomenon known as *photoelastic dispersion* or *dispersion of birefringence*) [6].

An important implication of the Stress-Optic Law is that the speed, and therefore

the phase retardation, of a light ray travelling in a birefringent medium is only affected by the principal stresses in the plane normal to the propagation direction. Hence, only one of Equations 2.3 is needed to describe the phase shift of light per direction of propagation. By substituting the appropriate Equation 2.3 into 2.2, the relative angular retardation of light propagating along axis $\hat{3}$ is

$$\Delta = \frac{2\pi hc}{\lambda}(\sigma_1 - \sigma_2). \tag{2.4}$$

Given that the light electric vector is modelled by a sinusoidal function, it is multivalued for retardations that are N (for $N \geq 0$) multiples of 2π. For this reason Equation 2.4 is often expressed in terms of the fringe number, or fringe order,

$$N = \frac{\Delta}{2\pi}, \tag{2.5}$$

so

$$\sigma_1 - \sigma_2 = \frac{N f_\sigma}{h}, \tag{2.6}$$

where $f_\sigma = \lambda/c$ is called the material *fringe value* and summarises the photoelastic response of the material.

Consider a set-up of two opposite circular polarising films in parallel, positioned as shown in Figure 2.1. As they are opposite in polarisation directions, the pair will absorb all the light that passes through them. If a birefringent sample material is placed in between them, circularly polarised light transmitted by one of the polarisers will no longer be circular after it is transmitted through the sample. This is because the polarisation of the transmitted light is affected by the sample having different directional refractive indices. As a result, the light transmitted through the second polariser will no longer be circularly polarised, but will have a residual phase change upon leaving the sample. On reaching the second polariser, the component of this light corresponding to a circular polarisation is absorbed by the second polariser, while the component associated to the change of phase may be transmitted through the setup. The intensity of the light transmitted through this system depends on the degree of phase shift created by the sample, which depends on the internal stress magnitudes, which in turn can be related to the external forces applied on the photoelastic sample.

An outside observer sees a black background with bright light patterns visible inside the photoelastic material. These patterns depend on the magnitude and direction of the load applied to the material, and the distribution of the internal stresses within the material. Unfortunately, the quantitative relationship between the observed light intensity and the external forces is not at all linear nor straightforward, but is proportional to the square of the light vector magnitude [9]. In the setup described, the

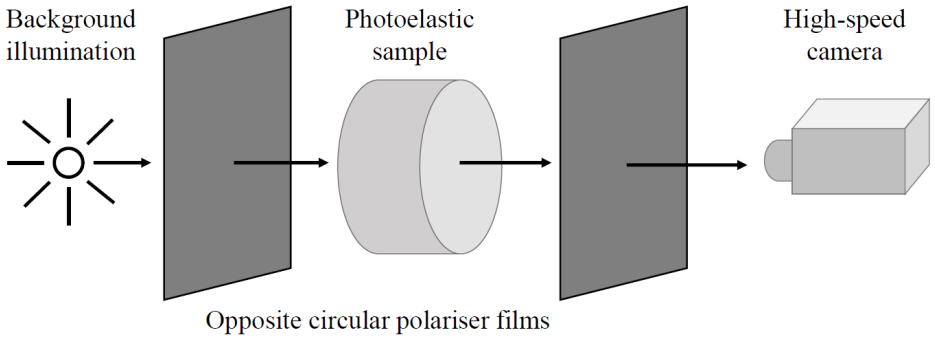

Figure 2.1: Sketch of the basic setup needed to visualise the photoelastic response of a sample.

intensity of the light transmitted can be directly related to the pressures applied to the material as

$$I = I_0 \sin^2(\frac{\Delta}{2}) = I_0 \sin^2\left[\frac{\pi h}{f_\sigma}(\sigma_1 - \sigma_2)\right], \tag{2.7}$$

where I_0 is the maximum light intensity detected, and σ_1 and σ_2 are once again the principal stresses at the point in question, which is in a plane perpendicular to the light propagation direction.

Notably, the Stress-Optic Law only relates the relative angular phase shift with the difference in the internal principal stresses, not with the magnitudes of the external forces. Several analytic and experimental stress-separation techniques have been developed to find the magnitudes of σ_1 and σ_2 from Equation 2.7 [29]. Alternatively, if the distribution of the stresses through a body can be modelled, they can be obtained by comparing the theoretical arrangement of fringes to the pattern observed. The latter is the method chosen to quantify forces in this project, as the cylindrical shape in which the photoelastic material is used provides a convenient geometry. A model for the distribution of the stresses inside a disc under multiple forces at any point and angle to the surface [6] is described next. Through this model we can predict the observable fringe pattern in a photoelastic disc for a set of forces of known magnitudes and directions.

Photoelasticity has become a widely popular choice for the experimental study of force distributions within granular systems. In the past decades alone, the photoelastic technique has been used to study the erratic stress fluctuations in sheared quasi-static granular matter [11, 2, 34], anisotropy of the contact force networks [18, 35], shear jamming [19, 3, 25, 36, 32], the dynamics of granular matter under impact [5, 17, 37], to identify inter-particle contacts [16], observe sound propagation [27, 20, 12], test the validity of statistical ensembles [23, 4] and examine sensitivity of granular systems to initial conditions [14], among others. A wide variety of force resolution has been achieved in these studies, depending mainly on the photoelastic material quality, image disc resolution and number of discs in the system. Some works report errors in the

force measurements as small as 5%, while in some others the resolution is so poor that they choose to only use the photoelastic information qualitatively.

2.2 Stress distribution in a 2D disc

2.2.1 Background theory of elasticity

Considering a disc of a linearly elastic material, in the absence of body forces the condition of equilibrium can be written as [6]

$$\frac{\partial \sigma_{ik}}{\partial x_k} = 0, \tag{2.8}$$

where σ_{ik} is the component of the internal stress in the k-direction on the plane with normal in the i-direction. If external forces are applied on the material surface, they will affect the choice of boundary conditions rather than Equation 2.8.

In three-dimensional space, if a very thin disc is considered, the components of the strain tensor in the direction $\hat{z}$ of the thickness, u_{zz}, u_{xz} and u_{yz} can effectively be neglected. As in a linearly elastic system the strains are directly proportional to the corresponding stresses, the stress tensor components σ_{xz}, σ_{yz} and σ_{zz} can also be neglected and only the components in the x-y plane remain. In this two-dimensional simplified case, the components of the stress tensor can be expressed in terms of Airy's stress function [6], χ, as

$$\sigma_{xx} = \frac{\partial^2 \chi}{\partial y^2} \qquad \sigma_{xy} = \sigma_{yx} = \frac{\partial^2 \chi}{\partial y \partial x} \qquad \sigma_{yy} = \frac{\partial^2 \chi}{\partial x^2}, \tag{2.9}$$

or in polar coordinates, as is more appropriate for the case of a disc,

$$\sigma_{rr} = \frac{\partial \chi}{\partial r} + \frac{1}{r^2}\frac{\partial^2 \chi}{\partial \theta^2} \qquad \sigma_{r\theta} = \sigma_{\theta r} = \frac{1}{r^2}\frac{\partial \chi}{\partial \theta} - \frac{1}{r}\frac{\partial^2 \chi}{\partial \theta \partial r} \qquad \sigma_{\theta\theta} = \frac{\partial^2 \chi}{\partial r^2}, \tag{2.10}$$

where χ is an arbitrary function. Redefining σ in the equilibrium balance Equation 2.8 in terms of χ results in that the stress function that defines the stress tensor components must satisfy the biharmonic equation

$$\nabla^2 \chi = 0. \tag{2.11}$$

2.2.2 Point force on a two-dimensional semi-infinite plate

This simplified problem consists of a point force $\boldsymbol{F}$ applied at point Q at an angle α to the edge of a semi-infinite plate that is effectively two-dimensional. We wish to derive

the internal stresses at any point P at a distance $|r|$ away from Q, as illustrated in Figure 2.2.

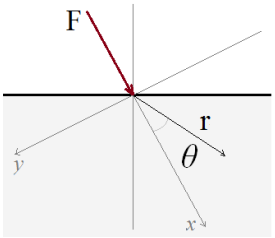

Figure 2.2: Illustration of the problem of a point force on a semi-infinite thin plate.

We assume that the internal pressure should decrease with the distance away from the point of load application (radially), so Equation 2.10 in polar coordinates is appropriate. We choose a solution [9] that satisfies the biharmonic Equation 2.11

$$\chi = Cr\theta \sin\theta, \tag{2.12}$$

where C is a constant. It follows that at a point at distance r and angle θ from the axis of force application the components of the stress tensor are

$$\sigma_{rr} = -2C\frac{\cos\theta}{r} \qquad \sigma_{r\theta} = \sigma_{\theta r} = 0 \qquad \sigma_{\theta\theta} = 0. \tag{2.13}$$

The constant C can be found by applying Newton's third law, which requires that the applied force be equal and opposite to the integral of the internal stress exerted by the whole solid. That is to say,

$$F = -2\int_0^{\pi/2} (\sigma_{rr}\cos\theta) r d\theta = -C\pi, \tag{2.14}$$

so

$$C = -\frac{F}{\pi}, \tag{2.15}$$

and finally,

$$\sigma_{rr} = -\frac{2F}{\pi}\frac{\cos\theta}{r}. \tag{2.16}$$

2.2.3 General solution to M non-concentric forces on a disc

This problem, illustrated in Figure 2.3, consists of a force $\boldsymbol{F}$ applied on the edge of a thin disc of radius R. It is noted that the applied force cannot be assumed to be concentric given that in practice disc borders may have a non-negligible friction coefficient, allowing for tangential stresses as well as normal. The main difference with Figure 2.2 is that the boundary condition requires that the disc edge be a free surface.

All components of the stress tensor must be zero at the boundary of the disc except at the points of load application.

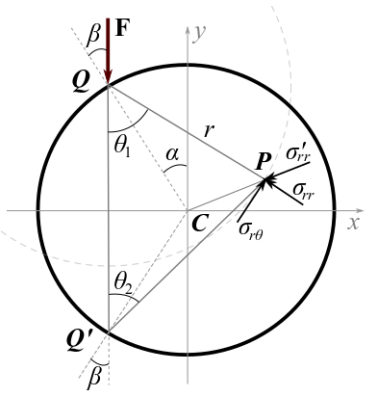

Figure 2.3: Illustration of the problem of a concentrated force on a thin disc.

At any point P inside the disc the a components of the internal stress due to force $\boldsymbol{F}$ are given by Equation 2.16. Transforming σ to an axis with origin at the disc centre C,

$$\begin{aligned} \sigma'_{rr} &= \sigma_{rr}\sin^2\theta_2 = -\tfrac{F}{2\pi r}\sin(\theta_1+\theta_2) - \tfrac{F}{2\pi r}\sin(\theta_2-\theta_1), \\ \sigma'_{r\theta} &= \sigma_{r\theta}\sin\theta_2\cos\theta_2 = -\tfrac{F}{2\pi r}\cos(\theta_1+\theta_2) - \tfrac{F}{2\pi r}\cos(\theta_2-\theta_1), \\ \sigma'_{\theta\theta} &= 0. \end{aligned} \tag{2.17}$$

The free surface boundary condition requires stresses to be zero all around the disc perimeter, which Equation 2.17 is not. The final expression for the internal stresses therefore consists of Equation 2.17, corrected by the value each component of σ takes evaluated at $r = R$:

$$\sigma = \begin{Bmatrix} \sigma'_{rr} - \sigma'_{rr}|_{r=R} & \sigma'_{r\theta} - \sigma'_{r\theta}|_{r=R} \\ \sigma'_{\theta r} - \sigma'_{\theta r}|_{r=R} & 0 \end{Bmatrix} \tag{2.18}$$

Historically, the photoelastic technique has been applied in static systems, where particle equilibrium simplifies Equation 2.17. Torque balance implies that the shear stress on the boundary must equal zero and similarly force balance requires the normal and tangential stresses stress in direction $\hat{r}$ to be zero. In contrast, this work aims to study dynamic systems where none of these stress components can be simplified thus.

If more than one force is present at the disc surface, at any point inside the disc the total stress will be a sum of the contributions from all of the forces. In addition, in order to compare this model to experimental images of the same problem, it is convenient to express the components of the stress tensor in Cartesian coordinates. Finally, the

general solution to any number M of external point forces on a disc surface is given by

$$\begin{aligned}
\sigma_{xx} &= \sum_{i}^{M} -\frac{2F_i}{\pi r_i}\cos^3\theta_{1i} + \sum_{i}^{M}\frac{F_i}{2\pi R}\sin\left(\theta_{1i}+\theta_{2i}\right), \\
\sigma_{yy} &= \sum_{i}^{M} -\frac{2F_i}{\pi r_i}\cos\theta_{1i}\sin^2\theta_{1i} + \sum_{i}^{M}\frac{F_i}{2\pi R}\sin\left(\theta_{1i}+\theta_{2i}\right), \\
\sigma_{xy} &= \sum_{i}^{M} -\frac{2F_i}{\pi r_i}\cos^2\theta_{1i}\sin\theta_{1i}.
\end{aligned} \tag{2.19}$$

Figure 2.4 shows the distribution of the stress according to Equation 2.19 when two equal and opposite diametrical forces are applied on the surface of a disc from above and below. Here the colours black and white represent the minimum and maximum internal stress tensor determinant at each point, respectively.

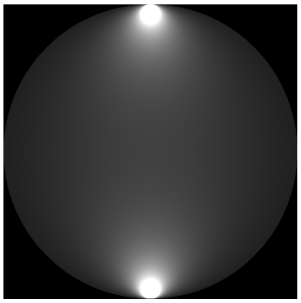

Figure 2.4: Theoretical distribution of stresses for the case of two opposite forces on a disc.

Equation 2.19 relate the position of a point inside the disc to the Cartesian internal stresses exerted there according to the theoretical distribution of the load. By calculating the eigenvalues of the resulting stress tensor, the principal stresses can be determined to be

$$\sigma_{1,2} = \frac{-(\sigma_{xx}-\sigma_{yy}) \pm \sqrt{(\sigma_{xx}-\sigma_{yy})^2 + 4\sigma_{xy}^2}}{2}. \tag{2.20}$$

Therefore,

$$\sigma_1 - \sigma_2 = \sqrt{(\sigma_{xx}-\sigma_{yy})^2 + 4\sigma_{xy}^2}, \tag{2.21}$$

is the quantity that determines the intensities observed in the disc by the detection system at coordinates x and y according to

$$I(x,y) = I_0 \sin^2\left[\frac{\pi h}{f_\sigma}(\sigma_1-\sigma_2)\right]. \tag{2.22}$$

Figure 2.5 shows, on the left, the theoretical intensities that would be observed

from the stress distribution shown in Figure 2.4, according to Equations 2.19, 2.21 and 2.22, using an arbitrary value for f_σ. The experimental image on the right shows the pattern resulting from observing a photoelastic particle under compression between polarisers. Clearly, there is a very good correspondence between the model developed and the experimental observations, except close to the points of force application. It is suspected that the difference between the images in this area may be due to the fact that the forces are not applied in concentrated points but over a finite area in the experiments [13].

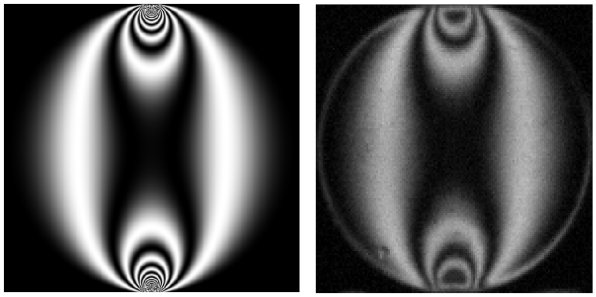

Figure 2.5: (Left) Theoretical distribution of the fringes for the case of two opposite concentric forces on a disc. (Right) Experimental image of the same case.

2.3 Force evaluation

In order to observe the effect of force magnitude on the photoelastic fringe pattern, we set up a calibration experiment for which we captured the patterns produced when applying known forces to a disc. In the experimental setup shown in Figure 2.6, a micrometer screw gauge compressed a disc while a *Chatillion Digital Force Sensor* measured the magnitude of the forces applied. A *PixeLINK PL-A742* camera located 1.4 m above the apparatus recorded the fringe patterns for a series of ten increasing forces, of which some are shown in Figure 2.7.

It is clear from Figure 2.7 that the specific observable pattern depends on the magnitude and direction of the loads applied to the material. In addition, we can see that the intensity at each specific point is multivalued for increasing values of internal stress: for example, the disc shown in Figure 2.7 has maximum intensity at the disc centre around $F = 0.8$, 1.9 and 3.0 N. Because the quantitative relationship between the observed light intensity and the external forces is not linear nor straightforward (Equation 2.22), forces must instead be calculated by post-processing the photoelastic light patterns, or fringes. The two most popular approaches to quantifying the forces that produce a specific photoelastic pattern are explained next: the G^2 and the *inverse-problem* methods.

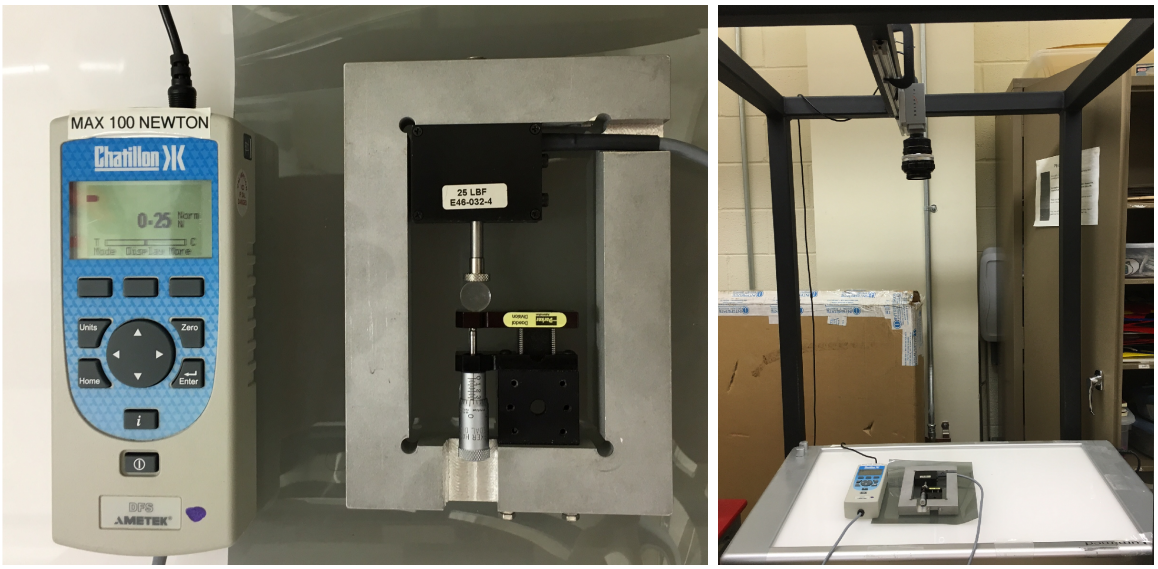

(a) (b)

Figure 2.6: View from the (a) top and (b) side of the experimental apparatus used to capture the photoelastic fringe patterns produced by simultaneously-measured forces. This setup belongs to the Daniels lab at NCSU, and was used in collaboration with J. Kollmer, Z. Tang and K. E. Daniels.

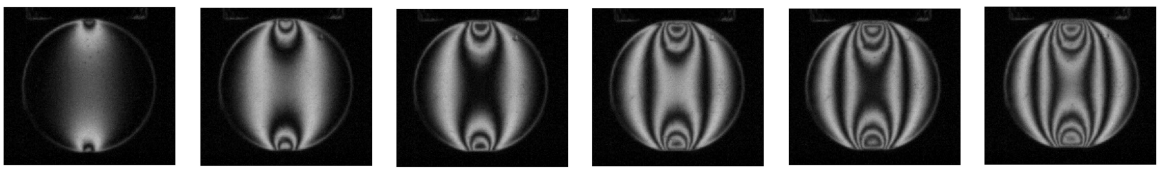

Figure 2.7: Examples of changing photoelastic pattern and increasing fringe number, within a disc under two known concentric forces.

2.3.1 G^2 method

Given the linear relationship between the forces applied and the disc fringe number, Behringer and co-workers [11] argued that a disc average pixel intensity gradient squared is an empirical measure of the 2D stress on that disc. They defined this quantity as

$$\begin{aligned}\langle G^2 \rangle = \sum_{i,j} \Bigg[& (I_{i+1,j} - I_{i-1,j})^2 + (I_{i,j+1} - I_{i,j-1})^2 \\ & + \frac{1}{2}(I_{i+1,j+1} - I_{i-1,j-1})^2 + \frac{1}{2}(I_{i+1,j-1} - I_{i-1,j+1})^2 \Bigg],\end{aligned} \tag{2.23}$$

and showed that there is a monotonic relationship between $\langle G^2 \rangle$ and the mean force exerted on a disc, for a given disc imaging resolution.

This estimative method of approximating inter-particle forces is known as the gradient-squared (G^2) method, and has been applied to systems at a variety of scales [5, 7, 15]. Despite the lower accuracy, this method is much less computationally expensive and can work at lower resolutions than the inverse problem method. Therefore this approach is usually preferred for studies where the researcher does not wish to compromise time and computational costs for accuracy.

2.3.2 Inverse problem method

The intensity of the light transmitted through a photoelastic particle depends on the difference between principal stresses, and not on the internal stresses themselves. In addition, they are related by a multivalued sine function, so it is not possible to find the forces exerted on a disc directly from individual pixel intensities. Instead, the force measurement is done by finding the magnitudes $\mathbf{F}$ that, for pixel i out of M, produce a theoretical fringe pattern, $I_i(\mathbf{F})$, most similar to that observed one, $I_{obs,i}$. In other words, the forces are found by solving the minimisation problem

$$\min(S^2) = \min \sum_{i=1}^{M} \left[I_{obs,i} - I_i(\mathbf{F}) \right]^2, \tag{2.24}$$

where S^2 is the sum of residual squares function.

The Levenberg-Marquadt algorithm (also known as the 'damped least squares' algorithm) was chosen to solve Equation 2.24 as it is a robust method, particularly easy to apply to numerical problems, of which many efficient packages have been implemented in most programming languages. This is an iterative technique for non-linear least-squares fitting that, given an initial estimation of the fitting parameters, in each

iteration estimates a correction $\delta_{\mathbf{F}}$ such that

$$S^2(\mathbf{F} + \delta_{\mathbf{F}}) < S^2(\mathbf{F}). \tag{2.25}$$

Like all iterative optimisation procedures, the Levenberg-Marquadt algorithm is prone to converging to a local minimum if the initial parameters are not close enough to the global minimum [10, 31, 24]. This is an increasingly important issue as the number and the magnitude of the contact forces rises. If the initial values for the contact forces are set very low, the algorithm will tend to produce sequentially increasing values for $\mathbf{F}$ in each iteration. When the fringe numbers in the experiment are larger than 1, the algorithm will find a local minimum when the proposed forces form the first fringe pattern that fits one of the fringes observed in the experiment. In conclusion, the Levenberg-Marquadt algorithm can be expected to fail to find the global minimum for high fringe numbers ($M > 1$), especially when the number of forces is larger than 2, unless an initial estimation of the forces is made for each particular case.

2.3.3 Implementation

Given the large volume of data expected to be collected, we wish to automate as much as possible the process of evaluating the magnitudes and directions of point forces on photoelastic discs from captured images of the corresponding fringe patterns. For this purpose, we adapted the force-measuring Matlab implementation *PeGS* (Photoelastic Grain Solver), an open source programme written by Jonathan Kollmer [21, 8] and inspired by James Puckett's *peDiskSolve* [22].

PeGS is split into three parts:

1. *PeGSDiskPrep.m*: identifies particles, finds neighbours and validates the transfer of forces at the contacts.

2. *PeGSDiskSolve.m*: analyses photoelastic patterns to estimate the forces exerted between particles.

3. *PeGSForceAdjMat.m*: a post-processing tool to quantify the reliability of results.

Identification of force-bearing contacts: *PeGSDiskPrep.m*

PeGSDiskPrep.m aims to pre-process experimental images containing photoelastic patterns within discs. All variables specific to the system of interest are introduced by the user in this first programme so that its output can feed directly into the optimisation-problem solver, which in turn returns lists of force magnitudes and directions.

Firstly, *PeGSDiskPrep.m* contains a section of code that, if enabled, implements the Matlab function *imfindcircles*. This function requires user-supplied parameters to apply a Hough Transform to detect circular elements in the input images. With the discs centres and radii, *PeGSDiskPrep.m* proceeds to identify pairs which are close enough to be in contact. Two discs are considered to be in contact if their centres are distanced by less than the sum of their radii plus a user-supplied tolerance *dtol*. If two discs satisfy this criterion, a single point of contact is determined to exist between them along the line that connects the two centres.

All potential contacts between pairs of discs are then analysed further to filter those that are *force-bearing* contacts. Forces between discs can only be estimated if there is a sufficiently high photoelastic response in the contact vicinity resulting in a visible fringe pattern. Hence, the pixels contained in a circle of arbitrary radius *g2cr* adjacent to the potential contact are evaluated for intensity variations. If the pixels inside this circle have an average G^2 value larger than a threshold $g2threshold$, then the contact is deemed to transfer a sufficiently high force. The contacts that do not satisfy this criterion are discarded, as the photoelastic technique would be unable to reliably estimate a force exerted at this point. Figure 2.8a shows an arrangement of photoelastic discs under compression. Figure 2.8b shows a zoom-in of the same arrangement where the large particles have been circled in red, the small in blue, and green circles mark the area near force-bearing contacts that measured G^2 values larger than $g2threshold$.

The values for parameters *dtol*, *g2cr* and $g2threshold$ must be supplied by the user, and will be different for each system. In particular, the combination of *g2cr* and $g2threshold$ defines the lowest force magnitudes that will be considered to form part of the force network; if $g2threshold$ is set too low for a given *g2cr*, then all particles and contacts will be considered to be contributing to the force network. Factors that affect the outcome of the programme *PeGSDiskPrep.m* are the disc pixel resolution, level of image light saturation, accuracy of the disc centre location and radii, diffusive elements in or on the particles and the photoelastic coefficient. Figure 2.8c shows the force network detected for the arrangement in Figure 2.8a, for the *g2cr* and $g2threshold$ values used to construct Figure 2.8b.

For each image supplied, the programme returns a single *.mat* file containing a list of identified particles. Each particle in the list is associated with a unique *id* number, the position of its centre in the image, its radius in pixels and in meters, a list of the *id*s of other particles it is in contact with and the corresponding contact locations, and a structure containing the pixels of the whole disc extracted from the original image. This is the input file for the second step in PeGS.

Photoelastic pattern optimisation solver: *PeGSDiskSolve.m*

PeGSDiskSolve.m processes the output files of *PeGSDiskPrep.m*. This code separately evaluates every structure in the list contained by these files, each of which represents a photoelastic disc identified in an experimental image.

In summary, this step in the programme fits force magnitudes and directions on each supplied contact on every disc. Because the prediction of the fringe patterns depends on the particle properties (see Equation 2.22), the disc physical thicknesses and photoelastic coefficients need to be specified by the user. This programme offers the option to enable or disable the condition of equilibrium (force and torque balance) at the user's discretion. If applicable, this condition simplifies the internal stress distribution model and provides a quicker initial guess for the iterative optimisation algorithm. If the condition of equilibrium is not applicable, the initial guess is estimated by applying the G^2 method.

As each disc is evaluated independently of the rest, this step in the programme is parallelised and can be run efficiently on a high-performance computer. The output is files of the same structure as the input, but with added columns for contact force magnitudes and directions.

Result visualisation: *PeGSForceAdjMat.m*

PeGSForceAdjMat.m reads the output of *PeGSDiskSolve.m* and computes a synthetic force image and a (weighted) adjacency matrix for the contacts evaluated. Figure 2.8d shows the synthetic force image constructed by this part of the programme, from the forces calculated from the experimental Figure 2.8a, which was taken from a static experiment.

In each of the three sections of PeGS, we only edited the parameters specific to our system. This includes the particles photoelastic coefficient, scale of each image, G^2 function for our system, the variables $dtol$, $g2cr$ and $g2threshold$, the location of the baseline, and the precision and maximum number of iterations for the optimisation algorithm. We disallowed the function that considered the forces to be balanced, which is not applicable in our dynamic system. We also disabled the function that located discs in the experimental images to insert our own circle-finding algorithm (explained in detail in Section 3.2.1), which was custom-made to maximize the accuracy of particle locations specifically for our system.

Using this code, the forces that would produce a specific fringe pattern can be estimated with errors as low as 5% [8, 21] when the experimental images have high enough resolution. In our implementation, however, the technique is highly sensitive to the input parameters: as little as a two pixel error in the radius or in the location of

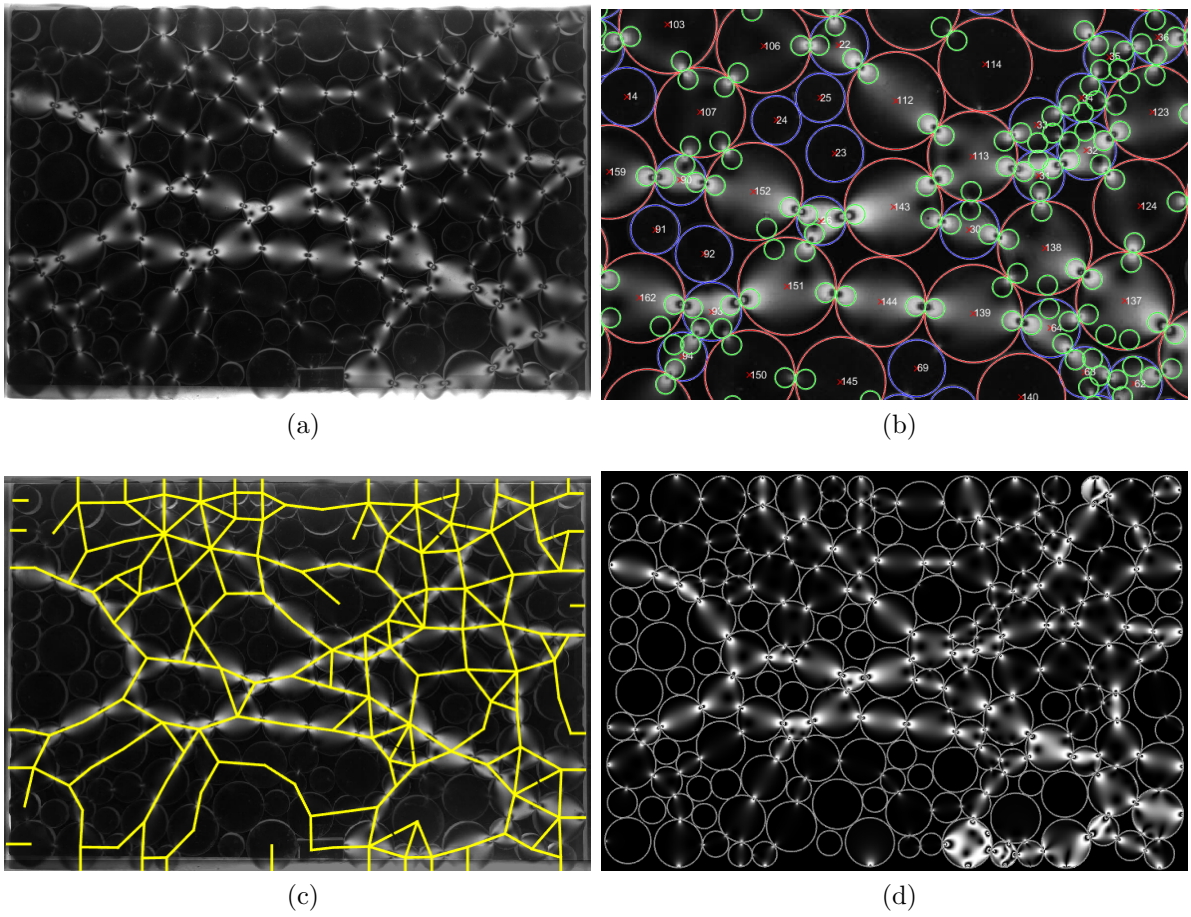

(a) (b)

(c) (d)

Figure 2.8: (a) Experimental view of a random arrangement of photoelastic discs under compression. (b) Zoom into the centre of (a) where the discs have been located and circled in blue and red depending on disc size. Here the regions near the contacts where the G^2 method is used to successfully determine whether contacts are force-bearing are circled in green. (c) Force network found from the contacts that have been determined to be force bearing. (d) Synthetic reproduction on the experimental image (a) using the forces calculated using PeGS [21].

the contact point, can cause force-bearing contacts to be missed altogether. Daniels *et al.* (2017) [8] recommends ensuring an accuracy in the location of the disc centres of at least $0.05d$ to guarantee the successful inversion of the fringe pattern. The limits of the technique lie in the resolution of the experimental images (due to camera resolution and diffusion in the photoelastic material) and in the trade-off between computational cost and accuracy. The right choices of photoelastic base material and experimental design, and the availability of computational resources, make significant differences in the accuracy of the results. For the current implementation, the typical experimental errors are explored in Section 3.2.3.1.

2.4 Photoelastic particle production

Most clear materials are photoelastic to different degrees. Given that we expect our experiments to involve small forces in a large set of particles, great effort was put into finding a material to produce photoelastic discs (hereafter called granular particles) with a reasonable trade-off between affordability and a high stress-optic coefficient.

Possible options were (1) buying custom made particles, (2) cutting discs from sheets of a known photoelastic material, and (3) casting a similar product out of the base polymer. Many authors have resorted to *Vishay Precision Group, Inc.* to produce commissioned particles of specific hardness and shape, which are considered highly photoelastic, uniform in properties and stable under typical experimental conditions. However, they are relatively expensive and have long lead times. Another increasingly popular option is to drill particles out of polyurethane sheets, which are produced in mass for industrial purposes. The drawback to this alternative is that irregular shapes are difficult to produce, and that the cutting of the sheets often introduces permanent stresses that interfere with the force measurements. Finally, urethane-based rubbers can be cast for a fairly low cost to produce stress-free particles of any shape and colour. Unfortunately, the process is usually time-consuming and includes handling toxic chemicals.

We chose to adopt the last option. With advice from Dr Jonathan Barés [1, 2], at the time at Duke University, the castable urethane rubber *Clear Flex 50* was bought from *Smooth-On* to produce the photoelastic particles. These were cast on a mould made from *Mold Star 15 SLOW* (*Smooth-On*), a soft but strong silicone rubber that is tear- and heat-resistant, exhibits low shrinkage and is safe and easy to use. This mould was in turn cast on an aluminium mould shaped precisely with a *Computer Numerical Control* (CNC) machine at DAMTP. This way, the *Clear Flex 50* was cast on a flexible mould that allowed their extraction without excessive forcing but had the precise shape given by the CNC machine. Figure 2.9 shows a picture of the materials used. The casting procedures were fine-tuned several times before obtaining an acceptable particle quality, and the final casting protocols followed are detailed in the Appendix.

2.4.1 Photoelastic calibration

Photoelastic calibration is the procedure by which the stress-optic coefficient of a material is determined. It involves compressing a disc of radius R with known forces F whilst measuring the fringe number N at the centre. The stress distribution in a disc

Figure 2.9: Casting materials for the *Mold Star* mould and *Clear Flex 50* particles.

(see Section 2.2) gives a linear relationship between F and N,

$$N = \frac{4c}{\pi\lambda R}F. \tag{2.26}$$

We used the experimental setup shown in Figure 2.6 to estimate the fringe number at the disc centre each time the micrometer screw gauge was tightened, while simultaneously measuring the force applied with the force sensor. To estimate the fringe number N at the disc centre, we take the profile of intensities across a line passing transversally across the fringe pattern, as shown in Figure 2.10a. Knowing that the edge of the disc is a free surface it follows that on the disc perimeter the change of phase of the transmitted light is zero, and thus so the fringe number on the disc surface is also zero. From the disc edge inwards, the next peak corresponds to a change of phase due to photoelasticity of $\Delta = \pi$, or $N = 0.5$, according to Equation 2.5. Next, the following minimum corresponds to $N = 1$, and so on. By fitting a sinusoidal function to the shape of the intensity profile shown in Figure 2.10b, the exact fringe number at the disc centre, N, can be calculated.

After repeating this process with four particles produced by Vishay, four cut from a sheet of polyurethane 50A and from another sheet of hardness 60A, and four cast from *Clear Flex 50*, the results were plotted in the fringe number vs. force graph shown in Figure 2.11. Finally, the stress-optic coefficient of each was calculated from the line of best fit using Equation 2.26.

The *Clear Flex 50* particles show the weakest photoelastic response of the four ($c = 2430\ Br$), but its stress-optic coefficient is still very high in comparison with

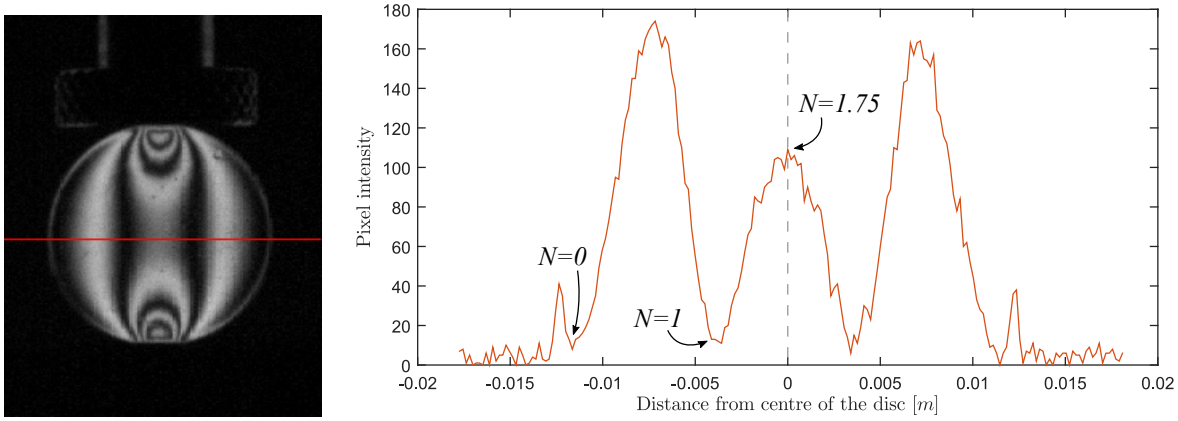

(a) (b)

Figure 2.10: (a) Photoelastic disc under known compressive concentric forces. The red line shows the profiles of intensities represented in (b), used to find the fringe number at the centre of the disc.

other clear materials. For instance, glass [33, 26] and polymer optic fibres [30] have a stress-optic coefficient of order 1 Br. Moreover, the force/radius ratio experienced in inter-particle collisions is not expected to exceed 300 N/m, and in this range the difference in photoelastic response between the four types of particles is reasonably small. Otherwise, the *Clear Flex 50* particles are superior to the others in transparency and in fringe visibility, as they are cast into the disc shape and therefore never have frozen-in stresses as the polyurethane particles do, and they are significantly cheaper to produce than to order from *Vishay*. All further work will be carried out using discs cast from *Clear Flex 50*.

2.4.2 Particle elasticity

Once the working material was chosen, its mechanical properties were investigated in collaboration with Elze Porte, at the Department of Mechanical Engineering of Imperial College London. Using a displacement-controlled *Biomomentum MACH-1 Mechanical Testing System*, several particles were subjected to different strains and strain-rates and the stresses produced were measured. Figure 2.12 shows the result of a particular test in which a particle of 6 mm thickness and 12 mm diameter, lying flat on its circular area, was compressed at a constant deformation-rate of 0.05 mm/s for 3 s and then kept compressed at 0.15 mm for a further 5 s. It can be seen that the deformation does not increase linearly with the force applied and that it relaxes at constant strain, which is typical viscoelastic behaviour.

When a stress is applied to most polymers, parts of the long constitutive chains rearrange, causing the strain induced by a constant stress to change over time. Sim-

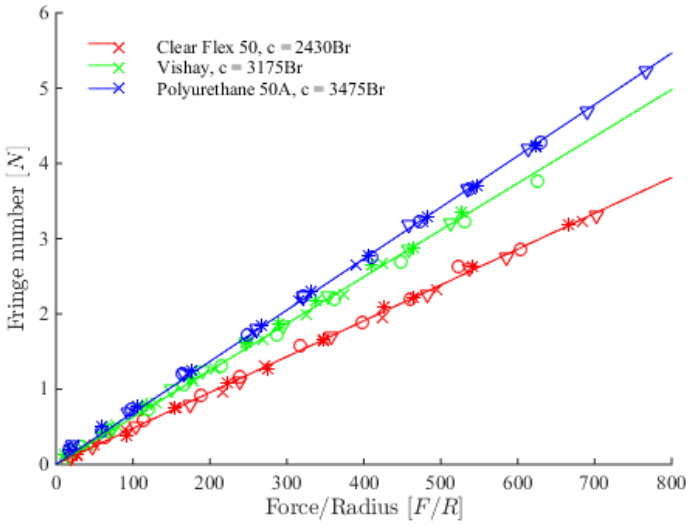

Figure 2.11: Fringe number vs. force graph from the photoelastic calibration of particles from four different sources. The colours differentiate tests carried out with different materials. For each material, four discs, represented using different symbols, were tested with a range of forces. The forces are measured with an approximate error of 0.25% with the equipment shown in Figure 2.6, while the fringe number measurements carry an estimated error of 0.1 N at most.

ilarly, if the polymer is strained by a fixed, constant amount, such rearrangements cause the stress to decrease over time (*stress relaxation*). Therefore, the relationship between stress and strain in viscoelastic materials is not linear, but exhibits a hysteresis where the area inside the loop accounts for the energy dissipated by the polymer chain rearrangements.

In Figure 2.12b, immediately after contact with the particle, the stress seems to increase exponentially with strain, which is attributed to imperfections in the disc shape. As the particles were cast, the side which was upwards during the curing often presented a slight meniscus, either inwards or outwards. Hence, the area of force application is expected to grow during the beginning of the compression.

On the other hand, stress relaxation is obvious, as the stress can be seen to level-off exponentially once the strain-rate is brought to zero. However, after performing three stress-relaxation tests at different strains on five particles, it was found that the total relaxation is never above 8% of the initial stress. Moreover, we notice that the force magnitude necessary to view this viscoelastic behaviour is two orders of magnitude larger than the magnitudes expected in our experiments. The viscous component of the material is thus weak enough to allow upper- and lower-estimations of its Young's modulus within a reasonably small range by using the peak and equilibrium stresses, respectively, reached for a given strain. This way, the modulus of elasticity of *Clear Flex 50* was determined to be within 15.7 - 16.3 MPa, which is of the expected order of magnitude [28]. The duration of inter-particle collisions is of the order of milliseconds,

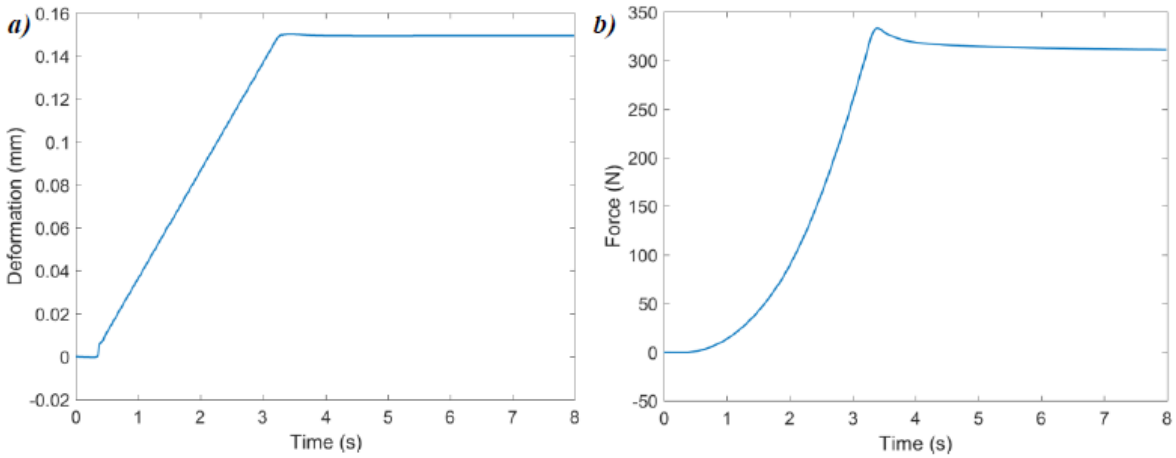

Figure 2.12: *(a)* Deformation and *(b)* force vs. time graphs of a stress-relaxation test performed on a *Clear Flex 50* particle of 6 mm thickness and 12 mm diameter.

which is very quick and does not allow for considerable stress-relaxation. Hence, the Young's modulus is expected to be closer to the upper boundary in reality.

2.5 Discussion

We have described the experimental technique that we apply in order to study the distribution of forces in a granular flow, and particularly the motivating questions introduced in Chapter 1. The experiments themselves apply the photoelastic technique to measure forces between individual pairs of particles in a two dimensional flow of discs. Understanding how the material property of photoelasticity works was essential in the design of the experimental setup, which will be explained in the next chapter. Chapter 3 describes and justifies the design decisions of the experimental setup, many of which rely on principles that are described here of how the technique works. In the next chapter we also explain the procedure we follow to obtain data from experiments, in the form of images of photoelastic patterns, as well as how we implement the force-calculating algorithm. Then, in Chapters 4, 5 and 6 we report the results of the analysis performed on different sets of experiments.

Bibliography

[1] J. Barés. Photoelastic methods: https://git-xen.lmgc.univ-montp2.fr/PhotoElasticity/Main/wikis/home.

[2] J. Barés, D. Wang, D. Wang, T. Bertrand, C. S. O'Hern, and R. P. Behringer. Lo-

cal and global avalanches in a two-dimensional sheared granular medium. *Physical Review E*, 95(5):052902, 2017.

[3] D. Bi, J. Zhang, B. Chakraborty and R. P. Behringer. Jamming by shear. *Nature*, 480:355–358, 2011.

[4] E. S. Bililign, J. E. Kollmer and K. E. Daniels. Protocol Dependence and State Variables in the Force-Moment Ensemble. *Physical Review Letters*, 122(3), 2019.

[5] A. H. Clark, L. Kondic, and R. P. Behringer. Particle scale dynamics in granular impact. *Physical Review Letters*, 109(23):238302, 2012.

[6] J. W. Dally and W. F. Riley. *Experimental stress analysis*. New York: McGraw-Hill, Inc, 3 edition, 1991.

[7] K. E. Daniels, J. E. Coppock, and R. P. Behringer. Dynamics of meteor impacts. *Chaos: An Interdisciplinary Journal of Nonlinear Science*, 14(4):S4–S4, 2004.

[8] K. E. Daniels, J. E. Kollmer, and J. G. Puckett. Photoelastic force measurements in granular materials. *Review of Scientific Instruments*, 88(5):051808, 2017.

[9] M. M. Frocht. *Photoelasticity*, volume 1. J. Wiley, 1941.

[10] H. Gavin. The Levenberg-Marquardt method for nonlinear least squares curve-fitting problems. *Department of Civil and Environmental Engineering, Duke University*, pages 1–15, 2011.

[11] D. Howell, R. P. Behringer, and C. Veje. Stress fluctuations in a 2D granular Couette experiment: a continuous transition. *Physical Review Letters*, 82(26):5241, 1999.

[12] G. Huillard, X. Noblin and J. Rajchenbach. Propagation of acoustic waves in a one-dimensional array of noncohesive cylinders. *Physical Review E*, 84:016602, 2011.

[13] K. M. Hung and C. C. Ma. Theoretical analysis and digital photoelastic measurement of circular disks subjected to partially distributed compressions. *Experimental Mechanics*, 43(2):216–224, 2003.

[14] J. E. Kollmer and K. E. Daniels. Betweenness centrality as predictor for forces in granular packings. *Soft Matter*, 15(8):1793-1798, 2018.

[15] J. Krim, P. Yu and R. P. Behringer. Stick–slip and the transition to steady sliding in a 2D granular medium and a fixed particle lattice. *Pure and Applied Geophysics*, 168(12):2259–2275, 2011.

[16] S. Lherminier, R. Planet, G. Simon, L. Vanel and O. Ramos. Revealing the Structure of a Granular Medium through Ballistic Sound Propagation. *Physical Review Letters*, 113(9):098001, 2014.

[17] M. X. Lim, J. Bares, H. Zheng and R. P. Behringer. Force and mass dynamics in non-newtonian suspensions. *Physical Review Letters*, 119(18):184501, 2017.

[18] T. S. Majmudar and R. P. Behringer. Contact force measurements and stress-induced anisotropy in granular materials. *Nature*, 435(7045):1079, 2005.

[19] T. S. Majmudar, M. Sperl, S. Luding and R. P. Behringer. Jamming transition in granular systems. *Physical review letters*, 98(5):058001, 2007.

[20] E. T. Owens and Karen E. Daniels. Sound propagation and force chains in granular materials. *Europhysics Letters*, 94(5):54005, 2011.

[21] J. E. Kollmer. Photoelastic grain solver: https://github.com/jekollmer/pegs.

[22] J. G. Puckett. *State Variables in Granular Materials: An Investigation of Volume and Stress Fluctuations*. PhD thesis, North Carolina State University, 2012.

[23] J. G. Puckett and K. E. Daniels. Equilibrating temperaturelike variables in jammed granular subsystems. *Physical Review Letters*, 110(5):058001, 2013.

[24] M. Quinten. *A Practical Guide to Optical Metrology for Thin Films*. John Wiley & Sons, 2012.

[25] J. Ren, J. A. Dijksman and R. P. Behringer. Reynolds pressure and relaxation in a sheared granular system. *Physical Review Letters*, 110(1):018302, 2013.

[26] T. Scharf. *Polarized light in liquid crystals and polymers*. John Wiley & Sons, 2007.

[27] A. Shukla. Dynamic photoelastic studies of wave propagation in granular media. *Optics and Lasers in Engineering*, 14(3):165–184, 1991.

[28] Smooth-On. *Specification Sheet*.

[29] M. Solaguren-Beascoa Fernández, J. M. Alegre Calderón, P. M. Bravo Diez, and I. I. Cuesta Segura. Stress-separation techniques in photoelasticity: a review. *The Journal of Strain Analysis for Engineering Design*, 45(1):1–17, 2010.

[30] M. K. Szczurowski, T. Martynkien, G. Statkiewicz-Barabach, W. Urbanczyk, L. Khan, and D. J. Webb. Measurements of stress-optic coefficient in polymer optical fibers. *Optics Letters*, 35(12):2013–2015, 2010.

[31] M. K. Transtrum, B. B. Machta, and J. P. Sethna. Geometry of nonlinear least squares with applications to sloppy models and optimization. *Physical Review E*, 83(3):036701, 2011.

[32] D. Wang, J. Ren, J. A. Dijksman, H. Zheng, and R. P. Behringer. Microscopic origins of shear jamming for 2d frictional grains. *Physical Review Letters*, 120:208004, 2018.

[33] R. M. Waxler and A. Napolitano. Relative stress-optical coefficients of some National Bureau of Standards optical glasses. *Journal of Research of the National Bureau of Standards*, 59(2):121–125, 1957.

[34] A. A. Zadeh, J. Bares, J. Socolar and R. P. Behringer. Seismicity in sheared granular matter. *arXiv preprint*, arXiv:1810.12243, 2018.

[35] J. Zhang, T. S. Majmudar, A. Tordesillas and R. P. Behringer. Statistical properties of a 2d granular material subjected to cyclic shear. *Granular Matter*, 12(2):159–172, 2010.

[36] H. Zheng, J. A. Dijksman and R. P. Behringer. Shear jamming in granular experiments without basal friction. *EPL (Europhysics Letters)*, 107(3):34005, 2014.

[37] H. Zheng, D. Wang, D. Z. Chen, M. Wang and R. P. Behringer. Intruder friction effects on granular impact dynamics. *Physical Review E*, 98:032904, 2018.

CHAPTER 3

Experimental methods

Synopsis

This chapter discusses the design, execution procedure, and post-processing of experiments that reveal the distribution of dynamic forces in the bulk of granular free-surface flows. The experiments from which the main results of this work are drawn consist of a two-dimensional avalanche of discs in a narrow inclined chute where we can observe and record the photoelastic patterns produced during inter-particle interactions.

The first aim of this chapter is to explain the design choices, focusing on how they allow the application of the photoelastic technique, explained in detail in the previous chapter, to measure forces within the avalanches. We also give estimations of the experimental error in the photoelastic force measurements in our setup, which outline the limitations of the results we will describe in the next chapters. Furthermore, we describe the design of a separate custom-made sensor arrangement that combines measurements of shear and normal forces on the chute base.

In the second part of this chapter, our implementation of the experimental image post-processing for the extraction of useful data is described. This includes the steps taken to maximise the accuracy of the particle tracking and contact force estimations. Since we only obtain point-based, discrete data from the experimental images, this chapter also contains a summary of the coarse-graining techniques used to obtain continuous profiles of the kinematic and dynamic fields of interest.

Finally, this chapter describes preliminary experiments carried out to ensure the analysed portions of the flow are in steady state and to estimate the minimum sample rate appropriate to study short-lived, dynamic forces.

3.1 Photoelastic avalanche experiments

3.1.1 Experimental setup and procedure

The experiment is set up as shown in Figure 3.1, so as to observe a single layer of 6 mm thick photoelastic discs avalanche down an incline. We created the inclined channel by pressing together two 2 m-long and 0.5 m-high acrylic panels separated by 8 mm of plastic and aluminium framework. The 8 mm spacing provides enough space for the discs, which are 6 mm thick and at least 11 mm in diameter, to roll freely within the channel without significant toppling in the direction of the disc axis. The complete setup is just over 3 m high and 3.5 m long, and permanently inclined at an angle of 20° to the floor. Due to its size and weight, the framework is bolted for support to the wall and floor from strategic points by beams that secure it in place, which prevents the adjustment of the slope angle.

A few components of the experimental setup crucial to this investigation are shown more closely in Figure 3.2. Here the reader can visualise (Figure 3.2a) a view from above of one of the hoppers, two-thirds full, being filled with a secondary funnel-like structure for convenience; (Figure 3.2b) the hopper system that supplies a stream of discs at an arbitrary rate to the channel where recordings are taken; (Figure 3.2c) the mechanism by which a strip of plastic is clamped to the base of the chute to create a rough bottom boundary condition; and (Figure 3.2d) the positioning of the camera whose recordings are later analysed.

Clamping the strip with semi-discs (as shown in Figure 3.2c) to add roughness to the chute base allows the exchange of basal configurations. Removing the strip altogether allows us to carry experiments over the smooth, flat aluminium separator, while adding different patterns of topography allows us to vary the shear introduced into the flows by the base. Discs of 12 mm ('small') and 21 mm ('large') diameter were cut in half and glued to thin plastic strips in three different configurations: only small, only large, and both alternating. Figure 3.3 demonstrates the four different basal topographies experimented with. The small-discs base is the least rough strip (aside from the smooth-base case), while the alternating-disc base is the most frictional.

Before an experiment, discs (with 10% polydispersity within each 'large' or 'small' disc species) are introduced from above into either or both hoppers seen on the left of Figure 3.1. Figure 3.2a shows the left hopper two-thirds full of small discs, and the auxiliary structure placed above it to aid the filling. To start an experiment, a plastic gate located at the base of each hopper (seen as dark grey plastic strips in Figure 3.2b) is manually slid outwardly to release the discs into the channel, where the experimental data is collected. Simultaneously to the release of the gate, we trigger a Phantom

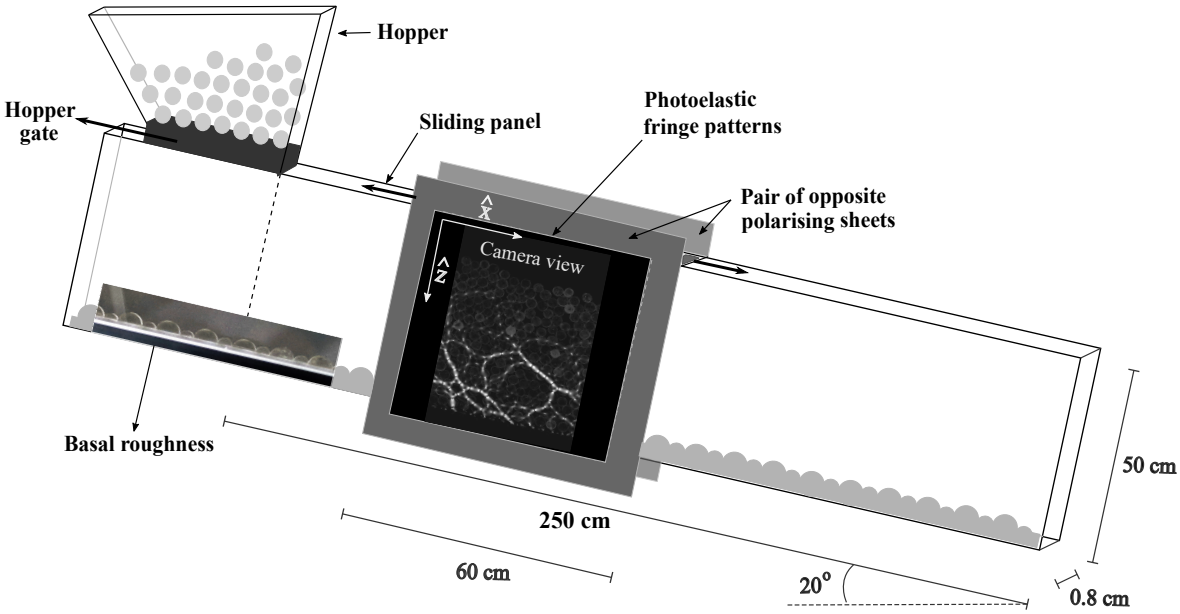

(a)

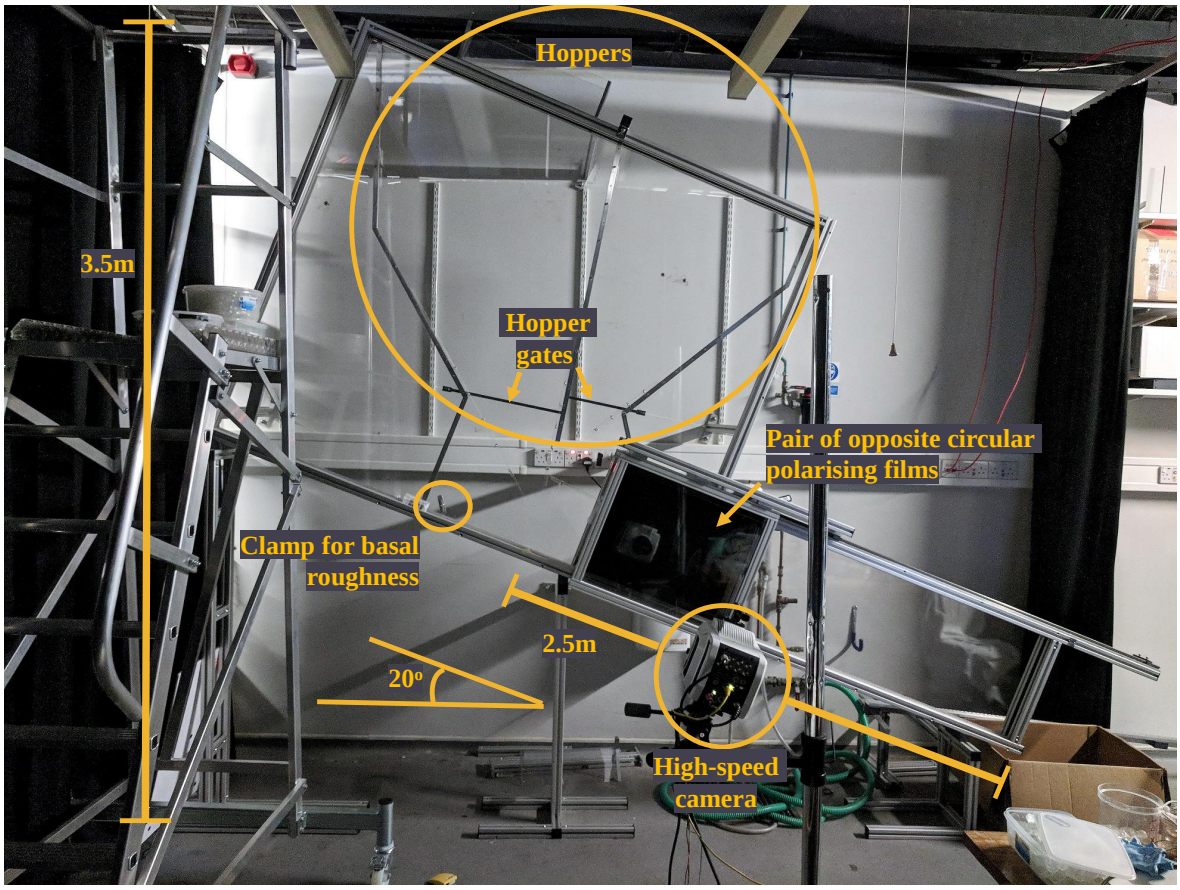

(b)

Figure 3.1: (a) Diagram and (b) labelled photograph of the experimental setup for the observation of forces within a 2D avalanche of photoelastic discs.

v2012 Ultrahigh-Speed Camera (Vision Research), mounted with a *Nikon* 80 mm lens, to record the flow of photoelastic discs at a fixed position down the avalanche channel.

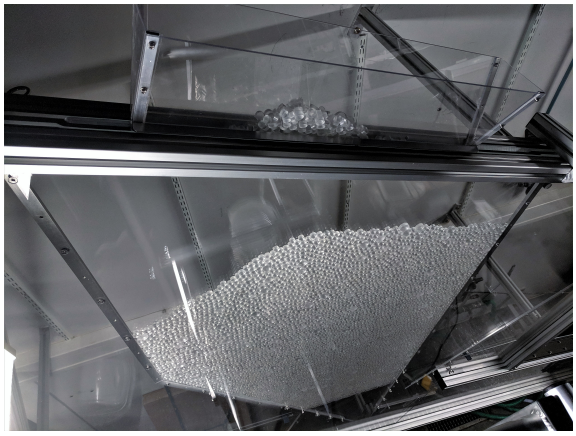

(a) Hopper two-thirds full of mixed-sized discs, and hopper filling mechanism, as seen from above.

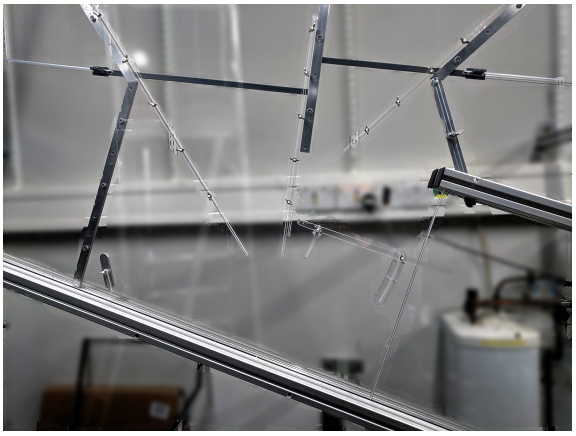

(b) Hopper gate mechanism, adjustable-width opening and second hopper mesaline.

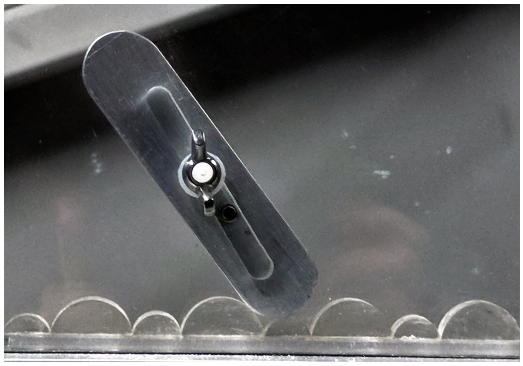

(c) Clamp mechanism to secure the basal topography strip with glued semi-discs. Four different topographies were made available.

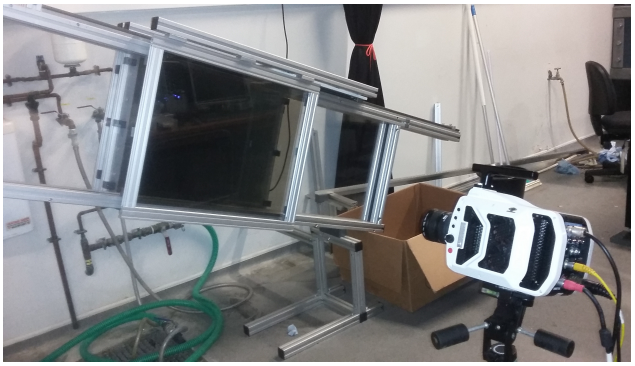

(d) Polarizer set placed on either side of the chute to define the viewing window to which the high-speed camera is aligned. A box at the end of the chute collects the discs.

Figure 3.2: Zoom into different components in the experimental setup for the observation of forces within a 2D avalanche of photoelastic discs.

(a) Smooth base.

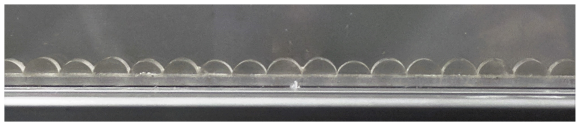

(b) Only 12 mm diameter semi-discs glued to the base

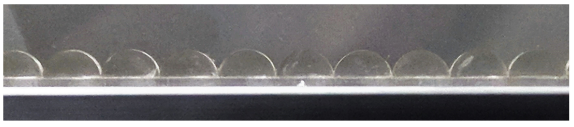

(c) Only 21 mm diameter semi-discs glued to the base

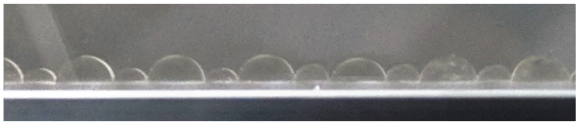

(d) Alternating 12 and 21 mm diameter semi-discs

Figure 3.3: Four different basal topographies available to experiment with.

The camera records experiments at a frame rate of 1000 fps and an exposure of 1/8000 s, as determined from the preliminary experiments described later on in Section 3.4.1. The background illumination is provided by an array of TruOpto OSPM-R5030ETS Red LED and a diffuser, while a pair of opposite circular polarisers, one on either side of the chute, reveals the discs photoelastic response to forces exerted on them. The polarisers are 60 cm long and 50 cm tall, so this is the maximum size of the window within which the camera can record photoelastic patterns. We can adjust the location of the viewing window along the chute by moving the combination of LED light panel and polarisers along a runway on top of the chute, after which the external camera field of view can be aligned as shown in Figure 3.2d. When the *Clear Flex 50* discs move in between the polarisers, the camera captures the photoelastic response to inter-particle interactions as bright light patterns on a dark background.

Finally, a large box placed beneath the lower end of the incline collects the discs as they exit the lower end of the chute freely. To reduce the frictional effect of the chute walls on the flowing discs, they are regularly lightly coated in cornflour when gathered within this box. The flour coating is slowly lost when the discs were handled so care was taken to keep a consistent disc lubrication. Comparisons of the velocity profiles of several subsequent experiments show high consistency and repeatability (discussed in more detail in Section 3.4.5).

3.1.2 Combined shear and normal force sensor

With the aim to verify and supplement the force measurements obtained from photoelastic patterns, we installed a separate non-intrusive force sensor in the chute. For this purpose, our collaboration with *Freeman Technology* enabled the access to a custom-designed sensor to simultaneously measure normal and shear forces on the base of the chute at DAMTP. The apparatus consists of a *Lenterra* Shear Stress sensor combined with an off-the-shelf load cell to measure normal forces. Both independent sensors are held together by a plastic 3D-printed head designed to fit on the chute base and transfer the forces from the photoelastic disc avalanche onto the corresponding force sensors.

Design

The *Lenterra* Shear Stress Sensor system was originally designed for in-line, real-time measurements of shear stress exerted by fluid or powder on a wall. It consists of a Drag Force Flow (DFF) Sensor, a *Lenterra* optical interrogator (LOI), and measurement software. The DFF sensor works by measuring the deflection of a cantilever 'needle' mounted on a stationary base. It was designed to quantify the drag force when

completely submerged in a fluid or powder, where the beam would deflect in response to shear stress. Deflection of the needle (in the direction marked by a line on the base) produces bending of two fibre optic gauges contained within it. A fiber-optic microresonator connected to them has its resonance centred at a particular light wavelength, and a strain on it causes a shift in the resonant wavelength that is proportional to the shear stress. The particular probe used can measure shear forces on the needle of up to 4 N with 0.6 mN resolution [10]. Figure 3.4a shows, in the front plane, the DFF needle of 2.8 mm diameter and 40 mm length, on a metal flange with three screw holes that can be used to secure the sensor. An optic fibre transmits information on the needle deflection to the LOI, seen in the back plane of Figure 3.4a as a white box on which the computer rests. The LOI in turn transmits interpreted data to a USB port on the laptop computer, which in Figure 3.4a is showing the custom-made software that interprets and displays in real-time the forces applied on the DFF.

The normal force sensor is a *Tedea Huntleigh* Model 1004 Aluminium Single Point Load Cell of 3 N capacity and a reported output relative error of 0.0067% [11]. The cell contains a strain gauge that strains when a load is applied on the top bar, and as it deforms changes electrical resistance. An analogue-to-digital converter then transmits the signal to a custom software installed on the same computer as the *Lenterra* programme. Figure 3.4b shows the load cell, including the power source input and the converter that feeds data to another USB port in the laptop that simultaneously reads shear forces. The load cell is mounted on a plastic base that can in turn be screwed to the chute base.

Figure 3.4c shows how both shear and normal force sensors are attached through a plastic 3D-printed head, which in this particular case is black. A number of plastic heads were printed and attached with different combinations of *Clear Flex* semi-discs to match the basal roughness strips (see Figure 3.3). The head is screwed onto one side of the load cell, next to which a hole allows the DFF to be secured by more screws through its flange.

In order to install the sensor at the chute base, seven 50 mm long gaps in the bottom surface of the chute, which is only 8 mm wide, were introduced at 20 cm intervals to create different positions where the sensor could be deployed. The 7 gaps were centred 25, 50, 75, 100, 125, 150 and 175 cm downstream from the beginning of the chute. The plastic heads are 47 mm long, 6 mm wide and 40 mm tall, so the arrangement fits flush in the gaps, and the plastic base can be screwed to washers in the aluminium framework via long screws and aluminium spacer rods. Figure 3.5a shows the sensor installed at one of the gaps at the bottom of the chute. We introduced two roughness strips from either end of the chute and clamped so that their ends sit around 2 mm from either end of the sensor head, so the sensor would sit flush on the base with minimal impact

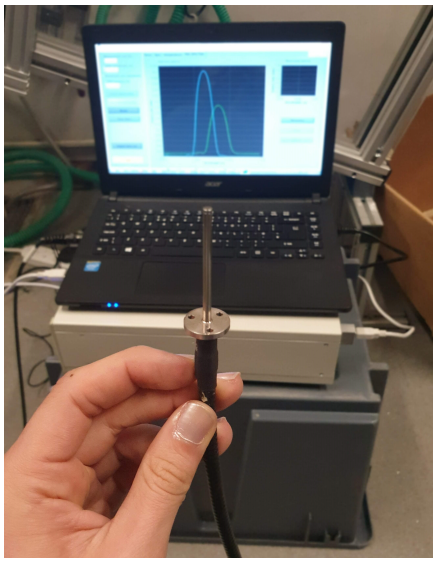

(a) Shear force sensor

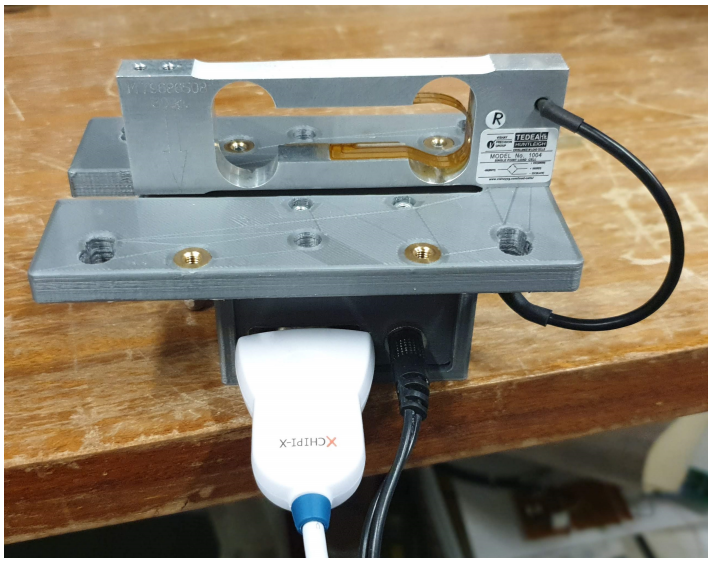

(b) Normal force sensor

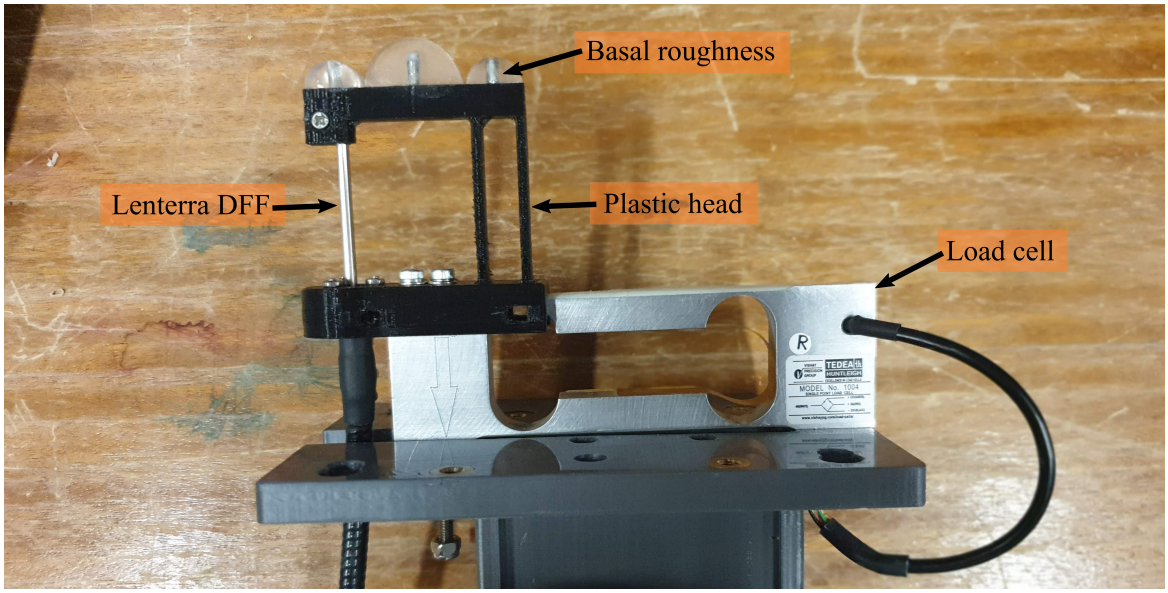

(c) Combined force sensor

Figure 3.4: Components of the combined shear and normal force sensor: (a) Shear force sensor, consisting of a *Lenterra* DFF in front of the computer displaying the custom software, resting on top of the Optical Interrogator (white box); (b) normal force sensor, consisting of a 4 N load cell mounted on a plastic base that can be screwed to removable washers on the chute base; and (c) plastic 2D-printed head (blue) that combines and transfers forces onto both shear and normal force sensors.

on the flow. It is important that the sensor head remains at least 1 mm clear from the components around it, so that it is free to compress and deflect, thus transmitting an accurate force to the load cell and *Lenterra* DFF. When the sensor is not installed in a certain gap, a T-shaped plug fills the gap in the framework, as shown in Figure 3.5b.

This is an atypical use of both sensors in that they are not measuring forces directly

(a) (b)

Figure 3.5: (a) Installation of the combined shear and normal force sensor on the chute base, and (b) T-shaped aluminium plug fit into the gaps at the chute base when the sensor is not installed.

from the sources they were designed for, particularly the shear sensor. Successful combined shear and normal force measurements, besides providing useful information about basal forces, are therefore also valuable as proof of concept for future instrument designs.

Calibration

Figure 3.4c shows the plastic structure that is compressed down and deflected sideways to transmit forces to the corresponding sensors. Normal forces are transmitted onto the compression load cell unaffected by the design of the head, but the same cannot be said of the shear forces. Shear force measurements rely on the deflection of the *Lenterra* DFF, but shear forces on the head are also diffused by the two plastic columns that support the other end of the slab to which the semi-discs are stuck. As a result, the deflection of the DFF does not reflect the total shear force on the head and the readings need to be calibrated.

To model the relationship between the shear forces deflecting the head to the magnitudes measured by the *Lenterra* probe, the sensor was clamped vertically to a table as seen in Figure 3.6a. A slightly long rectangle of 3D-printed plastic was fit tightly around the head, and a series of hanging brass calibration weights (*Scales & Balances*) were suspended from the rectangle as shown. For each known calibration mass we

recorded the force magnitude measured by the *Lenterra* system. Figure 3.6b shows the calibration plot and best-fit exponential curve that relates the measured forces to the real force applied on the head.

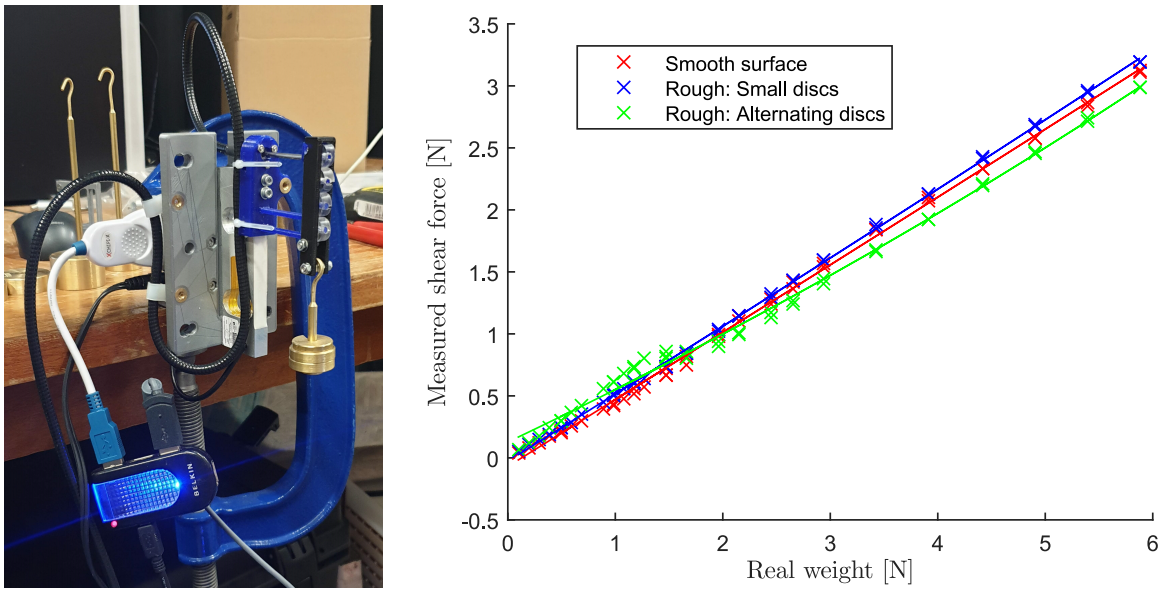

(a) Shear stress calibration setup. (b) Shear stress calibration plot for the four heads avilable.

Figure 3.6: Calibration (a) setup and (b) plot to relate the real force applied on the head to the force measured by the *Lenterra* shear stress sensor. Shear forces are measured with a resolution of 0.6 mN, and the normal forces are obtained with a relative error of 0.007%.

Each head was printed from a different batch of plastic, and the shear force measurements were additionally slightly affected by the tightness of the screws that fixed the DFF and its flange to the head. Thus, this calibration needed to be performed each time the head was changed.

3.2 Extraction of discrete data

The collection of experimental data is made through the images captured by the high-speed camera. The saved frames have a black background, and the discs are weakly identifiable due to refraction effects at the disc edges and a slight murkiness of the disc faces due to the light flour coating. In contrast, the photoelastic patterns within the discs are bright and almost reach pixel saturation. The flour coating causes pixel intensities to be a few pixel values higher than the average background noise, but much less intense that the intensities due to photoelasticity. Considering pixel values vary between 0 and 255, the average background pixel has a value of around 5 and the pixels within the flour coated discs have intensities of approximately 15, while the photoelastic fringes show intensities that go up to 200.

3.2.1 Particle tracking

Figure 3.7a exemplifies an image captured by the camera. The background illumination is less bright close to the image edges, so henceforth only the middle half (delimited by red lines in Figure 3.7a) is analysed, simultaneously reducing parallax error. In experiments where the whole width of the image needs to be used, the circle-finding algorithm described next is applied to the outer left and right quarters of the image separately.

Within this middle section of the image with uniform background illumination, it can also be seen that the disc edges appear faint next to the force-chains intensities. The transparency of *Clear Flex 50* raises the photoelastic signal quality of the discs seen here above that of different materials used in literature because it retains no residual stresses at the edges and contains very few diffusive agents that scatter light, increasing the observable fringe pattern resolution. On the other hand, locating discs in the images becomes difficult, as they become very dark next to the intense photoelastic force response. The force-finding algorithm is very sensitive to errors in the disc edge detection, so the experimental images were subjected to several filters to improve the circles-finding accuracy.

The Hough Transform (HT) was the chosen method for circle detection in the experimental images, for its reasonable combination of robustness, efficiency, and usability in Matlab (*imfindcircles* function [7]). After applying a border detection filter, such as Sobel, all pixels that are recognised as part of a border add a vote in an accumulator matrix in all the possible locations where the centre could be. If the approximate radius of the circles is known, the algorithm would add a vote to all the pixels of the accumulator that are a radius away from the pixels in the circumference. Then, locations in the accumulator with vote values larger than a threshold (which determines the algorithm sensitivity) are returned as centres. The method is very robust and can work for noisy and partial circles. However, because it relies on the border-detection filter, the algorithm is affected by the sharp edges of the force chains and by the faintness of the actual discs edges. Therefore, before applying the Hough Transform function, an image of the viewing window before an experiment is run (a background image) is subtracted from the experimental one, and the result is made to saturate at a cut-off intensity empirically found to be larger than the circle edge brightness but smaller than that seen from force chains. Figure 3.7b shows the middle half of the image after the pixel intensities have been readjusted in this way.

Still, because the disc edges are so indistinct in the raw experimental images, even the noise introduced by the flour coating makes it impossible to define a set of values for the cut-off pixel intensity and for the function sensitivity that would find all the

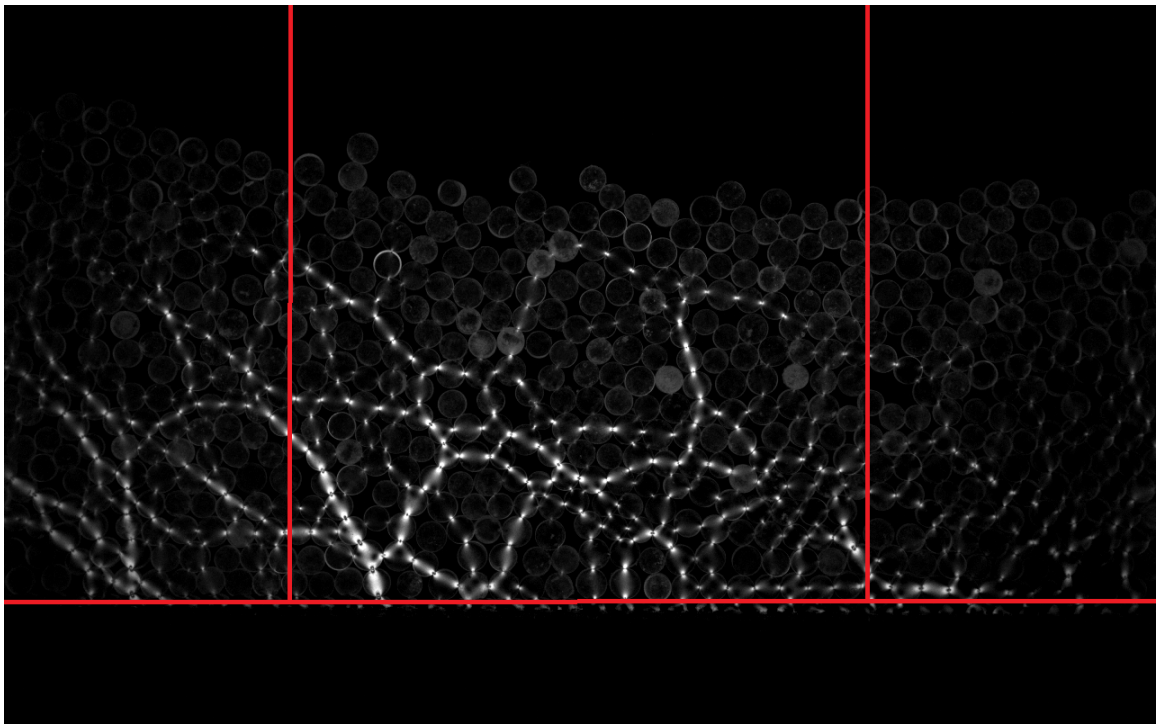

(a) Raw experimental image just as captured by the camera at with an exposure of 1/8000 s. Only the middle half of the image, delimited by vertical red lines is used.

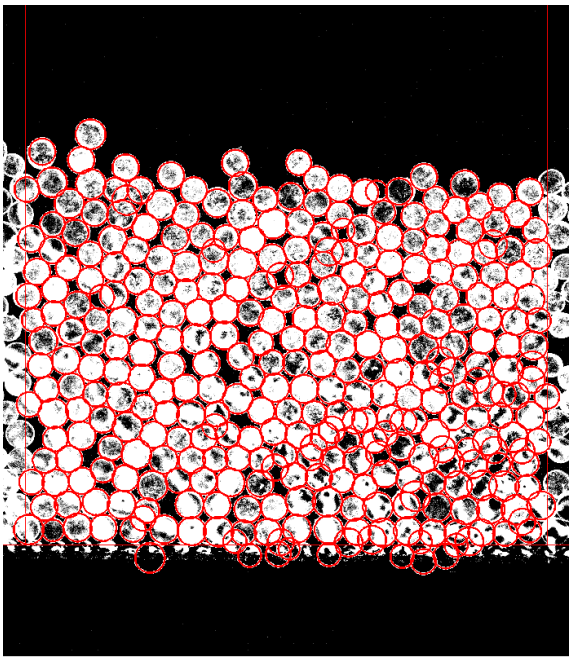

(b) Result of running a Hough Transform to find discs on the experimental image with readjusted brightness.

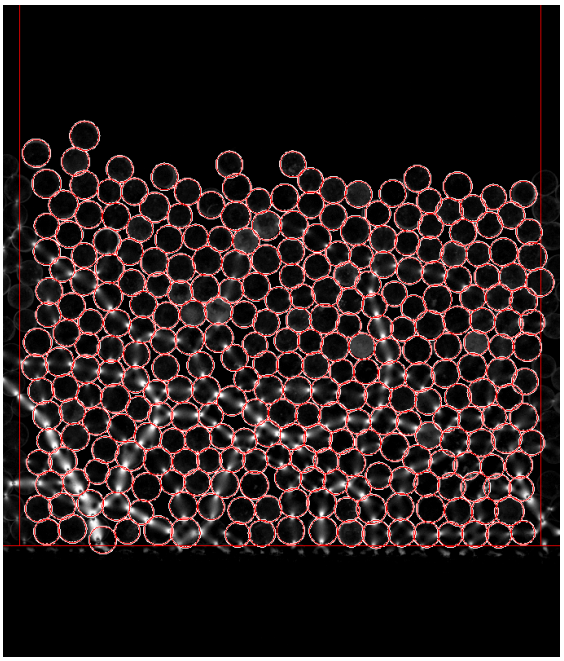

(c) Discs resulting from applying empirical criteria on the result of a high-sensitivity HT.

Figure 3.7: Example images extracted at different stages of the disc-locating algorithm.

discs with no error. Either extra circles would be identified, or some actual discs would not. Instead, it was found that the best results were obtained by applying a highly sensitive HT and then filtering out the coordinates of the circles that suited certain empirical criteria. The locations and radii of the circles found by the sensitive HT are ordered in a list, and the following criteria are applied on them to remove the circles that do not correspond to actual discs:

1. A sensitive HT is applied to the first frame of interest, frame f, as well as on the previous $(f-1)$ and following $(f+1)$ frames. Only the discs that could be tracked across all three frames were considered in the next step. As the discs, with average diameter of 40 $pixels$, moved at a maximum velocity of slightly over 1 m/s, corresponding to at most 5 $pixels/frame$, we expect them to have moved only a few pixels in between consecutive captures, making them easy to track. Discs whose centres lie below the baseline are discarded.

2. The list of discs remaining for frame f is ordered by percentage area that overlaps with other discs in the list, and the top disc is discarded. This is repeated until no disc is overlapped by others in more than 20% of its area.

3. The horizontal and vertical velocities are recorded as the average between the speeds required for the disc to move from its position in frame $f-1$ to where it was tracked to in $f+1$.

4. A sensitive HT is applied on all subsequent frames ($f = f+1$). From the second analysed frame onwards, discs that are matched to a disc on the list resulting from the previous frame were kept. For all new discs found, the criteria described in (1) and (2) are applied to determine whether they are legitimate discs that entered the camera view. Thus, new discs were added to the particle-tracking list corresponding to each frame.

5. If a disc found in the previous frame cannot be matched to a disc in the current frame, then a HT are applied to a square of width 1.5 times larger than the disc diameter, centred where the disc would be estimated to be if it continued to move with the velocity recorded in the previous frame. If it is still not found in this refined region or if its centre can no longer be expected to lie in the useful part of the image, it is removed from the list.

Figure 3.7b shows the raw image 3.7a after applying a threshold to exacerbate the noise introduced by the flour coating on the particle. On this adjusted image we applied the Matlab Hough Transform function with high sensitivity. Only the discs

that obey the empirical criteria just described, resulting in Figure 3.7c, are considered as the result of the particle-tracking algorithm.

In this way, for each frame analysed a list with a set of centre positions, radii and velocities are recorded. Overall, the success of the method relies on disc centres not being more than about a diameter and a half apart, or extra discs may be tracked in the gaps, and on the setting of a high-enough (but not exaggerated) sensitivity, or some discs might be left out. As it was implemented, on average no more than 1 in every 100 discs is either a false negative (when a disc is not recognised) or a false positive (disc detected where there is none).

When tracking particles in a bi-dispersed medium, the Hough Transform is run separately for the 'large' and the 'small' particles. In each case, the HT uses a range of radii that include all three sizes of discs in each species.

3.2.2 Location of the free surface

Much of the analysis that will follow this Chapter relies on knowing where the flow free surface is located. This is not straightforward as the flows produced in our setup are thin and the saltation of a single particle will have a large impact on the thickness of the flow at that downstream location.

To estimate the location of the free surface for each frame, we use the collection of discs tracked following the algorithm described in the previous subsection. We then divide the width of the tracked discs into intervals of $1.5d$ (where d is the mean disc diameter), and find the highest point of the top disc with centre within each interval. Figure 3.8 shows all the discs identified in an example frame as red circles, while the blue discs are those that have been identified as belonging to the top layer. Green crosses mark the highest points identified for each blue circle. We finally calculate the line of best fit using these highest points to obtain an estimate for the location of the free surface. The gray line in Figure 3.8 shows the estimated free surface location of the example frame.

Over a whole experiment the free surface line we draw for each frame varies in distance from the base by a diameter or two, and often changes in slope. However, in the steady-state stage of the flow, though the free surface oscillates, the average flow thickness or height of the free surface H remains contact. The average slope of the free surface in experiments over a smooth base is 20° to the laboratory ground (same angle as the chute inclination), and in both the small-disc and alternating-disc rough base cases the free surface angle is approximately 25° (5° more than the chute basal inclination). Thus we henceforth calculate H by averaging the distance between the chute baseline to the gray line over all frames extracted from the steady-state stage of the flow.

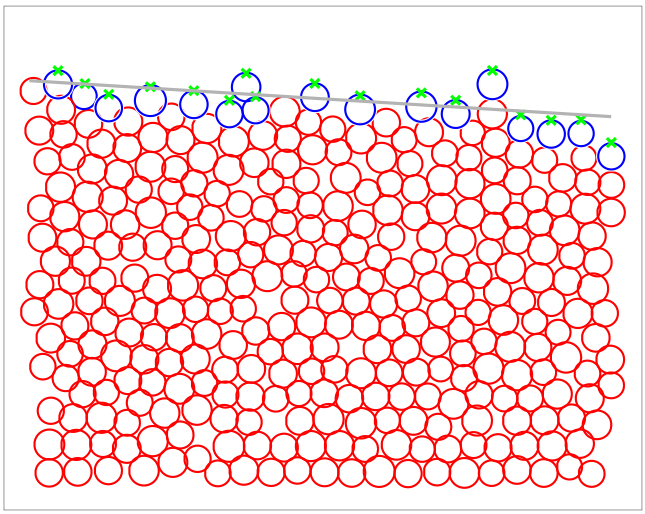

Figure 3.8: Auxiliary information used to estimate the location of the free surface for an example frame. The circles correspond to the discs found in the example frame. Blue circles, in particular, correspond to top layer discs. The highest points of the blue circles, marked with green crosses, are fitted with a linear function to estimate the location of the free surface, plotted as a gray line.

3.2.3 Force measurements

Once confident about the automated location of the discs in the experimental images, the pixels within them were extracted one disc at a time to be introduced into the force-calculating function. This algorithm is based on the light patterns, i.e. the pixel intensity patterns, observed by the camera within the photoelastic discs, following the procedure described in the previous chapter. To remind the reader, this procedure consists of virtually reproducing the photoelastic pattern that the disc would be expected to show if a force of estimated magnitude were acting on it at a known location. Then the virtual light pattern would be compared to the experimental image and an optimization algorithm would provide an improved estimation of the force magnitude and direction. With these better estimations the function would produce an improved image of what the photoelastic pattern is expected to look like, and the process is repeated until sum of pixel intensities squared differences between the virtual and experimental images falls below an 0.01 N (half the technique sensitivity, as determined in the next subsection), or until a pre-determined number of iterations has been reached.

Implementation

As mentioned in Section 2.3.3, the implementation of the algorithm is an adaptation of the open-source programme PeGS [8, 1, 3]. PeGs consists of three parts: *PeGSDiskPrep.m*, *PeGSDiskSolve.m* and *PeGSForceAdjMat.m*. The parameters specific to the system are input in the first part, and the second solves the optimisation problem

to return the estimated magnitudes and directions of the inter-particle forces. The third part serves verification purposes, and can be optionally used to visually verify the accuracy of the results.

PeGSDiskPrep.m contains a section of code that carries out a simple Hough Transform to find circles of a given radius, but we disabled this section of code to apply our own circle-finding algorithm instead, which was custom-made to maximise accuracy for our specific system. The programme was adapted to read previously created files containing the locations of the centres and radii of the discs detected in the image, as described in Section 2.2.1. The force-measuring algorithm is sensitive to errors in the disc centre locations and radius estimations, which is why the high temporal and computational cost of the disc-locating function is deemed worth the improved result accuracy. If a disc is not well centred or its radius is incorrectly estimated then it is more likely that there will be an error in the location of the point of force application. If so, the virtually produced photoelastic pattern will have a low correlation with the experimental image, leading to a bad estimation of the force magnitude and direction, as well as to a higher chance of the optimisation algorithm finding local minima (leading to a wrong result) for the other forces being estimated on that disc.

The contact location relies on the position and radii of each disc pair. PeGS determines a contact exists if the distance between both centres is smaller than the sum of their two radii plus an arbitrary tolerance distance *dtol*, which has to be determined by the user. The purpose of this variable is to allow for errors in the supplied centre locations and radii. In this investigation, *dtol* was set to be 1/4 of the pair smallest diameter, which is a generous amount that ensures a large proportion of neighbouring discs are evaluated as potentially in contact. If two discs satisfy this criterion, a single point of contact is determined to exist between them along the line that connects the two centres.

Once the point of contact between two discs is located, we estimate the direction of the contact force between them. We begin by drawing a line between the disc centre and the contact point, and then we draw another auxiliary circle of arbitrary radius *g2cr* from the contact point with its centre lying on the line drawn. If the sum of intensities within this circle is higher on one side of the drawn line then the force direction estimation is corrected. A new line is drawn in the new direction, and the process is repeated until the sum of intensities close to the contact on either side are equal, based on the fact that the photoelastic pattern seen from a contact is symmetric along the direction of force application. The final line defines the initial guess for the direction of the force applied at the contact to be used by the second component of PeGS.

Then, the intensities in this auxiliary circle of empirical radius *g2cr* are investigated

to determine whether a measurable force is actually being transferred there, and to obtain a sensible initial guess for the force magnitude and direction. If the pixels inside this circle have an average G^2 value larger than a threshold $g2threshold$, then the contact is deemed to transfer a sufficiently high force. The contacts that do not satisfy this criterion are discarded, as the photoelastic technique would be unable to reliably estimate a force exerted at this point. The combination of $g2cr$ and $g2threshold$, as implemented in PeGS, is defined by the user for each image such that the network obtained using this combination matches the visible force chains but not the particles that don't exhibit visible photoelastic responses. These values are set specifically for each experiment, as $g2cr$ needs to be larger in experiments where the camera is placed closer to the chute and the disc resolution is higher. Then, $g2threshold$ additionally depends on the thickness of the flour coating on the discs, which is applied after an arbitrary number of experiments and slowly wears off. Figure 3.9a shows an example of the network extracted from Figure 3.9b using an empirically determined combination of $g2cr$ and $g2threshold$ values.

Finally, from the intensities within the auxiliary circle obtained from the corrected contact point and force direction, an initial guess of the force magnitude is estimated using the G^2 method. This whole process is extremely expensive computationally (it can take up to half an hour per frame), but it maximises the chances of the algorithm accurately falling into global minima, and in practice makes a huge difference in the reliability of the results because of the algorithm's high sensitivity to errors. Figure 3.9c shows the theoretically reconstructed photoelastic patterns that could be expected from the output of PeGS. The similarity in the fringe pattern between both images (Figure 3.9a and Figure 3.9c) vouches for the technique accuracy.

Force measurement error

The measurement error depends mostly (1) on the optically diffusive properties of the base photoelastic materials, (2) on the experimental image resolution and (3) on the initial guess accuracy. Hence, an estimation for the measurement error has to be determined for the specific experiments where the technique is meant to be applied. We chose the clearest (most transparent) possible photoelastic material (*Clear Flex 50*) and used the camera with best resolution available to us at the required frame rate, but still there are limits to the technological capabilities available to us.

In order to investigate the measurement error specific to our experimental system, we numerically produced images of photoelastic fringe patterns for discs under $M = 2$, 3 and 4 concentric forces of equal magnitudes F, evenly distributed around the disc surface. M represents the number of forces applied on the disc. These images were then reduced to a resolution similar to that in which the experimental discs are observed,

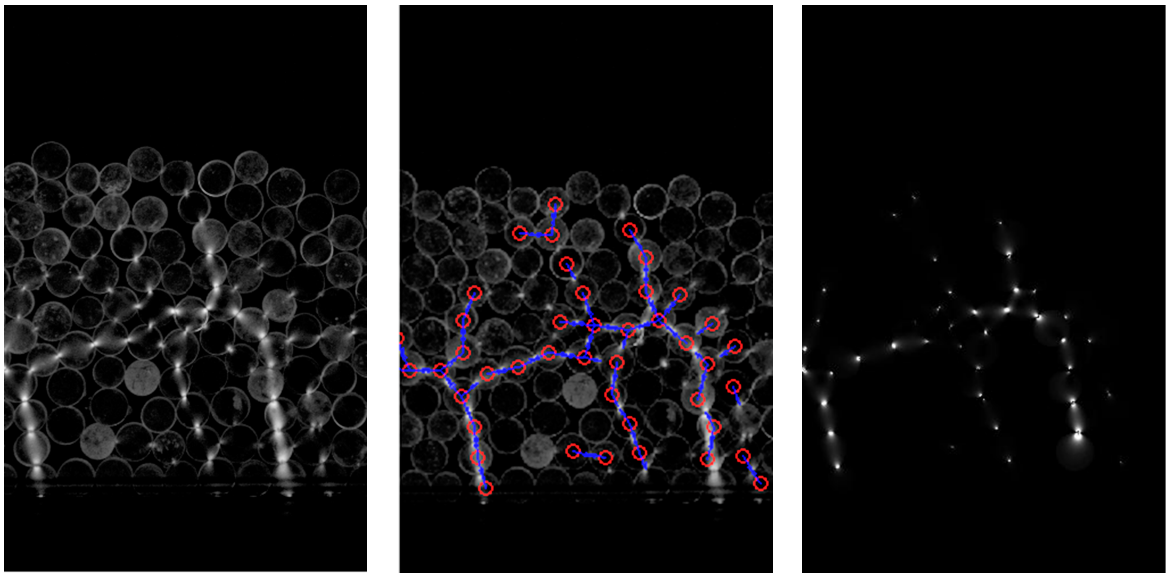

(a) (b) (c)

Figure 3.9: Demonstrative images of different steps in the contact location and force direction correction algorithm. Figure (a) is a raw experimental image as captured by the high-speed camera; (b) shows blue lines connecting the centres of the discs (red circles) identified to form part of the force network and; (c) shows the synthetic reproduction of the photoelastic fringes built using the results of the force-estimating algorithm on (a).

and a random noise of the order of the experimental one was added to the figures. Then, the force magnitudes in the result were resolved by PeGS (without considering that the discs are force-balanced) and plotted against the original real F, as shown in Figure 3.10.

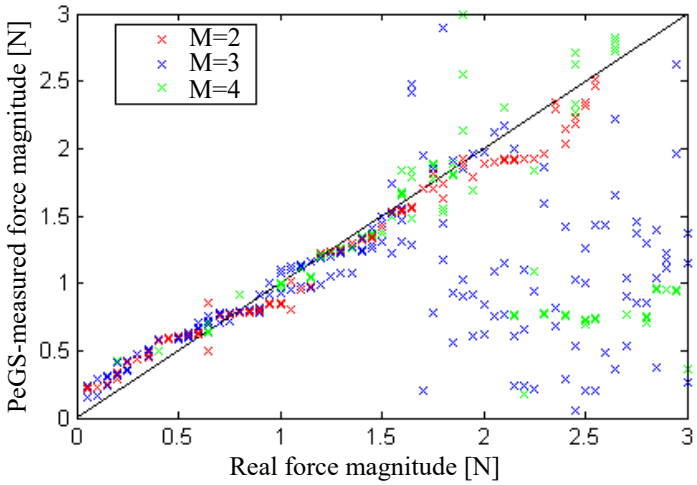

Figure 3.10: Correlation between the real forces exerted on a photoelastic disc and the measured magnitudes. This allows us to estimate the technique force measurement error, dependent on the number of forces acting on a single disc, M.

From Figure 3.10 we infer that there is a systematic error of approximately 0.05 N for forces below 0.5 N that originates from the experimental noise caused by the flour coating. The minimum force that can be consistently resolved by PeGS is 0.02 N, which produces the minimum photoelastic response larger than the noise in the disc face. The edge is ignored because in the experimental images it often shows a marked intensity difference due to the edges of the discs being inevitably slightly rounded. The sensitivity lower bound of our measurements depends on the inherent photoelastic response of *Clear Flex 50*, the thickness of the discs and the image resolution intrinsic to the camera. The measurement of even smaller forces could be achieved by increasing either the disc thickness, the image resolution, or the material photoelastic coefficient, but in our current set-up we are limited by the sensitivity lower bound of 0.02 N.

The random error of the technique can be as large as 20% between the lower bound set by the technique sensitivity and a critical value that depends on the number of forces acting on the disc. When the disc displays a large fringe number, the optimisation algorithm is prone to falling into local minima rather than the global minimum. Hence, there is a maximum force magnitude beyond which the technique becomes unreliable, which depends on how many forces act of the disc. The limits are approximately 2.5 N when $M = 2$, 1.6 N when $M = 3$ and 1.2 N when $M = 4$. However, the forces involved in the experiments are rarely stronger than 0.5 N, and particles are rarely subject to more than 2 or 3 contacts that transmit such large loads. Below forces of 0.5 N the systematic error measured is similar for whatever M, so this value is subtracted from all measurements. In our experiments, approximately 1 in 100 discs is subject to three or four force-bearing contacts, and in these cases two of them are usually dominant by at least an order of magnitude.

3.3 Coarse-graining for continuous avalanche dynamic fields

The result of the image processing functions is a list for every frame of all the discs tracked in it. Each disc i has a unique id number associated to it, centre coordinates x_i and y_i in the image, radius r_i in pixels and metres, number of forces acting on it z, and substructures with the z force magnitudes $|\mathbf{F_{i,z}}|$ and directions ($\alpha_{i,z}$ and $\beta_{i,z}$ values), as well as ids of the neighbours it is interacting with. The experimental images are not used henceforth and this list constitutes the raw experimental data on which all the following analysis is based.

All the individual disc information extracted is associated to the location of the disc centre, implying that the density ρ_{CM} and momentum p_{CM} carried are concentrated

at the centre of mass. Mathematically, treating the discs as point masses means that at position $\mathbf{r}$ and time t

$$\rho_{CM} = \sum_i m_i \delta(\mathbf{r} - \mathbf{r}_i(t)), \qquad p_{CM} = \sum_i m_i v_{x,i} \delta(\mathbf{r} - \mathbf{r}_i(t)), \tag{3.1}$$

where m_i represents the average mass of disc i in kg, $v_{x,i}$ its velocity in the downstream direction $\hat{x}$, $\mathbf{r}_i(t)$ the position of its centre of mass at instant t, and δ the Dirac delta.

Our exposure time (1/8000 s) implicitly defines a length of time over which photoelastic intensities are averaged. Spatially, averages can be drawn by binning the collected discrete data in space and averaging in time, but this method is sensitive to the choice of bin size, and because these flows are under 20 particles deep, the result will still probably be coarsely discretised. Instead, coarse-graining theory supplies a calibration procedure to determine the most appropriate averaging lengthscales. These will be large enough to average over several particles (or frames) so that microscopic variations due to discrete particle-to-particle fluctuations can be ignored, but smaller than the distances across which macroscopic changes can be seen.

The coarse-grained model consists in a convolution of the discretised data directly obtained from the particle tracking process with a coarse-graining function of space, $\varphi(r)$, where r represents the distance to a disc centre, that distributes the local information over a pre-calibrated characteristic coarse-graining lenghscale, w. Thus, for each frame the coarse-grained equivalents of Equations 3.1 would be

$$\rho_{CG} = \sum_i m_i \varphi(r_i, w), \qquad p_{CG} = \sum_i m_i v_{x,i} \varphi(r_i, w). \tag{3.2}$$

The function φ can be chosen arbitrarily, as long as it satisfies that [12]:

- φ is non-negative, $\varphi \leq 0$, ensuring the density ρ is always positive, and that the moment p has the same sign as the particle velcity.
- φ is spatially normalized, $\int_{\mathbb{R}^3} \varphi = 1$, to hold mass and momentum conservation.
- There exists a cut-off c such that $\varphi(r) = 0$ for $|r| > c$, ensuring that the effect of each variable is constrained within a definite distance defined by the lengthscale w.

In this work, the coarse-graining function used was

$$\varphi(r, w) = \begin{cases} Ce^{(1-|r/w|^2)^{-1}} & |r| < w \\ 0 & |r| \geq w, \end{cases} \tag{3.3}$$

where C represents the total volume of φ over the whole domain. This function was chosen (1) because it naturally tends to zero at lengths equal to w, and (2) because it provides an easy visualization of the coarse-graining length-scale based only on w, which may have different components in the vertical and horizontal directions (here, w_z and w_x, respectively).

Figure 3.11 shows colourmaps of the continuous density fields obtained by coarse-graining the data extracted from the same frame shown in Figure 3.7 according to Equation 3.3. Each subfigure corresponds to a different characteristic length-scales in the $\hat{x}$ and $\hat{z}$ directions, w_x and w_z respectively, resulting in different degrees of discontinuities. The ideal coarse-graining length-scale w depends on the system and on the coarse-graining function φ. In each case, Goldenberg *et al.* (2006) [4] stipulated the optimal w is large enough to average over microscopic changes (for example, mass variations between individual grains) but small enough to not average over macroscopic changes (for example, if part of a system has lower packing fraction than another). In other words, w must be the smallest value such that using the function $\varphi(w)$ results in smooth profiles within sub-w length-scales. For the experiments described in this paper, the optimal w was found to be $3d$, where d is the average disc diameter. However, we notice that the flow does not change significantly in the stream-wise direction (horizontal, $\hat{x}$), while it does vary rapidly in the cross-flow direction ($\hat{z}$). Thus, we use different coarse-graining length-scales for the two directions depending on what aspect of the flow we wish to study.

In addition, the method first proposed by Goldhirsch (2010) [5] and later further developed by Weinhart *et al.* (2012) [13] was applied to furthermore transform the discrete point forces from the photoelastic analysis into continuous fields. The expression proposed by them has the added benefit of ensuring that the resulting continuous data inherently obeys the laws of mass and momentum conservation.

$$\sigma_{\alpha\beta} = \sigma^k_{\alpha\beta} + \sigma^b_{\alpha\beta} + \sigma^w_{\alpha\beta}, \tag{3.4}$$

where α and β are dimensions of the stress tensors.

This expression separates the *bulk* or *collisional* components of the stress tensor, σ^b, from the *kinetic* or *streaming*, σ^k, and accounts for the stresses that originate due to interactions with the walls, σ^w:

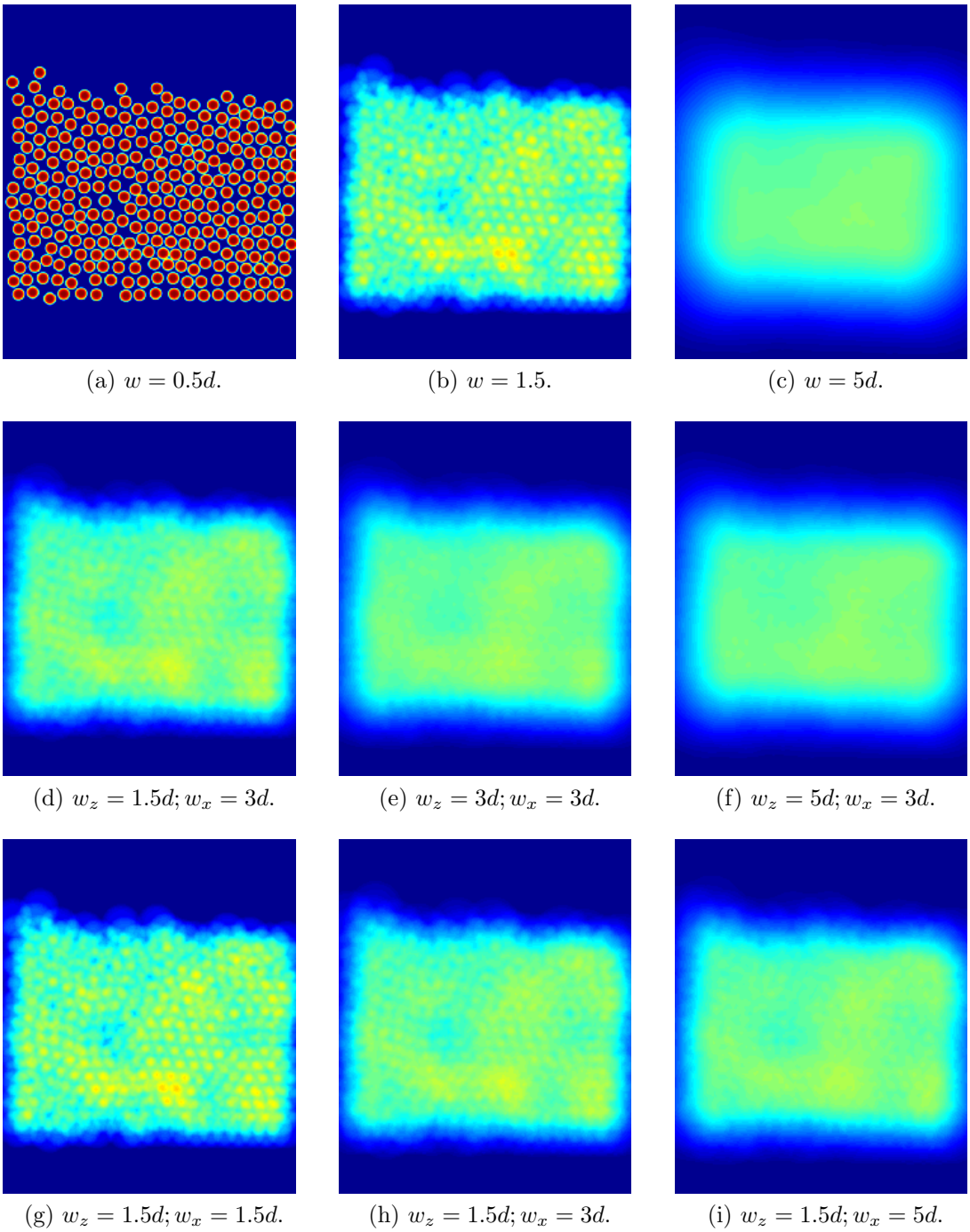

(a) $w = 0.5d$. (b) $w = 1.5$. (c) $w = 5d$.

(d) $w_z = 1.5d; w_x = 3d$. (e) $w_z = 3d; w_x = 3d$. (f) $w_z = 5d; w_x = 3d$.

(g) $w_z = 1.5d; w_x = 1.5d$. (h) $w_z = 1.5d; w_x = 3d$. (i) $w_z = 1.5d; w_x = 5d$.

Figure 3.11: Coarse grained density field for different coarse-graining characteristic length-scales.

$$\sigma^k_{\alpha\beta} = -\sum_{i=1}^{N} m_i v'_{i\alpha} v'_{i\beta} \varphi(\mathbf{r} - \mathbf{r}_i),$$
$$\sigma^b_{\alpha\beta} = -\sum_{i=1}^{N} \sum_{j=i+1}^{N} f_{ij\alpha} r_{ij\beta} \int_0^1 \varphi(\mathbf{r} - \mathbf{r}_i + s\mathbf{r}_{ij}) ds, \tag{3.5}$$
$$\sigma^w_{\alpha\beta} = -\sum_{i=1}^{N} \sum_{k=N+1}^{N+K} f_{ik\alpha} a_{ik\beta} \int_0^1 \varphi(\mathbf{r} - \mathbf{r}_i + s\mathbf{a}_{ik}) ds,$$

where $f_{ij\alpha}$ represents the force applied between particles i and j along component α, $r_{ij\alpha}$ is the distance between their centres, and $a_{ij\alpha}$ the distances between the centres and the contact between them.

3.4 Preliminary experiments

A series of preliminary experiments were carried out to understand the system better before committing to an experimental design - changes to which would have been costly given the technical challenges of seting up an experiment of this physical magnitude (see Figure 3.1).

3.4.1 Minimum sample rate analysis

One of the main concerns in applying this technique to a dynamic system was whether it was possible to set up a detection system fast enough to capture the force transmission. To study the behaviour of the forces actually involved in the impact between particles, an experiment was carried out where a single particle was ejected onto an array of nine particles arranged horizontally in a line. A *Photron* FASTCAM SA1.1 high-speed camera, located perpendicularly to and approximately 50 cm away from the experimental setup, recorded the fringe patterns appearing within the particles at 6250 frames per second. Figure 3.12 shows four images taken during the experiment illustrating the transmission of force along the chain. Circles were drawn in red over the discs after being located using the Hough Transform and labelled according to their position. Because it was difficult to make the collision perfectly horizontal, the first particle hit redirected substantial force to the channel floor, so only the remaining 8 discs were considered for the following analysis.

The intensities of the pixels within each red circle were then extracted and used to solve the inverse problem described in Section 2.3.2 and thus obtain the contact forces along the chain. Figure 3.13 shows the time evolution of the forces measured at each

Figure 3.12: Experimental images of a row of photoelastic discs being impacted by another particle from the right.

contact for every particle numbered as shown in Figure 3.12. Each colour represents a different particle, the solid lines represent the forces at points where the particles are hit (force 1) and the dashed lines represent the force magnitude at the point of transmission (force 2).

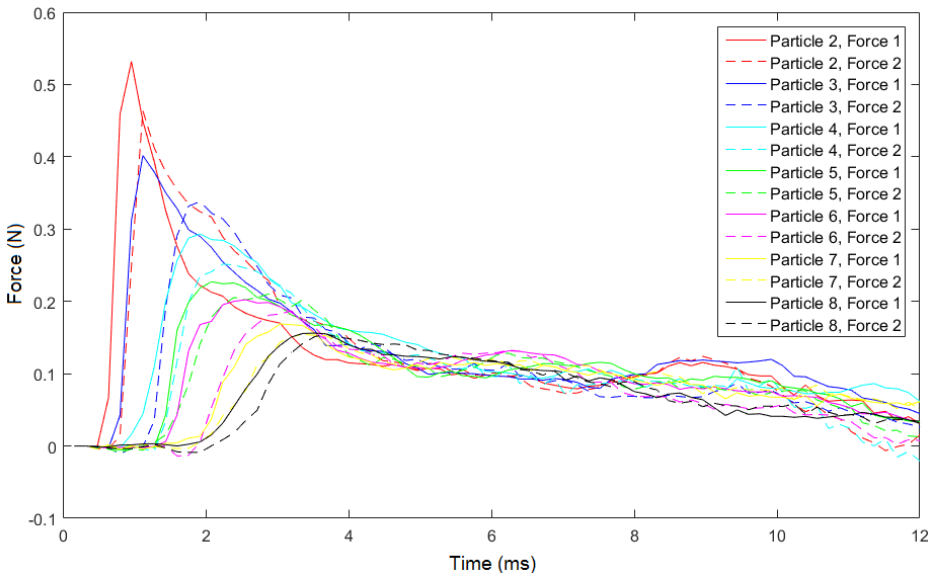

Figure 3.13: Temporal distribution of the force at each interparticle contact, measured within each circle through photoelasticity. Forces are measured with absolute errors of ± 0.05 N, as per Section 3.2.2.2.

Figure 3.13 demonstrates that, on collision, particles exert a continuous distribution of forces on each another. The forces measured at each contact point resemble a skewed Gaussian function, where the viscoelastic properties of the material cause the long tail. The skewness and height of the distributions both decrease as the force pulse travels along the chain, which is attributed to both to the inelasticity of the material and energy dissipation to the channel base and walls. In any case, Figure 3.13 shows that the main effect of the impact is visible within only 1 ms, so visualisations involving

moving and colliding particles must be carried out at exposures smaller than 1/5000 s. Hence, recordings whose purpose was to measure forces were henceforth carried out with the smallest possible exposure time that would produce images with a complete range of intensities (from 0 to 1), which was 1/8000 s (determined in the preliminary experiment described in Section 2.4.1).

The collision duration is comparable to the time of force transmission along the chain of particles. Figure 3.14*(a)* plots the instant at which each contact, located at known distances from the initial impact, exhibits a peak force. From this graph the speed of the force pulse along the chain was calculated to be of around 46 m/s, which means that in the time taken for a particle to show most of the force it is impacted with (1 ms), the force pulse can travel more than twice the diameter of a large particle (2 cm). It would be interesting to calculate the dissipation between consecutive collisions, for which the maximum force measured at each contact was plotted against its position along the chain in Figure 3.14*(b)*. This graph demonstrates that the force decays exponentially with the length travelled, but in the present experiment this energy dissipation must be due primarily to transmissions towards the chute base, rather than due to the inelasticity of collisions.

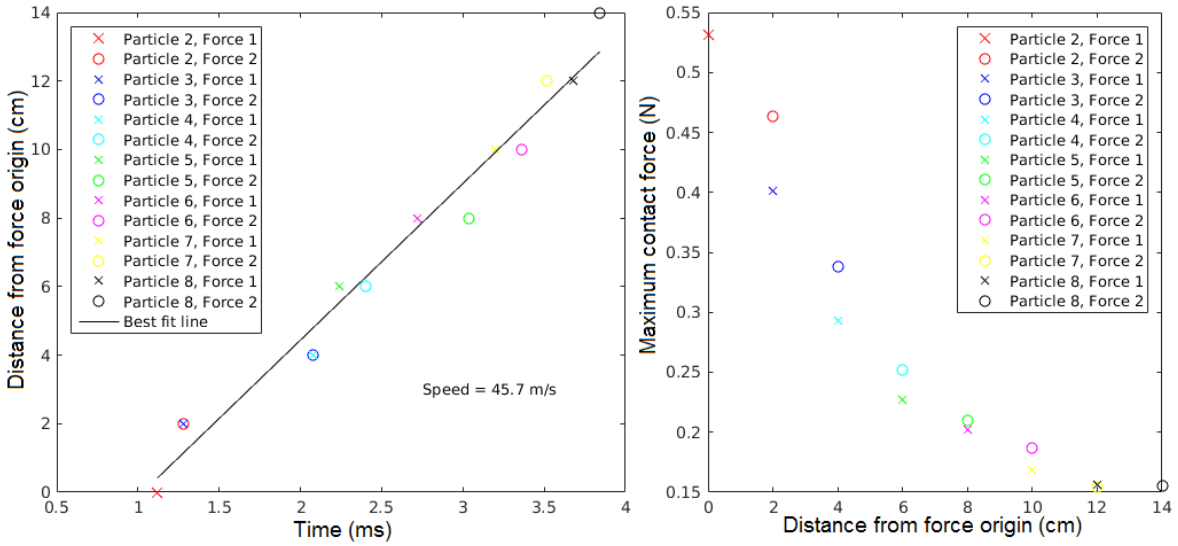

Figure 3.14: (a) Instant of peak force and (b) force peak magnitude plotted against corresponding contact distance from the initial impact origin. These plots provide a measure of the force propagation speed and force dampening, respectively. Forces are measured with absolute errors of ± 0.05 N, as per Section 3.2.2.2, while the locations of the contact points between discs carry an error or $\pm 5 \times 10^{-4}$ m.

The physics behind the propagation of forces along a chain of granular media is highly interesting but extremely complex and beyond the scope of this investigation. Such dynamic experiments could be used to study the topic further, and indeed more

experiments were carried out in collaboration and support of the theory developed in Shrivastava *et al.* (2017) [9]. However, in the interest of focusing the work to do in the limited project duration, further modelling of force transmission in this complex media was put aside.

3.4.2 Hopper discharge analysis

Janssen's effect [6] is an example of a behaviour unique to granular media. This effect explains how hoppers will discharge granular material at a constant rate that depends only on the hopper dimensions for most of the flow. Hence, we investigated whether this effect still holds in 2D hoppers filled with large particles (relative to the discharge opening), and whether such an arrangement would be appropriate as a feeding mechanism to my experiments.

It was experimentally observed that when a funnel is filled with a granular material, the discharge can be expected to depend only on the ratio between particle diameter, d and opening aperture diameter D [6]. This result contrasts with the behaviour of classical fluids, where the pressure, and therefore the discharge rate, at the opening depends directly on the height of the fluid column above it. Janssen [6] explained that the accumulated weight of a column of granular material is periodically redirected through force chains towards the walls of the container it is in. Hence, while the funnel is filled to a height larger than a critical value, which is determined by the ratio d/D, the granular discharge rate out of a hopper will be constant.

The present problem differs from Janssen's studies in the geometry, so it was still deemed necessary to prove that the effect he described holds in 2D as well as in 3D. The discharge out of a 2D hopper was investigated experimentally to test whether it makes an appropriate feeding mechanism for the targeted quasi-steady avalanche. A narrow funnel with adjustable opening was built from acrylic. The reason for choosing a V-shaped hopper was to ensure that all particles were driven down the opening in mass flow (in contrast, flat-based hoppers discharge as a funnel flow and tend to entrap some at the edges). The discharged particles were then fed into an equally narrow short inclined chute, where the first stages of avalanche development could be observed. Figure 3.15 shows the experimental setup design and a photograph of the hopper filled with discs and ready for use.

This setup allows the investigation of the velocity and acceleration fields of the flow developed within the hopper, in the discharge zone and in the subsequent short incline. The main aims of the experiments carried out with it were to (1) ensure it is possible to produce a constant discharge flux from a 2D hopper, (2) quantify how the discharge flux increases with the gate width, and (3) determine what is the minimum hopper filling height that allows this regime.

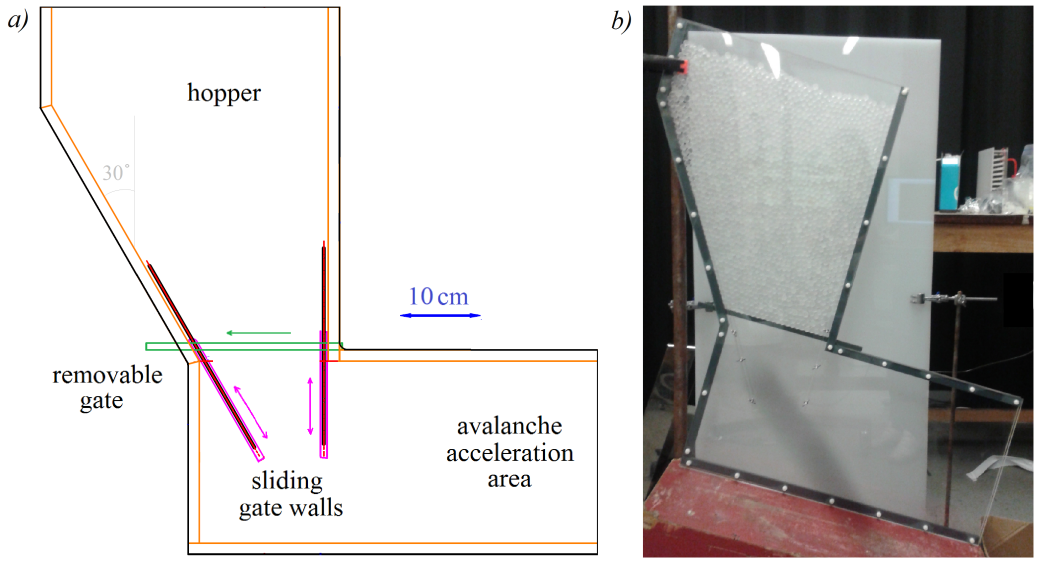

Figure 3.15: (a) Hopper design and (b) setup picture.

Several experiments were run with different gate openings while a high-speed camera recorded the particles motion directly above and below the gate at 1000 frames per second. For these experiments the setup, as drawn on Figure 3.15a, was inclined between 10° and 20° clockwise. The hopper was then filled with the small range of *Clear Flex 50* discs (11, 12 and 13 mm radii) uniformly mixed. Once the gate was released (simply by pulling), the fact that the particle radii were known allowed their location via a Hough Transform to be effective. The chosen frame rate was fast enough that the particles always moved by less than a radius between frames, which facilitated an efficient particle tracking. In this way, a simple algorithm counted the number of discs that crossed a line arbitrarily located along the gate opening and another across the incline over certain number of frames. Figure 3.16a shows a random frame taken from one of the experimental videos, over which the two lines across which the flux was measured were drawn. The line across the hopper gate was painted blue, and the one across the incline was drawn in orange. Figure 3.16b plots the time evolution of the flux across each line averaged over 50 frame intervals ($1/20s$). In this particular experiment the average diameter was $d \approx 12$ mm, the width of the hopper aperture was $W \approx 130$ mm and the distance between the opening and the channel base was $H \approx 240$ mm.

The first aspect that stands out of Figure 3.16 is that the flow takes a certain adjustment time, hereafter called t_a, to develop a steady regime. From Figure 3.16 we infer that from this example $t_a \approx 1.5$ s. The flow across the hopper gate (blue line) peaks during the first instants as the particles fall accelerated solely by gravity. Once the first discs reach the channel base, they are almost stationary before they are accelerated down the incline. At that point they collide with the discs that fell from

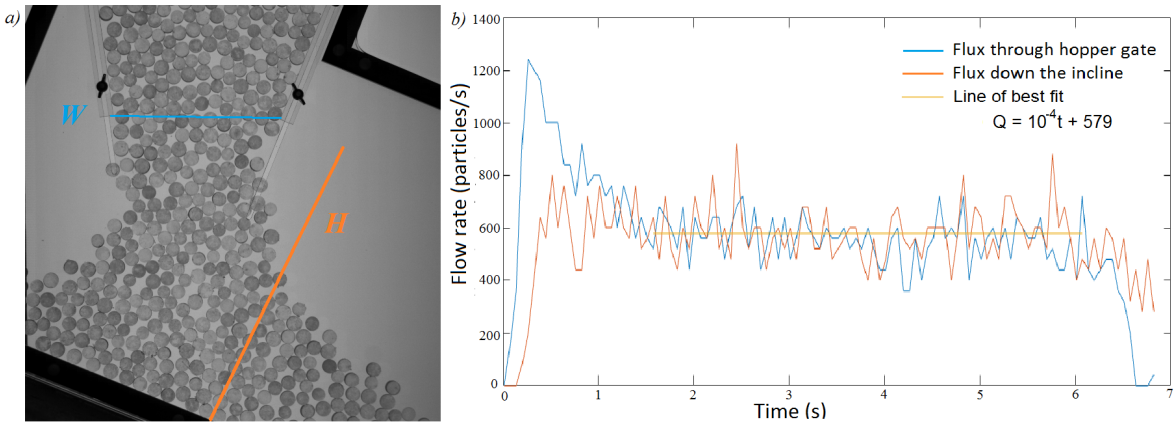

Figure 3.16: (a) Example frame of an experimental video taken to study the flow discharged from a 2D hopper, with lines drawn to illustrate where the flux was measured. (b) Time evolution of the flux averaged over 1/20s intervals. The blue lines plot the flux across the gate and the orange across the incline. The yellow line is the best fit to the flux measurements in the stationary regime, for which the slope is very small and the average Q is given in the legend.

the hopper after them, slowing down the whole column above. In this way, a quasi-stationary region develops upstream of the hopper opening in the channel over which the particles then roll at constant speed. If viewed between polarizers, this region would probably show force chains reaching from the channel base to the particles above the gate line. Until this region is fully formed, the flux through the hopper gate is faster than that down the incline, but afterwards both fluxes across both lines are reasonably consistent with each other and constant in time until the hopper is depleted below a critical value. A linear regression of the fluxes after the adjustment stage shows that the slope is very small ($10^{-4} \sim 0$, from Figure 3.16), proving that the flux in this regime is practically constant. In answer to the first issue posed, this design of a 2D hopper does allow a constant discharge flux, hereafter referred to as Q.

The time t_a is expected to depend on (1) the ratio between gate width W and particle diameter d, (2) the distance H between the hopper gate and the chute base, as this is affects how long the force chains in the flow need to be before they reach above the hopper gate, and the channel inclination θ, which will affect how fast the discs are removed from the stagnant region and accelerated down the chute. It is expected that for ratios dH/W larger than a critical value, or for sufficiently inclined channels, the acceleration down the chute becomes large enough to prevent the formation of vertical force chains longer than H. However, the setup is not capable of replicating these conditions so the discharge out of the hopper is a function of W/d, H and θ.

Nevertheless, in our setup W is increased by increasing H (Figure 3.15). For any increase of W, H increases by a known amount, which can be calculated in terms of

the inclination with respect to the vertical of the sides of the funnel-shaped hopper, ϕ. For a segment sliding of the left gate δd, W increases by $\delta d \sin\phi$ and H increases by $\delta d \cos\phi$, which means that

$$H = H_0 + (W - W_0)/\sin\phi,$$

where H_0 is the perpendicular distance between the channel base and the gate left wall when it is at the smallest aperture W_0. For this particular experimental setup, $W_0 = 10cm$, $H_0 = 15cm$ and $\phi = 30°$. Thus, for the case considered, H is not a free parameter as it can be expressed in terms of W, and if in addition the chute inclination θ is fixed, then it is expected that the stationary discharge flux generated from the hopper can be determined by varying only the gate width W. Figure 3.17 plots the dependence of Q with W, which visually appears to be linear. From the experimental flux measurements, the second aim of quantifying Q in terms of W for a specific particle diameter d was achieved.

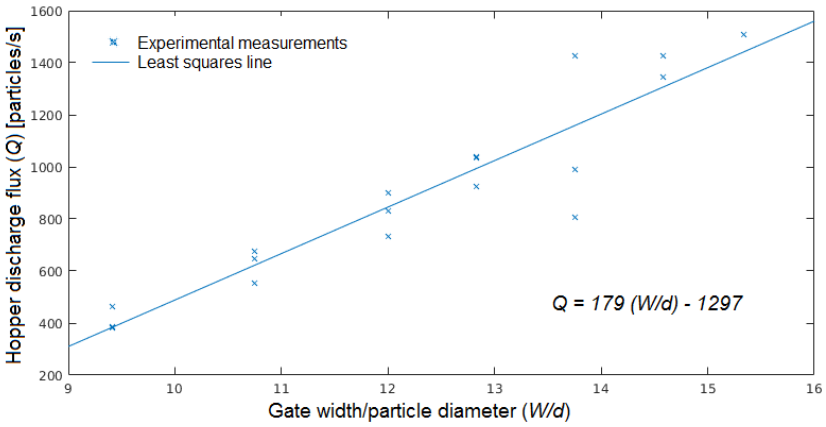

Figure 3.17: Stationary hopper discharge flux plotted against the dimensionless hopper gate opening (in terms of the average particle diameter). The hopper discharge flux is estimated with a 5% error, as determined from the standard deviation of the flux measured throughout the steady state stage of an experiment. The error of the gate width/particle diameter is dominated by the error in the determination of the particle diameter, which is approximately 9%.

Finally, the velocity field within the hopper was investigated to determine the minimum filling height h required for a constant discharge. As a consequence of granular weight redistribution towards the walls through force chains, it is only the region directly above the hopper opening whose velocity is substantially affected by the width of said opening. This is the region where the particles' weight is not completely redirected towards the container walls and therefore they fall with a speed greater than the bulk. Elsewhere the particles move with relatively small, uniform and dominantly vertical velocity. In a hopper where the grains are allowed to fall freely, it is therefore expected

that the discharge will be constant only as long as the reservoir is filled to a height that covers this region completely, as only the accumulated weight of the particles directly above the opening plays a role in the pressure across said opening.

However, it was found that the discs in the present experiments do not fall freely, but are slowed down by the stagnant structure that forms below the opening, so further testing was in order. From Figure 3.16b, taken for a ratio $W/d \approx 10.7$, it was observed that the amount of particles falling down the chute per second is practically constant in all cases until the hopper discharges completely. At this point the blue line drops immediately to zero and the orange line only then begins to trail off. In conclusion, the hopper gate width affects the stagnant region size, and the flux of discs down the chute is given by how fast they are accelerated from rest from this region. The pressure at the gate is not large enough to substantially push the particles down the inclined channel.

Using the same experimental setup shown in Figure 3.15, inclined by 10° clockwise, the camera was focused on the funnel-shaped area initially filled with discs. Several discharges of the hopper with different gate apertures were recorded and using the particle tracking algorithm described in Section 3.2.1, we observed the velocity field. We partitioned the area within the funnel walls into squares with lengths of slightly more than a disc diameter. Then, we we averaged the horizontal and vertical velocities of the particles that passed within each partition during the first half of the frames corresponding to the steady flux regime. In Figure 3.18 lines were drawn on an image taken of the experiment to represent the measured velocity within each partition. Both arrow lengths and colour (from blue to red) represent the particle speed at the partition centre averaged over most of the constant-discharge-flux stage. It can be noticed that in at least the upper half of the hopper the particle velocity is essentially uniform; it is only along the gate and in the region directly above it that the dominating arrow colour is red. In addition, Figure 3.18 evidences that below the hopper opening, the particles upstream of the discharge are practically stationary, whereas downstream they are accelerating.

3.4.3 Flow stages

For each experiment performed, the camera records the discs passing between the polarisers from the moment the gate is pulled until the hopper is completely depleted and the flow stops, which total to a flow duration between 10 and 30 s, depending on the flow rate. All recordings henceforth are carried out with an exposure time of 1/8000 s, but only 1000 frames per seconds are saved to allow for rearrangements between captures. The experimental videos of the flow past a given point are divided into three stages: initially the flow quickly thickens and slows as the *avalanche head*

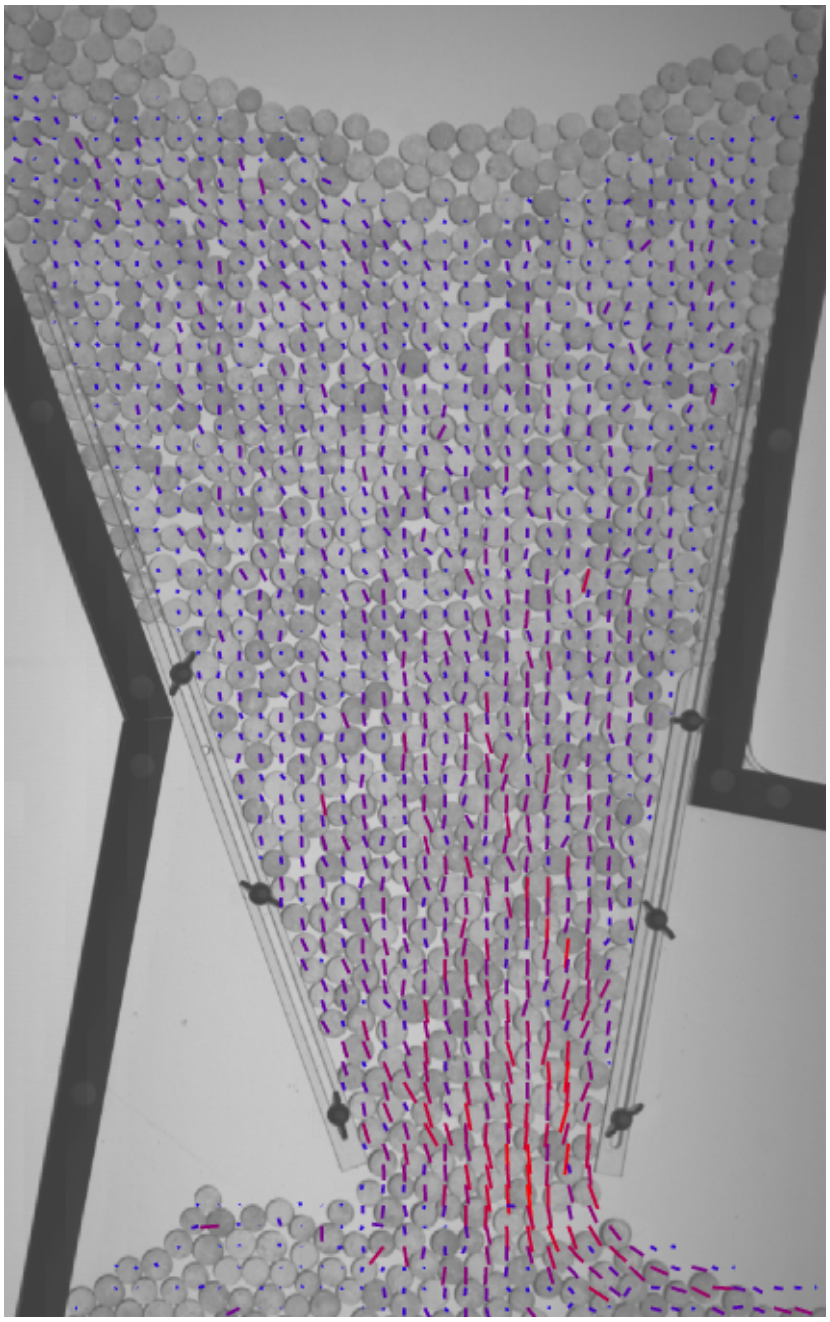

Figure 3.18: Velocity field inside a 2D hopper with an opening width $W \approx 12cm$. The average velocity of the particles for a grid of points where discs are detected at any time during a discharge is marked in coloured lines. The length and colour of the lines represents the average speed of particles at that point: short blue lines show small speeds, while long red lines represent high speeds. The direction of the lines represents the direction of the particles as they pass that point.

passes the observation point, until it reaches a *steady state* where a constant height and velocity profile is maintained for several seconds, after which the flow *decelerates* and *thins*. Figure 3.19 shows the velocity profile time series (obtained by binning rather than coarse-graining for simplicity) measured at a location 75 *cm* from the hopper for an experiment performed over a rough base. In sequence, the initial stage where the flow thickens (stage 1) transitions into a steady-state that lasts for approximately 10 *s* (stage 2), after which the flow slows, thins and drains (stage 3). Once the hopper is depleted beyond a certain level, the flow slows and thins and eventually stops altogether. In the *rough base* cases, a layer of static discs, forming an angle in the lab frame of about 23°, remained deposited on the base even after the experiment finished. For this work, we ignore the transient developments and focus on the middle section in the time series, marked 'stage 2', which is characterised by a constant flow height.

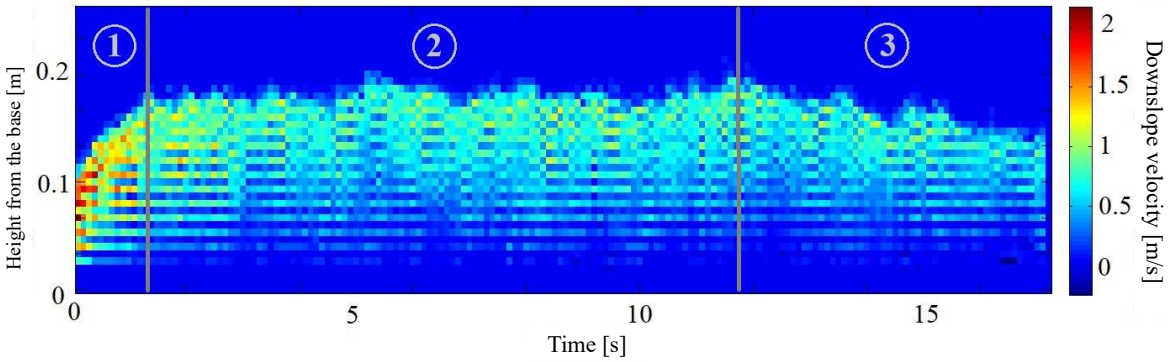

Figure 3.19: Evolution in time of the binned particle streamwise velocities as they pass through a mark 75 *cm* downstream from the hopper.

From the approximately constant height and velocity profile during the middle stage, we infer that the hopper supplies a constant flux of discs into the chute. For a full hopper, the duration of this second stage for flows over each basal roughness type depends solely on the hopper gate aperture. The hopper gate aperture was kept at a constant width of 12 cm (approximately 10 particle diameters), which offers a reasonable trade-off between a relatively long steady-state stage and a wide range of velocities for experiments over a rough base.

3.4.4 Minimum representative sampling set

The analysis of the data is computationally expensive: the circle-finding algorithm and the three parts of the force calculation typically take between half an hour and an hour per frame. For the purpose of efficiency, we want to economise the number

of frames needed per experiment. We therefore investigate the minimum number of frames needed to obtain representative coarse-grained fields.

We compare the results of averaging a field over the first 10, 50, 100, 200, 300, 500, 750 and 1000 frames of the steady state stage of an experiment. We use an experiment performed with a mono-dispersed media (discs of 11, 12 and 13 mm in diameter in equal numbers) over a base of alternating large (22 mm) and small (12 mm diameter) discs, filmed by centring the window 25 cm from the beginning of the chute where the flow is thickest. This modality of experiment was chosen because it produces the slowest and thickest flows. The field we chose to test the consistency of these averages is the mean time T taken for pixels to change, because it is the variable that requires most sampling points to calculate accurately, and all other variables we study are measured by post-processing the image intensity distributions.

We measure the average time for a pixel to change intensity, by first taking the time series of each pixel brightness B for the selected number of frames. We then measure the autocorrelation coefficient $C(\Delta t)$ across the entire time series:

$$C(\Delta t) = \frac{\sum_t \left[B(t) - \bar{B}\right] \left[B(t+\Delta t) - \bar{B}\right]}{\sum_t \left[B(t) - \bar{B}\right]^2}. \tag{3.6}$$

We then fit the first peak of $C(\Delta t)$ by an exponential function of the form $C(\Delta t) \propto \exp[-\Delta t/T]$, where $T(x, z)$ represents the typical lifetime of the intensity of a pixel with coordinates (x, z) to decay. We then average across all rows (because in our thin flows we expect fields to vary only vertically in our camera frame) to determine the dependency of T with depth, $T(z)$. Figure 3.20 shows the profiles $T(z)$ extracted using different numbers of frames.

When the sample of frames analysed is too small, pixels do not vary enough to accurately measure the average time taken for them to fade. For large numbers of frames, on the other hand, the profiles of $T(z)$ collapse. The minimum number of frames needed for the corresponding profile to collapse with the results for longer experiments is 400. Just to be sure, for all experiments analysed from now on, we average all variables over at least 500 frames. Moreover, having determined that the longest change in pixel intensity lasts up to 0.08 s (from Figure 3.20), 0.5 s (the actual recording time to capture 500 frames) allows for plenty of rearrangements. We thus determine that 500 frames are enough to ensure representativity of results without spending unnecessary computational resources.

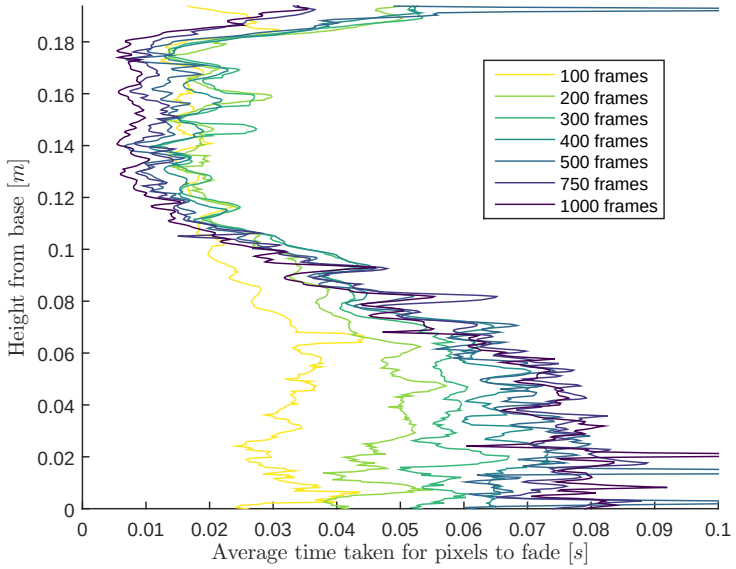

Figure 3.20: Average time T taken for pixels to decay in intensity. The different coloured lines correspond to measurements of T made using different number of frames of an example experiment.

3.4.5 Experimental repeatability

The addition of flour to lubricate the system is necessary, or friction between the plastic discs and the acrylic walls would prevent flow altogether. On handling the discs during and between experiments, the flour coating wears off, so when we perceive the flow slowing, we reapply a light coating. This raises the question of whether the arbitrariness in the flour coating thickness causes too much variability in the flow characteristics.

To investigate this issue we measure the variability in the flux of discs produced during 7 mono-dispersed experiments (made of discs of 11, 12 and 13 mm in diameter in approximately equal numbers) over each of the topography types. The experiments analysed were performed non-consecutively over two years and many experiments were carried out for different purposes in between each repetition. The flux measurements are summarised in Table 3.1.

Flux [discs/s]	1	2	3	4	5	6	7	**Average**	**Std. dev.**
Smooth base	987	951	907	910	873	907	840	**907**	**50**
Small discs base	379	373	382	407	391	372	392	**385**	**12**
Alternating discs base	386	287	249	281	244	226	259	**276**	**53**

Table 3.1: Flux, measured as discs crossing a given cross-stream line per second, measured 7 times over each of the used basal modalities.

Table 3.1 shows that the standard deviation in the flux measurements can reach up to 20%. This is quite a high value and must be taken into account during the analysis and interpretation of results. When comparing results from different experiments, we must take into account that there is a 20% error in the flux found from the area of the velocity profiles.

3.4.6 Creep of a freshly deposited bed

Every experiment over a rough base leaves a deposit that can be up to 5 or 6 particles deep. We wish to examine the stability of such seeming static deposits, since reports in the literature show that freshly sedimented beds settle and creep over long periods of time, even under subcritical stresses [2]. Usually, such creeping is expected to decay exponentially with time [2]. The preparation of the following experiment, camera setup and the code to capture and analyse the results were developed side-by-side with co-worker Karol Bacik, of whose input we are very grateful.

We investigate the creep of freshly deposited discs by creating a barrier in the lower end of the chute, and realising a hopper-full of a bi-dispersed mixture of discs that deposits along the base. We use large discs 21, 22 and 23 mm in diameters (in equal numbers) and small discs 11, 12 and 13 mm in diameter (also in equal numbers), in a ratio of small to large discs of 1:20. Figure 3.21 shows the adapted experimental setup (Figure 3.1) after the discs have been released into the blocked channel. The discs deposit forming an angle approximately equal to the inclination of the chute, and a ISVI IC-X12CXP camera, mounted with a *Nikon* 60 mm lens (f/2.8), recorded the discs photoelastic response within a viewing window centred about two thirds up the chute.

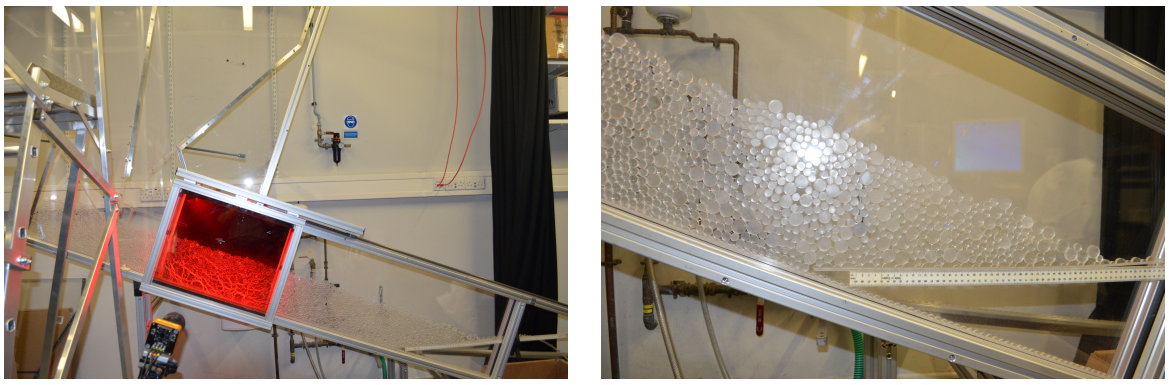

(a) Experimental chute (Figure 3.1) adapted to contain a thick deposit of discs.

(b) Zoom into the inclined partial barrier placed at the lower end of the chute.

Figure 3.21: Experimental setup to measure creep in a freshly deposited layer of photoelastic discs.

The camera recorded one frame every 5 min, with an exposure time of 1/50 s,

for 25 days. We compare each frame with the one after through finite differences by calculating, for each frame, the average absolute value of the difference between each pixel in an image and the corresponding pixel in the next frame in the sequence,

$$\langle \delta I \rangle(t) = \frac{1}{4096 \times 3072} \sum_{i=1}^{4096} \sum_{j=1}^{3072} |I_t(i,j) - I_{t+t_s}(i,j)|, \tag{3.7}$$

where $I_t(i,j)$ represents the intensity of the pixel with coordinates (i,j) in the image taken at time t, $t_s = 5$ min is the time step between consecutive frames, and 4096×3072 is the camera resolution. Because the pixel intensity is highly correlated to the photoelastic response within the discs, this quantity then measures rearrangements in the force network as well as in the discs positions. Figure 3.22 plots the time evolution of this quantitative measure of the differences between consecutive frames.

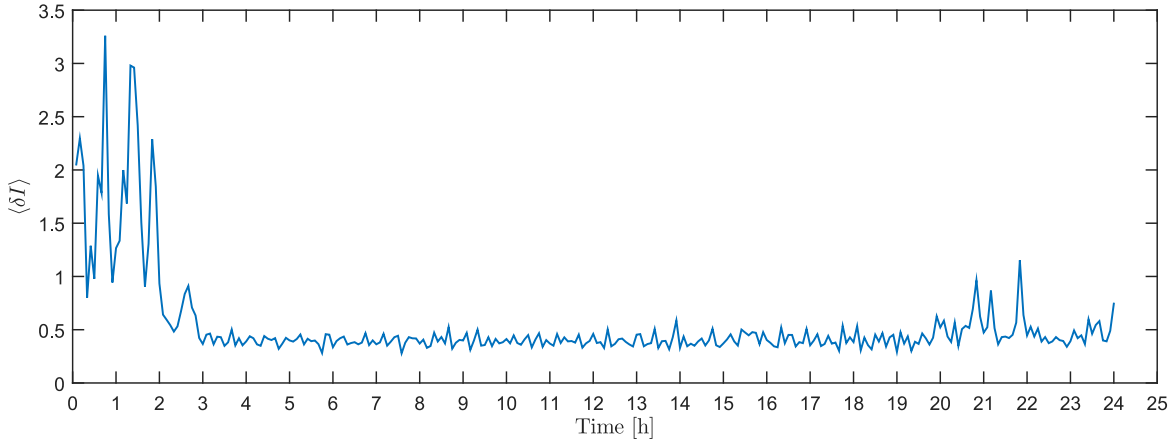

(a) First day.

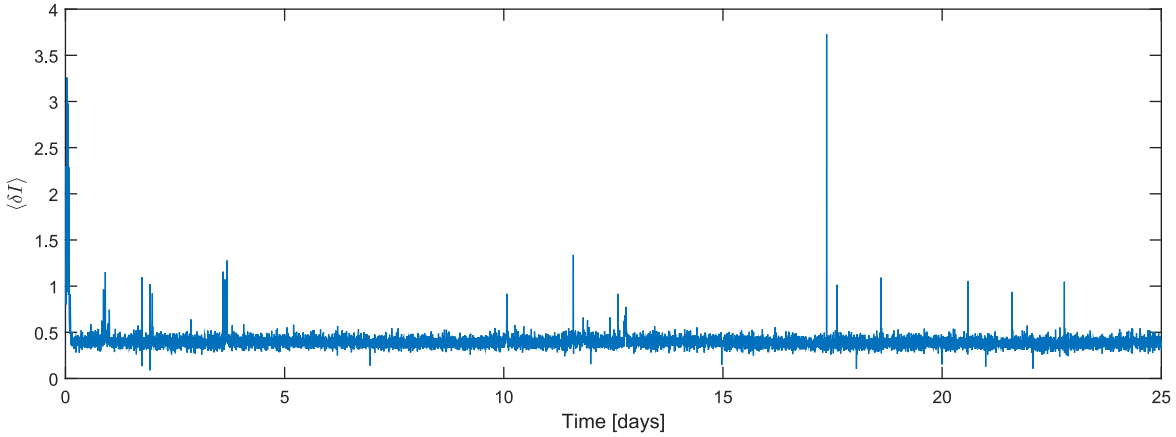

(b) First 25 days.

Figure 3.22: Creep of an initially static deposit of photoelastic discs.

From Figure 3.22 we take 0.4 as the value of $\langle \delta I \rangle_{min}$ due to random error originating in the camera and background illumination. Sporadic force rearrangements are

measured as peaks in $\langle \delta I \rangle$ that take values of at least twice the minimum measured $\langle \delta I \rangle_{min}$. In the first two hours, we observe peaks due to particle position rearrangements every 20 min approximately with very high peaks. After the first few hours, rearrangements are sporadic but do not stop, even after 23 days.

We thus show that we cannot presume the deposit is completely static. The creeping can only be expected to slow down exponentially over periods of time several orders of magnitude longer than the duration of a single experiment.

3.5 Discussion

We have described the experimental setup in which 2D avalanches of photoelastic discs are produced, and the procedure followed to extract relevant data from them. The purpose of the experiments carried out here is to investigating the distribution of stresses in avalanches to answer the motivating questions brought up in Chapter 1. To do this, we designed the setup with the aim of quantifying inter-particle forces using the technique described in Chapter 2. The next three chapters focus on different sets of experiments carried out in this setup to study different aspects of granular gravity-driven flows.

Bibliography

[1] Photoelastic grain solver: https://github.com/jekollmer/pegs.

[2] B. Allen and A. Kudrolli. Granular bed consolidation, creep, and armoring under subcritical fluid flow. *Physical Review Fluids*, 3(7):074305, 2018.

[3] K. E. Daniels, J. E. Kollmer, and J. G. Puckett. Photoelastic force measurements in granular materials. *Review of Scientific Instruments*, 88(5):051808, 2017.

[4] C. Goldenberg, A. Atman, P. Claudin, G. Combe, and I. Goldhirsch. Scale separation in granular packings: Stress plateaus and fluctuations. *Physical Review Letters*, 96:168001, 2006.

[5] I. Goldhirsch. Stress, stress asymmetry and couple stress: from discrete particles to continuous fields. *Granular Matter*, 12(3):239–252, 2010.

[6] Z. Janssen. Experiments on corn pressure in silo cells. *Verein Deutsch. Ing*, 39:1045, 1895.

[7] MathWorks. Matlab *imfindcircles*: find circles using circular Hough Transform.

[8] J. G. Puckett. *State Variables in Granular Materials: An Investigation of Volume and Stress Fluctuations*. PhD thesis, North Carolina State University, 2012.

[9] R. K. Shrivastava, A. Thomas, N. Vriend, and S. Luding. Long wavelength coherent pulse of sound propagating in granular media. *World Academy of Science, Engineering and Technology, International Journal of Mechanical, Aerospace, Industrial, Mechatronic and Manufacturing Engineering*, 11(10):1707–1714, 2017.

[10] *Lenterra*. Drag Force Flow Sensor Specifications Sheet.

[11] *Tedea-Huntleigh*. Model 1004 aluminum single point load cell.

[12] D. R. Tunuguntla. *Polydisperse granular flows over inclined channels*. University of Twente, 2015.

[13] T. Weinhart, A. R. Thornton, S. Luding, and O. Bokhove. From discrete particles to continuum fields near a boundary. *Granular Matter*, 14(2):289–294, 2012.

CHAPTER 4

2D flows in narrow channels

Synopsis

In this chapter we analyse results from experiments where mono-dispersed 2D avalanches of photoelastic discs are released over different basal boundary conditions. The effect of side-wall friction on the velocity profile is dependant on the choice of basal topography. The flows we produce all have inertial numbers $I \leq 1$ and in experiments over a rough base we observe regions in solid- (quasi-steady) and fluid-like (inertial) regimes.

We measure constant and uniform density and quasi-linear velocity profiles through particle tracking at several points down the chute. The photoelastic technique allows the visualisation and quantification of instantaneous forces transmitted between particles during individual collisions, as explained in Chapters 2 and 3. The discreteness of the system leads to highly fluctuating individual force chains which form preferentially in the directions of the bulk external forces; in this case gravity and basal friction.

Then, from the measured forces we obtain coarse-grained profiles of all stress tensor components at various positions along the chute. The behaviour of the coarse-grained stress tensor within a dynamic granular flow is analogous to that of a continuous fluid flow, in that we observe a linear increase of the mean pressure with depth. Furthermore, we identify a preferential direction for the principal stress orientation, which depends on the local magnitudes of the frictional and gravitational forces. These results allow us to draw an analogy between discrete and continuous flow models.

4.1 Introduction

In this chapter we aim to understand the flows produced in the setup described in the previous chapter (see Section 3.1.1), varying only the basal roughness. The experiments described here are all composed of 11, 12 and 13 mm diameter discs in approximately equal numbers. The 10 % polydispersity is enough to avoid crystallisation effects [22], but not enough to induce noticeable segregation. Therefore, these experiments are classified as *mono-dispersed*. The large species of discs, of 21, 22 and 23 mm diameters, that were also produced are not used as flowing particles in this chapter, but only to form the 'alternating-disc' basal roughness condition.

The window from which the camera records the experiments has a limited width of 60 cm while the chute is over 200 cm long. Hence, we slide the viewing window along seven positions down the chute to characterise the downstream evolution of the flow over different realisations. The most upstream position that can be covered by the polariser pair is defined as the 0 cm coordinate, which is 30 cm downstream from the right end of the hopper opening. A seam between two acrylic sheets that form the walls of the chute located at this 0 cm location makes measuring from this point easy. We focus on positions 25, 50, 75, 100, 125, 150 and 175 cm downstream from this origin. At each location we use particle tracking and photoelastic force measurements to understand the evolution of the flow in the downstream direction. All experiments produce flows that are in steady state for a short time after an initial acceleration (see Section 3.4.3), and we henceforth use the first 500 frames (see Section 3.4.4) captured during this steady-state stage where the flux is constant (as demonstrated in Section 3.4.2).

First, via the particle tracking method described in Section 3.2.1, we characterise the density and velocity profiles. Then, we analyse the discrete photoelastic force measurements statistically to find patterns in the force network. These measurements are also coarse-grained to produce continuous profiles of the internal stress tensor, from which we extract profiles for the principal stresses and their directions. The kinematic and dynamic behaviours described here define the parameter space from which we draw the results described in the following chapters.

4.2 Kinematic characterisation

4.2.1 Density profiles

In order to analyse the grain density distribution, we coarse-grain [6, 21] the particle mass and position information obtained by particle tracking. We defined $w_z = 3d$

as the optimal coarse-graining length-scale to obtain smooth profiles, averaged over microscopic variations (see Section 3.3). However, by using a $w_z < 3d$ for this particular analysis only, we forfeit a smooth profile in lieu of a plot where we observe the effect of layering in the packing fraction profile. For the following analysis we half the optimal w_z, setting it to the arbitrarily small value of $1.5d$, so that microscopic vertical changes can be observed, but we keep $w_x = 5d$ in order to ensure the coarse-graining space is large and representative of the flow. Indeed, no spatial variations are measured for any variable in the $\hat{x}$-direction within the viewing window.

We track the particle coordinates and coarse-grain as described in Section 3.2.1 and Section 3.3 respectively, along the central vertical line on each frame. This line passes through the cross-section of the chute at fixed downstream distances of exactly 25, 50, 75, 100, 125, 150 and 175 cm away from the hopper gate. We obtain a vector of coarse-grained densities, $\rho_{CG}(z)$, with a length equal to the vertical pixel resolution, for different depths z within the flow. This vector is produced for every frame and the results for 500 frames were averaged to obtain a single plot of density versus height from the chute base. Figure 4.1 shows a representation of this data converted into packing fraction (we measured cured *Clear Flex 50* to have a density of 1120 kg/m^3) as a function of height for different downstream positions (shown in different colours, or shades of gray) and increasing basal roughnesses: for (a) the smooth base, (b) the rough base composed of small semi-discs, and (c) alternating large and small semi-discs.

Several interesting features of Figure 4.1 stand out. Firstly, the flow thickness, which can be tracked as the horizontal lines that mark the free surface, is noticeably affected by the basal topography. The flow thickness across the smooth base remains fairly constant in downstream direction, but thins dramatically in the rough-base cases to about 60% of the initial thickness. The flow thinning behaviour is similar in the small-discs and alternating-discs basal conditions. Interestingly, the thickness at the most downstream chute location ($x = 175$ cm) for all three roughness types is $9 - 10d$.

Secondly, the average packing fraction is effectively constant throughout the flow thickness at about $\phi_{avg} = 0.81 \pm 0.07$ for all experiments performed. This result is only slightly smaller than the 2D random close packing fraction of $\phi_{rcp} = 0.84$ for 2D systems made of monodispersed circles [9], bearing in mind that the experiments performed in this work have a tri-dispersed distribution with approximately 10% polydispersity. Besides justifying the assumption of a uniform constant density, the similarity between ϕ_{avg} and ϕ_{rcp} unequivocally places all the experiments discussed into the same regime of dense granular flows.

The third relevant characteristic of Figure 4.1 is that, despite the broad coarse-graining area (see Section 3.3), wide undulations can be seen at sub-w_z distances. Although an even longer vertical coarse-graining length-scale would provide a smoother

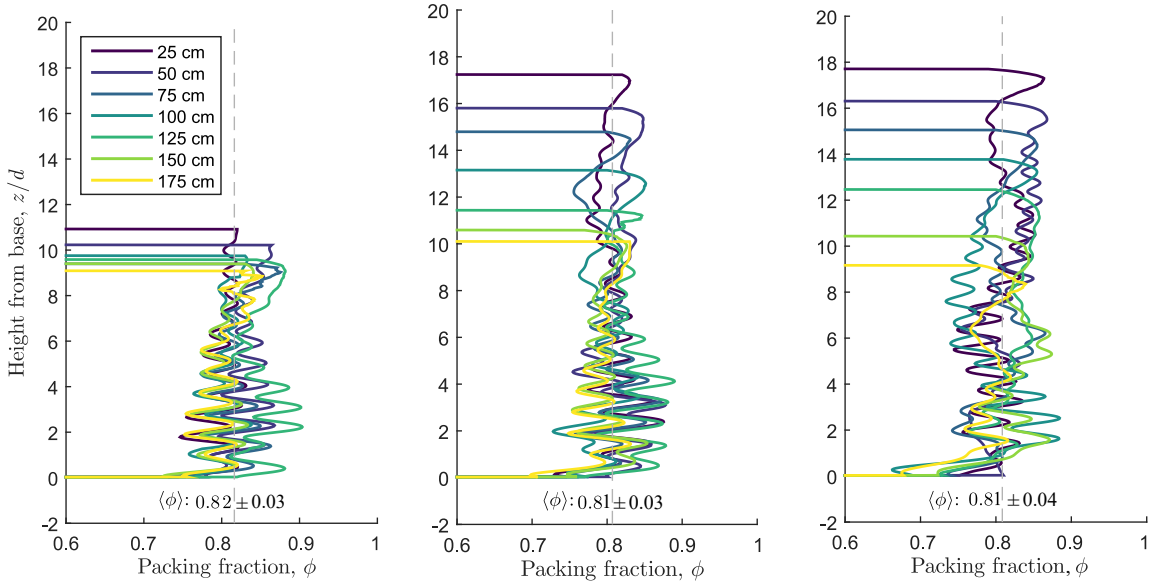

Figure 4.1: Coarse-grained density profiles at seven positions down the chute for flows over (a) a smooth base, (b) a rough base composed of small semi-discs, and (c) alternating semi-discs. The three subfigures apply the same colour-scheme for the profiles measured at different downstream positions. The mean packing fraction was obtained by averaging the seven profiles, each of which already represents an average of the packing fraction profiles over 500 frames at each downstream location.

profile, important physical meaning can be deduced from this behaviour. We observe in Figure 4.1 for all downstream positions that the undulations all show the same wavelength (separation of the peaks) but their amplitudes (distance of the peaks from the average ϕ) decrease with height from the base. An autocorrelation analysis for both smooth- and rough-base experiments shows a consistent separation between density peaks of 1.08 ± 0.02 cm, which is equivalent to $0.9d$, throughout the flow depth. This result implies that the discs flow in well-defined layers, which are equally distanced throughout the depth, but with smaller vertical velocity fluctuations closer to the base. The fact that the undulations decrease in amplitude, but not in wavelength, with height, suggests a higher disorder at the top of the flow (addressed later in Section 4.2.3). These results agree with Weinhart *et al.* (2013) [20] numerical study of dry, frictional, steady-state granular flows down rough inclines, where they found that particles flowed in slightly interlocked layers separated by $0.907d$. This was true for all slow and intermediate flows and they also observed that the layering was most organised closer to the base but that the undulation amplitude decayed over larger distances for slower flows ($I \leq 0.2$).

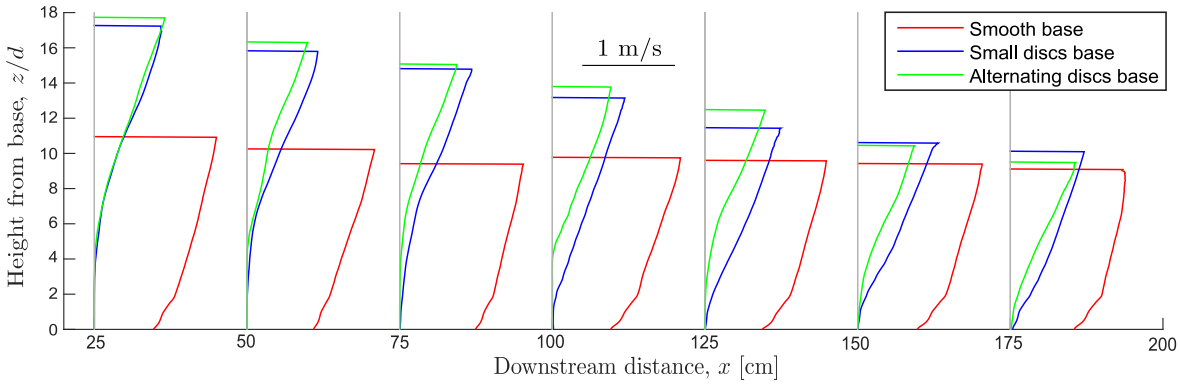

Figure 4.2: Evolution of the coarse-grained downstream velocities profiles at seven positions down the chute for flows over three different topographies. Each profile represents the coarse grained particle velocities averaged over 500 frames in the steady state of a single experiment. The velocities in experiments over a smooth base have a relative error of approximately 6%, while those over a rough base are measured with a relative error of about 10% on average. The flux measured by counting the discs that travel within the camera view matches the flux calculated by integrating the velocity profiles along the z-coordinate (within the stated errors).

4.2.2 Downstream velocity profiles

We apply the expression for coarse-grained velocity presented by Weinhart *et al.* (2012) [21] with φ as defined in Section 3.3, and now again $w_z = 3d$ and $w_x = 5d$. Figure 4.2 shows the resulting plots of downstream velocity against height from the base for experiments carried out over the three types of basal roughness, measured at seven different locations downstream.

The free surface can be tracked by the horizontal lines marking the top of the profiles. The velocity profiles seem to evolve downstream, particularly in the rough-base cases, where the flow thins visibly. However, Figure 4.3 shows that by plotting the velocity against depth from the free surface rather than against height from the base, the velocity profiles in fact collapse. Moreover, the flowing layer in the rough-base experiments has the same thickness as the flow over a smooth-base, albeit moving at slower velocities.

The velocity profiles reflect that while the particle density remains constant and uniform throughout all experiments, the flux depends strongly on the topography. In the smooth base case there is high slippage and a quasi-linear increase of the downstream velocity with height. Faug *et al.* (2015) [4] reported obtaining high slippage and a Bagnold profile in similar experiments over gentle slopes, but with only 10 layers of particles it is difficult to confirm or rule out a Bagnold profile over a linear profile. Except in the experiment recorded at a position closest to the hopper (25 cm), all profiles are remarkably similar to each other with no obvious thinning or acceleration.

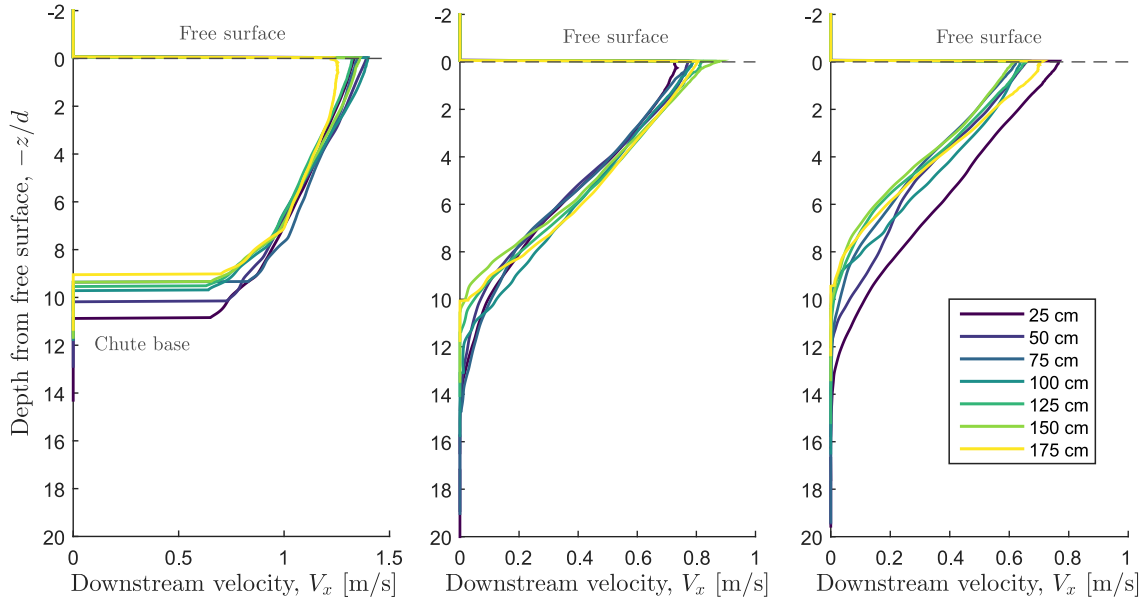

Figure 4.3: Collapse of the coarse-grained downstream velocities profiles at seven positions down the chute for flows over three different topographies: (a) smooth base, (b) rough base made of small semi-discs, and (c) rough base made of alternating large and small semi-discs. All subfigures use the same colour-scheme for the profiles measured at the different downstream positions. Each profile represents the coarse grained particle velocities averaged over 500 frames in the steady state of a single experiment. The velocities in experiments over a smooth base have a relative error of approximately 6%, while those over a rough base are measured with a relative error of about 10% on average.

This implies that the gravitational downstream forces are balanced by the friction introduced by the base. If the chute were inclined less than the 20° it was built at, the gravitational component would not be large enough to maintain a flow. In other words, the experiment is inclined at the dynamic angle of repose corresponding to a near monodisperse system of discs made of *ClearFlex 50* flowing over a smooth base. In contrast, by forming a 2D pile of discs and tilting it slowly and smoothly until the first discs topple, it was found that the system's static angle of repose is $31 \pm 2°$, which is as expected larger than its dynamic counterpart.

The picture is completely different when basal roughness introduces shear into the system. Here the dynamic angle of repose is larger because the increased basal friction requires a stronger gravitational downstream component to balance the higher shearing forces. To provide a steeper flowing angle and stronger gravitational component, a static layer forms at the bottom. It is this layer that thins while the moving layer on top maintains its thickness and quasi-linear velocity profile throughout. Overall, the flows over an alternating-disc base are slightly slower and thicker than in the small-

disc-base case, implying the alternating-disc base introduces a higher degree of friction to the system. The free-surface forms an angle of $25 \pm 1^\circ$ degrees to the floor, 5° larger than in the smooth-base case. Furthermore, we verified that all particles in the flowing layer travel parallel to the free surface, confirming that the frictional boundary with the quasi-static layer effectively increases the system dynamic angle of repose. The static layer is referred to as a *superstable heap* (SSH), and many authors [17] have attributed it, and the shape of the velocity profile of the flow (both in the flowing layer and SSH) [8], to the effect of the chute side-wall friction on the flowing particles.

Indeed, super-stable heaps have been widely observed in granular flows within narrow chutes and are associated with specifically a Coulomb-type friction with the channel walls. Furthermore, as the hopper depletes and the flux rate decreases, the inclination angle of the free surface decreases from $25 \pm 1^\circ$ when the flow is in steady state to $23 \pm 1^\circ$ when the flow stops completely. This is indicative of an increase of friction with depth, as particles need a steeper angle to flow when they are under pressure. This result suggests there is a relationship between the flowing layer thickness and the angle made by the free surface, as proposed by Taberlet *et al.* (2003) [17] assuming a Coulomb-type friction at the side-walls. In any case, friction at the side-walls has a significant effect on the flow velocity profile, but lack of photoelastic response in fast-moving rattlers (particles that do not form part of a force-chain, identifiable in Figure 3.7a) regardless of particle depth, suggests side-wall friction is not large enough to interfere with the measurement of inter-particle forces.

The observations presented so far agree with other reports [15, 10, 11] that say that the packing fraction in slow-intermediate flows is practically uniform. Said authors also report that the packing fraction is only a decreasing function of the inclination angle. In all experiments a combination of relatively slow hopper discharge flux and small inclination angles causes the flow to have the minimum recorded flow thickness possible for gravity-driven flows [12]. The observations made here therefore correspond to flows with the slowest possible speed and thickness. It is reasonable that the mean packing fraction in these cases would tend to the 2D random close packing fraction.

Also confirming the 'slow and thin regime' is the fact that the velocity profile is linear [16, 2]. As illustrated in Figure 4.3, all flows (excluding the static layer in rough-base experiments) are approximately $10d$ in thickness, which is significantly below the estimated thickness of $20d$ at which Bagnoldian velocity profiles are observed [3]. However, in this case, the side-wall effect is also potentially responsible for the velocity profile linearity [10].

No less significant is that the similarities between the experiments described in this work with those reported by other groups confirm the small effect of the particle stiffness [5] or normal restitution coefficient on the behaviour of dense flows [14, 7]. The

restitution coefficient of *Clear Flex 50* is likely to be lower than that of the particles used in said studies, yet the kinematics of these photoelastic flows are analogous to all flows in the same regime, regardless of the constitutive particle material.

4.2.3 Cross-stream velocity

The decrease in the layer prominence with height, evident in the packing fraction profiles, Figure 4.1, can be related to an increase in particle vertical displacements. If we model the layer mass to be *distributed normally* around $\mathbf{r}_i$, with variance σ^2, then the standard deviation σ effectively represents the mean squared vertical displacement, $\langle \delta z^2 \rangle$, of the discs from the ith layer midpoint. Knowing that layers contain the same particle density and that they are all equally spaced by $0.9d$, we model the corresponding coarse-grained density profile, calculated as

$$\rho^n_{CG}(\mathbf{r}) = \sum_{i=1}^{N} \varphi(\mathbf{r} - \mathbf{r}_i) \int_{-\infty}^{\infty} m_i(\mu_i, \sigma_i^2, z) dz, \tag{4.1}$$

where the mass function m_i for layer i is normally distributed along the z axis around the layer centre μ_i with variance σ_i^2, φ represents the coarse-graining function defined in Section 3.3, and N the number of particles within a coarse-graining length-scale of each point along the profile.

Figure 4.4a plots in red the continuous mass distribution obtained when the standard deviations associated to the mass at each layer in arbitrarily increased linearly from 0.1 at the bottom to 0.3 diameters at the top. By doing this the profile of the normal mass distribution (in red) shows a clearly less pronounced layering at the top than at the bottom. Figure 4.4a plots in blue the discrete distribution of masses, and Figure 4.4b plots, also in blue, the corresponding coarse-grained density profile for this case. The experimentally obtained density profile across the smooth base, and recorded at a distance of 25 cm downstream from the flow source, is also plotted as an example in Figure 4.4b in black. A comparison between the three profiles shows that the continuous mass distribution model captures the amplitude decrease with height well, while maintaining the undulation wavelength observed experimentally.

By fitting each layer's variance σ^2 to best fit the measured density profile, values for each layer's mean squared displacement, $\langle \delta z^2 \rangle$ were obtained for all smooth base experiments. Only smooth-base experiments were used for this analysis because the mean particle velocity is parallel to the base, which is not true for the top moving layer of the rough-base experiments. Besides, the rough-base experiments include different depths of a bottom static layer, and we wish to compare the vertical displacement of layers of particles in motion. Interestingly, we find that all experiments show a similar

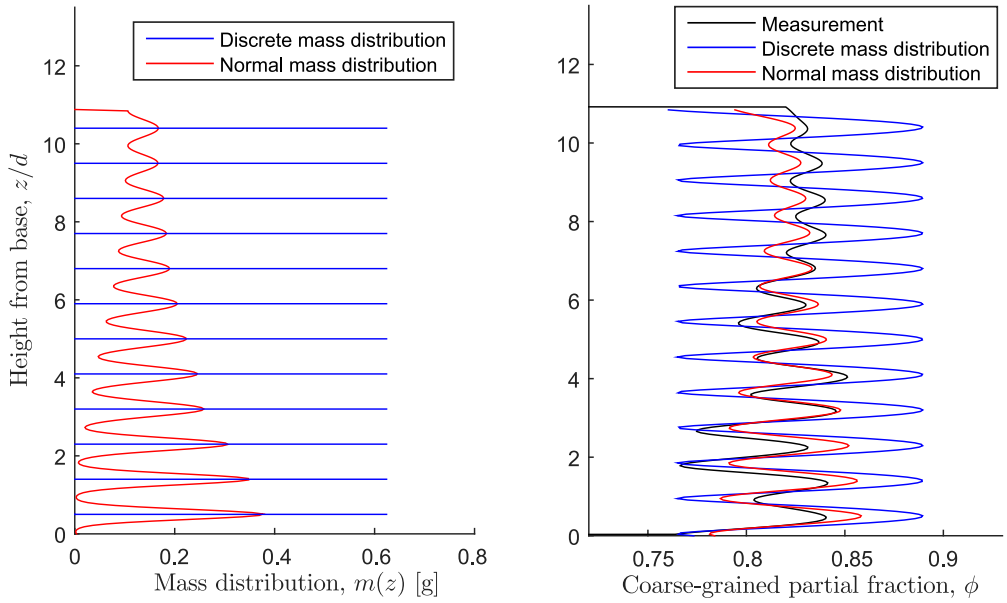

Figure 4.4: (a) Mean mass versus height from base if the flow were perfectly layered 1.08 cm apart. Blue representing a perfectly layered system, while red models a normal distribution of masses around the layer centres. The (red) normally distributed model increases the standard deviation from narrow at the bottom ($0.1d$) to wide ($0.3d$) at the top of the flow. (b) Corresponding coarse-grained density profiles, and an experimentally obtained example density profile (black line) for the smooth base case taken at a downward distance of 25 cm.

seemingly linear increase in δz with height, as evidenced by Figure 4.5.

The displacements obtained for the bottom layer match the particle tracking error, implying the vertical fluctuation in this bottom layer is minimal. In fact, direct observation of the experimental videos shows that discs in this layer do not fluctuate around the layer centre at all, but mostly slide over the base. The mean vertical displacement from the layer centre of these discs is measured to be of 1 mm, which coincides with the difference in radius between the smallest ($d = 11$ mm) and largest ($d = 13$ mm) disc. Therefore, the result for the mean displacement we obtained for the bottom layer is reasonable.

4.3 Dynamic characterisation

From the density and velocity profiles we observe that the experiments carried out over small- and alternating-discs bases produce similar flows. Overall, the latter type are slightly thicker and slower, and in the particular experiments carried out show a slightly more pronounced super-stable heap containing quasi-static particles. However, the differences between the flows over the two rough types of bases lie within the

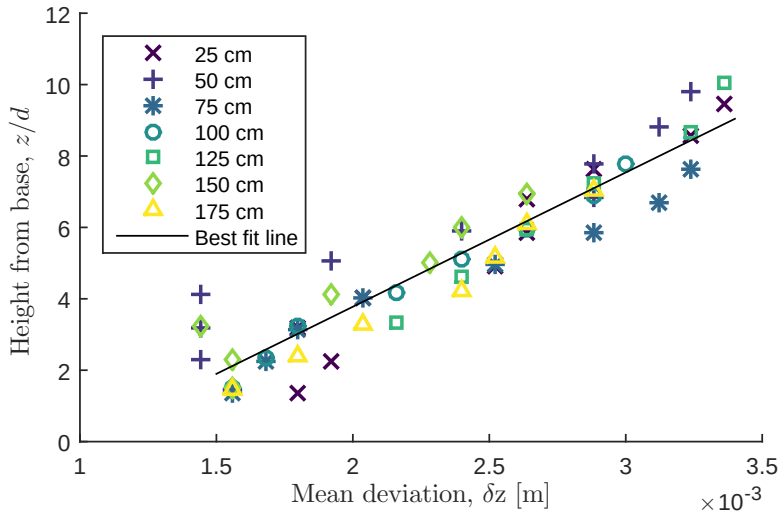

Figure 4.5: Fitted standard deviation of the mass normal distribution around each layer centre, representative of the mean particle deviation from the layer centre, plotted against the layer height. Results are shown for the seven experiments carried out over a smooth base.

experimental error (see Section 3.2.2 and 3.4.5). Hence, in this section we focus on the differences between experiments over a smooth base and over the small-discs rough base only.

4.3.1 Forces statistical analysis

By collecting all the information on the instantaneous inter-particle force magnitudes, directions and application points, we extract a network of forces within the avalanching flow. We first notice that the total number and mean magnitude of the inter-particle forces observed in each direction varies. By binning each force according to the direction they are applied in into 5° wide bins between $-90°$ and 90°, the preferred direction and the mean magnitude of the inter-particle forces is revealed.

In Section 3.2.3, we explained that the minimum real force perceptible from the photoelastic response within the discs depends on the values arbitrarily assigned to the variables $g2cr$ and $g2threshold$ in PeGS. If the $g2threshold$ is set too low for a given $g2cr$, irregularities in the flour coating can make a contact be wrongly classified as force-bearing. Therefore, we must take into account that the number of forces measured per frame has an additional random error that originates from the arbitrary nature of how $g2cr$ and $g2threshold$ are assigned.

Figure 4.6 shows the mean number of forces per frame, N_f, recorded within each bin for the experiments performed over both a smooth and rough base. The forces measured in the rough-base experiments were further separated according to whether

they were measured at depths of up to $11d$ from the free surface (corresponding to the flowing layer, according to Figure 4.3), and those at $z > 11d$ (where velocities are practically zero as observed in Figure 4.3). The flowing layers in both type of experiments have approximately the same thickness, which is consistent along the chute, so Figure 4.6a shows the mean number of forces measured in each direction per frame in the flowing layers over both types of basal roughness, averaging the results obtained at all 7 positions along the chute. On the other hand, because the quasi-static layer decreases in thickness along the chute, we plot N_f measured at each position along the chute in Figure 4.6b. In all cases the data is time-averaged over 500 frames per experiment.

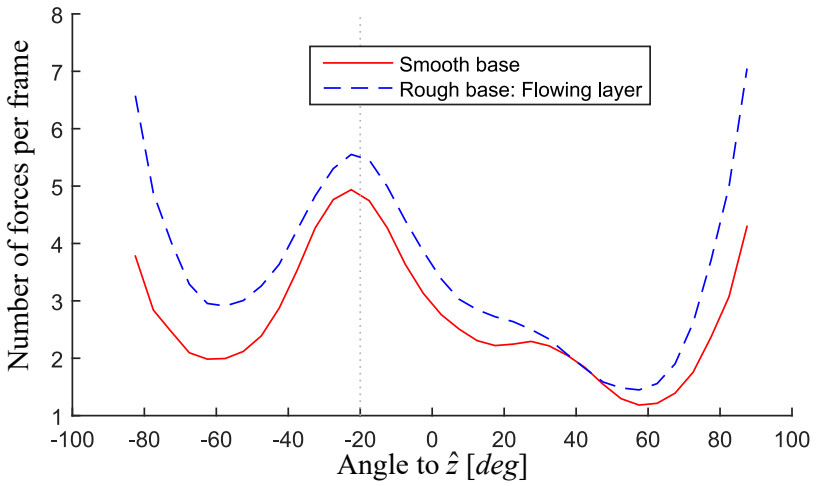

(a)

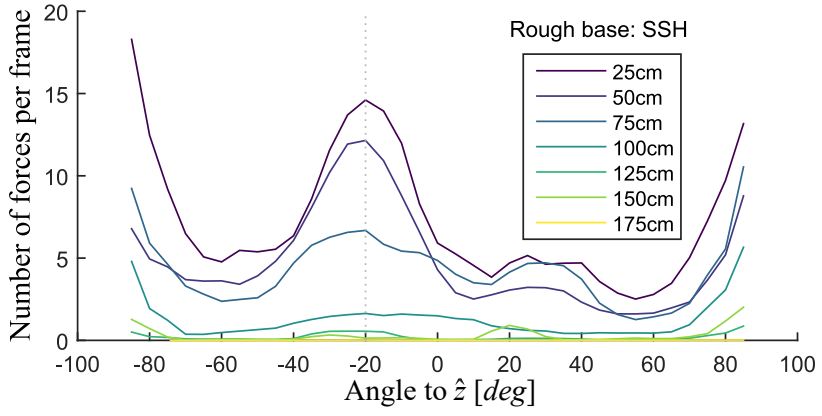

(b)

Figure 4.6: Average number of forces per frame measured acting in angles to the cross-flow direction $\hat{z}$, for (a) experiments over a smooth base and for the flowing layer (top $11d$) of experiments over a rough base, and (b) for the quasi-static layer of experiments over a rough base. The two figures were separated because the flow thickness in (a) is constant along the downstream direction, while the SSH analysed in (b) decreases in thickness along the chute.

From Figure 4.6a we observe peaks in the number of forces measured to act at angles of 90° (parallel to the chute base), and close to −20° (direction of gravity). At depths $z > 11d$ we observe the middle peaks coincide exactly with −20°, as seen in Figure 4.6b, but as the static layer thins the number of forces measured decreases. In contrast, in the flowing layer the middle peak is slightly skewed to a more negative angle, which we attribute to the friction accompanying interactions between particles in different layers. In all cases we see that the ratio of forces acting at 90° to the number acting at −20° is larger in all rough-base experiments than in those with smooth base.

We also observe a secondary peak in the number of forces at an angle of approximately 35°. This peak is apparent in all experiments so it is accepted as a real physical phenomenon, but an explanation of its origin remains to be investigated in depth. It would be interesting to explore whether the angle at which this secondary peak occurs is at all related to the direction of the complementary stress, as defined in soil mechanics.

Figure 4.7a plots the mean force magnitudes, $\langle F \rangle$, in each direction, for the flowing layers in the smooth- and rough-base experiments and within the static layer in the rough-base case. With the purpose of understanding the spread of the measurements used to calculate the averaged quantities shown in Figure 4.7a, Figure 4.7b shows their standard deviations.

In all three cases we measure peaks in mean force magnitude around the direction of gravity. In the smooth-base case we observe that the forces acting at 90° are significantly weaker than those at −20°. In contrast, in experiments over a rough base the forces at 90° are as important in the flowing layer, and even more significant within the SSH, than those at −20°. In addition, we notice that in rough-base experiments, peaks in $\langle F \rangle$ are more pronounced in the static layer than in the moving layer. We surmise that the motion of particles allows for the formation of force chains in a wider spread of angles and curvatures, but that there is a tendency for the inter-particle force direction for low velocity regions.

From Figures 4.6 and 4.7 we conclude that force chains tend to form preferentially in the directions of the two external forces acting on the flow bulk: gravity and basal friction. When particles in neighbouring layers that are moving at different speeds interact, friction causes the force chains to skew slightly up-slope (to more negative values). Moreover, we measure less and weaker force chains acting parallel to the chute base in smooth- than in rough-base experiments. We associate this observation with the high slippage at the base (Figure 4.3a) and weaker friction between layers within the flow. On the other hand, in the rough-base case we observe more and stronger force chains forming in the direction of friction acting on the particle layers. We observe that the peaks are sharper in the static layer, suggesting force chains bend and branch more

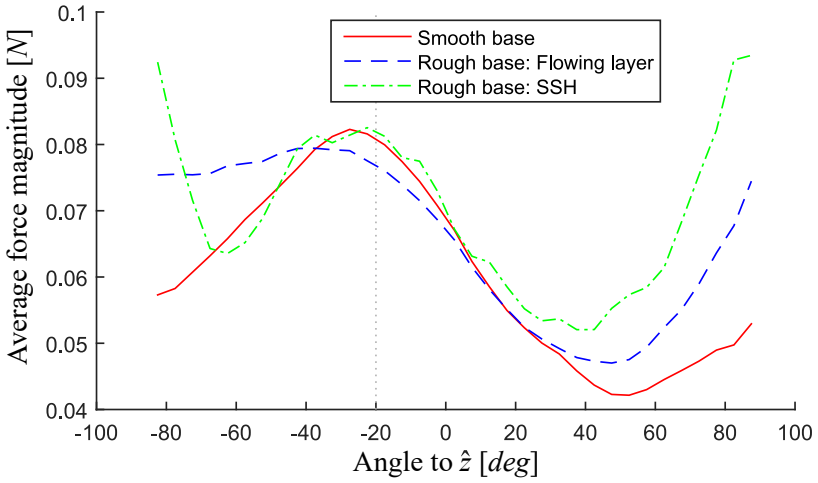

(a)

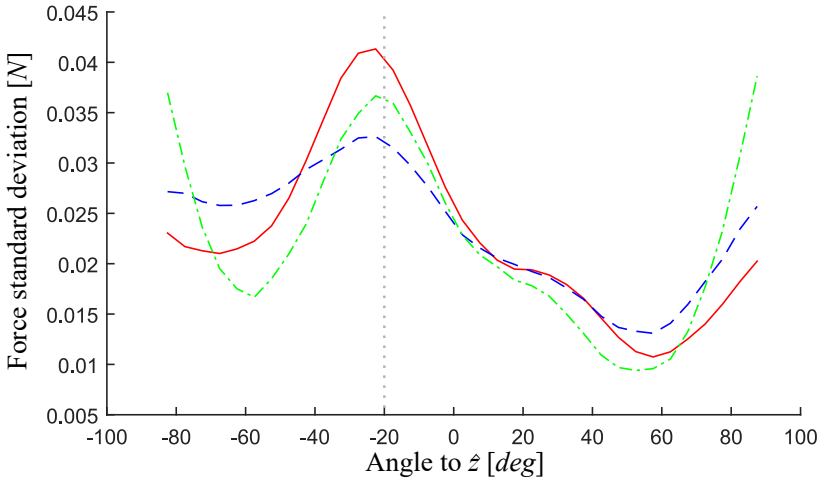

(b)

Figure 4.7: (a) Mean force magnitude measured acting in angles to the cross-flow direction $\hat{z}$, and (b) the force measurements standard deviation. Both plots follow the same line style and colour scheme.

in the moving layer. From the fact that we do not observe stronger forces at $-20°$ in the SSH than in the moving layer, we deduce that particles in force chains carry similar loads. The extra weight supported by the SSH is spread into *more* strong particle contacts, but those contact forces were not significantly *stronger*. However, because force chains often intersect, individual particles do, on average, carry heavier loads at larger depths.

4.3.2 Coarse-grained internal stresses

Considering a fully developed steady continuous flow that does not change in time nor along the downstream direction $\hat{x}$, momentum balance requires

$$-\bar{\nabla} \cdot \bar{\bar{\sigma}} + \rho \bar{g} = 0, \tag{4.2}$$

where σ represents the flowing system stress tensor, ρ the density and g the acceleration of gravity. Assuming constant and uniform density ρ, resolving the streamwise ($\hat{x}$) and cross-flow ($\hat{z}$) directions and solving for σ predicts a hydrostatic increase in pressure and shear,

$$\begin{aligned} \sigma_{zz} &= (h - z)\rho g \cos\theta_{fs}, \\ \sigma_{zx} &= (h - z)\rho g \sin\theta_{fs}, \end{aligned} \tag{4.3}$$

where h represents the height of the free surface over the chute base and θ_{fs} the angle made by the free surface in the laboratory frame of reference.

Stress tensor component profiles

The consistency in time and $\hat{x}$-direction of the density and velocity profiles over a smooth base implies this is indeed a steady, fully developed flow. The packing fraction profiles (Figure 4.1) suggest the density is indeed constant and uniform, and we furthermore assume that even if the flow were compressible, a change in solid volume fraction makes very little difference to the linear pressure distribution (Figure 4 in Barker *et al.* (2017) [1]). Therefore we expect the corresponding pressure and shear profiles to behave as predicted by Equation 4.3. To compare that model to the discrete forces measured experimentally, the coarse-graining equations originally put forward by Goldhirsch (2010) [6] and later extended by Weinhart *et al.* (2012) [21], were applied to obtain continuous expressions for the four stress tensor components. The same coarse-graining function introduced in Section 3.3 was used for this purpose, with $w_z = 3d$ and $w_x = 5d$ (also determined in Section 3.3).

We calculated the stress tensor component profiles according to Weinhart *et al.* (2012) [21] for each frame. Figure 4.8 shows the time series of the coarse-grained σ_{zz} component over 500 frames in the steady-state stage of an experiment over a smooth base recorded 75 cm downstream from the beginning of the chute. This figure shows instants of high stresses, which increase with depth, and also instants where the stress profile is barely significant, which is indicative of granular *breathing*. However, an auto-correlation analysis of the stress peaks does not reveal any characteristic frequency at which the oscillations in stresses occur. Similar time series obtained from experiments

over a rough base show less significant variations in the stresses with time. This may be attributed to the flows over rough bases being thicker and slower, so there are no frames where no forces are measured.

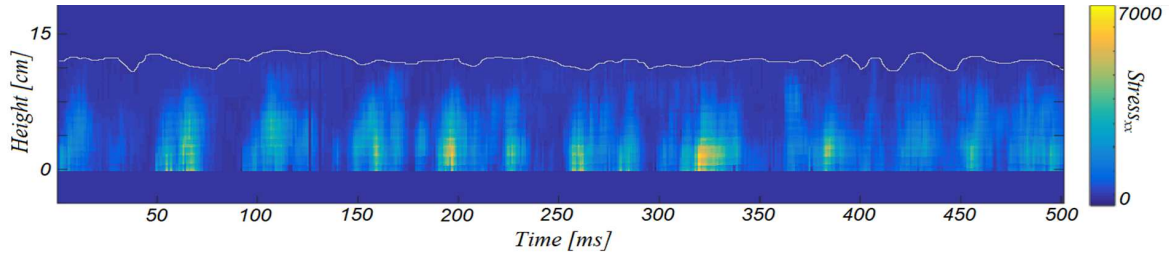

Figure 4.8: Time series of the coarse-grained stress tensor component σ_{zz}, as defined by Weinhart *et al.* (2012) [21] and introduced in Section 3.3. These measurements were obtained from 500 frames in the steady-state stage of an experiment over a smooth base recorded 75 cm downstream from the top end of the chute.

As we cannot discern a characteristic frequency of stress oscillation, we then averaged all the stress tensor components over the 500 frames extracted from each experiment. Because the magnitudes of σ_{zz} and σ_{zx} depend only on depth from the free surface and angle of inclination, all seven profiles collected along different downstream positions collapse, for both smooth- and rough-base experiments. In Figure 4.9 we show the mean stress component profiles in solid lines, and bound the confidence intervals in dashed lines. The bounds of this interval are determined by the standard error of averaging the seven profiles, proving they all collapse within acceptable limits. Different stress tensor components are drawn in Figure 4.9 in different colours (shades of gray), while the grey straight lines show the hydrostatic gradient predicted by Equation 4.3 for $\rho = \rho_{CG}$ and measuring h to be the average height of a *spline* though the highest points of the discs on the flow top layer. Within a coarse-graining length $w_z = 3d$ from both the base and free surface, the lines are shown in faded colours, as the coarse-grained results here are likely to be affected by the closeness to the boundaries.

In the rough-base experiments, it is the static layer that thins with distance downstream (Figure 4.3) in classic super-stable heap (SSH) behaviour [17]. From Figure 4.2 we saw that the flowing layer remains practically constant in thickness and the velocity profile. It follows that the flowing layer should experience a hydrostatic pressure increase, but scaling with the cosine of the effective layer inclination angle, 25°, rather than with the inclination of the chute, 20°. Figure 4.9b shows the components of the stress tensor resolved relative to the free surface and to the normal to that direction, having rotated the camera frame of reference by 5° to match the new $\hat{x}$ to the direction of the free surface.

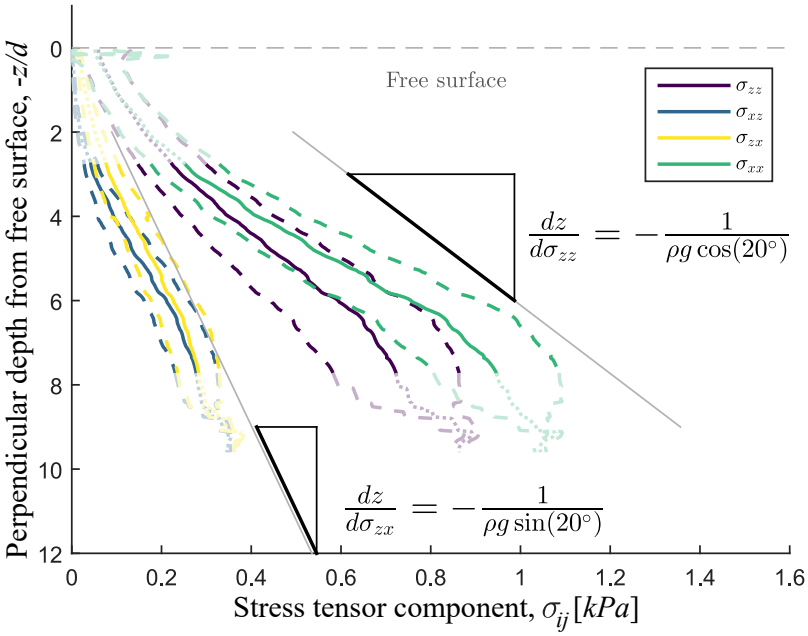

(a) Stress tensor component profile of experiments over a smooth base.

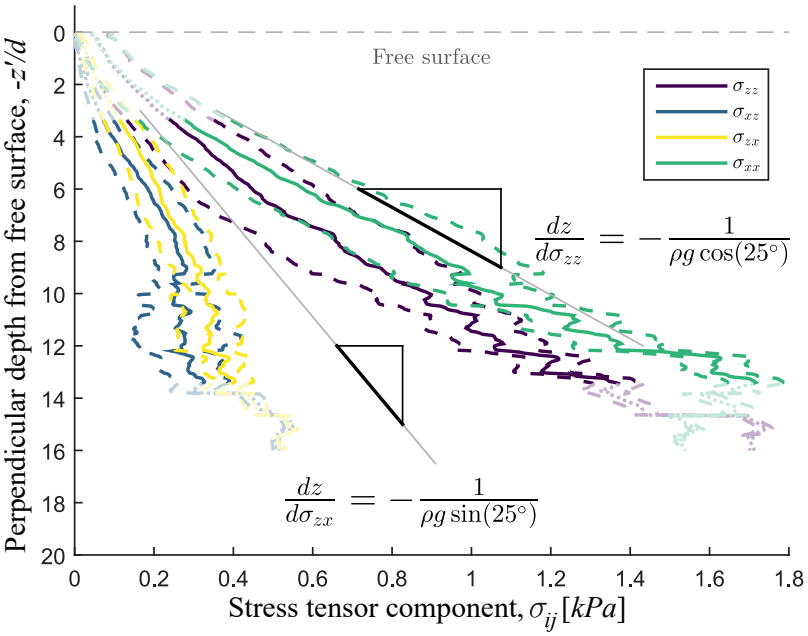

(b) Stress tensor component profile of experiments over a rough base.

Figure 4.9: Coarse-grained 2D stress tensor component profiles for (a) smooth-base and (b) rough-base experiments. The profiles resulting from averaging the seven experiments measured at different downstream locations are plotted in solid lines, while the dashed lines delimit the standard error of he averaging. The straight grey lines show the gradient corresponding to a hydrostatic increase in pressure as predicted by Equation 4.3 with $\theta_{fs} = 20°$ for (a) and $\theta_{fs} = 25°$ for (b). z' represents the perpendicular distance from the free surface, which is inclined 5° to the horizontal in the camera frame in (b), while in (a) the free surface is parallel to the horizontal in the camera frame.

Principal stresses

Since we can obtain from experiments all four components of the 2D internal stress tensor $\bar{\bar{\sigma}}$, we can calculate the in-plane *principal stresses*. These are defined as the two (for 2D systems) pressures σ_1 and σ_2 that act in a what is known as the *principal stress directions*. They have an analogous effect on the system, with no shearing stresses, as the full $\bar{\bar{\sigma}}$ in the original plane. If the original stress tensor is symmetric, then the principal stress directions are orthogonal, and in such a case the principal stresses represent a rotation of $\bar{\bar{\sigma}}$ by a given single anticlockwise angle α_p, referred to as the *principal orientation*.

$$\begin{bmatrix} \sigma_1 & 0 \\ 0 & \sigma_2 \end{bmatrix} = R\left(\begin{bmatrix} \sigma_{xx} & \sigma_{xz} \\ \sigma_{zx} & \sigma_{zz} \end{bmatrix} \right)_{\alpha_p} \tag{4.4}$$

The magnitudes of the principal stresses are the eigenvalues of the stress tensor, and the corresponding eigenvectors represent the directions of the axes in the principal stress plane. These can be found easily by computing

$$\sigma_{1,2} = \frac{\sigma_{xx} + \sigma_{zz}}{2} \pm \sqrt{\left(\frac{\sigma_{xx} - \sigma_{zz}}{2} \right)^2 + \sigma_{xz}\sigma_{zx}}. \tag{4.5}$$

The eigenvalues corresponding to the collapsed, depth-dependent stress tensors presented in the previous section are plotted against depth from free-surface in Figure 4.10a.

We found that the corresponding eigenvectors for the experimental stress tensor presented in the previous section form an orthogonal basis. This means that the principal stress directions can be represented by the angle of anticlockwise rotation α_p,

$$\tan(2\alpha_p) = \frac{\sigma_{xz}\sigma_{zx}}{\sigma_{xx} - \sigma_{zz}}. \tag{4.6}$$

We therefore report the direction of only one principal stress, the *principal orientation* α_p, bearing in mind that the second direction forms a normal angle to this one. To facilitate comparison, we calculated α_p for the coarse-grained stresses in the camera frame of reference, for experiments over both types of topography. The principal orientation corresponding to the principal stresses just obtained are also plotted against depth from the free surface in Figure 4.10b.

Interestingly, the principal stress magnitudes are very similar in both smooth and rough-base experiments. On the other hand, the angle α_p is lower for the smooth-base than for the rough-base experiments, but in both cases the principal orientation lies between the direction of gravity (20° to the cross-flow direction $\hat{z}$) and basal shear (90° anticlockwise from $\hat{z}$, see Figure 4.6). These are the two body forces acting on

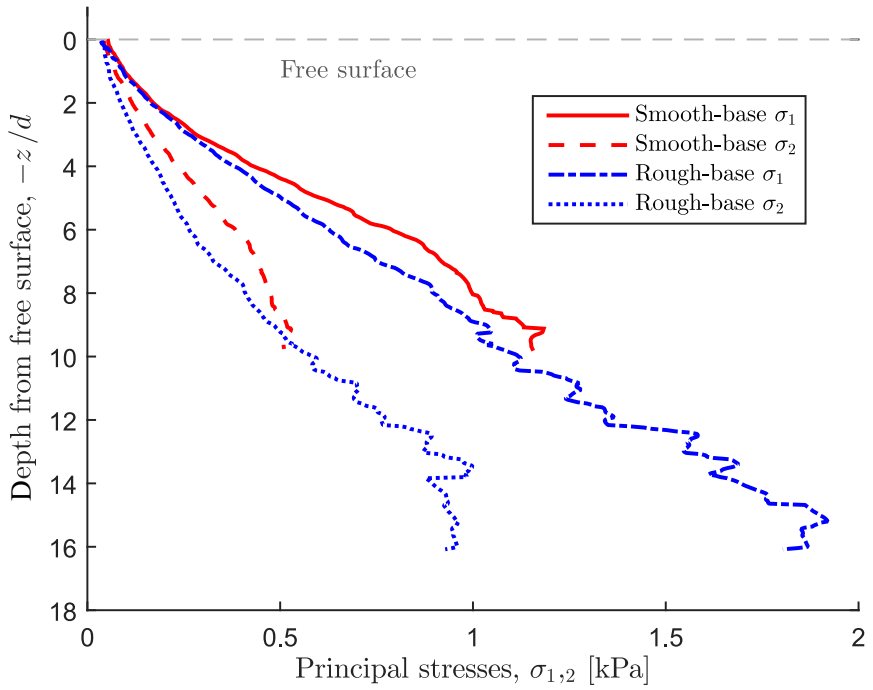

(a)

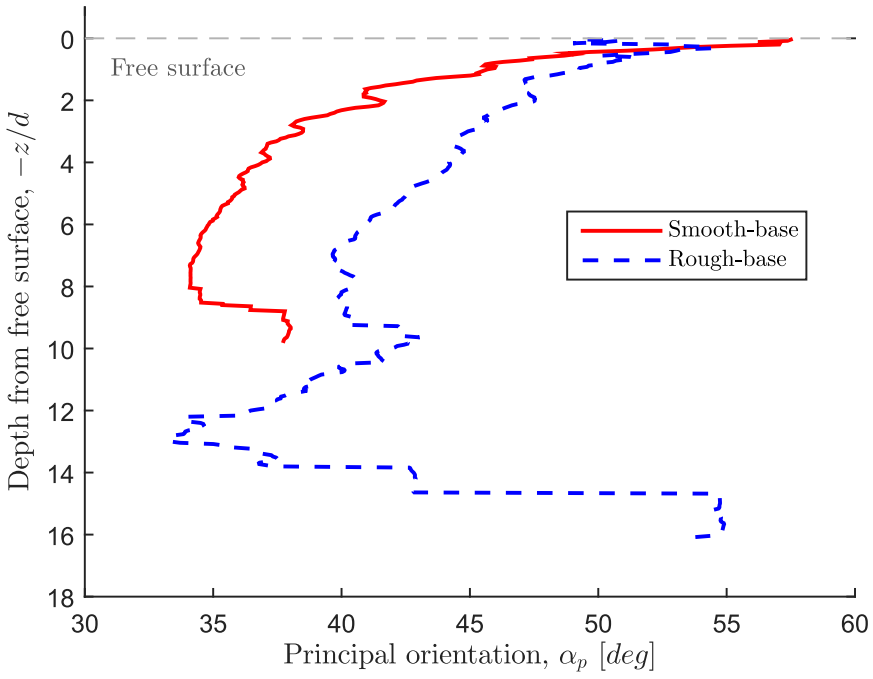

(b)

Figure 4.10: (a) Magnitudes of the principal stresses for the stress tensors obtained by collapsing the results of all experiments of equal type. The dashed blue lines represents the results of experiments performed over a smooth-base while solid red lines correspond to rough-base experiments. (b) Orientation of the system principal stresses and their dependence with depth. The dotted and dash-dot blue lines represents the results of experiments performed over a smooth-base while solid and dashed red lines correspond to rough-base experiments.

the flow bulk, so it seems reasonable that the main principal stress would be directed somewhere in between them ($35 - 50°$ anticlockwise from $\hat{z}$).

We propose that the principal orientation in these experiments depends on the local relative importance between inter-layer shear and hydrostatic pressure. In the smooth-base case there is high slippage at the chute base and the shear rate is smaller than in the rough-base case. Hence, shearing forces are less important in the smooth-base case. On the other hand, hydrostatic pressure depends only on depth from the free surface and inclination angle. Although the flowing layer in the rough-base case has the same depth of $\sim 10d$ as the flow over a smooth base, the super-stable heap (SSH) increases the effective angle of inclination of the flowing layer in the former case. The ratio of shear forces ($90°$ from $\hat{z}$) to gravitational forces ($20°$ from $\hat{z}$) is higher in the rough-base case than in the smooth-base case. Thus, we infer from the larger α_p in the top $10d$ that the principal orientation leans towards the direction of shear in the rough-base case more than in the smooth-base case, due to the larger relative importance of shear in the system.

Nevertheless, both lines in Figure 4.10b follow the same trend within the flowing layer (approximately the top $10d$ in both cases). Close to the free surface the only surface force acting on the particles is shear (hydrostatic pressure is minimal), so the major principal stress tends towards $90°$ to the vertical in the camera frame. The velocity profile within the flowing layers was determined to be linear, so inter-layer shear remains constant in depth within these flows. As the hydrostatic component increases with depth, the principal orientation leans more towards gravity (which acts at $20°$ to the cross-flow direction $\hat{z}$). Then, shear increases suddenly at the chute base (in the smooth-base case) as well as in the transition between the flowing and static layers (in the rough-base case), and so α_p increases at these boundaries. Within the static layer that forms the SSH (only visible in the rough-base experiments) a dip in α_p is observable as shear is most relevant at the boundary with the flowing layer ($\sim 10d$ depth) and with the chute base (most visible at $\sim 16d$ depth).

4.3.3 Basal stress ratio

We complement the photoelastic force measurements with separate measurements of shear and normal forces at the base using the sensor custom made for our setup by *Freeman Technology*. This sensor comprises a Lenterra DFF to measure shear and a single point load cell to measure normal forces, combined through a 3D printed plastic head as described in Section 3.1.2. For each experiment, the device is fitted at one of seven gaps at the base of the chute. When not in use, these gaps are filled with a removable t-shaped plug that sits flush at the base without interfering with the flow.

The shear and normal forces on the 4.8×0.6 cm upper surface of the plastic head are

transmitted to the respective sensors simultaneously. Up to four discs fit on the sensor head at any time. These discs can spend as little as 0.06 s on the sensor head (in the smooth-base case, where the discs travel fastest), and transmit forces to it in at least 0.001 s (see Section 3.4.1). The normal sensor collects data every 0.038 ± 0.03 s while the shear sensor sampling rate is one every 0.02 s. This means that every measurement of the sensors is an average of the forces transmitted by multiple particles (up to four) over 0.038 or 0.02 s, respectively.

Figure 4.11 shows the measurements obtained from experiments over a smooth (a) and rough (b) base, of the shear forces in blue, and of the normal forces in purple. Because forces are so short lived the measurements seem very erratic and dispersed. In addition, we take into account that forces are not distributed evenly along the chute base, but instead force chains separated by a couple of diameters on average transmit localised forces to the base. To account for these oscillations in the measured forces we henceforth use the corresponding smoothed spines, drawn in Figure 4.11 in red.

By dividing the values of the shear smoothed spline by the corresponding normal force spline we obtain the evolution of the stress ratio μ (see Equation 1.5) in time. Figure 4.12 shows the respective profiles of $\mu(t)$ for experiments over a smooth (a) and rough (b) base.

For each experimental repetition, we furthermore calculate the mean μ measured by the sensors at the base by averaging the $\mu(t)$ curves shown in Figures 4.12a and 4.12b over the period where the avalanche is in steady state. The beginning and end of the steady-state stage in the experiments shown in Figure 4.11 are marked by vertical gray dotted lines.

We repeated experiments over smooth and rough bases, installing the sensor at different downstream locations to obtain a range of mean basal μ measurements. Often the reading of the sensors before and after an experiment would not be zero, despite no discs resting on them any longer. We assume this error occurred due to small rearrangements in the positioning of the sensor, despite installing it as securely as possible every time. The results of the experiments where this happened were discarded, and those from all the useful repetitions are shown in Figure 4.13.

The results shown in Figure 4.13 are still quite dispersed, which we attributed to small differences in how the sensor was installed in the chute each time and perhaps also to hysteresis in the plastic (PLA) material that makes the 3D-printed head. We do not observe an obvious slope in μ along the different downstream locations. We therefore calculate the mean μ_{base} for the smooth- and rough-base cases and find that they are within each other's experimental error. We thus estimate that the average basal stress ratio μ_{base} does not change downstream, and is similar for both basal roughness cases. The average μ_{base} is approximately 0.34, which is higher than the $\mu_s = 0.26$ value

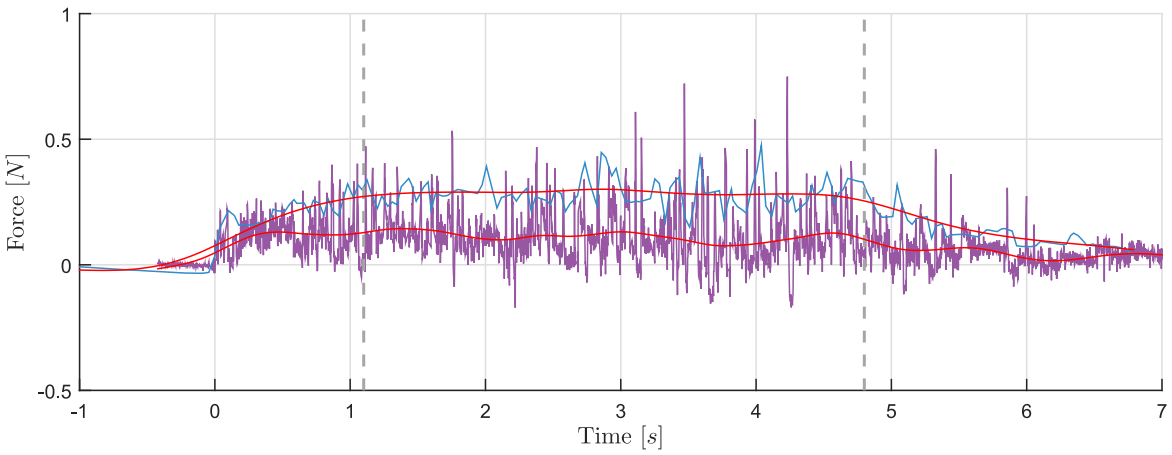

(a)

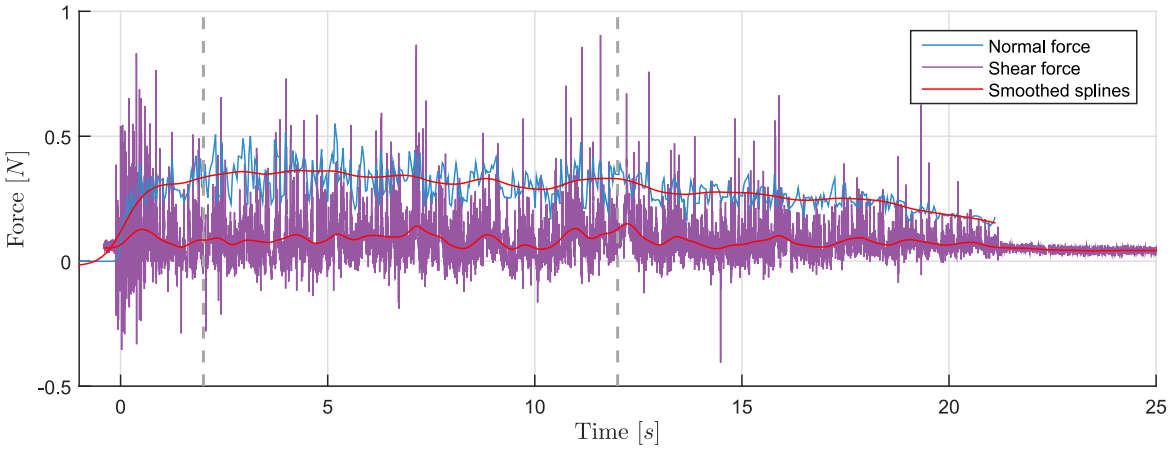

(b)

Figure 4.11: Raw data obtained from the basal combined shear and normal stress sensor. The normal force measurements are plotted in blueand shear force measurements are plotted in purple. Smoothed splines for both datasets are drawn in red. The vertical grey dashed lines delimit the steady-state phase of the experiment (see Section 3.4.3) on which this work is focused.

determined for our discs by our collaborator in NCSU, USA, Zhu Tang, using the experimental setup and method described in Tang *et al.* (2018) [19].

The results shown in Figure 4.13 will be used to verify our photoelastic force measurements, as in the next Chapter we obtain similar averages (albeit with similar errors) using the coarse-grained stress tensor results (Section 5.2). In any case, it shows that although we cannot measure many small forces due to the sensitivity of the technique, the errors due to this source are within the photoelastic technique experimental error. Moreover, these results imply that $\mu_{base} > \mu_s$ and that therefore no part of these flows are in non-local regime where $\mu < \mu_s$. This inference is particularly significant to the next chapter, where we consider how our flows fit with different rheology models. Finally, through this use of the shear and normal stress sensors we tested an unusual

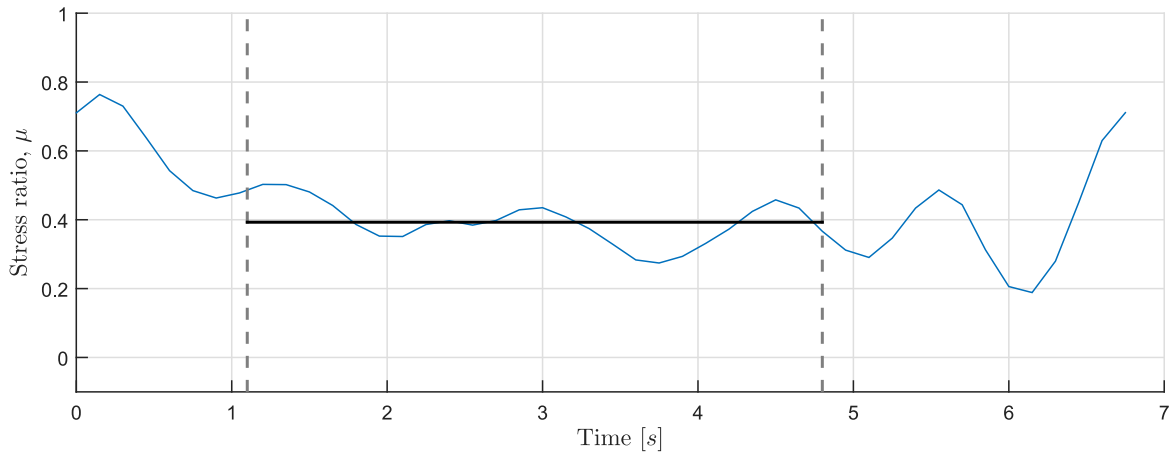

(a)

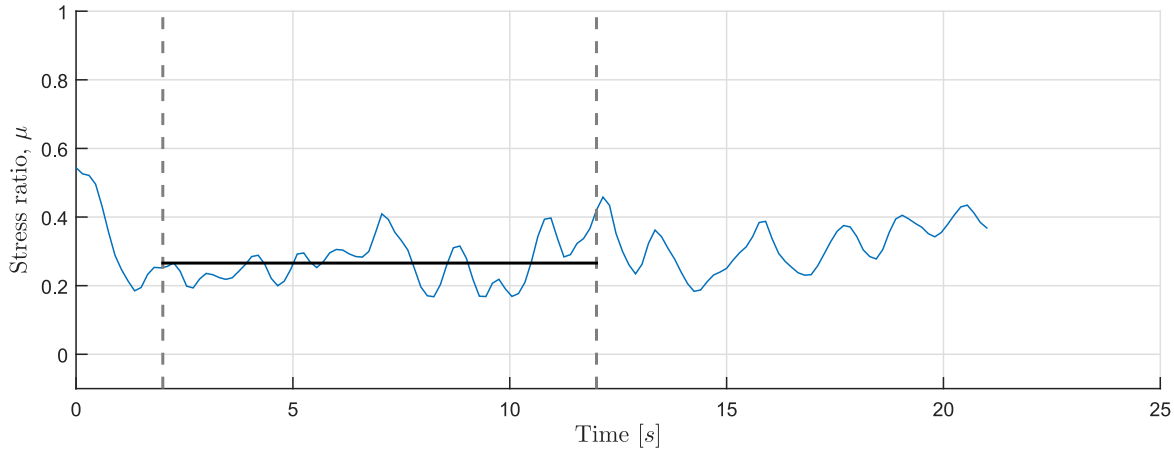

(b)

Figure 4.12: Evolution of the stress ratio $\mu = \tau/P$ (Equation 1.5) throughout the experiments over (a) a smooth base and (b) a rough base shown in Figure 4.11. The blue line is obtained by dividing the value of the shear stress measurement smoothed spline by the normal stress measurement smoothed spline. The vertical grey dashed lines delimit the steady-state phase of the experiment (see Section 3.4.3) on which this work is focused. Finally, The horizontal smooth black line shows the average μ obtained for these experiments over the steady-state stage.

application of these sensors. Our feedback regarding the design of the combined sensor will potentially lead to future product development at Freeman Technology, as no real-time flush sensor of simultaneous shear and normal stresses exists to this day.

4.4 Discussion

The first main result of the work described in this chapter is the success in quantifying forces using the photoelastic technique in dynamic systems for the first time. We apply the photoelastic technique to obtain innovative experimental measurements of

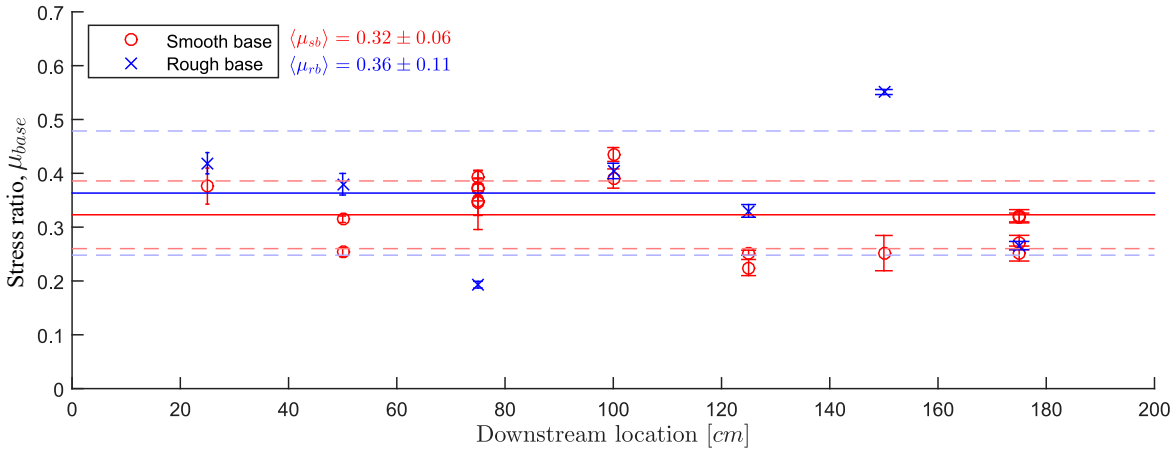

Figure 4.13: Measurements of the stress ratio μ measured using the combined shear and normal stress sensor described in Section 3.1.2. Each experimental value reported in this plot corresponds to the ratio of mean shear and normal forces, averaged over the steady state stage of each experiment. The blue crosses represent measurements taken from experiments over a rough base, while the red circles correspond to experiments over a smooth base. The solid lines represent the mean off all experiments of each type, while the dotted lines delimit their standard errors.

forces within the bulk of 2D free-surface, gravity-driven, dry granular flows. Side wall effects play a significant role in the kinematics of the flows produced, but the intrinsic relationships between flow kinematics and dynamics discussed here are nonetheless applicable to all dry granular avalanches [13]. In particular, by coarse-graining the results of this original experiment, we test the extent to which such a discrete system can be modelled as a continuum.

From a discrete point of view, less than half the particles (as seen in Figure 3.7a, although the exact proportion depends on depth) of the flow constitutive particles carry a measurable significant load. These particles, that form part of force-chains, transport loads one or two orders of magnitude larger than a single particle weight. Regardless of the force network dynamics, we have shown through coarse-graining that the average stress-tensor is equivalent to that of a continuous flow, including a hydrostatic increase of pressure with depth (Figure 4.9). Despite the technique sensitivity limitations, we verified our results for the normal and shear forces at the base with a separate custom-designed sensor.

Furthermore, we determined that force-chains form preferentially in the directions of the forces acting on the bulk. In this case, the two external force sources are gravity and the shear induced by the basal topography, and a larger number of force-chain forces are directed in these two directions (Figure 4.6). From comparisons between the results from configurations where gravity and basal shear bear different relative importance, we propose that the system main principal stress is directed somewhere

in between the two, leaning closer to the the most relevant locally.

Bibliography

[1] Thomas Barker, D G Schaeffer, Michael Shearer, and J M N T Gray. Well-posed continuum equations for granular flow with compressibility and μ (i)-rheology. *Proceedings of the Royal Society A: Mathematical, Physical and Engineering Sciences*, 473(2201):20160846, 2017.

[2] G. Berton, R. Delannay, P. Richard, N. Taberlet, and A. Valance. Two-dimensional inclined chute flows: Transverse motion and segregation. *Physical Review E*, 65(5):051303, 2003.

[3] W. Bi, R. Delannay, P. Richard, and A. Valance. Experimental study of two-dimensional, monodisperse, frictional-collisional granular flows down an inclined chute. *Physics of Fluids*, 18(12):123302, 2006.

[4] T. Faug, P. Childs, E. Wyburn, and I. Einav. Standing jumps in shallow granular flows down smooth inclines. *Physics of Fluids*, 27(7):073304, 2015.

[5] A. Favier de Coulomb, M. Bouzid, P. Claudin, E. Clément, and B. Andreotti. Rheology of granular flows across the transition from soft to rigid particles. *Physical Review Fluids*, 2(10):102301, 2017.

[6] I. Goldhirsch. Stress, stress asymmetry and couple stress: from discrete particles to continuous fields. *Granular Matter*, 12(3):239–252, 2010.

[7] J. T. Jenkins. Dense shearing flows of inelastic disks. *Physics of Fluids*, 18(10):103307, 2006.

[8] Pierre Jop, Yoël Forterre, and Olivier Pouliquen. Crucial role of sidewalls in granular surface flows: consequences for the rheology. *Journal of Fluid Mechanics*, 541:167–192, 2005.

[9] S. Meyer, C. Song, Y. Jin, K. Wang, and H. A. Makse. Jamming in two-dimensional packings. *Physica A: Statistical Mechanics and its Applications*, 389(22):5137–5144, 2010.

[10] GDR MiDi. On dense granular flows. *The European Physical Journal E*, 14(4):341–365, 2004.

[11] N. Mitarai and H. Nakanishi. Bagnold scaling, density plateau, and kinetic theory analysis of dense granular flow. *Physical Review Letters*, 94(12):128001, 2005.

[12] O. Pouliquen and N. Renaut. Onset of granular flows on an inclined rough surface: dilatancy effects. *Journal de Physique II*, 6(6):923–935, 1996.

[13] S. P. Pudasaini and K. Hutter. *Avalanche dynamics: dynamics of rapid flows of dense granular avalanches*. Springer Science & Business Media, 2007.

[14] J. Rajchenbach. Some remarks on the rheology of dense granular flows. *The European Physical Journal E*, 14(4):367–371, 2004.

[15] L. E. Silbert, D. Ertaş, G. S. Grest, T. C. Halsey, D. Levine, and S. J. Plimpton. Granular flow down an inclined plane: Bagnold scaling and rheology. *Physical Review E*, 64(5):051302, 2001.

[16] L. E. Silbert, J. W. Landry, and G. S. Grest. Granular flow down a rough inclined plane: transition between thin and thick piles. *Physics of Fluids*, 15(1):1–10, 2003.

[17] N. Taberlet, P. Richard, A. Valance, W. Losert, J. M. Pasini, J. T. Jenkins, and R. Delannay. Superstable granular heap in a thin channel. *Physical Review Letters*, 91(26):264301, 2003.

[18] J. Tang and R. P. Behringer. How granular materials jam in a hopper. *Chaos: An Interdisciplinary Journal of Nonlinear Science*, 21(4):041107, 2011.

[19] Z. Tang, T. A. Brzinski, M. Shearer, and K. E. Daniels. Nonlocal rheology of dense granular flow in annular shear experiments. *Soft Matter*, 14(16):3040–3048, 2018.

[20] T. Weinhart, R. Hartkamp, A. R. Thornton, and S. Luding. Coarse-grained local and objective continuum description of three-dimensional granular flows down an inclined surface. *Physics of Fluids*, 25(7):070605, 2013.

[21] T. Weinhart, A. R. Thornton, S. Luding, and O. Bokhove. From discrete particles to continuum fields near a boundary. *Granular Matter*, 14(2):289–294, 2012.

[22] Y. Zhou, P. Ruyer, and P. Aussillous. Discharge flow of a bidisperse granular media from a silo: Discrete particle simulations. *Physical Review E*, 92(6):062204, 2015.

CHAPTER 5

Rheology and non-locality

Synopsis

In this chapter we analyse the rheology of gravity-driven, mono-dispersed dry granular flows in physical experiments where we measure individual forces within the flow bulk. As in the previous chapter, we produce a 2D flowing layer over a super-stable heap where particles creep. The flows are mono-dispersed, dense ($\phi \approx 0.8$), thin ($h \approx 10d$), and in the slow to intermediate regime ($I < 1$). Using particle tracking and photoelastic force measurements we report coarse-grained profiles for packing fraction, velocity, shear rate, inertial number and stress tensor components. In addition, we define a quantitative measure for the rate of generation of new force chain networks and we observe that fluctuations extend below the boundary between dense flow and quasi-static layers. Finally, we evaluate several existing definitions for granular fluidity, and make comparisons among them and the behaviour of our experimentally-measured stress tensor components.

Our measurements of the non-dimensional stress ratio show that our experiments lie within the local rheological regime, yet we observe rearrangements of the force network extend into the quasi-static layer where shear rates vanish. This elucidates why non-local rheology models rely on the notion of stress diffusion, and we thus propose non-local effects may in fact be dependent on the local force network fluctuation rate.

5.1 Introduction

The novel ability to experimentally measure forces within dynamic flows offers an unprecedented opportunity to test granular rheology assumptions and models. In particular, in this chapter we test the appropriateness of the definitions made in the

three rheological models [19, 13, 3] described in Section 1.4, using experiments at low-intermediate values of I where non-local effects become relevant.

For this purpose, we focus our attention on experiments carried out with a monodisperse mixture of discs (with 10% polydispersity as in the previous chapter), over a rough base of alternating 12 and 22 mm diameter semi-discs (see Chapter 3, Figure 3d). In Section 4.2 we determined that the flows over this type of topography show the thickest super-stable heap, so they exhibit the best conditions to study the differences in the force network between the flowing and quasi-static layers. Furthermore, instead of comparing results taken from multiple downstream locations, we focus specifically on the most upstream location, where the quasi-static layer is thickest. In this particular section, we consider four repetitions of experiments with the viewing window centred at 25 cm from the top end of the chute.

The results presented in this chapter are interpreted in the context of the flow regime they are measured in: quasi-static, dense inertial or collisional. To classify the flow regime, we use the criteria introduced in Section 1.2 in terms of the dimensionless inertial number I [9],

$$I \equiv \frac{\dot{\gamma} d}{\sqrt{P/\rho_0}}, \tag{5.1}$$

where $\dot{\gamma}$ represents the shear rate, $d = 12\ mm$ the particle diameter, P the local pressure and ρ_0 the density of the particle material, 1200 kg/m^3 [1].

In addition, to evaluate the applicability of current rheology models, we need to evaluate whether sections of the system are in a *local* or *non-local* regime. This second classification relies on the local values of the stress ratio μ, defined from the decomposition of the stress tensor,

$$\bar{\bar{\sigma}} = P\bar{\bar{\mathcal{I}}} + \frac{\mu P}{||\bar{\bar{\mathcal{T}}}||}\bar{\bar{\mathcal{T}}}. \tag{5.2}$$

where $\bar{\bar{\mathcal{T}}}$ represents the rate of shear strain tensor and then μ represents the ratio between shear (τ) and normal stress P [15]. Local models interpret μ as an effective friction coefficient that depends solely on I, which would only apply if the local τ is a function solely of shear rate $\dot{\gamma}$. One popular local model for the relationship between μ and I was successfully developed by Jop *et al.* (2006) [12],

$$\mu(I) = \mu_s + \frac{\mu_2 - \mu_s}{I_0/I - 1}, \tag{5.3}$$

where μ_s is the effective static coefficient of friction (see Equation 1.2), μ_2 is the maximum stress ratio attainable by the system, and I_0 is a free parameter,.

In particular, we measure the force chain fluctuation rate and compare its behaviour to the shear rate, allowing for experimental tests of three proposed non-local rheology

models [19, 13, 3], as well as confirming whether the force chain fluctuations are able to identify the value of μ_s [22]. Using the methods described in Tang *et al.* (2018) [22], the Daniels group in North Carolina State University (NCSU) estimated that for the particles used in this work the yield stress ratio is $\mu_s = 0.26 \pm 0.01$. This group has obtained similar values of μ_s for discs of other materials [22], as have Wandersman and Van Hecke (2014) [23]. These values are low compared to those typical in the field of geophysics, which are usually closer to twice this result, but they interpret the low value as a result of μ_s not really being the ordinary coefficient of friction in this case but the resistance to secondary flow in an already flowing granular material. We also test whether the shear rate is an appropriate variable in the description of fluidity at all, given that even for static granular packings, force chain configurations are not solely determined by particle positions [20, 14]. Instead, there is an ensemble of possible force arrangements, the force network ensemble (FNE) [20], which can fluctuate independent of, and in addition to, particle rearrangements under shear. Therefore, we additionally consider some alternatives for defining the fluidity g.

In the following sections we first characterise the flow packing fraction, velocity and shear-rate profiles for four experiments carried out under exactly the same experimental conditions. The differences between the results of individual experiments are those due to differences in the lubricating flour coating (see Section 3.4.4, on the experimental repeatability). Next, we use the photoelastic force measurements to calculate coarse-grained profiles of the stress tensor components, and with these we evaluate the behaviours of the principal stresses and the stress ratio, μ, across the boundary between flowing and quasi-static layers. Then, we use the pixel intensities (which are linked to the presence of force chains) to evaluate a profile for the average duration of forces within the flow bulk, and compare this to the assumptions on which current granular rheology models are based.

Part of the content of this chapter has been developed in collaboration with the Daniels lab group in NCSU. All experiments described here and their characterisation were carried out by the author of this thesis. The codes to calculate the force chain fluctuation frequency (Section 5.3.1) and the photoelastic intensity variance (Section 5.3.2) were developed side-by-side with PhD student Zhu Tang, and the analysis around Section 5.3.3 is a result of lengthy discussions with Zhu Tang and Karen Daniels, both at NCSU at the time.

5.2 Flow characterisation

We calculate the continuous density profile $\rho(z)$ applying the coarse-graining equations introduced in Section 3.3, and use this to measure the packing fraction profile $\phi(z) =$

$\rho(z)/\rho_0$, where $\rho_0 \approx 1200\ kg/m^3$ is the density of cured *Clear Flex 50*. As previously observed in Section 4.2.1, we find that $\phi(z) \approx 0.81 \pm 0.07$, which is slightly lower than random close packing for 2D discs ($\phi_{RCP} = 0.84$ [5, 18]). Louge *et al.* (2003) [16] reported low packing fractions in the upper flowing layer, but the value we measure is uniform (within our experimental error) along the whole profile, in both quasi-static and upper flowing layer. Although we measure no significant variations in ϕ with depth, we observe that all layers are equally spaced from each other by $0.9d$ [24]. However, the degree of layering becomes less pronounced closer to the free surface. It is possible that the packing fraction indeed decreases towards the free surface, but by an amount smaller than the experimental error or that this is dampened by coarse-graining.

For each of the four experimental runs, the flow thicknesses H are between $17d$ and $20d$, but differ primarily in the amount of material that accumulates as a quasi-static basal layer, while the flowing layer remains at a constant thickness. Therefore, in the plots that follow this paragraph we examine the properties of the flows as a function of the vertical coordinate z, as measured with the origin placed at the free surface. As shown in Figure 5.1a, we observe that the four downstream velocity profiles, $V_z(z)$, are consistent in their shape and magnitude.

A quasi-static layer forms below a depth of about $12d$. In Figure 5.1a, we shade the area where the particles move up to 100 times slower than their free surface counterparts. As shown in Section 4.2.2, along the whole chute, this quasi-static layer forms a super-stable heap that is thickest closest to the hopper, and decreases to zero thickness at the lower, open end of the chute. For our particular system, the super-stable heap effectively increases the inclination of the steady-state flow above it by 5°. As in other reports of experiments where super-stable heaps form in narrow channels [21, 10, 6], we observe quasi-linear velocity profiles in the flowing layer, $0d < z < 12d$.

Using the mean velocity profile, taken across all four runs, we calculate the shear rate $\dot{\gamma} = dV_x/dz$ by taking second-order central finite differences. The resulting profile $\dot{\gamma}(z)$ is shown in Figure 5.1b. We observe that it obtains near-zero values in the quasi-static bottom layer, and gradually increases in the transition to the flowing layer. A maximum value of $\dot{\gamma} = 6\ \mathrm{s}^{-1}$ is reached at a depth of approximately $6d$. A decrease close to the free surface, in the region shaded light gray in Figure 5.1b, is surprising given that we observe uniform packing fraction throughout the flow, as presented in Figure 4.1c. However, as the depth of maximum shear rate ($z = 6d$) is below the cut-off of boundary effects on the coarse-graining ($z = 3d$), we accept it as a physical phenomenon. On the other hand, it is possible that our measurements of the packing fraction ϕ within this region are overestimated by an amount smaller than our experimental error. If so, as the shear rate has been shown to be extremely sensitive to the packing fraction [17, 26], a slightly smaller ϕ can still cause significant differences in the shear rate. Even though

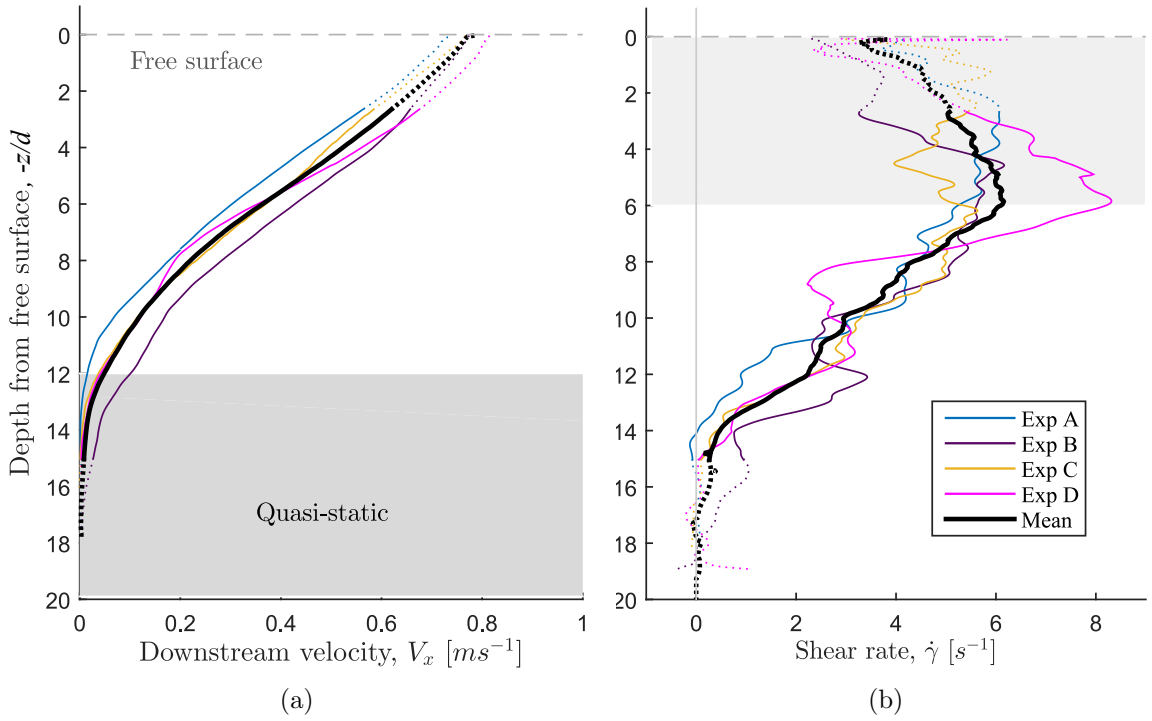

Figure 5.1: (a) Coarse-grained downstream velocity profile $V_z(z)$, and (b) mean flow shear rate profile $\dot{\gamma}(z)$ of the steady flow measured at a distance 25 cm from the hopper opening, with individual runs aligned to have $z = 0$ at the free surface. The gray shades denote regions of different observed behaviour. On (a) the shaded region contains quasi-static particles, as opposed to the flowing layer above. On (b) the region shaded in light gray shows shearing rates decreasing with particle velocities, perhaps related to a decrease in packing fraction, too small to measure directly. In both plots the dotted lines represent values affected by coarse-graining near boundaries.

this region is not in the collisional state where the packing fraction would be expected to decrease much more dramatically, we interpret this region to be transitioning to a high-I state.

We calculated the continuous stress tensor components σ_{ij} from discrete force measurements according to the technique proposed by Weinhart *et al.* (2012) [25]. The coarse-grained profiles $\sigma_{ij}(z)$ are shown in Figure 5.2a. As a reminder to the reader, the absolute values of the profiles have a large systematic error (see Section 2.2.3.2), particularly towards the top of the flow, where the proportion of small forces below the experimental technique sensitivity is largest. However, the gradients in σ_{ij} coincide with the expected hydrostatic increase with depth of the normal and shear stresses. It follows that the stress ratio $\mu = \tau/P$, is constant in the dense flow region. In contrast, we observe μ decreases with depth below the boundary with the quasi-static layer. Interestingly, μ does not fall below the measured value of $\mu_s \approx 0.26$, which is observed to be reached only at the base. Figure 5.2b raises the interesting question of whether we do not observe non-local regions, where $\mu < \mu_s$, because the quasi-static region is

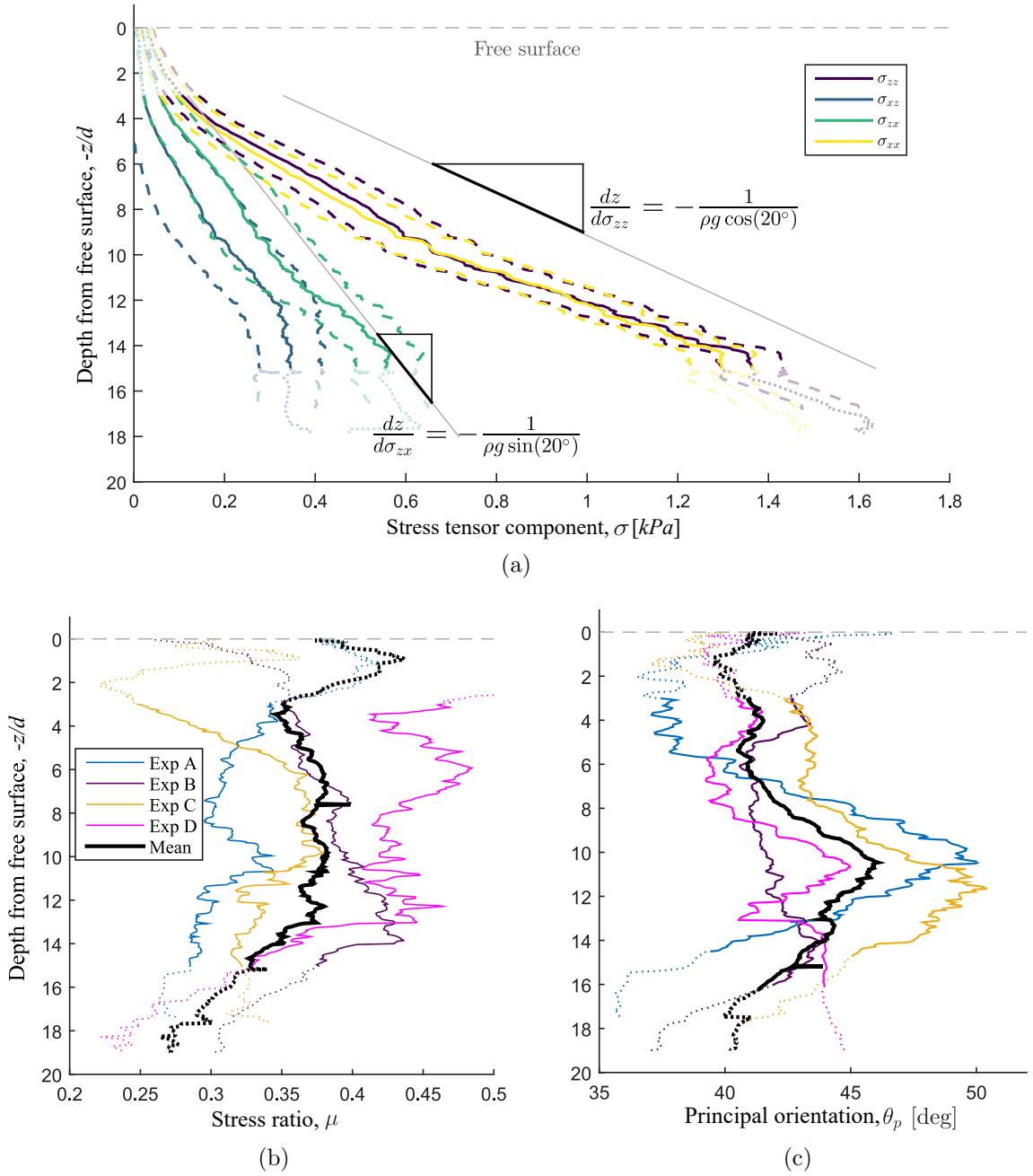

Figure 5.2: Analysis of the stress tensor coarse-grained according to Weinhart *et al.* (2012) [25]: (a) The solid coloured lines represent each of the four stress tensor components, coarse-grained and averaged over the four experiments, while the dashed lines delimit the error bounds, defined by the data standard error. The straight gray lines show the gradients expected in the case of hydrostatic pressure and shear; (b) the shear ratio and (c) the principal orientation obtained from the profiles shown in (a), for each experiment (coloured lines) and their mean (solid black line). Values within $3d$ of the free surface or base are plotted in dotted lines and light colours as their measurements are affected by proximity to a boundary.

not deep enough to reach it. These results are consistent with previous analyses [**? ? ?**] on the impact of side-wall friction on the rheology of flows in narrow channels. As

the pressure on the side-walls increases with depth, so do the frictional forces at the walls. In consequence, μ is predicted to decrease with depth from the free surface.

The principal stresses show a change of direction, measured via the principal orientation, θ_p (as defined in Section 4.3.2.2), shown in Figure 5.2c. The peak in θ_p coincides in position with the transition between static and flowing layers. This peak is on average 5° larger than the value of θ_p measured close to the free surface and bottom boundary. Incidentally, 5° is the angle the flowing layer velocity vector makes to the base, as the super-stable heap that forms at the chute base effectively increases the inclination of the flowing layer by this amount. In other words, we observe a 5° angle between the velocity components V_x and V_z in our frame of reference aligned with the setup inclination.

Since we now have experimental coarse-grained measurements for the pressure P from the symmetric component of our measured $\bar{\bar{\sigma}}$, we calculate a profile for the inertial number I, defined in Section 1.4.1, with depth. This plot of the experimental results is shown in Figure 5.3. We find that the inertial number decreases steadily with depth from the free surface within the flowing layer. However, in the quasi-static layer where the shearing effect of the rough base is expected to be most important, the shear rate approaches zero, and therefore so does I. In this region, I is small but non-zero while the velocities are non-zero.

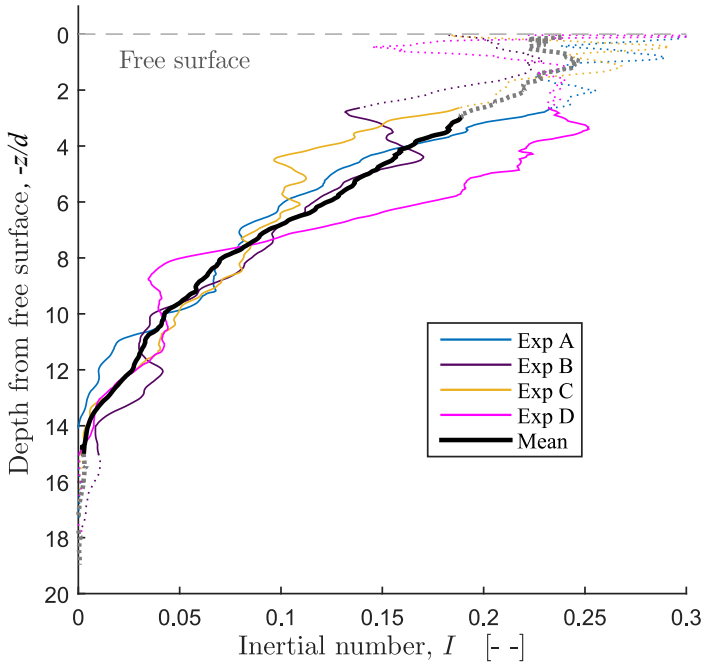

Figure 5.3: Profile $I(z)$ of the inertial number, as defined in Equation 5.1. Data collected at distances within a coarse-graining length $w_z = 3d$ of the free surface and chute base are shown with a dotted line, as these points are affected by proximity to the boundaries.

With profiles for both μ and I, we investigate the relationship between them. By plotting them against each other in Figure 5.4, we see a rapid increase of μ at low values of I, and a plateau at the maximum value of μ_s. These are characteristics modelled by Jop *et al.* (2006) [12] in the form of Equation 5.3. A fit of this $\mu(I)$ model to the experimental data, fixing $\mu_s = 0.26$ (measured separately using the apparatus described by Tang *et al.* (2018) [22]), is shown in red in Figure 5.4, and obtains $I_0 = 0.004$ and $\mu_2 = 0.376$. The values found for I_0 and μ_2 are different for every material and geometry, but are consistent with other values obtained for different materials [12] (taking into account their error margins).

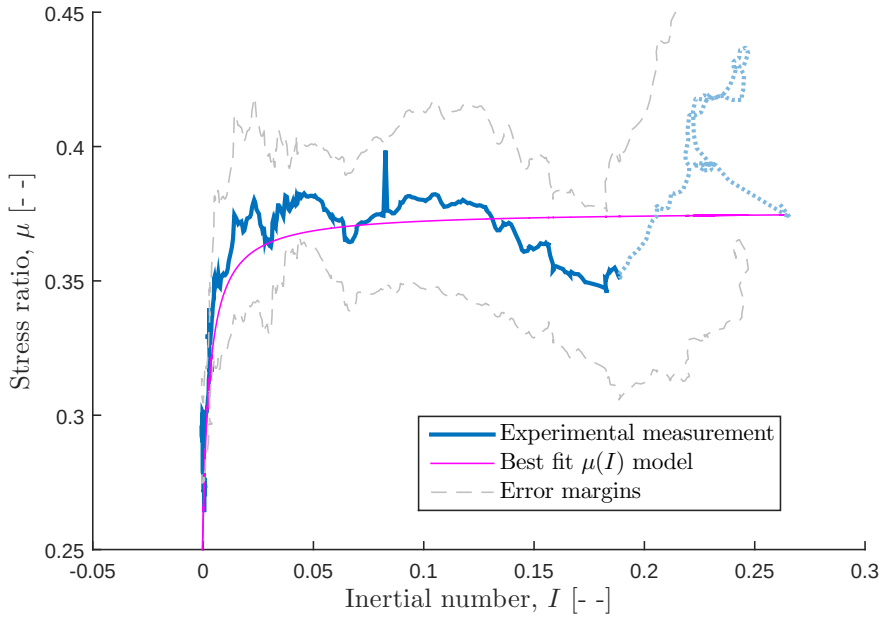

Figure 5.4: Measured values of μ (Figure 5.2b) as a function of the corresponding values of I (Figure 5.3), plotted in blue. The light gray dashed lines denote the experimental error margins. The red line shows the best fit of the $\mu(I)$ model proposed by Jop *et al.* (2006) [12] (Equation 5.3), for a fixed $\mu_s = 0.26$ (± 0.01 [22]), and fitted $\mu_2 = 0.38 \pm 0.01$ and $I_0 = 0.004 \pm 0.001$. Data collected at distances within a coarse-graining length $w_z = 3d$ of the free surface and chute base are shown in dotted lines, as these points are affected by proximity to the boundaries.

5.3 Results

5.3.1 Force network fluctuations

It has previously been observed that spatial and temporal fluctuations in the interparticle forces provide a measure of how close/far a system is from the boundary between flowing/non-flowing regions or regimes [11, 4, 22]. In order to identify whether this ef-

fect is an important factor in the three nonlocal rheologies [19, 13, 3], we make similar measurements for our avalanching flows. To measure the duration of time that a particular point in the flow shows a force (or a photoelastic response to a force), we treat each pixel brightness as an individual time series $B(t)$. In our flows, the particles only rarely have more than one photoelastic fringe (due to the combination of material and disc thickness chosen, as explained in Section 2.3.2). Therefore, a growing or decaying brightness approximately quantifies the growth or destruction of a force chain.

For each pixel, we measure the autocorrelation coefficient $C(\Delta t)$ across the entire time series:

$$C(\Delta t) = \frac{\sum_t \left[B(t) - \bar{B}\right]\left[B(t+\Delta t) - \bar{B}\right]}{\sum_t \left[B(t) - \bar{B}\right]^2}. \tag{5.4}$$

The first peak is well-fit by a function of the form $C(\Delta t) \propto \exp[-\Delta t/T]$, where T represents the typical lifetime of a force chain at that depth. At each depth, we average all such measurements of T to determine a typical lifetime of force chains, and report these values as a fluctuation rate $\omega \equiv 1/T$. The resulting $\omega(z)$ observed for each of the four runs are shown in Figure 5.5, along with their average. This analysis quantifies our visual observation that force chains are reconfiguring faster close to the free surface of the flow ($z = 0$).

Several features of Figure 5.5 stand out. First, we bear in mind that only forces that are about an order of magnitude greater than the average disc weight produce a measurable photoelastic response. For this reason pixels corresponding to discs in the top few layers may not reach maximum intensities, and often will not display intensity variations at all. Secondly, the location of the free surface is measured by averaging the highest points of the discs that we track on the free surface throughout the duration of the steady state flow (see Section 3.2.2). Occasionally the flow is thinner than the mean flow thickness H, so at these times pixel intensities do not vary significantly. We thus strongly suspect that the results shaded in light gray in Figure 5.5, extending up to a depth of $3d$ are underestimated.

Below a depth of $3d$, ω decreases with depth, which coincides with the direct observation of force chains fluctuating faster at the top of the flow. However, even within the quasi-static region, at depths of at least $12d$ according to Figure 5.1a, ω remains larger than zero. This implies that the force network rearranges even when particle positions do not change at all, epitomizing the ensemble of force configurations for a given configuration [20, 14]. This result coincides with geomechanics observations for pseudostatic granular systems that also show that force fluctuations may occur in the absence of particle rearrangements.

Using the profile $\omega(z)$, combined with $\dot{\gamma}(z)$ reported in Figure 5.1b, we can now test the proposal by Pouliquen & Forterre (2009) [19] that the rate of plastic deformation is

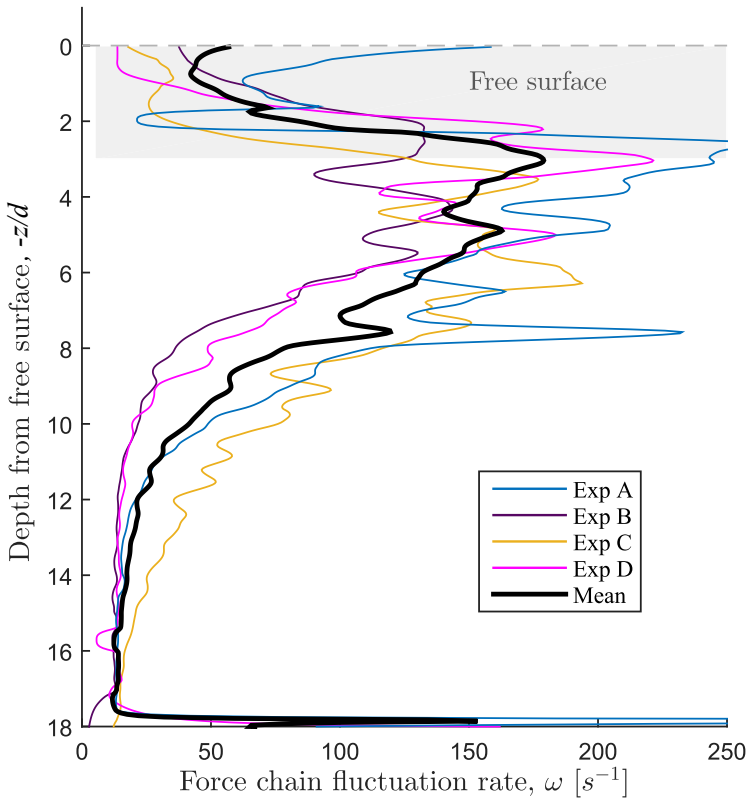

Figure 5.5: Profile of the pixel brightness fluctuation frequency, representative of the force-chain rearrangement rate. Each colour represents the coarse-grained result of a different individual experiments, and the thick black line shows their average.

proportional to the rate of generation of new random force networks within a granular flow. As shown in Fig. 5.6, we observe that within the region in intermediate-I regime ($3d < z < 12d$) the relationship between $\dot{\gamma}$ and ω is indeed approximately linear [27]. However, we also observe that for low shear rates ($\dot{\gamma} < 2$ Hz), ω decreases slower with $\dot{\gamma}$, and reaches a minimum value of approximately 20 Hz rather than zero. This result is linked to the previous observation that force chains fluctuate even within the quasi-static region, where shear rates are practically zero. The force network fluctuations [20] decrease slowly with distance from the boundary between flowing and quasi-static layers. We reason that as long as the force network rearranges, and there exists a configuration in the force network ensemble that may lead to a localised high shearing force, motion *may* occur. Therefore, we believe the lengthscale where we measure force chain rearrangements in the quasi-static region is indicative of the lengthscale at which non-local effects may be observable, even where μ may be lower than μ_s.

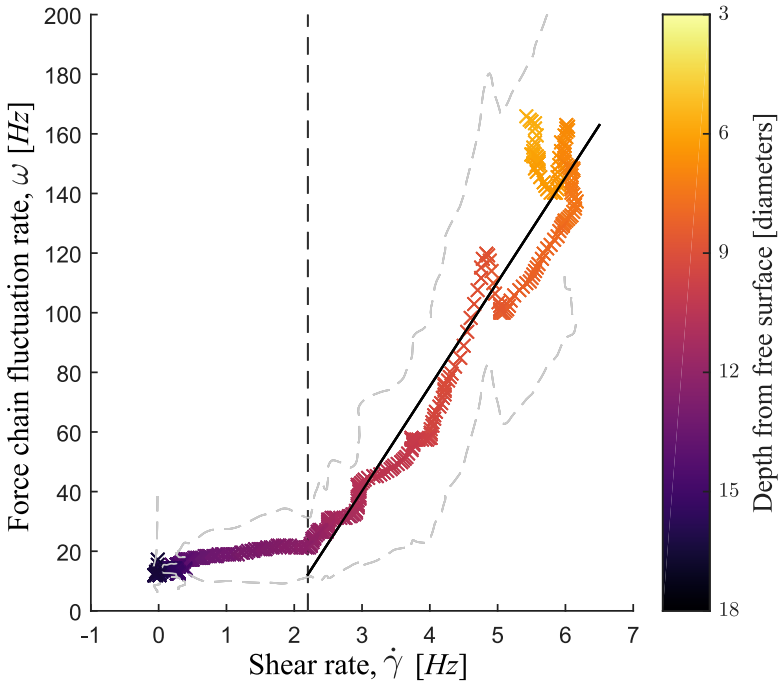

Figure 5.6: Parametric scatter plot of $\omega(z)$ and $\dot{\gamma}(z)$ using the data shown in Figures 5.5 and 5.1b. The colour of each experimental point represents the depth at which the data was taken. The light gray dashed lines denote the experimental error margins. The dark gray dashed line separates the points collected at depths larger than $12d$, in quasi-static state (left of the line), with those obtained in the flowing layer (right of the line). The solid gray line shows a linear regression (correlation coefficient $R = 0.97$) for $3d < z < 12d$, the region interpreted to be in the intermediate-I regime.

5.3.2 Photoelastic intensity variance and μ_s

Tang *et al.* (2018) [22] observed that a sharp change in the force chain fluctuations, quantified via δB (the standard deviation of the pixel intensity or brightness B), identified the location in the flow at which μ dropped below μ_s. As shown in Fig. 5.7, we compute how δB varies as a function of depth. While we observe a distinct peak in $\delta B(z)$, at a depth of $10d$ below the free surface, this location does not coincide with the depth at which $\mu = \mu_s = 0.26$. As recorded in Figure 5.2b, the μ threshold is crossed quite close to the base, at a depth below $18d$. Therefore, this peak is therefore not the same feature reported in Tang *et al.* (2018) [22]. Instead, this feature likely arises through two limiting effects: particles near the top have low δB because they sustain only small forces, while particles at the bottom have low δB because they are not flowing (small force fluctuation rate ω). Between these two extremes, there is therefore is a peak value.

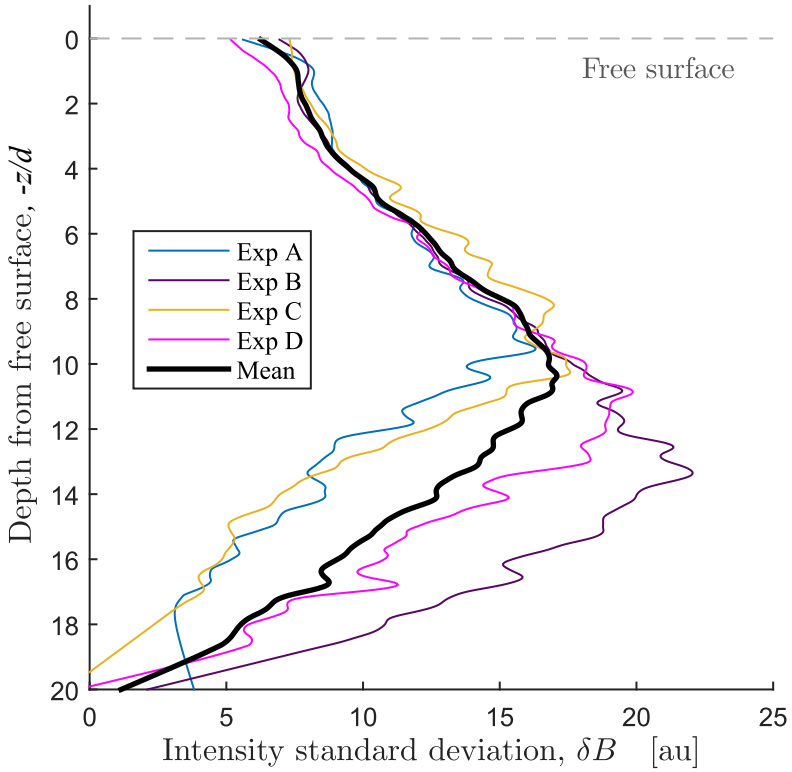

Figure 5.7: Profile of the horizontally-averaged pixel intensity standard deviation, as defined by Tang *et al.* (2018) [22]. They interpreted the position of the peak is indicative of $\mu = \mu_s$, but here the peak in δB is found at an approximate depth of $10d$, where $\mu > \mu_s$. Each colour represents the coarse-grained result of a different individual experiments, and the thick black line shows their average. Data collected at distances within a coarse-graining length $w_z = 3d$ of the free surface and chute base are shown in light colours and dotted lines, as these points will be affected by proximity to the boundaries.

5.3.3 Evaluating granular fluidity proposals

In Figure 5.8, we compare (1) the behaviour of (purple/darkest line) the granular fluidity $g = \dot{\gamma}/\mu$ (Equation 1.11), defined in analogy to classical fluids as the inverse of viscosity, with (2) (blue/intermediate shade line) that of the inertial number I, and finally with (3) (orange/lightest line), the quantity presented in the previous section, the force fluctuation rate ω. Each of the regimes introduced so far have been demarcated by the grayscale background. From the bottom up:

1. Quasi-static from $z > 12d$ (darkest shading) identified from the mean downstream velocity V_x shown in Figure 5.1a;

2. Intermediate-I, dense flow regime from $12d > z > 6d$ identified from packing fraction and velocity measurements;

3. Still intermediate-I regime for $6d > z > 3d$, but although we do not observe

significant variations in the packing fraction within the flowing layer, we noticed a change in the behaviour of the shear rate, $\dot{\gamma}$ (Figure 5.1b). This may be due to a very slight change in the packing fraction smaller than our experimental error, that may still affect $\dot{\gamma}$. If so, we interpret the flow within the range $6d > z > 3d$ to be slowly transitioning to a collisional state.

4. Nearly-collisional surface flow from $3d > z > 0d$ (lightest shading) is the region within which the free surface fluctuates in position and ω values are underestimated.

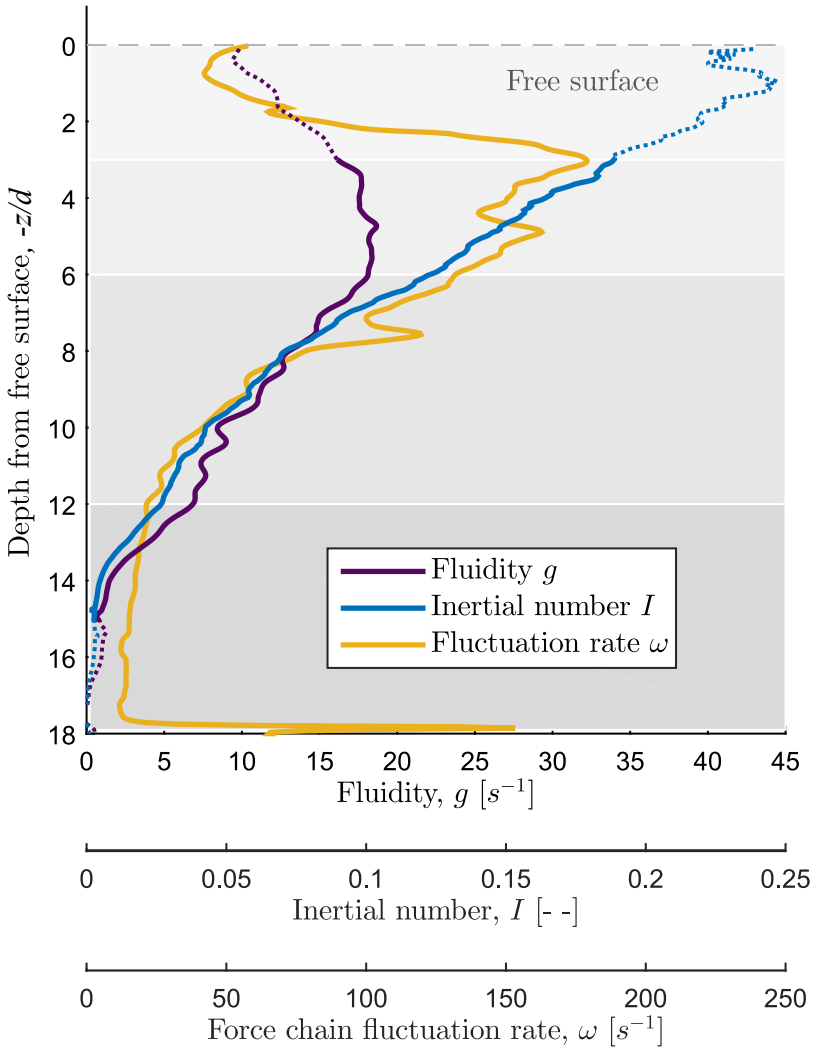

Figure 5.8: Comparing three proposed definitions of fluidity: g, I, and ω. Each shaded region distinguishes the four flow regimes described in the text, from quasi-static (bottom) to nearly-collisional (top).

Within the heap at the bottom, motion occurs as sporadic, localised rearrangements of small clusters of particles. Under an assumption that this region should have

zero fluidity because velocities are small and discontinuous, then g and I could be considered as describing the granular fluidity within this region, since both g and I are accordingly nearly zero for $z > 12d$. However, we instead interpret that because in our experiments the force chains fluctuate within what is in fact a not closely-packed *quasi*-static flow, the fact that particles *may* move should imply a fluidity that, like ω, is appropriately non-zero. Estep & Dufek (2012) [7] also reported significant force network rearrangements within a small, confined erodible bed over which a similar 2D avalanche of photoelastic discs flowed. Having studied a closely and tightly packed substrate, they observed no particle rearrangements, but their results had important implications for our understanding of bed entrainment. In fact, in our experiments discrete particle rearrangement events [8] are rare within the super-stable heap, but they undeniably exist. The significance of this is that we measure ω to be non-zero where there is creeping flow, even if no motion is observable for the duration of a single experimental run.

Non-local models originally extended the fluidity to regions where non-local effects were empirically observed. These models rely on *stress diffusion* as a physical mechanism to justify the use of a diffusive term in the definition of granular fluidity, but the lengthscale to which such diffusion extends (the *cooperative length* [3]) remains unexplained and needs to be determined empirically. Only recently have microscopic definitions for granular fluidity been proposed, including functions of strain-rate [**?**] and velocity fluctuations [26] (introduced in Section 1.3.3). Indeed, the photoelastic response we measure as pixel intensities is due to strains both within the particles and at the contacts between two discs. This links the observed photoelastic responses to displacements of order smaller than a millimetre, and ω is related to fluctuations in particle velocities. As we interpret Figure 5.8, the force network fluctuation rate would capture where particles *may* flow, in both local and non-local regimes. Therefore, we propose ω is a local indicator of the susceptibility of a granular system to flow, and an indicator of granular fluidity in quasi-static state.

We notice that within depths of $6d - 12d$, where the flow is in dense inertial regime, all three variables, g, ω and I are proportional to each other. They may therefore be expected to be interchangeable as measures of fluidity in the models for dense flows. However, I is easy to measure and a universally valid representation of fluidity for flows in dense inertial regime.

In the flowing layer, we are faced with two problems when interpreting Figure 5.8. First, up to a depth of $3d$ below the free surface, besides involving forces that are mostly weaker than the technique sensitivity, pixel intensity fluctuations are small at times where the flow thickness is smaller than the average. In this region, measurements for ω based on photoelasticity are therefore underestimated. Secondly, we need to consider

the effect of changes in packing fraction on ω. Because the shear rate decreases towards the free surface above depths of $6d$ while μ is constant, so does g. Only I continues to increase all the way up to the free surface, but we attribute this to our underestimation of the pressure obtained from coarse-grained photoelastic measurements. In the transition to a collisional state, we suspect ω, I and g will no longer be proportional to each other. While such measurements are not accessible to us in our current dataset, Figure 5.8 raises the interesting question of how ω behaves in the dilute limit. A link between ω and packing fraction is speculated upon here but is more clearly stated in Section 7.2.2.

We propose the force network fluctuation rate ω is a local indicator of the likelihood of flow. We suggest ω is an appropriate descriptor of granular fluidity in both quasi-static and dense inertial regimes. Nonetheless, we suspect ω should depend on the packing fraction, so it would be interesting to investigate how this parameter behaves in the transition to collisional regime.

5.4 Discussion

In this chapter we analyse the force network fluctuations in flows that are in the dense, intermediate-I regime, flowing over an inclined layer of quasi-static discs. This provides insight into the dynamics near the boundary between dense inertial and quasi-static regimes. We find that the stress ratio $\mu = \tau/P$ is approximately constant within the dense flow, which is consistent with our expectation for a steady regime based on momentum conservation. The value of μ decreases slightly where the static layer begins near the bottom of the flow, but does not drop below the yield criterion μ_s. The resulting relationship between the μ and the inertial number I can be described by the local rheological model proposed by Jop *et al.* (2006) [12], Equation 5.3.

We use the experimental image pixel intensities forming the photoelastic patterns to define the force chain average fluctuation rate ω. Using these measurements we validate that there is a monotonic relationship between $\dot{\gamma}$ and ω [19] for flows in intermediate-I regime. However, Figure 5.5 suggests this proportionality breaks down for small shear rates. We hypothesize that this may be due to differences in magnitude of the force fluctuations in normal and shear directions for values of the stress ratio close to the yield criterion. Because rearrangement events [8] are infrequent in a quasi-static state, velocity and shear rate measurements may be underestimated, and so may the definitions of fluidity based on V_x and $\dot{\gamma}$. On the other hand, we interpret that $\omega > 0$ indicates regions where particles *may* flow, and we observe $\omega > 0$ even within the quasi-static layer. The force network rearranges even where particles lie practically

stationary, although such rearrangements are less frequent further from the boundary with the flowing layer.

This observation elucidates why non-local models [13, 2] relied on the notion of stress diffusion to empirically extend the granular fluidity into regions where $\dot{\gamma} = 0$. Our results suggest that ω may provide a universal local quantification of the susceptibility of flow, and therefore may be a local variable that underlies granular fluidity, especially for quasi-static and low-I regimes. This interpretation complements the use of strain-rate and/or velocity fluctuations as measures of granular fluidity in the quasi-static regime. In particular, the photoelastic response creates a measureable signal in response to minuscule displacements (in fact smaller than could be measured with confidence for velocity fluctuations, as characterized by Xu *et al.* (2004) [**?**]). In this way, ω provides an experimentally-approachable measurement technique. Moreover, while a change in particle positions will cause a change in the forces, there are many valid configurations of forces for any one set of positions (the "force network ensemble" [20, 14]). Since the forces set the yield criterion, we propose that their dynamics are an important control on fluidity, beyond simply the fluctuations in particle positions or velocities. Furthermore, in the dense-inertial regime where strain-rates and velocity fluctuations may be hidden in the larger-scale motions of the flow, ω is still easily measurable and scales with g and I.

A caveat against using ω is the sensitivity of the technique, which causes measurements to be underestimated near the free-surface. In addition, the results shown in this region raise the question of how changes in packing fraction affect the force fluctuation rate, and whether ω is a good descriptor of the susceptibility of flow in the dilute limit at all. Moreover, it would be interesting to further investigate how ω compares to the decoupled isotropic and anisotropic stress fluctuations, as well as the correlations between ω, I, shear and strain rate and velocity fluctuations in experiments where our discs can be observed at much higher resolution.

Another important implication of our measurement of ω is the potential use of the photoelastic technique to characterise the depth into the super-stable heap to which the flow may creep. If similar experiments were carried out over a deeper quasi-static region, then we propose that the depth at which $\omega = 0$ can be related to the *cooperative length* used in nonlocal models.

Bibliography

[1] Clear flex 50 series; technical data sheet. `https://www.smooth-on.com/tb/files/CLEAR_FLEX_50_95_TB.pdf`.

[2] M. Bouzid, A. Izzet, M. Trulsson, E. Clément, P. Claudin, and B. Andreotti.

Non-local rheology in dense granular flows. *The European Physical Journal E*, 38(11):125, 2015.

[3] M. Bouzid, M. Trulsson, P. Claudin, E. Clément, and B. Andreotti. Nonlocal rheology of granular flows across yield conditions. *Physical Review Letters*, 111:238301, 2013.

[4] S. Chialvo, J. Sun, and S. Sundaresan. Bridging the rheology of granular flows in three regimes. *Physical Review E*, 85(2):021305, 2012.

[5] K. W. Desmond and E. R. Weeks. Random close packing of disks and spheres in confined geometries. *Physical Review E*, 80(5):051305, 2009.

[6] S. C. Du Pont, P. Gondret, B. Perrin, and M. Rabaud. Wall effects on granular heap stability. *Europhysics Letters*, 61(4):492, 2003.

[7] J. Estep and J. Dufek. Substrate effects from force chain dynamics in dense granular flows. *Journal of Geophysical Research: Earth Surface*, 117(F1), 2012.

[8] M. L. Falk and J. S. Langer. Dynamics of viscoplastic deformation in amorphous solids. *Physical Review E*, 57(6):7192, 1998.

[9] Y. Forterre and O. Pouliquen. Flows of dense granular media. *Annual Review of Fluid Mechanics*, 40:1–24, 2008.

[10] Y. Grasselli and H. J. Herrmann. On the angles of dry granular heaps. *Physica A: Statistical Mechanics and its Applications*, 246(3-4):301–312, 1997.

[11] D. Howell, R. P. Behringer, and C. Veje. Stress fluctuations in a 2D granular Couette experiment: a continuous transition. *Physical Review Letters*, 82(26):5241, 1999.

[12] P. Jop, Y. Forterre, and O. Pouliquen. A constitutive law for dense granular flows. *Nature*, 441(7094):727, 2006.

[13] K. Kamrin and G. Koval. Nonlocal constitutive relation for steady granular flow. *Physical Review Letters*, 108(17):178301, 2012.

[14] J. E. Kollmer and K. E. Daniels. Betweenness centrality as predictor for forces in granular packings. *Soft Matter*, 2019.

[15] R. Lespiat, S. Cohen-Addad, and R. Höhler. Jamming and flow of random-close-packed spherical bubbles: an analogy with granular materials. *Physical Review Letters*, 106(14):148302, 2011.

[16] M. Y. Louge. Model for dense granular flows down bumpy inclines. *Physical Review E*, 67(6):061303, 2003.

[17] M. Y. Louge, A. Valance, P. Lancelot, R. Delannay and O. Artières. Granular flows on a dissipative base. *Physical Review E*, 92(2):022204, 2015.

[18] S. Meyer, C. Song, Y. Jin, K. Wang, and H. A. Makse. Jamming in two-dimensional packings. *Physica A: Statistical Mechanics and its Applications*, 389(22):5137–5144, 2010.

[19] O. Pouliquen and Y. Forterre. A non-local rheology for dense granular flows. *Philosophical Transactions of the Royal Society of London A: Mathematical, Physical and Engineering Sciences*, 367(1909):5091–5107, 2009.

[20] J. H. Snoeijer, T. J. H. Vlugt, M. van Hecke, and W. van Saarloos. Force network ensemble: a new approach to static granular matter. *Physical Review Letters*, 92(5):054302, 2004.

[21] N. Taberlet, P. Richard, A. Valance, W. Losert, J. M. Pasini, J. T. Jenkins, and R. Delannay. Superstable granular heap in a thin channel. *Physical Review Letters*, 91(26):264301, 2003.

[22] Z. Tang, T. A. Brzinski, M. Shearer, and K. E. Daniels. Nonlocal rheology of dense granular flow in annular shear experiments. *Soft Matter*, 14(16):3040–3048, 2018.

[23] E. Wandersman, and M. Van Hecke. Nonlocal granular rheology: Role of pressure and anisotropy. *EPL (Europhysics Letters)*, 105(2):24002, 2014.

[24] T. Weinhart, R. Hartkamp, A. R. Thornton, and S. Luding. Coarse-grained local and objective continuum description of three-dimensional granular flows down an inclined surface. *Physics of Fluids*, 25(7):070605, 2013.

[25] T. Weinhart, A. R. Thornton, S. Luding, and O. Bokhove. From discrete particles to continuum fields near a boundary. *Granular Matter*, 14(2):289–294, 2012.

[26] Q. Zhang and K. Kamrin. Microscopic description of the granular fluidity field in nonlocal flow modeling. *Physical Review Letters*, 118(5):058001, 2017.

[27] J. Zheng, A. Sun, Y. Wang, and J. Zhang. Energy fluctuations in slowly sheared granular materials. *Physical Review Letters*, 121(24):248001, 2018.

CHAPTER 6

Size segregation

Synopsis

In this chapter we describe results from experiments where we quantify instantaneous forces between individual particles in the bulk of bi-dispersed 2D gravity-driven dry granular flows. In particular, we compare avalanching flows composed of (1) a single particle size type, (2) a uniform bidisperse mixture of two size types, and (3) experiments where a single large particle is tracked in a flow of smaller type particles. We analyse how differences in the force network between mono- and bi-dispersed avalanching granular media lead to the mechanisms that drive granular size segregation.

Firstly, we observe that large particles are relatively more likely to form part of force chains than the small species, and show that consequently force chains form in a wider spread of directions in bi-disperse media. We then link these two results, and the fact that force chains tend to form in preferential directions, to the factors that influence squeeze expulsion and kinetic sieving as the main segregation mechanisms. This work provides new evidence of the physical processes that drive granular size segregation, and particularly those behind the upward thrust on larger particles. In particular, we show that the levering mechanism we observe is both size- and direction-preferential, and explain why the degree of polydispersity, the flow inclination angle, and the shear rate profile affect the local rate of segregation. In doing so, our revised kinetic sieving and levering model overcomes the criticisms to segregation models based on the geometric probabilities of the different physical mechanisms that may take place.

6.1 Introduction

In this chapter we use our novel insight into the force network in granular flows to explore the mechanisms that drive size segregation. Our first aim is to analyse how bi-dispersity affects the kinematics and dynamics of the flow. Secondly, where segregation is observed, we want to link the bi-dispersed force network characteristics to an uneven distribution of forces that results in an upward thrust of large particles.

We carry out two modalities of experiments: uniformly bi-dispersed and mono-dispersed with a single large particle (the intrusion limit). The uniformly bi-dispersed flow is composed of small discs that are 11, 12 and 13 mm in diameter and large discs 21, 22 and 23 mm in diameter. Within each species the different size discs are dispersed in equal numbers, while the ratio of total small to large disc numbers in the bulk is 35:1. This ratio was chosen so that most large particles were completely surrounded by small particles in the hopper when we set up the experiment. For this modality, we carry out experiments along the chute with two boundary conditions: over a smooth base and over a rough base made of small semi-discs (Figures 3.3a and 3.3b, respectively).

Next, we analyse mono-dispersed experiments made of small discs over a rough base of small semi-discs. These experiments are almost identical to the set described in Chapter 4 over a base of 12 mm diameter semi-discs, but we introduce a single large particle (22 mm in diameter) in the middle of the hopper full of small particles. This intruder particle enters the chute at a different depth in each experiment, roughly determined by the location where we initially place it in the hopper. Then, over many repetitions, we draw an average path for each depth of entry of the intruder.

Finally, we closely observe and describe the mechanism by which large particles are forced onto the layer above the one it was originally travelling on. Our observations are consistent with mechanisms previously proposed [6, 2], namely kinetic sieving, squeeze expulsion and diffusion. We combine the theoretical existing mechanisms with new observations to revise the squeeze expulsion mechanism in particular, and propose a mechanism based on the levering, rather than squeezing, of particles in force chains.

6.2 Bi-disperse flow

We produce uniformly bi-dispersed flows by filling the hopper with a random mixture of a small (11, 12 and 13 mm in diameter) and large (21, 22 and 23 mm in diameter) species of photoelastic discs. In every frame of all experiments, we count 35 ± 6 small discs per large disc. The discs are introduced carefully so that most large discs are completely surrounded by small ones. Figure 6.1 shows an example of the distribution of the two disc species.

Figure 6.1: Example of disc distribution in the hopper before each experiment is carried out. The ratio of small to large discs is 35:1. All discs are carefully released so that most of the large discs are completely surrounded by small discs.

We carry out experiments with this uniform distribution of discs 14 times, 7 over a smooth base and 7 over a rough base made of small semi-discs. The experiments over each type of base are recorded at one of seven different locations along the chute: at 25, 50, 75, 100, 125, 150 and 175 cm from the chute start.

6.2.1 Flow characterisation

We apply the same coarse-graining equations as used in Section 4.2.1 to calculate the continuous density profile $\rho(z)$, shown in Figure 6.2. We calculate this profile for the central vertical line of each frame and average the profiles over 1000 frames, twice as many as were used to obtain the mono-dispersed profiles. We use a larger number of frames than in the previous chapters to ensure enough large particles are considered, given that they are dilute in the flows (1 large every 35 small ones on average). As before, the coarse-graining length-scale was half the optimal in order to observe microscopic changes in the distribution - specifically the degree of layering. We find that the packing fraction $\phi(z) \approx 0.80 \pm 0.07$, for experiments over both types of basal roughness, is approximately uniform and constant within the steady-state flows. This value is only slightly lower than the average packing fraction measured for mono-dispersed flows of small discs, but within our error bounds. Hence, we are unable to determine whether the disc density is lower in our bi-dispersed flows.

Bi-dispersity does have a more obvious impact on the layering of the flow. Compared to the packing fraction profiles of the mono-dispersed flows (see Section 4.2.1), the undulations that mark higher densities in the layer centres (and lower densities between

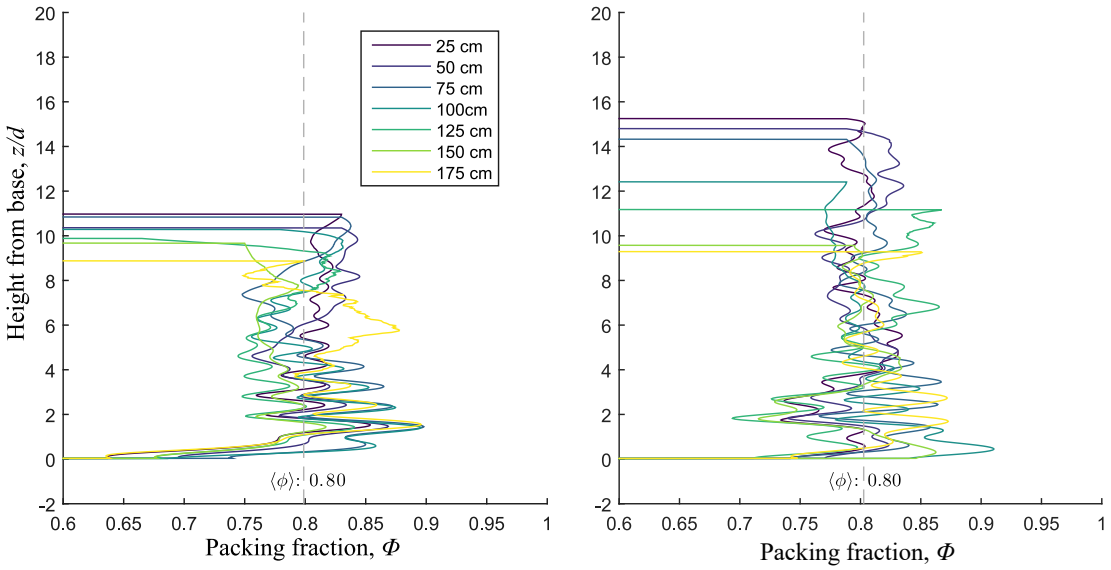

Figure 6.2: Collapsed coarse-grained packing fraction profiles from seven positions down the chute for flows over (a) a smooth base and (b) a rough base composed of small semi-discs. Both figures apply the same colour-scheme for the profiles measured at different downstream positions.

them) have smaller amplitudes and collapse only in the bottom few layers closest to the chute base in the bi-dispersed case, as opposed to the bottom $8d$ in the mono-dispersed case. This is not surprising given that in this case the flow contains sparse particles of diameters that span twice the distance between layers measured in the mono-dispersed case (Figure 4.1).

When the total packing fraction is divided into the partial fractions corresponding to the small and large particle species, we obtain Figure 6.3. Since the proportion of small discs is so much larger than that of large discs, the partial packing fraction corresponding to the small species is very similar to the total packing fraction profile. The large proportion of small discs is what allows layers to still form with the same separation as in the mono-dispersed case, particularly in the layers closest to the chute base. On the other hand, the large discs, being so sparse, require many more frames or repetitions of the experiments to be averaged into a smooth profile. Regardless, in experiments over both types of basal roughness, the partial packing fraction of large discs is 0.05 ± 0.01, and segregation is not discernible in this set of experiments.

Figure 6.4 shows the velocity profiles, obtained at each downstream location in the same way as for the mono-dispersed flows in Section 4.2.2. These are even more noticeably affected by the bi-dispersity, especially in the rough-base case. Although in the latter case the discs move only a couple of centimetres per second along the base, there is no clear super-stable heap (SSH) formation. Instead, the flow thins and

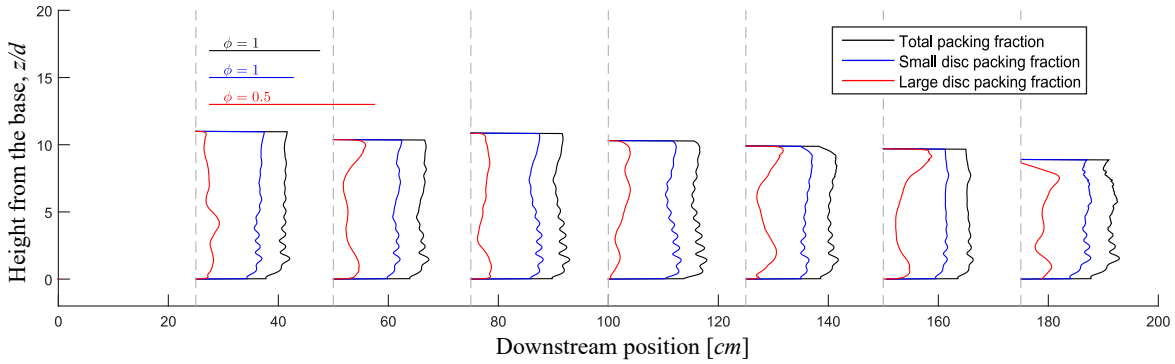

(a)

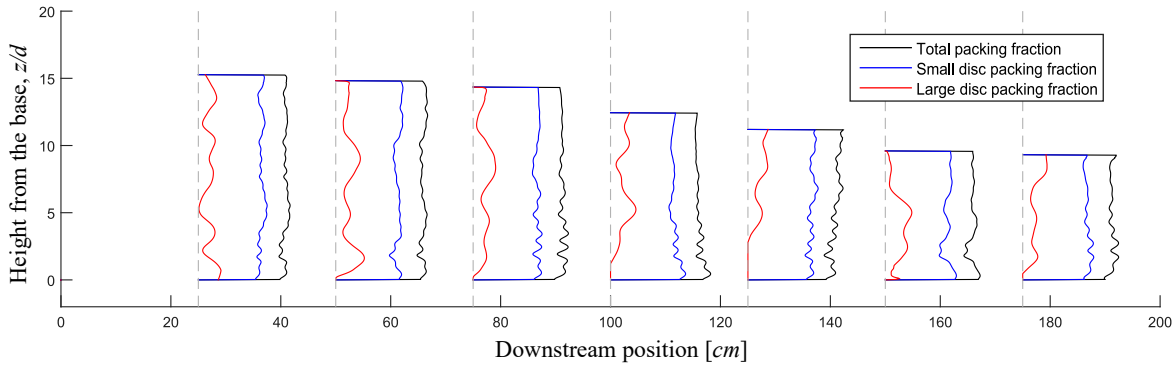

(b)

Figure 6.3: Coarse-grained total and partial packing fraction profiles at seven positions down the chute for flows over (a) a smooth base and (b) a rough base composed of small semi-discs. The black lines represent the total packing fraction, blue represents the small particle partial packing fraction, and red the profiles corresponding to the large particles partial packing fraction. Both figures apply the same colour-scheme and scales for the profiles.

accelerates along the chute.

The profiles are linear within our experimental error, and therefore each profile has a constant shear rate. For flows over a smooth base the constant shear-rate (outside regions too close to the boundaries) is 3.57 ± 0.05. In the rough-base case, the shear rates are also constant for each experiment but increase downstream, as shown in Table 6.1.

Downstream position [cm]	25	50	75	100	125	150	175
Shear rate [1/s]	2.67	3.38	4.08	5.49	5.76	7.37	8.28
Error [1/s]	0.03	0.06	0.07	0.09	0.11	0.08	0.15

Table 6.1: Shear rates for the linear velocity profiles measured for bi-dispersed experiments over a rough base, shown in Figure 6.4b.

This deviation from the SSH behaviour previously reported within this chute is attributed to a combination of potential factors. Firstly, the lack of a SSH may be

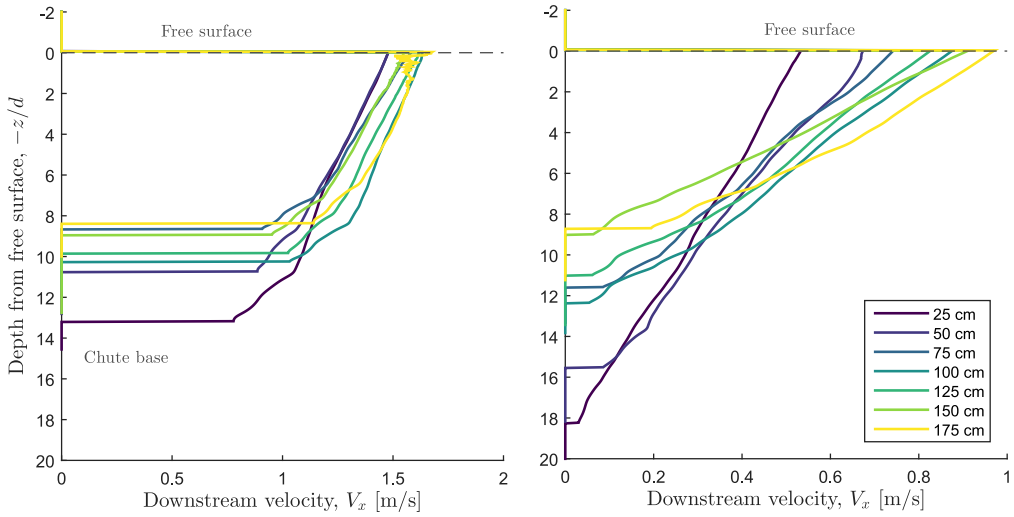

(a) (b)

Figure 6.4: Velocity profiles of bi-dispersed flows over (a) a smooth base and (b) a rough base made of small semi-discs. Each profile corresponds to a different downstream location along the chute.

in part due an increase of shear strength associated with an increase in polydispersity (for a fixed volume fraction) [3, 8]. Being able to observe undulations in Figure 6.3 indicates that the proportion of small discs is large enough that they may form regions of flow that are layered with the same layer separation as in the mono-dispersed case (approximately 11 mm). Then, a large particle that spans two of these layers (22 mm) will increase the drag between the two layers. As a result different layers in the flow have a stronger shearing effect on each other and shear rate gradient can be expected to be smaller than in the mono-dispersed.

It is also unclear whether a reduced packing fraction plays a role in the kinematics of this set of experiments. A small change in packing fraction can have a large effect on the kinematics of a granular glow. Given that our discs are so clear (which aid the accuracy of the photoelastic force measurements), our particle tracking method is fallible and carries too large an error (10%) to determine with certainty whether the packing fraction is lower by less than 10% in the bi-dispersed case than in the mono-dispersed.

Moreover, it is noted that an accumulation of flour on the chute side walls after years of carrying out experiments in this setup, may have reduced the effect of side-wall friction on the flow velocity. The fact that the velocity profiles for flows over both types of topography are still linear indicates that side-walls continue to play an important role in the flow kinematics, but it may have been reduced for the bi-dispersed experiments. Comparison with a mono-dispersed experiment carried out during the same time period when the bi-dispersed experiments were carried out show velocity profiles that are very

similar to those presented in Section 4.2.2. This result implies that deposition of the lubricant (flour) on the inside of the chute over years of use had only a small effect on the bi-dispersed flow.

In any case, the effect of polydispersity on the flow kinematics and dynamics is beyond the scope of this work. This setup would offer a novel experimental perspective to this line of investigation too, and more careful work can be carried out with a wider range of polydispersity to study this issue in the future. For the moment, we focus on the distribution of forces due to inter-particle interactions only. These are measured in terms of their photoelastic response, which is unaffected by forces applied by the side-walls. Friction opposes motion, so it will act upstream, while we are interested in the origin of the forces that cause particles to move in the cross-stream direction.

6.2.2 Force network characteristics

By applying PeGS [5, 1] on the experimental images, after particle tracking according to the algorithm described in Section 3.2.1, we obtain a list of magnitudes and directions of inter-particle forces. We remind the reader that the force-measuring technique is limited in sensitivity, and therefore naturally filters force-chains. Since we can also determine the sizes of particles, we can have a measure of what proportion of large and small particles form part of force chains.

We first classify discs depending on whether we measure a large enough G^2 value (see Section 2.3.1) near any of its contacts. If we do, it means there is a significant photoelastic response near at least one of the contacts, and that the disc is under a force measurable through the photoelastic technique. Discs on which there is at least one force-bearing contact are labelled 'forced', and the ones on which we do not are labelled 'not forced'. Simultaneously, we classify the discs into 'large' and 'small' depending on their radius, which was measured during particle tracking. This information was gathered for the new bi-dispersed experiments at all seven downstream locations and averaged for both smooth and rough base (of small semi-discs) cases. No significant differences were seen in these percentages at the different downstream locations. Table 6.2 summarises the results of this classification.

	Species	Not forced	Forced
Smooth base	Small	57.0%	43.0%
	Large	20.5%	79.5%
Rough base	Small	57.3%	42.7%
	Large	27.2%	72.8%

Table 6.2: Percentage of small and large discs on which we measure at least one force, for experiments over a smooth and rough base (made of small semi-discs).

The proportions of small and large discs that form part of force chains is similar for experiments over a smooth and rough base. However, we see that a much larger percentage of large particles are forced on average than small ones. This seems reasonable considering that large discs have a larger surface area, and as they are mostly surrounded by small discs, they are in contact with a larger number of other discs at any time. We interpret from this result that large particles are much more likely to form part of force chains than small particles. This experimental result validates similar finding obtained theoretically and numerically [9, 4, 7].

Next, we classify all forces from all 1000 frames taken per experiment according to the direction they are exerted. As in Section 4.3.1, we call the vertical direction in the camera frame 0°, and bin all forces into 5° wide intervals according to the angle they make to the vertical line in the camera frame of reference. The downslope direction then corresponds to a 90° angle, and forces at −90° are exerted upstream. Figure 6.5 plots the mean number of forces found in each direction per frame, averaged over all downstream locations, for mono-dispersed and bi-dispersed experiments over smooth and rough base.

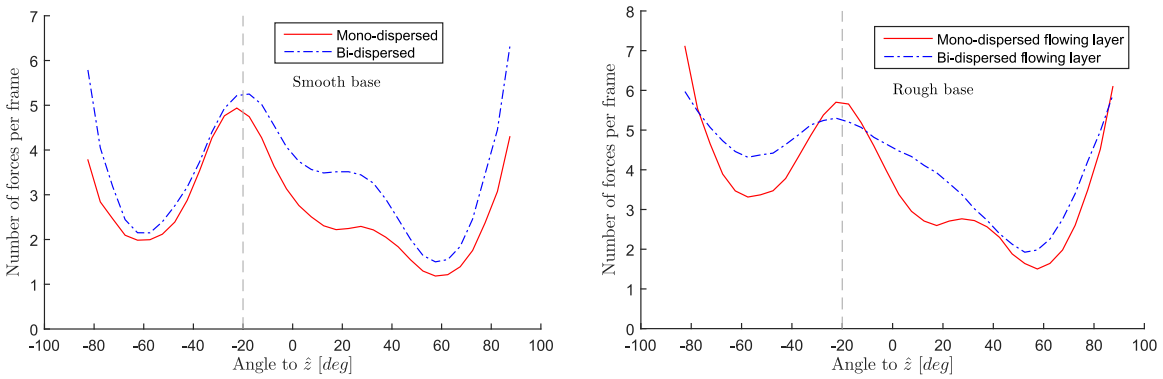

(a) Smooth base

(b) Rough base

Figure 6.5: Number of forces measured per frame in (a) smooth base and (b) rough base cases, averaged over all frames from experiments carried out at all seven downstream locations. The solid red lines represent the values measured in mono-dispersed experiments (presented in Section 4.3.1), while the dash-dotted blue lines correspond to bi-dispersed experiments.

We take into account that subtle differences in the thickness of the flour coating on the particles, or slightly different choices for the variables *dtol*, *g2cr* and *g2threshold* in the first part of PeGS for each experiment can impact the lower threshold in the contact forces that are included in the calculations to produce Figure 6.5 (see Section 2.3.3.1). This means that different experiments may be slightly more or less prone to false positive and negative detections of force bearing contacts. Assuming that this issue introduces a random error, the curves shown in Figure 6.5 may be vertically

shifted, but contrasts in their shapes still convey valuable information.

Figure 6.6 shows the mean magnitude of the forces according to the direction they are applied in. Differences in the flour coating and optimal choice of *dtol*, *g2cr* and *g2threshold* may cause these plots to flatten or stretch vertically, but the shapes of these curves are distinct enough to make inferences from them.

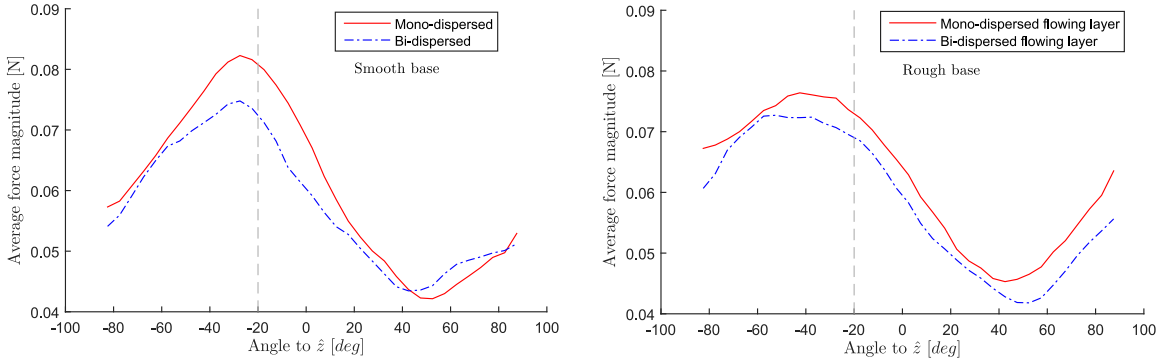

(a) (b)

Figure 6.6: Average force magnitude measured per frame in (a) smooth base and (b) rough base cases, averaged over all frames from experiments carried out at all seven downstream locations. The solid red lines represent the values measured in mono-dispersed experiments (presented in Section 4.3.1), while the dash-dotted blue lines correspond to bi-dispersed experiments.

In Figures 6.5 we observe very clear peaks in the number and magnitude of forces directed at $-20°$ (the direction of gravity) and at $\pm 90°$ (basal friction). The peaks of mono-dispersed and bi-dispersed experiments match in position for both smooth and rough base cases. Interestingly, the peaks in average force magnitude, shown in Figure 6.6 are wider and centred between -30 and $-40°$. Mono- and bi-dispersed experiments results match very well in the shape of their average force magnitude, from which we infer the error due to our choices of *dtol*, *g2cr* and *g2threshold* is not too great. However, the shapes of the number of forces curve do show a contrast, particularly in the rough-base experiments. In bi-dispersed media the central peaks in Figures 6.5 are wider, implying force chain directional spread is affected by bi-dispersity.

6.3 Single large particle in a mono-dispersed flow

Although the bi-dispersed mixture does not fully segregate, we do directly observe instances where individual large particles are pushed up to a layer above the one they were originally travelling in. The occurrence of these instances is stochastic in that we cannot predict with certainty when and how individual particles will move in the cross-stream direction, but we can define a probability distribution for the location of

a particle at a given distance downstream.

In order to investigate the rate at which large particles are raised in a flow, we carry out experiments at the intrusion limit. These experiments consist of flows made of small discs (11, 12 and 13 mm in equal numbers), with a single large particle in its midst. Because the flow is composed of essentially small particles, the velocity and shear rate profiles are remarkably similar to those presented in Section 4.2.2.

From the tests on the hopper discharge (see Section 3.4.2) we can estimate where a disc will be in the flow depending on where it was introduced in the hopper. Thus, when filling the hopper with small discs for the intrusion experiments, at each repetition we place the large particle in a strategic place. As our camera viewing window is constrained by the size of the polarisers to capture up to 60 cm in the downstream direction, we cannot track the intruder particle along the whole flow. Instead, we place a Samsung 9 phone to record where the large particle enters the chute, and use the Phantom v2012 Ultrahigh-Speed Camera to track the intruder as it passes a different downstream location on each experiment.

Figure 6.7a shows an example of the intruder particle in the hopper before an experiment, and Figure 6.7b shows an example of a frame used to measure the depth at which the intruder enters the flow. As mentioned in Section 4.1, a seam between two acrylic sheets marks the 0 cm downstream coordinate used in all experiments. We take the depth of the intruder particle from the free surface when it was captured passing through this seam as the depth at which it enters the flow. As can be seen in Figure 6.7, the intruder particle was painted red to facilitate tracking. The background illumination behind the polarisers is red, so painting the intruder in this colour has no effect on the photoelastic pattern captured by the high-speed camera.

6.3.1 Average path

We carry out sets of 15 experiments at each of 7 locations spread along the length of the chute. For each of the experiments we place the intruder particle in a location in the hopper where we can estimate the depth at which it will enter the channel. We try to obtain a broad range of intruder initial depths for each set, but there is some degree of randomness in the intruder initial depth in the flow given its original placement in the hopper.

We separate the 105 experiments carried out into categories according to the depth from the free surface at which the intruder was measured to have passed across the seam that marks the beginning of the channel. In Figure 6.7 we show six graphs where we plot the depths from the free surface where the intruder particle was tracked in the channel. Each plot corresponds to a group of experiments where the intruder was measured to have entered the chute within each of six bins: at depths of (a) up to 2 cm,

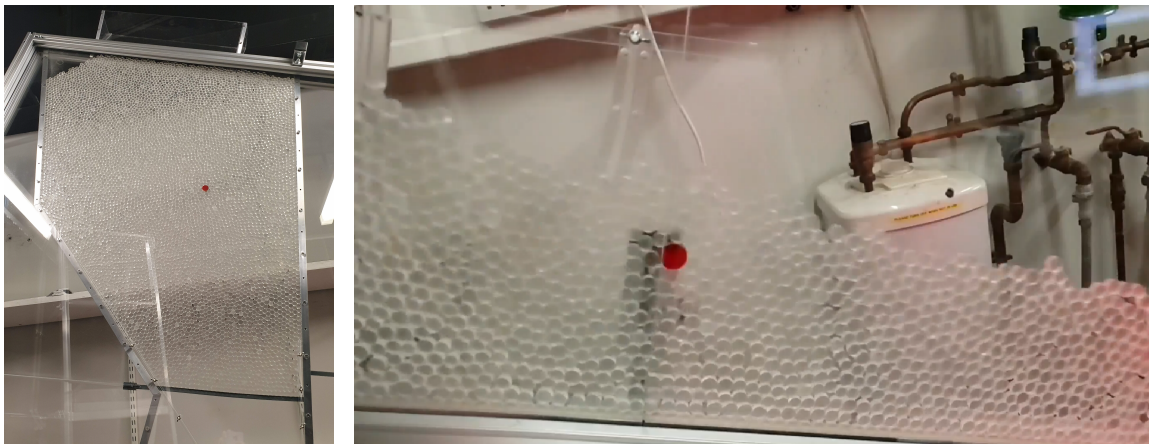

(a) (b)

Figure 6.7: Example pictures of the intruder large particle (painted red to facilitate tracking) in a bed of small particles. (a) shows the intruder in the hopper having been deliberately placed to enter the channel at a depth of approximately 4 - 6 cm. (b) shows an example frame from the mobile phone video that tracked the depth of the intruder as it passed through a seam between the acrylic sheets that make the side-walls. This is an example of a frame used to measure the depth at which the intruder enters the chute.

(b) between 2 and 4 cm, (c) between 4 and 6 cm, (d) between 6 and 8 cm, (e) between 8 and 10 cm, and (f) over 10 cm. The discs that entered the chute at depths larger than 13 cm were too slow to be transported significant depths during the steady-state phase of the flow. For all plots, we also colour the points of each experiment according to the intruder initial depth, to see the dispersion of results within each bin.

The first feature that stands out from Figure 6.7 is that no path tracked for any experiment is perfectly straight. Instead, the depth of the intruder oscillates as it travels with an amplitude of around two diameters d (average small particle diameter). This oscillation brings some error to the measurement of the initial intruder depth, as we only measure its depth as it passes along the seam in the acrylic walls. We cannot determine whether the intruder is then at a crest or trough of an oscillation, as we may inadvertently pass the natural vertical velocity fluctuations for transfers of the particle between layers.

In any case, we observe that many particles continue at the same depth at which they entered the chute, but some are tracked closer to the free surface further downstream. We very rarely track, further downstream, particles at depths larger than the one they entered the chute at. We infer from this data that diffusion plays a small role in the downwards transport of large particles (although, we do not discard that kinetic sieving may cause diffusion to have an asymmetric effect on the cross-stream transport of large particles). In Figures 6.7a and 6.7b the intruder seems to mostly

oscillate within the topmost layers. On the other hand, in the rest of the subfigures we observe at least one instance of the intruder travelling in a layer much higher than the initial one. We interpret that segregation mechanisms are indeed in play on the intruder particles, but that we would need a longer channel to observe the bi-dispersed flows segregate completely.

Figure 6.8 shows the averaged paths of the six categories of experiments as lines of

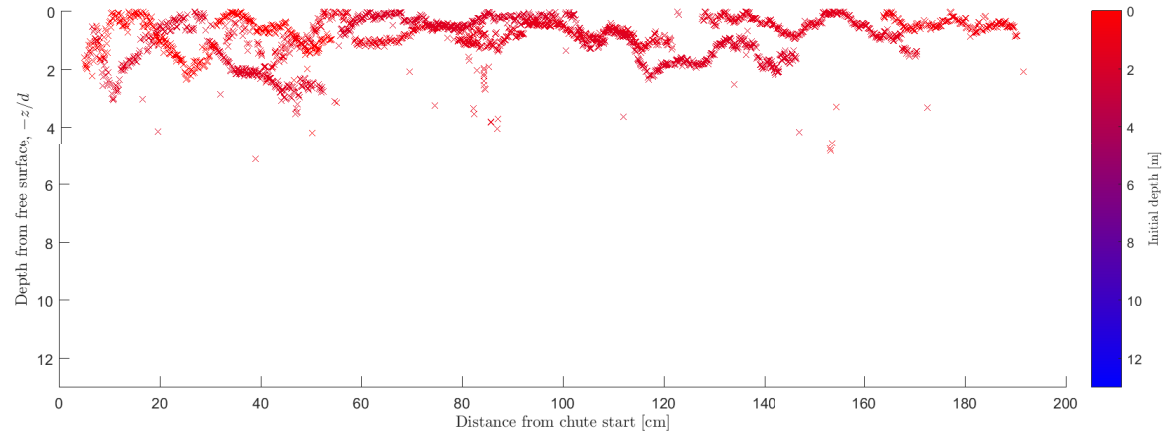

(a) Experiments with intruder initial depth of up to 2 cm.

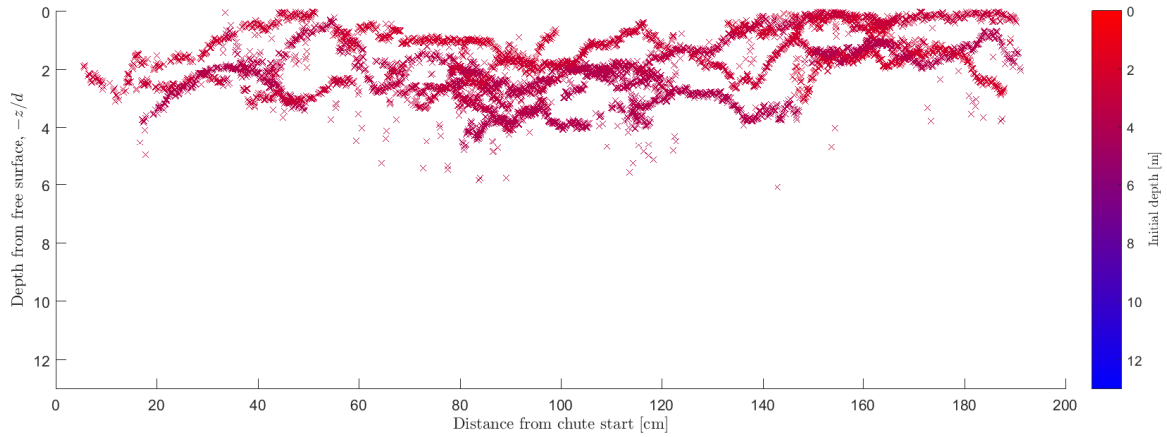

(b) Experiments with intruder initial depth between 2 and 4 cm.

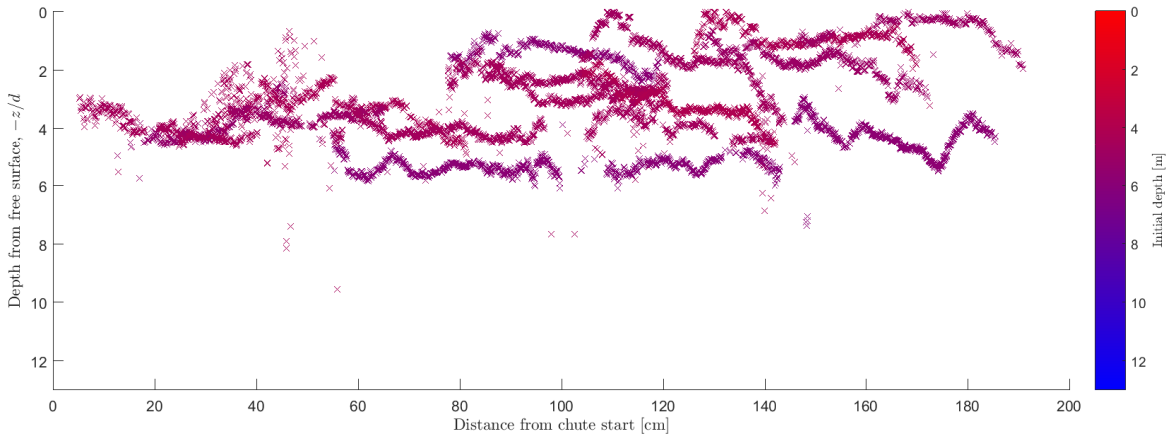

(c) Experiments with intruder initial depth between 4 and 6 cm.

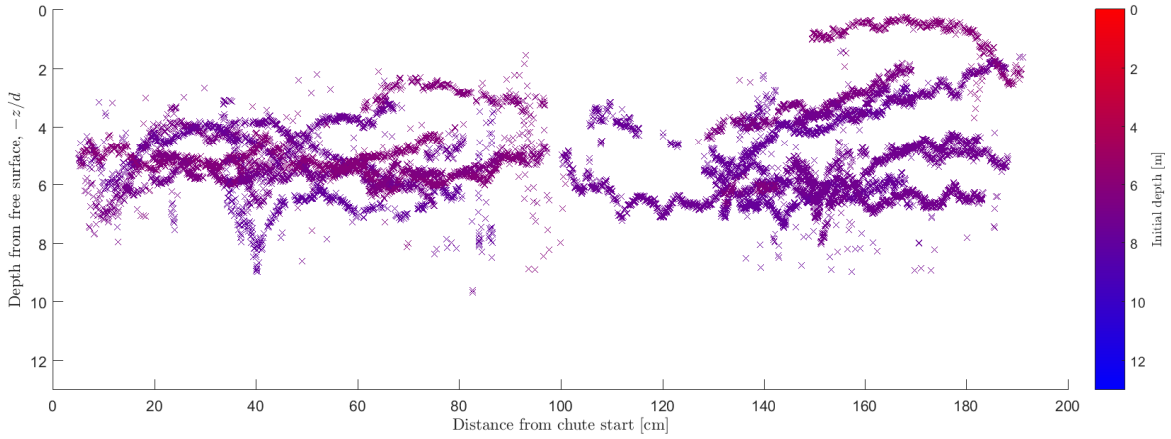

(d) Experiments with intruder initial depth between 6 and 8 cm.

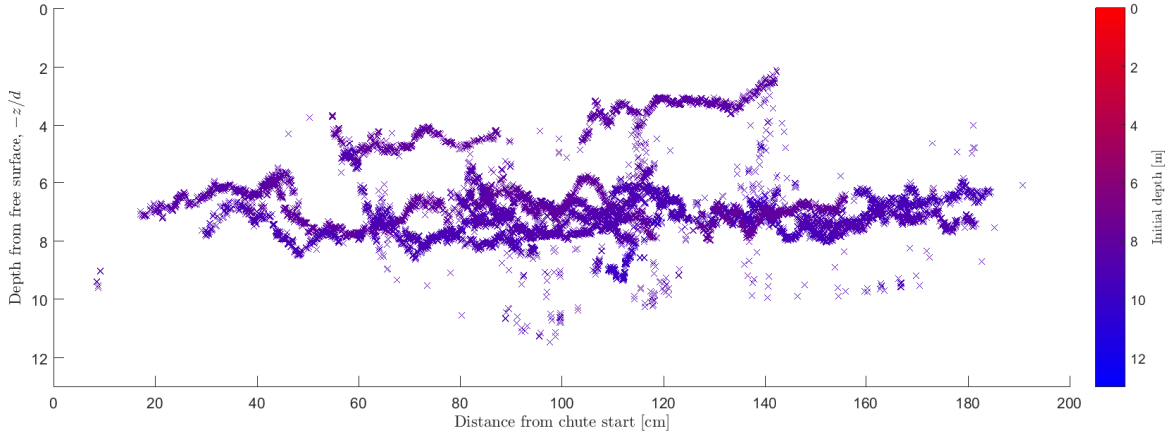

(e) Experiments with intruder initial depth between 8 and 10 cm.

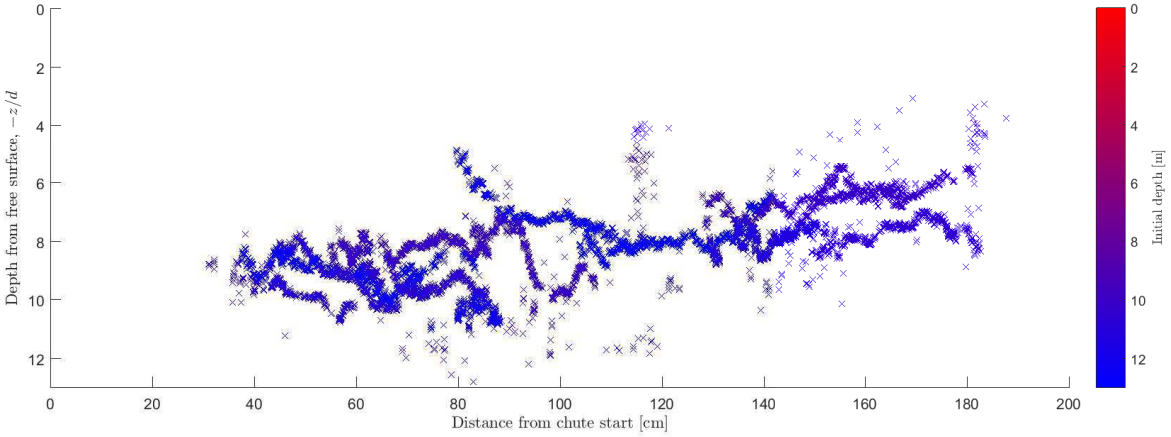

(f) Experiments with intruder initial depth over 10 cm.

Figure 6.7: Tracking of the large intruder particle in a flow of small discs. Each plot shows the results corresponding to experiments whose intruder entered the flow within a given depth interval. The colour of the experimental plots marks the intruder initial depth.

different colours. The colours represent the average initial depth of the intruders corresponding to each experiment. The shaded regions of colours matching the respective

lines show the standard deviation of the averaged ensembles.

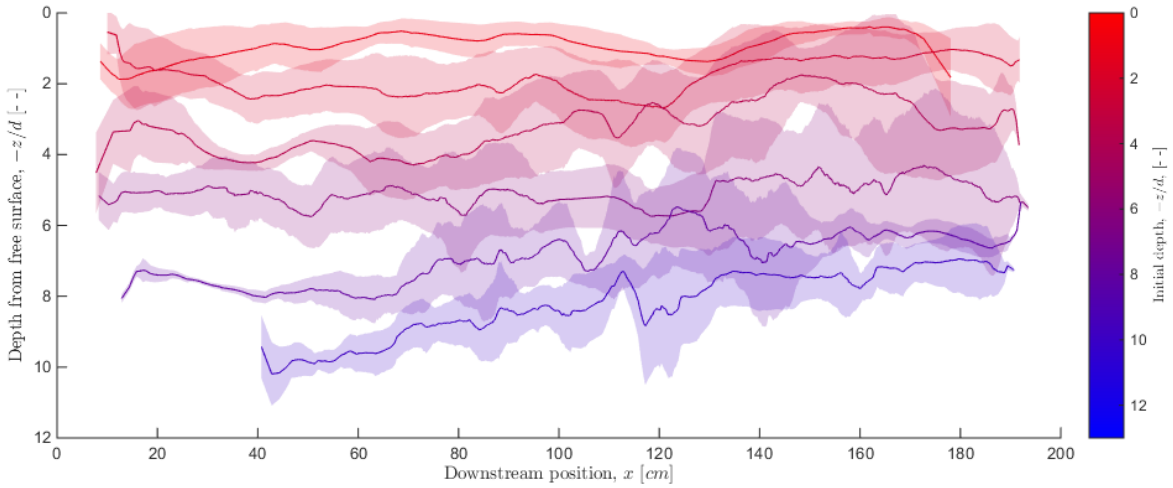

Figure 6.8: Average paths and standard deviations of an intruder large particle (22 mm in diameter) in a steady flow of small ones (11, 12 and 13 mm). Each line from the top down, corresponds to the depth-averaged results shown in Figures 6.7a-f. The shaded regions bound the standard deviation of the measurements of each category at each location.

Ideally, we would require a large data set that captures the intruder particle travelling along each possible path. In Figure 6.7e we see a clear example of a path of a segregating particle not being completely tracked along the chute. In consequence we are aware that many more experiments need to be carried out in order to have a thorough set from which to make probabilistic inferences.

Nevertheless, Figure 6.8 does show a tendency for the averaged paths to approach the free surface as the intruder travels downstream, particularly for intruder particles that entered the flow at depths larger than 4 cm. In addition, we observe that the standard deviation of the data tends to increase downstream as well. We interpret that this latter observation is a consequence of a higher likelihood of intruder particles to have been raised onto upper layers further downstream. We thus confirm that the probability of an intruder to rise in the flow is larger than the probability that it descends, so the distribution of probabilities will follow a skewed normal distribution rather than a standard one. However, we need more experimental data to determine the exact shape of this distribution, and its dependency with the flow kinematic variables.

6.3.2 Segregation mechanisms

We take a closer look at the experiments where the intruder particle moves up a layer as it is tracked in a single experiment. Because we can clearly distinguish which contacts carry forces from the photoelastic response around it, we look for patterns in the force

network when these jumps or *segregation events* occur. We find that the intruder mostly oscillates with the surrounding small particles, except when it distinctively jumps a layer to end up above the particles that used to surround it. We distinguish two distinct types of mechanisms by which segregation events happen.

Most often, we observe that the intruder particle is forced onto an upper layer. In these events, we see distinct force chains extending from the base of the flow and through the large particle. Then, as the small particles in the layer above it travel faster, they apply visible shear on the intruder so that is levered over a small particle below/in front of it, that also formed part of the force chain. Figure 6.9 shows an example experimental image and a diagram of the mechanism at work. The blue depict that the top particles travel faster in the flow than the lower ones. The red line joins the particles that form part of a force chain, which is likely to be directed at $-20°$ to the direction of flow, as inferred from Figure 6.5. At this angle, consecutive particles along a chain will be in different layers, and will therefore travel at different speeds. Focusing on a large particle in the chain, the forces on its load-bearing contacts (the orange arrows in Figure 6.9b) have a compressive component originating in the formation of the force chain, and a shearing component due to the shear rate. As the particle above it in the force chain moves faster, it produces a forward shear force, and vice versa at the lower contact. As a result, we observe the large particle is levered over the lower contact and pushed upwards.

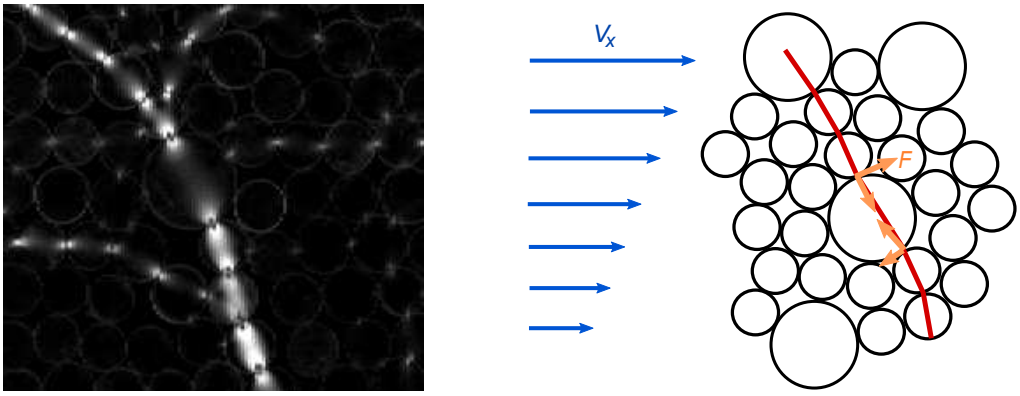

(a) (b)

Figure 6.9: (a) Experimental image and (b) diagram of the segregation mechanism we observe causing the large particles to be pushed upwards. The blue arrows represent the velocities of the particles in each layer increasing linearly with height. The red lines represent the path of the force chain for this particular example. The orange arrows represent the forces acting on a large particle, which are due to the compressive forces forming the force chain and shear forces originating in the difference in velocities between particles at different heights.

This mechanism is not quite *squeeze expulsion*, because the force chains we observe do not break from being compressed, but as a consequence of the particles that form

the force chain travelling in different layers and therefore at different speeds. Squeeze expulsion would require larger compressive forces and small frictional forces at the load-bearing contacts (otherwise the chain would not buckle). Instead, the forcing of an intruder onto an upper layer is due to a *levering* effect, brought on by shearing forces between particles in different layers.

This mechanism includes chains of particles rather than random forces between individual pairs of particles. Therefore, we can relate this result with the characteristics of force chains we were able to draw earlier. We found that in both mono-dispersed and uniformly bi-dispersed media (and we assume, for every bi-dispersed distribution in between), force chains tend to form in preferential directions. For this experiment in particular, we saw a larger proportion of forces exerted in the direction of basal friction and gravity. We can approximate that most force chains in the bulk of a flow form in the direction of gravity, which is at an angle to the direction of flow in gravity-driven flows. Then, this mechanism will cause particles to be thrusted towards the free surface into upper layers. Moreover, we found from the uniformly bi-dispersed experiments that large particles are more likely to form part of force chains, which would indicate a preference for this upward-thrusting mechanism to affect large particles over smaller ones.

On a few occasions, an intruder is observed to move onto a layer above it smoothly without it being affected significantly by surrounding force chains in the levering mechanism just described. On these occasions the intruder is led upwards by the inherent oscillations with which it travels in any layer. These instances of a segregation event are attributed to diffusion. As we only track the intruder as it moves up layers but never down, we interpret that diffusion has an asymmetric effect on large particles. This may be explained as a coupling of diffusion and kinetic sieving causing a larger likelihood of smaller particles to fall, while diffusion and the levering mechanism raise large particles towards the free surface.

6.4 Discussion

By investigating the distribution of forces in bi-dispersed flows we obtained two relevant results. The first result is that Large particles are more likely to form part of force chains and secondly that force-chain directional spread is affected by bi-dispersity.

Firstly, we showed that the large species of particles is more likely to form part of force chains than the smaller species. This result agrees with previous reports in literature [9, 4, 7], and is explained by the fact that larger particles have more surface area on which it can form contacts with other particles. It is therefore more likely that one of the numerous contacts on large particles will be force bearing, than it is for the

fewer contacts on small particles.

Secondly, by plotting a histogram of the number of forces measured in all directions, we found that although force chains in both mono- and bi-disperse media are more likely to form in the directions of the bulk forces, we are relatively more likely to find forces in other directions in bi-dispersed flows. We interpret from this result that force chains form in a wider spread of directions in the bi-dispersed case. This can be explained by the increase in disorder in bi-dispersed media, which is evidenced by the fact that the packing fraction profiles, Figure 6.2, have smaller amplitudes and collapse up to a lower height. It would be interesting to quantify, in the future, how the degree of poly-dispersity affects the force direction distribution.

These two results are relevant because they impact the main mechanism that we observed causes large particles to be pushed towards the free surface. By tracking a single large intruder particle, we were able to isolate distinct occasions when it is visibly forced onto the layer above the one it had been travelling in. On these occasion, the large particle was compressed in a force chain. As the different particles usually travel along different layers, the top of the force chain travels faster than the lower end. Then, strong downstream shear forces between particles in the force chains in different layers are sometimes enough for the sheared particles to be levered over the lower particles, and thus they are pushed upwards towards the free surface. Whether these shearing forces are enough to lever a particle into the upper layer depends on the strength of the compressive forces, the angle of the chain and the particle frictional properties. This levering mechanism is strongly dependent on the structure of the force chains. The fact that large particles are more likely to form part of force chains implies that a higher proportion of large particles than small ones are likely to be affected by this levering mechanism. Moreover, as force chains tend to form in the direction of gravity, this mechanism explains why gravity plays a role in the size segregation of particles in free-surface flows. Force-chain directional spread being affected by bi-dispersity furthermore suggests that the ratio of large to small particles, and eventually the degree of polydispersity, also affects the rate of segregation.

On some other occasions, the lack of significant forces indicates diffusion plays a role in the segregation of the different-sized particles. However, the lack of cases where large particles seem to fall implies that kinetic sieving is more important than diffusion in our relatively slow and dense flows. We surmise that the speed of the particles and the packing fraction will affect the likelihood of particles falling into gaps due to gravity (higher for slow flows) or due to diffusion (higher in fast flows), as well as the likelihood of large particles falling (higher for dilute cases) as opposed to only the small ones (higher for dense flows).

Bibliography

[1] K. E. Daniels, J. E. Kollmer, and J. G. Puckett. Photoelastic force measurements in granular materials. *Review of Scientific Instruments*, 88(5):051808, 2017.

[2] V. N. Dolgunin and A. A. Ukolov. Segregation modeling of particle rapid gravity flow. *Powder Technology*, 83(2):95–103, 1995.

[3] F. Göncü and S. Luding. Effect of particle friction and polydispersity on the macroscopic stress–strain relations of granular materials. *Acta Geotechnica*, 8(6):629–643, 2013.

[4] K. M. Hill and D. S. Tan. Segregation in dense sheared flows: gravity, temperature gradients, and stress partitioning. *Journal of fluid mechanics*, 756:54–88, 2014.

[5] J. E. Kollmer. Photoelastic grain solver: https://github.com/jekollmer/pegs.

[6] S. Savage and C. Lun. Particle size segregation in inclined chute flow of dry cohesionless granular solids. *Journal of Fluid Mechanics*, 189:311–335, 1988.

[7] L. Staron and J. Phillips. Stress partition and microstructure in size-segregating granular flows. *Physical Review E*, 92(2):022210, 2015.

[8] L. Staron and J. C. Phillips. How large grains increase bulk friction in bi-disperse granular chute flows. *Computational Particle Mechanics*, 3(3):367–372, 2016.

[9] C. Voivret, F. Radjai, J.-Y. Delenne, and M. S. El Youssoufi. Multiscale force networks in highly polydisperse granular media. *Physical Review Letters*, 102(17):178001, 2009.

CHAPTER 7

Conclusions

7.1 Summary of results

This thesis investigates the distribution of forces in free-surface granular flows. Unlike in classical fluids, forces in granular media are distributed unevenly along paths called force chains. Despite this marked difference in the fundamental structure of force distribution, granular media are often modelled as a continuum. Our first aim is to characterise the distribution of forces while assessing how side-wall friction affects our results. Secondly, we wish to evaluate existing rheology theories in an experimental context to test the fundamental physical processes that assume relationships between the flow kinematics to the dynamics. Finally, given the success of the continuum approach towards describing some granular behaviour, we want to explain what properties of the granular force distribution are behind phenomena that do not occur in classical fluids. We focus on size segregation as a clear example of a granular-specific phenomenon.

Our study of the distribution of forces in 2D granular flows is based on novel experiments that apply the photoelastic technique to observe and quantify inter-particle forces in the bulk of an avalanche. This technique (described in detail in Chapter 2) is based on the material property of *photoelasticity*, by which clear materials change refractive index anisotropically when a force is applied on them. As a result, the polarisation of the light transmitted through a clear photoelastic material under stress changes by an amount that depends on the magnitude and direction of the forces applied on the material. In our experimental setup (described in detail in Chapter 3), we create an avalanche of 2D photoelastic discs, and record (with a high-speed camera) the profile of the avalanche as it passes in between a pair of opposite polarisers. The polarisers allow the transmission of light when the photoelastic discs that make the avalanche are under stress. Then, besides tracking the individual particles as they pass

in front of the camera, we can relate the light patterns recorded in every frame to inter-particle forces. The experimental setup was used for three sets of experiments, that are described in Chapters 4, 5 and 6, respectively.

In Chapter 4, we produce mono-dispersed avalanches over two types of topography: smooth and rough. The gravity-driven dry granular flows are in the slow to intermediate regime ($I \leq 1$), dense ($\varphi \approx 0.8$) and thin ($h \approx 10d$). We measure constant and uniform density and quasi-linear velocity profiles through particle tracking at several points down the chute. In rough base experiments we show that an increase of basal roughness implies an increase of the dynamic angle of repose, and the formation of a super-stable heap over which the particles flow in dense inertial regime. From the measured forces we obtain coarse-grained profiles of all stress tensor components at various positions along the chute. The discreteness of the system leads to highly fluctuating individual force chains which form preferentially in the directions of the bulk external forces; in this case gravity and basal friction. The behaviour of the coarse-grained stress tensor within a dynamic granular flow is analogous to that of a continuous fluid flow, in that we observe a linear increase of the mean pressure with depth. Furthermore, we identify a preferential direction for the principal stress orientation, which depends on the local magnitudes of the frictional and gravitational forces.

Chapter 5 focuses on experiments over an even rougher base where the super-stable heap is thickest. Using particle tracking and photoelastic force measurements we also report coarse-grained profiles for packing fraction, velocity, shear rate, inertial number and stress tensor components, from which we find that the stress ratio effectively decreases with depth. Then, we look at the transition between a dense-inertial flow and a creeping zone underneath it. We define a quantitative measure for the rate of generation of new force chain networks and we observe that fluctuations extend below the boundary between dense flow and quasi-static layers. Our measurements of the non-dimensional stress ratio show that our experiments lie within the local rheological regime, yet we observe rearrangements of the force network extend into the quasi-static layer where shear rates practically vanish. Our results therefore suggest that in quasi-static regime the shear rate is no longer proportional to the rate of generation of new force chains, as is assumed in local models. This elucidates why non-local rheology models rely on the notion of stress diffusion, and we thus propose non-local effects may in fact be dependent on the local force network fluctuation rate. We furthermore propose the local force fluctuation rate as an appropriate measure of granular fluidity, and suggest that our method of measuring it through photoelasticity could be used to fully characterise the cooperative length used in non-local models.

Chapter 6 describes results from experiments where we produce bi-dispersed 2D flows. We compare the mono-dispersed avalanching flows discussed in Chapters 4 and

5 to experiments where flows are composed of a uniform bidisperse mixture of two size types, and experiments where a single large particle is tracked in a flow of smaller type particles. We make direct observations on how differences in the force network between mono- and bi-dispersed avalanching granular media lead to the mechanisms that push large particles towards the free surface, driving granular size segregation. Firstly, we observe that large particles are relatively more likely to form part of force-chains than the smaller type, and show that the force direction distribution has a wider spread in bi-disperse media. We then link these two results, and the fact that force chains tend to form in preferential directions, to the factors that impact squeeze expulsion and kinetic sieving as the main segregation mechanisms. This work provides new evidence of the physical processes that drive granular size segregation, and particularly those behind the upward thrust on larger particles. In particular, we show that squeeze expulsion can be both size- and direction-preferential, and reason how the degree of polydispersity, the flow inclination angle, and the shear rate profile affect the local rate of segregation. In doing so, our revised squeeze expulsion model quells the criticisms made to segregation models based on the geometric probabilities of the different segregation mechanisms taking place.

Up to this point, each of the results chapters have focused on the observations drawn from the set of experiments they describe. In the following section, we assess how the results from all experiments explained in the previous chapters combine to build answers to the questions that motivated this study.

7.2 Answers to the motivating questions

In broad terms, this thesis has been motivated by the current lack of full understanding of how forces distribute in granular flows. Experimental studies in the field of granular rheology are particularly scarce due to the experimental limitations brought on by the opacity of granular particles and the difficulty to measure forces within flows non-intrusively. For this PhD work we therefore aimed to carry out an experimental study based on a new application of the photoelastic technique, where individual inter-particle forces can be quantified. We aimed to put this information, which has never been collected experimentally before, in the context of existing theories, and draw our own conclusions on their validity.

In the Introduction chapter we laid out three specific questions on which we focused our research, which we aimed to investigate experimentally by applying the photoelastic technique. These questions are complementary to each other and summarise our subtopics of interest within granular flows. The motivation of this work was to apply the photoelastic technique to (1) characterise the force network in granular flows in

confined channels, (2) describe non-local effects in terms of microscopic local variables, and (3) describe how the force network in granular media differs from the force distribution in classical fluids in a way that leads to granular-specific behaviour, specifically size segregation.

7.2.1 Force networks in granular flows in narrow channels

Unfortunately, at this stage the photoelastic force-measuring technique is not sensitive enough to determine what fraction of particle motion is due to inter-particle interactions as opposed to side-wall friction. The experimental technique sensitivity naturally filters the forces due to inter-particle interactions that are a few times larger than the average disc weight. However, with this information we have access to the contacts that form the strongest force chains.

We found that these force chains tend to form in the directions of the external forces acting on the bulk: in this case gravity and basal friction. This means that force chains that seem random in fact form in preferential directions. This is true in both in mono- (see Section 4.3.1) and bi-dispersed (see Section 6.2.2) media, but we show that the dispersion in the mean number of forces that are exerted in each direction indicates that the spread of force direction distribution is sensitive to the degree of polydispersity. Moreover, regardless of the trends in the distribution of inter-particle forces, our coarse-grained stress tensor component profiles show that on average pressure increases linearly with depth.

In Section 4.2.2 we confirm that 2D flows of discs over a rough base form the characteristic velocity profile in depth of 3D granular flows in narrow channels [16, 9, 4, 1, 6]: a moving layer in dense inertial regime flows with a linear velocity profile over a super-stable heap (SSH) in the quasi-static state. The motion of particles in the quasi-static layer tails off exponentially with depth from the boundary between layers. The significance of this result is that it implies pressure from the particles on the walls increase linearly with depth on average, which is not necessarily obvious for 2D particles as they are not all in contact with the walls at the same time. If pressure on the side-walls increases with depth from the free surface, then so does side-wall friction.

Interestingly, the experiments over a smooth base also show a quasi-linear velocity profile, but these flows do not form a SSH. Instead, the flow approximately maintains its thickness and velocity profile shape along the whole chute. We interpret that the difference in velocity profile originates in the higher velocities achieved in experiments over a smooth base, which are possible due to the high slip condition at the chute base. The fact that the flow does not thin and accelerate indicates that side-wall friction at the speed at which the particles travel in smooth-base experiments balances the

downstream component of gravity. Indeed, we find that at an angle of inclination of 15° the flow does not reach a steady state, and we suspect that at higher angles than 20° the flow would accelerate downstream. Hence, we interpret that side-wall friction is sensitive to the particle velocities. In contrast, when the base is frictional, a higher inclination is needed to balance the upstream shear forces supplied by side-wall friction and basal roughness. This extra inclination is supplied by the SSH, where the combined shear transferred from the base through several layers of discs, and the side-wall friction (increased by the pressure discs transfer to the walls from the layers of particles above it) is large enough to balance the downstream component of gravity and prevent motion.

As side-wall friction is not a point force that applies on the disc edges but a shearing force on the disc faces, it does not affect our photoelastic measurements. The forces we measure through the photoelastic technique are only due to inter-particle interactions. Thus, because at higher depths from the free surface side-wall friction plays a greater role against particle motion, we see in Section 5.2 that the stress ratio μ measured using the photoelastic technique, decreases with depth, as predicted by Jop *et al.* (2007) [10]. Thus, our experimental results confirm that the pressure increases linearly with depth, and that a Coulomb type friction is also valid for discs in 2D flows. Furthermore, we validate the theoretical and numerical models that assume that the quasi-static heap that forms underneath a moving layer in granular flows in narrow channels is self-stabilised.

7.2.2 Microscopic description of fluidity and non-locality

We explained in Section 1.3 that local rheology theory is based on the assumptions that the shear stress depends only on the local shear rate and pressure, and that there is no flow when the stress ratio $\mu = \tau/P$ is valued below the effective coefficient of friction μ_s. However, there are instances where particle motion occurs where these conditions are not satisfied. These instances are explained as a consequence of the state of the system elsewhere and are therefore called *non-local* effects. Non-local rheological models [12, 3, 2] aim to extend the fluidity observed in *local* regimes to regions in the non-local regime whose kinematic behaviour differs from that expected according to classical fluid dynamics. Granular fluidity $g = \dot{\gamma}/\mu$ is thus often chosen as the variable to extend into non-local regions because g offers a constitutive relationship between kinematic and dynamic parameters. However, there is still disagreement on the fundamental definition of granular fluidity in terms of local microscopic variables [13, 11, 21].

In Chapter 5 we define the force-chain fluctuation rate ω from the local variation of the experimental image pixel intensities. Using ω, we show in Section 5.3.3 that there is a monotonic relationship between the $\dot{\gamma}$ and ω for flows in intermediate-I regime,

but that this proportionality breaks down for small shear rates. The result that the shear stress no longer depends on $\dot{\gamma}$ and P in the creeping region evidences why local rheology models often do not work in the quasi-static regime, as this is an assumption on which local models are based.

We furthermore propose ω as an appropriate measure of fluidity in the quasi-static regime. We observe that force chain fluctuations are non-zero where the flow creeps and shear rates are practically zero, and decrease slowly with distance from the boundary between flowing and static layers. We interpret that as long as the force network rearranges, it may sporadically arrange in a way that induces a large local shear force, causing the particles to move discontinuously. We also reason that the higher the fluctuation rate and amplitude, the more likely this is to happen. Therefore, ω provides a universal local valuation of the susceptibility of flow, and is therefore a local representative of granular fluidity.

Other microscopic variables that have been proposed to describe non-local effects are shear stress fluctuations [13], the standard deviation of the strain-rate tensor [11], and velocity fluctuations [21]. However, when flow is creeping, rearrangement events are infrequent, localised and discontinuous, and so we interpret that the definitions of fluidity based on particle velocity and strains will probably underestimate the fluidity. The force fluctuation rate defines fluidity as the likelihood of particle motion to happen, rather than a measure of the motion that actually occurs for the duration of an experiment. On the other hand, we acknowledge that the photoelastic response of our discs magnifies minuscule particle displacements, because the photoelastic response of a material is directly related to strain at the contact point between discs (see Section 2.1). We expect ω can be monotonically (but not linearly) related to strain-rate and velocity fluctuations.

In the dense-inertial regime, where we verify a monotonic relation exists between $\dot{\gamma}$ and ω, the flow is in local regime. Here we observe ω behaves proportionally to the local definition of fluidity, $g = \dot{\gamma}/\mu$, so we infer that ω continues to be an appropriate measure of g in the dense-inertial regime.

On the other hand, we were unable to measure the force chain fluctuation rate ω near the free surface. Firstly, in this region the inter-particle forces are usually light and often below the technique sensitivity. In addition, oscillations of the free surface cause our measurement of ω to be underestimated at depths of up to 2 average particle diameters below the mean location of the free surface. Finally, we suspect the packing fraction may be slightly lower at depths of up to 3 diameters below the surface, which raises the interesting question of how changes in packing fraction affect the force fluctuation rate. Because we expect ω to be affected by the packing fraction, we cannot infer from the current set of data whether ω is a good descriptor of the susceptibility

of flow in the dilute limit at all.

7.2.3 Granular force network and size segregation

Our third aim was to use our novel insight into the instantaneous distribution of forces to capture the mechanisms that drive granular size segregation. Kinetic sieving [14] and diffusion [5] are widely accepted as driving mechanisms, but there is no consensus particularly on the physical origin of the forces that push large particles upwards, away from gravity, and towards the free surface of dry gravity-driven flows. Squeeze expulsion as proposed by Savage & Lunn (1988) [14] is neither size nor direction preferential, so a levering mechanism has been proposed instead [7]. Our experiments provide the first opportunity to directly observe and verify from real experiments what mechanisms are really behind the upward thrust of large particles.

The main mechanism by which we observe large particles being forced onto the layer above the one in which they travelled is indeed more reminiscent of levering than squeezing. On these occasions, the large particle is compressed in a force chain that spans over several layers that travel at different speeds (a shear rate is necessary). Given that we find a high likelihood of forces to form in the direction of gravity, except for very large avalanche flow inclination ($> 45°$), force chains are likely to include particles travelling in different layers. Then, the top of the force chain then travels faster than the lower end, and consecutive particles in a chain exert high shears in a direction that is not parallel to the layer motion, but shifted towards the free surface. Thus, particles in a force chain are sometimes pushed upwards towards the free surface, when there is sufficient space in the layer above or the upward force is large enough to displace the rattlers there. This mechanism therefore explains the role of gravity in the size segregation of particles in free-surface flows. Moreover, the fact that large particles are more likely to form part of force chains [19, 8, 15], implies that a higher proportion of large particles than small ones are likely to be affected by this levering mechanism. Furthermore, kinetic sieving, which favours small particles falling but not large ones, explains why overall the large particles tend to segregate towards the top of the flow while the small ones segregate at the bottom.

We find that the likelihood of force chains forming in the directions of the bulk forces is true in bi-disperse, as well as mono-dispersed media. However, in bi-dispersed flows we observe a higher proportion of forces in other directions. We surmise that this observation is due to force chains having wider directional spread in the bi-dispersed case, which we explain as a consequence of the increase in disorder in bi-dispersed media. It would be interesting to quantify, in the future, how the degree of poly-dispersity affects the spread of the force directions. If the force-chain directional spread is indeed affected by bi-dispersity, then we infer that the ratio of large to small particles,

and eventually the degree of polydispersity, also affects the rate of segregation.

We occasionally also observe large particles moving up a layer without any visible forces being exerted on them. We interpret diffusion to be the driving mechanism in these cases, which would encourage mixing, as it would affect particles of all sizes to move both up and down the medium. However, the lack of cases where large particles seem to fall implies that kinetic sieving is more important than diffusion in our relatively slow and dense flows. We theorize that the speeds of the particles and the packing fraction affect whether particles fall into gaps as a result of gravity or diffusion. We interpret that diffusion will play a more important role in fast, dilute flows. When the flow is dense, large particles are less likely to fall into gaps, but if the flow is slow they have more time to fit into the gaps that do exist. In contrast, when the flow is dilute there is space for both small and large particles to fall into gaps.

7.2.4 Photoelastic technique in dynamic systems

With the aim of studying the distribution of forces in granular flows, we designed and built a complex novel experiment that takes the photoelastic technique beyond any previous application. Our sucess and limitations are in themselves a result of our work that can be useful to other research groups who may chose to use the photoelastic technique for their own research. We have tested the extent to which photoelasticity can be used in dynamic systems with several hundred particles per frame, but for different projects researchers may want to make different setup design decisions. Some examples of design decisions we made to maximise the accuracy of the force measurements by analysing photoelastic patterns are:

- We chose *Clear Flex 50* as the base photoelastic material in spite of having a lower photoelastic coefficient than the alternatives (cut plyurethane sheets and *Vishay* custom-made particles) because *Clear Flex*, once cured, is clearer and diffuses the light it transmits less. As a result the photoelastic patterns are sharper and more likely to be estimated correctly by solving the inverse problem method (see Section 3.4.2). In addition, by casting *Clear Flex 50* instead of cutting a larger piece of photoelastic material, we minimise the chances of residual stresses remaining in the particle rims. If an experiment requires discs under 1 cm in diameter, only *Vishay* would be able to provide particles consistent in shape and without large residual stresses. On the other hand, if a large number of particles are required then cutting polyurethane sheets is the most accessible option.

- The thickness of the discs was chosen specifically for *Clear Flex 50* to observe photoelastic patterns of fringe number smaller than one for the range of expected force magnitudes. The disc thickness is proportional to the fringe number of

the photoelastic patterns produced by a given force. For the magnitudes of the forces expected in our experiments, we chose the disc thickness such that the technique sensitivity naturally filters only the stronger forces (at least three times the average disc weight). Moreover, we wanted the range of expected force magnitudes to produce patterns of fringe number smaller than one, as larger fringe numbers increase the likelihood that the optimisation algorithm for the inverse problem will find a local minimum rather than the global minimum.

- The thickness of the channel was designed to be 2 mm wider than the particles to decrease side-wall friction, but not too thin as to allow for significant toppling that would interfere with the photoelastic measurements. Wider channels could be used for discs of larger diameters and widths.

- The discs needed to be regularly coated in flour to reduce friction with the walls. In addition, the flour coating had the purpose of improving particle tracking by making the transparent discs slightly more visible at the cost of error in the photoelastic force measurements. By adding a small noise to the background of discs, they were more easily found using a Hough Transform but this noise introduced a systematic error when measuring small forces by the inverse problem method (see Section 3.2.3.2).

- The viewing window was large enough to capture several hundred discs per frame. A smaller window would increase the resolution of the discs captured by the camera, which would improve the accuracy of the force measurements. On the other hand, we needed a wide window in order to guarantee it was worth coarse-graining spatially in the downstream and cross-flow directions. We chose the optimal window size such that this was wide enough to have enough discs per frame to coarse-grain but kept the particle resolution high enough to resolve forces through the photoelastic technique. Experiments with different geometries may have different optimal viewing window sizes.

- The circle finding algorithm was designed to minimise the number of false positive and false negative tracked discs. We chose to use a Hough Transform with an intentionally high sensitivity combined with a series of empirical criteria (see Section 3.2.1).

- The exposure time of the camera was chosen precisely so as to be smaller than the duration of inter-particle collisions. The frame rate, however, was chosen separately so as to ensure we captured significant differences between the force network in consecutive frames, as the camera memory size is limited.

In conclusion, the experimental setup was carefully designed to maximise the accuracy of the force measurements using the photoelastic technique. We do not think more accurate results can be obtained with the technology available at the time of writing of this thesis.

7.3 Future work

The technical challenge of applying the photoelastic technique to a dynamic system with hundreds of discs per frame lay in acquiring high quality images at very low exposure times. We feel we achieved the best possible results with the technology available to us, but we acknowledge that with further advancements in high-speed imaging the photoelastic force measurements we obtained can be much improved. In particular, larger memory space to store more frames at higher resolution could improve the performance of the particle tracking and the force-measuring programmes. With more accurate coarse-grained stress tensors, we could measure not only the force-chain fluctuations ω, but we could also investigate the behaviour of the isotropic and anisotropic components of the stress tensor. Pouliquen (2009) [13] proposed fluctuations in the shear stress fluctuations as a measure of fluidity, and decomposing ω into its isotropic and anisotropic components would allow us to compare our results to their theory.

With better image resolution, or a longer focal-length lens, it would also be interesting to experimentally verify the link between force chain fluctuations and strain rate and velocity fluctuations, which are other variables that have been proposed as representatives of granular fluidity. A theoretical approach would be highly dependant on the contact model, and the viscoelasticity of *Clear Flex 50* would greatly complicate a relationship between the observable photoelastic patterns and strains at the contact between discs. On the other hand, experimental studies of strain and velocity fluctuations require extremely high precision in the location of the discs [20], which our current set of data cannot provide. A better understanding of the relationships between the different alternative suggestions for the fundamental definition of fluidity would greatly help to unify the granular community in its use of fluidity to describe non-local models.

In any case, until a more precise stress tensor can be obtained from photoelastic force measurements, the force fluctuation ω as we define it in Section 5.3.1 can continue to offer valuable information. We propose that wherever we measure $\omega > 0$ in the super-stable heap of our experiment, particles may creep. It follows that the lengthscale where we measure force chain rearrangements in the quasi-static region is indicative of the lengthscale at which non-local effects may be observable, introduced by Kamrin & Koval (2012) [12] as the *cooperative length* ξ. This lengthscale is currently only found

empirically, but our method of measuring ω may be used to characterise ξ in terms of microscopic particle properties. If similar experiments were carried out over a deeper quasi-static region, then we propose that the depth at which $\omega = 0$ can be related to the cooperative length used in nonlocal models.

But even in the setup we use we have not used the full potential. The experimental setup was designed to allow for variations of our experiments which we did not have time to investigate in the course of this doctoral study:

- A fourth type of basal roughness, made of 22 mm diameter semi-discs, twice the diameter of the discs used for mono-dispersed experiments, was also prepared. This provides yet another example of a different lower boundary condition if the effect of basal friction were to be investigated in more depth.

- An opening at the top end of the chute was created to eventually attach the strips of semi-discs to a motor that would cause the base of the channel to oscillate. Such experiments would allow an investigation of the impact of basal oscillations on the fluidity of the flow above it.

- Our results presented in Section 6.2.1 suggest that the degree of bi-dispersity, or even poly-dispersity, has an effect on the flow kinematics and dynamics. More experiments can be carried out with a wider range of poly-dispersed mixtures of discs to study this issue in the future.

- All experiments reported in this thesis were produced by filling only one of the two hoppers designed into the setup. The second hopper dropped the discs onto a short mezzanine where they could accelerate before flowing onto the flow produced from discs from the first hopper. The intention for which this second hopper and mezzanine were designed was to be able to study mixing of different disc species, as well as their segregation.

Regarding the last point, we suspect that experiments investigating mixing will encounter the same issues as our experiments to study segregation. We conclude that segregation-driving events (where a large particle is pushed into a higher layer) definitely occur in the first 2 m of flow, but not at a fast enough rate to observe a consistent, clear-cut evolution of the species partial packing fraction profiles. In the experiments with a single large intruder particle, we were able to observe the mechanisms by which large particles were forced upwards, which was our aim. However, it would also be interesting to investigate further the downstream evolution of the mean path and its distribution. For this purpose we would require a smaller ratio of average disc diameter to chute length, and we suspect that mixing experiments would require similar dimensions. For both cases, if the forces are no longer being investigated but we only

wish to use particle tracking data, then smaller non-photoelastic particles could be used instead.

7.4 Final remarks

This work has produced two publications to the day of submission of this report: Thomas & Vriend (2019) [17] and Thomas *et al.* (2019) [18]. Parts of the work summarised in this thesis has been presented at multiple national and international conferences, including APS-DFD, the Granular Matter Gordon Research Conference, IFPRI AGM, Edwards Symposium for Soft Matter, and the 'Granular flows in the environment and industry' Special Interest Group meetings. In addition, we obtained additional funds for materials by fundraising for special exhibitions at public engagement events, including the Cambridge Science Festival 2017 and the Royal Society Science Museum Lates Event 2017.

Moreover, the quality of research carried out for this doctoral study and excellence in presentation skills have been recognised through a number of awards. Personal awards received for outstanding performance are the Vice-Chancellor's Public Engagement with Research Award, 2017 (£1000), IFPRI 2018 AGM Poster & Presentation First Prize ($1000); and STEM for Britain 2019 Bronze Award (£750).

Overall, I am satisfied to conclude years of work with a document that summarises all the results discussed above. I am proud to have made scientifically justified proposals that furthered the community's understanding of the rheology of granular flows, while learning and gaining skills that will further my career.

Bibliography

[1] R. Artoni and P. Richard. Effective wall friction in wall-bounded 3D dense granular flows. *Physical Review Letters*, 115(15):158001, 2015.

[2] M. Bouzid, A. Izzet, M. Trulsson, E. Clément, P. Claudin, and B. Andreotti. Non-local rheology in dense granular flows. *The European Physical Journal E*, 38(11):125, 2015.

[3] M. Bouzid, M. Trulsson, P. Claudin, E. Clément, and B. Andreotti. Nonlocal rheology of granular flows across yield conditions. *Physical Review Letters*, 111:238301, 2013.

[4] R. Delannay, M. Louge, P. Richard, N. Taberlet, and A. Valance. Towards a theoretical picture of dense granular flows down inclines. *Nature Materials*, 6(2):99, 2007.

[5] V. N. Dolgunin and A. A. Ukolov. Segregation modeling of particle rapid gravity flow. *Powder Technology*, 83(2):95–103, 1995.

[6] E. D. Fernández-Nieto, J. Garres-Díaz, A. Mangeney, and G. Narbona-Reina. 2D granular flows with the μ (I) rheology and side walls friction: A well-balanced multilayer discretization. *Journal of Computational Physics*, 356:192–219, 2018.

[7] J. M. N. T. Gray and V. A. Chugunov. Particle-size segregation and diffusive remixing in shallow granular avalanches. *Journal of Fluid Mechanics*, 569:365–398, 2006.

[8] K. M. Hill and D. S. Tan. Segregation in dense sheared flows: gravity, temperature gradients, and stress partitioning. *Journal of fluid mechanics*, 756:54–88, 2014.

[9] P. Jop, Y. Forterre, and O. Pouliquen. Crucial role of sidewalls in granular surface flows: consequences for the rheology. *Journal of Fluid Mechanics*, 541:167–192, 2005.

[10] P. Jop, Y. Forterre, and O. Pouliquen. Initiation of granular surface flows in a narrow channel. *Physics of Fluids*, 19(8):088102, 2007.

[11] P. Jop, V. Mansard, P. Chaudhuri, L. Bocquet, and A. Colin. Microscale rheology of a soft glassy material close to yielding. *Physical Review Letters*, 108(14):148301, 2012.

[12] K. Kamrin and G. Koval. Nonlocal constitutive relation for steady granular flow. *Physical Review Letters*, 108(17):178301, 2012.

[13] O. Pouliquen and Y. Forterre. A non-local rheology for dense granular flows. *Philosophical Transactions of the Royal Society of London A: Mathematical, Physical and Engineering Sciences*, 367(1909):5091–5107, 2009.

[14] S. Savage and C. Lun. Particle size segregation in inclined chute flow of dry cohesionless granular solids. *Journal of Fluid Mechanics*, 189:311–335, 1988.

[15] L. Staron and J. Phillips. Stress partition and microstructure in size-segregating granular flows. *Physical Review E*, 92(2):022210, 2015.

[16] N. Taberlet, P. Richard, A. Valance, W. Losert, J. M. Pasini, J. T. Jenkins, and R. Delannay. Superstable granular heap in a thin channel. *Physical Review Letters*, 91(26):264301, 2003.

[17] A. L. Thomas and N. M. Vriend. Photoelastic study of dense granular free-surface flows. *Physical Review E*, 100(1):012902, 2019.

[18] A. L. Thomas, Z. Tang, K. E. Daniels, and N. M. Vriend. Force fluctuations at the transition between granular inertial flow and quasi-static regions. *Soft Matter, under review*, 2019.

[19] C. Voivret, F. Radjai, J.-Y. Delenne, and M. S. El Youssoufi. Multiscale force networks in highly polydisperse granular media. *Physical review letters*, 102(17):178001, 2009.

[20] H. Xu, A. P. Reeves, and M. Y. Louge. Measurement errors in the mean and fluctuation velocities of spherical grains from a computer analysis of digital images. *Review of Scientific Instruments*, 75(4):811–819, 2004.

[21] Q. Zhang and K. Kamrin. Microscopic description of the granular fluidity field in nonlocal flow modeling. *Physical Review Letters*, 118(5):058001, 2017.

APPENDIX

Particle casting protocol

To produce photoelastic discs in-house, we apply the casting method recommended by Dr Jonathan Barés [1, 2], formerly at Duke University. Although based on his suggested protocol and the recommendations of the product manufacturers, the proportions of materials and exact timings required for the casting were fine-tuned several times before obtaining an acceptable particle quality. We next describe the steps followed to produce, first the mould into which the particles are cast, and secondly the procedure to cast the particles themselves.

Mould casting

The mould into which the particles were to be cast was itself cast from a polished mould cut from a solid aluminium block using CNC (Computer Numerical Control). This primary mould was then used to cast *Mold Star 15 SLOW* (*Smooth-On*), which is an easy to mix and pour two-part resin system, i.e. it is bought as two separate liquids that when mixed react irreversibly to form a platinum silicon rubber of 15A Shore hardness. For the mould casting the following protocol was obeyed, wearing at all times appropriate safety glasses, long sleeves and vinyl gloves (vinyl is the only glove material that does not inhibit the curing):

1. Clean the aluminium mould with a clean cotton bud with no solvent.

2. Pour equal volumes of parts A and B of Mold Star into different plastic cups. (Leave aside to rest for some minutes to allow the entrapped air bubbles to raise.)

3. Spray an appropriate release agent (*Bonda* A. F. H. Spray wax) on the aluminium mould:

    a. Shake well.

   b. Spray with valve fully depressed. When using the mould for the first time it is advised that 3 coats are applied.

   c. Allow to dry before using the mould or applying the next coat of release agent.

4. Pour the separated part B into part A (or vice-versa) and mix slowly and evenly until the mixture takes a uniform colour.

5. Pour the mixture slowly and evenly on the lowest point of the mould.

6. Shake and tap lightly by hand briefly to help the air bubbles out.

7. Allow to cure for at least 5 hours.

Each mould contained enough space for between 15 and 30 discs, depending on the size of the discs fit into the face of the aluminium primary block. The smallest disc size designed were 11 mm in diameter, while the largest were 22 mm in diameter, all of 6 mm thickness. Several moulds were cast for each desired disc size, in order to allow for the production of multiple batches of discs of different diameters at once.

Photoelastic disc casting

The photoelastic discs were produced by casting *Clear Flex 50* into the *Mold Star* moulds. *Clear Flex 50* is also a two-part resin system that cures to form a rubber of hardness 50A. The pot life (time between mixing and the beginning of the hardening reaction) is 25 min, during which time the viscosity of the mix is 0.25 Pa s. Once the reaction begins, the cure time (duration of the reaction) is 16 hr with negligible shrinking.

It is necessary to take appropriate safety precautions when handling this product, as both parts A (*Methylenedicyclohexyl diisocyanate*) and B (*Phenylmercury neodecanoate*) can have adverse health effects. Both parts are irritating to the skin and eyes, but part B is also toxic and can cause lung damage and sensitisation if inhaled. Thus, casting and curing were carried out in a fume cupboard wearing chemical-resistant gloves, long sleeves and goggles.

The casting protocol for *Clear Flex 50* discs from the *Mold Star* mould was as follows, where the asterisks denote optional steps that we did not follow:

1. Clean the rubber mould with a cotton bud.

2. Do not spray the mould with release agent as it sticks to the side of the polyurethane, compromising its clarity.

3. Premix part B briefly.

4. Pour parts A and B in a 1:2 ratio by weight into a plastic container.

5. Mix for at least 3 minutes, making sure to scrape the sides and bottom of the mixing container.

6. To remove trapped air bubbles, subject the mixture to a pressure of 29 in of mercury ($\approx$ 100 MPa) in a vacuum chamber for 2 - 3 minutes. Allow for 2 times volume expansion due to the expansion of bubbles trapped in the fluid.

7. With a syringe, pour the mixture slowly and consistently into the lowest point of the particle moulds. Looking from a position as parallel to the surface as possible, fill the mould until the cast fluid if level with the surrounding surface of the mould.

8. With the mixer or a small spatula remove the last bubble that forms in the mould after about 1 min of pouring. Replace any product removed in the process.

9. *Do not cover during the cure, as this prevents the escape of other bubbles that form.

10. Allow the castings to cure for at least 16 hrs at room temperature. *Best results are obtained if this stage is carried out in a pressure chamber at at least 0.41 MPa.

11. Once cured, allowed the particles to post-cure for 5-7 days at room temperature or for 4-6 hrs in a vacuum oven (that disposes of any toxic fumes that may be produced in the process) to remove the stickiness of their surfaces.

For the purpose of this doctoral study, we cast discs of 11, 12, 13, 20, 21 and 22 mm in diameter, all of which were 6 mm in thickness. Thousands of discs of each size were produced, adding up to a total of over 10 kg of discs.

Bibliography

[1] J. Barés Photoelastic methods. *https://git-xen.lmgc.univ-montp2.fr/PhotoElasticity/Main/wikis/home.*

[2] J. Barés, D. Wang, D. Wang, T. Bertrand, C. S. O'Hern and R. P. Behringer. Local and global avalanches in a two-dimensional sheared granular medium. *Physical Review E*, 5(95):052902, 2017.

Acknowledgements

I want to thank Karen Daniels for her teachings and support in applying the photoelastic technique. I was invited to learn and work with her team on three separate two-week visits, where I was able to gain expertise in the use of the advanced photoelastic equipment at the Daniels Lab in North Carolina State University (NCSU). During my stays, I worked in close collaboration with Jonathan Kollmer and Zhu Tang, with whom I am glad I was able to get to know and form friendly relationships. In addition, I would like to thank Jonathan Barés for his support in the development of the particle casting protocol, which is now applied by researchers at both NCSU and the University of Cambridge.

I am also thankful to Michael Shearer for his insight and support in the coarse-graining algorithm; to Karen Daniels, Michel Louge and Ken Kamrin for our interesting discussions on the interpretation of granular fluidity in terms of force fluctuations; and to Nico Gray, Olivier Pouliquen and Andy Woods for their insightful suggestions of possible research avenues.

But most importantly, I am grateful to Nathalie Vriend for her consistent guidance and instruction as my supervisor, and to Stuart Dalziel for his support as my advisor.

This work is funded by Royal Society Dorothy Hodgkin Fellowship DH120121, Royal Society research grant RG130403, the Cambridge Trust and an IFPRI collaboration grant.